2003

A search for higher twist effects in the neutron spin structure function

Kevin M. Kramer
College of William & Mary - Arts & Sciences

NOTE TO USERS

A SEARCH FOR HIGHER TWIST EFFECTS IN THE NEUTRON SPIN STRUCTURE FUNCTION $g_2^n(x, Q^2)$

A Dissertation

Presented to

The Faculty of the Department of Physics

The College of William and Mary in Virginia

In Partial Fulfillment

Of the Requirements for the Degree of

Doctor of Philosophy

---

by

Kevin M. Kramer

2003

APPROVAL SHEET

This dissertation is submitted in partial fulfillment of

the requirements for the degree of

Doctor of Philosophy

Kevin M. Kramer

Approved, August 2003

Todd Averett

David S. Armstrong

J. Michael Finn

J. Dirk Walecka

Jian-Ping Chen
Jefferson Lab

To the loving memory of John H. Kramer (1918-2003)

CONTENTS

ACKNOWLEDGMENTS

Looking back at the time when I first entered the College of William and Mary in 1997, its remarkable that I could have made such a beneficial life decision based on so little information. I remember thinking that the guy from William and Mary I talked to on the phone was nice and that there was fancy new lab called CEBAF or something nearby, so how bad could it be? It turns out it not only was it not bad, but I can't imagine better places to have studied and done research than the College of William and Mary and Jefferson Lab. This is mostly because so many people at both of these places were willing to invest their time and energy into making me a better scientist and person. I would like to take this space to thank as many of these people as possible for their contribution to this work and my education.

The most fortunate event in my graduate education was when I learned a new professor named Todd Averett was coming to William and Mary from Caltech. and was looking for a graduate student. From the first day I met Todd and joined on as his student, I have benefited from his incredible enthusiasm for science and endless support for all his students. I was lucky to work with an advisor who understood what a student needed to learn and had a great science program from which to learn from. It was also extremely beneficial for me to have an advisor with whom I could discuss the important things in life like the 'Dukes of Hazzard' and the greatness of Shiner Bock.

I was also fortunate to work with Jian-Ping Chen, who as head of the polarized ^{3}He target program in Hall A, was more or less my second advisor. I expect to see many of my fellow students in the polarized ^{3}He program to be running Jefferson Lab in the future because Jian-Ping is a person who not only expects great work from his students, but takes the time to teach the students how to do great work. All the people in the polarized ^{3}He collaboration are grateful for his constant assistance and guidance.

Though there a many people who helped running my thesis experiment I am especially appreciative of two. The first person is Wolfgang Korsch who was co-spokesperson on my experiment and was indispensable during the actual running of the experiment and in helping with the analysis. His hard work helping even with small tasks like winding coils and checking analysis code made being a graduate

student a little less stressful. The second person is Xiaochao Zheng who was the graduate student on the 'sister' experiment to E97-103 with whom I spent many a busy day and night preparing and running our experiments. I could not have asked for a better person to have worked with since she is not only an amazing physicist who did the work of three graduate students, but also a very sweet person who could draw a funny cartoon when the need arose.

I especially thankful for the five graduate students (Alexandre Deur, Karl, Steffen, Ioannis and Pibero) and the two post-docs (Seonho and Sebastien) from the E94-010 experiment who developed the foundation of knowledge on which the polarized ^{3}He experiment was built. Their many technical notes and personal help formed most of what I know about the ^{3}He target and analyzing data in Hall A.

I would like to thank my adviser Todd and William and Mary faculty member David Armstrong for the especially detailed correction work they did on my dissertation. I would also like to thank Keith Griffioen, Mike Finn, Jian-Ping and Dirk Walcecka for helping on my annual review and defense committee.

I would like to thank Xiaofeng Zhu for the help he gave me on my experiment, even though his time was cut short by the idiotic behavior of INS. I wish him well in whatever he does.

I would like to thank Hall A collaborators and staff members for helping run and analyze the experiment. I would point out Ed Folts, Kathy McCormick, Nilanga Liyanage, Bodo Reitz, Bob Michaels and Seonho Choi for taking an especially large share of the work.

I would like to thank the next generation of polarized ^{3}He students Vince Sulkosky, Jaideep Singh, Patricia Solvignon and Aidan Kelleher helping out with my experiment and my analysis.

I would like to thank Paul King, who put up with living with me for three years or so, whose mutual love of great cinema and delightful beverages made for many happy times.

Much gratitude is directed to the rest of the Friday afternoon Green Leafe regulars : Dan, Liz, Jessica, Julie, Wendy, Olivier, Rikki, John, Angus, Chris, Amy, Jason, Ruth, Josh, Keoki, Lisa, Dave, Andrew, and a bunch of other drunks who made every Friday afternoon the best time of the week.

Of course, I wouldn't of made it anywhere without the love and support of my parents, Jack and Kay and my sisters Barbara and Sandra. Needless to say they are the world's greatest family and always were understanding of the commitment and helpful in the completion of my work here at William and Mary.

LIST OF TABLES

LIST OF FIGURES

ABSTRACT

Jefferson Lab experiment E97-103 measured the spin structure function $g_2^n(x, Q^2)$ from $Q^2 = 0.57$ to 1.34 GeV^2 with a nearly constant $x \approx 0.2$. Combining this data with a fit to the world g_1^n data, the size of higher twist contributions to g_2^n can be extracted using the Wandzura-Wilczek relation. These higher twist contributions result from quark-gluon correlations and are expected to increase as Q^2 decreases. This experiment was performed in Hall A with a longitudinally polarized electron beam and a high density polarized ^{3}He gas target. This measurement reduced the error bars on g_2^n in this kinematic region by an order of magnitude and is the first definitive non-zero measurement of g_2^n in the deep inelastic scattering regime. The experiment also found a greater than two standard deviation difference between the experimental value for g_2^n and g_2^{WW} in the three lowest Q^2 points. This is the first evidence of higher twist effects in the deep inelastic scattering regime.

A SEARCH FOR HIGHER TWIST EFFECTS IN THE NEUTRON SPIN STRUCTURE FUNCTION $g_2^n(x, Q^2)$

CHAPTER 1

Introduction

The first evidence that the nucleon has substructure was the measurement by Esterman and Stern [1][2] of the magnetic moments of the proton and the neutron. Because the electron and proton have the same magnitude of electric charge the magnetic moment of the proton, corrected for the mass, was expected to be the same in magnitude as that of the electron. The measured moment of the proton turned out to be 2.7 times larger. Moreover, the neutron is electrically neutral and was expected to have no magnetic moment at all, but was instead found to have a magnetic moment almost twice as large as that of the electron! Consequently, one had to conclude that the charge in the nucleon was not point-like, but distributed in space in such a way that some (in the case of the proton) or all (in the case of the neutron) of the electric fields cancelled. Seventy years have passed since this experiment and there is still much to be learned about the charge distributions of the nucleon.

In the mid-1950s, McAllister and Hofstadter [3] began the first electron scattering experiments to study nucleon (meaning proton or neutron) structure. They found that the nucleon was indeed an extended object and many theories were constructed to describe what the nucleon was made of and what held it together. With Feynman's formulation of the parton model [4] and its subsequent confirmation by SLAC experiments in the late 1960's and early 1970's, the correct degrees of freedom for the nucleon became clear. These were interpreted to be the quarks and gluons proposed by Gell-Mann [5] and Zweig [6] in their efforts to explain hadron mass

spectroscopy.

The relativistic theory describing the interaction of quarks by exchange of gluons, and therefore the structure of the nucleon, become known as quantum chromodynamics (QCD). QCD is still the considered the correct theory of nucleon physics, but because it is a non-Abelian theory it is has been difficult to describe the properties of the nucleon using QCD formalism. The challenge for today's physicists studying nucleon structure is to untangle the more difficult aspects of QCD through experiments and theoretical insight so that a clearer picture of the nucleon and the strong interaction can emerge.

In the 1980's scientists became interested in using spin degrees of freedom to understand nucleon structure, as Estermann and Stern had used charge properties. Physicists developed new polarized beams and polarized targets to study how the total spin of the nucleon was distributed among the quarks and gluons. This work, which began at SLAC and continued at CERN, DESY and Jefferson Lab, showed that the study of nucleon spin structure provided a wealth of information about QCD and nucleon structure.

The experiment described by this dissertation, Jefferson Lab experiment E97-103, follows in the tradition of these experiments. It uses spin-dependent quantities to isolate and quantify the magnitude of quark-gluon interactions, known as higher-twist effects. This will provide important data to allow theorists to move beyond simple quark models that have been in use so far. It is hoped that a precise measurement of these higher twist effects will be a signficant step in understanding nucleon structure through QCD.

CHAPTER 2

Inclusive Electron Scattering

2.1 Introduction

There are many reasons that inclusive electron scattering is a useful tool for studying nucleon structure. First, electrons can interact with hadronic material only through the electromagnetic and weak interactions (gravity is, of course, negligible between small masses). This allows the electrons to probe the entire charge distribution of the nucleon or nucleus, unlike hadron-hadron scattering which typically probes only the surfaces of the hadronic material. Furthermore, electron scattering is dominated by the one-photon exchange electromagnetic interaction. This is fortunate since this ensures that the electron survives the scattering process and scatters in an uncomplicated manner.

In inclusive electron scattering, only the scattered electron is detected which means it is insensitive to any specific reactions and measures the scattering from all possible interactions. In exclusive or semi-inclusive scattering, one detects the scattered electron along with some or all of the other particles produced, which allows one to separate out specific reaction channels. Inclusive scattering has the experimental advantage of only requiring the detection of the scattered electrons. Unfortunately, it has the disadvantage that there is ambiguity about which interaction the electron underwent. Nevertheless, one-photon exchange dominates the cross-section and accurate measurements of the nucleon substructure are possible with some usually moderate corrections.

2.2 The Framework of Polarized Inclusive Electron Scattering

2.2.1 Kinematic Variables

In inclusive electron scattering experiments, the structure of a target nucleon or nucleus is described in terms of a differential cross section from the process

$$l(k) + N(p) \longrightarrow l(k') + X(p') \tag{2.1}$$

where $l(k)$ is an electron with four-momentum k, $N(p)$ is a nucleon or nucleus with four-momentum p and $X(p')$ is the hadronic final state with momentum p'. In inclusive electron scattering, all hadronic final states are included in the cross section. A Feynman diagram for this process is shown in Fig. 2.1. The weak interaction, though present, is small in comparison to the electromagnetic interaction and is ignored for this discussion.

Before writing the cross section for this process it is useful to describe some basic variables. Table 2.1 is a list of the most common kinematic variables used in parameterizing electron scattering. Table 2.2 is a list of invariant parameters.

In general, the structure functions (which will be mentioned later in the chapter) are parameterized in terms of Q^2 and x. This is because at high Q^2 the structure functions vary slowly with Q^2 and can be considered a function only of x (this is known as *Bjorken scaling* and will be discussed later in the chapter). However, it is often useful to present the structure functions as functions of Q^2 and W. This is because certain features of the cross-section, (such as the pion threshold, elastic and quasi-elastic scattering and the peak of the Δ resonance) take place at fixed values of W. Its also not unusual to see the structure functions in terms of Q^2 and ν since ν is a convenient variable for experimentalists.

The mass term M is the mass of the proton (even when describing a neutron cross-section) corresponding to the structure function measured. In the case of nuclear elastic scattering, the mass of the entire nucleus is represented by M_T.

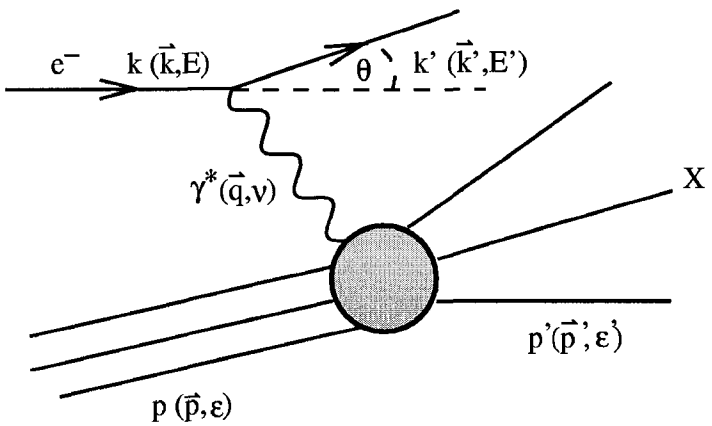

Figure 2.1: *Lowest order Feynman diagram for electron scattering on a fixed target.*

Parameter	Expression	Description
ε		initial target energy
ε'		scattered target energy
p	$(M,\vec{0})$	initial target 4-momentum (for a fixed target)
E		incident electron energy
E'		scattered electron energy
ν	$E-E'$	energy transfer
k	$(E,\vec{k})$	incident electron 4-momentum
k'	$(E',\vec{k'})$	scattered electron 4-momentum
θ		electron scattering angle
q	$k-k'$	4-momentum transfer

Table 2.1: *A table of important kinematic factors expressed in the lab frame.*

Parameter	Invariant Expression	Lab Frame Expression	Description
Q^2	$-q^2$	$4EE'\sin^2(\frac{\theta}{2})$	four-momentum transfer squared
W^2	$M^2+p\cdot q+q^2$	$M^2+2M\nu-Q^2$	squared invariant mass of resulting target system X
x	$\frac{Q^2}{2p\cdot q}$	$\frac{Q^2}{2M\nu}$	Bjorken scaling variable
y	$\frac{q\cdot p}{k\cdot p}$	$\frac{\nu}{E}$	fraction of energy loss

Table 2.2: *A table of important kinematic factors expressed in terms of invariants and in terms of lab frame parameters.*

2.2.2 Deriving the Differential Cross-section

The differential cross-section can be written in terms of a scattering matrix T_{fi} and kinematic factors [7]

$$d\sigma = \frac{\overline{|T_{fi}|^2}}{\mathcal{J}} \frac{d^3k'}{2E'(2\pi)^3} \frac{d^3p'}{2\varepsilon'(2\pi)^3} (2\pi)^4 \delta^4(k - k' + p - p') \tag{2.2}$$

where $\mathcal{J} = 4p \cdot k$ which reduces to $4M\varepsilon$ in the lab frame. The scattering matrix can be written :

$$T_{fi} = \frac{e^2}{q^2} \langle l(k')|j^\mu(0)|l(k)\rangle \langle X(p')|J_\mu(0)|N(p)\rangle \tag{2.3}$$

where j^μ and J^μ are the leptonic and quark electromagnetic currents as given by the Standard Model [8, 9, 10]. Squaring this matrix gives :

$$\overline{|T_{fi}|^2} = \frac{e^4}{q^4} L_{\mu\nu} W^{\mu\nu} \tag{2.4}$$

where $L_{\mu\nu}$ and $W^{\mu\nu}$ represent the leptonic and hadronic vertex tensors respectively. One can then write the differential cross-section as

$$\frac{d^2\sigma}{d\Omega dE'} = \frac{\alpha^2}{q^4} \frac{E'}{E} L_{\mu\nu} W^{\mu\nu} \tag{2.5}$$

where $\alpha = e^2/4\pi$.

2.2.3 The Leptonic and Hadronic Tensors

It is helpful that these tensors can be separated, since $L_{\mu\nu}$ is well-known from quantum electrodynamics (QED) [7]

$$L_{\mu\nu} = \sum_{s'} \overline{u}_s(k) \gamma_\mu u_{s'}(k') \overline{u}_{s'}(k') \gamma_\nu u_s(k) \tag{2.6}$$

$$= 2\left[k_\mu k'_\nu + k'_\mu k_\nu - g_{\mu\nu} k \cdot k' + i\epsilon_{\mu\nu\alpha\beta} s^\alpha q^\beta\right] \tag{2.7}$$

where $s_\mu = \overline{u}\gamma_\mu\gamma_5 u$ is the lepton spin vector and the electron mass is neglected.

The hadronic vertex tensor must contain all possible transitions from the nucleon or nucleus into any possible excited state [7]. This term is where the strong

interactions appear in the cross section. A general form of this vertex can be written

$$W_{\mu\nu}(P,q) = \frac{1}{2M}\sum_X \langle N_s(p)|J_\mu(0)|X(p')\rangle\langle X(p')|J_\nu(0)|N_s(p)\rangle \cdot (2\pi)^3\delta^4(q+p-p') \tag{2.8}$$

where the initial nucleon spin state is denoted by $s = \pm\frac{1}{2}$. This tensor can be presented in a form using the completeness of the states $|X\rangle$:

$$W_{\mu\nu} = \frac{1}{4\pi M}\int d^4z e^{iq\cdot z}\langle N_s(p)|J_\mu(z)J_\nu(0)|N_s(p)\rangle \tag{2.9}$$

or it can be written in terms of a current commutator as

$$W_{\mu\nu} = \frac{1}{4\pi M}\int d^4z e^{iq\cdot z}\langle N_s(p)|\left[J_\mu(z), J_\nu(0)\right]|N_s(p)\rangle \tag{2.10}$$

where the extra term, $J_\nu(0)J_\mu(z)$, gives a vanishing matrix element since it produces a delta function $\delta^4(q-p+p')$ that cannot be satisfied [7]. The four-vector z represents the separation on the light cone between the tensors.

The hadronic tensor has separable symmetric and antisymmetric parts as shown here:

$$W_{\mu\nu} = W^S_{\mu\nu} + W^A_{\mu\nu}. \tag{2.11}$$

The most general forms of these tensors, as limited by gauge invariance and parity conservation of the electromagnetic interaction, are:

$$W^S_{\mu\nu} = W_1(\nu,Q^2)\left(\frac{q_\mu q_\nu}{q^2} - g_{\mu\nu}\right) + \frac{W_2(\nu,Q^2)}{M^2}\left(p_\mu - \frac{p\cdot q}{q^2}q_\mu\right)\left(P_\nu - \frac{P\cdot q}{q^2}q_\nu\right) \tag{2.12}$$

and

$$W^A_{\mu\nu} = i\epsilon_{\mu\nu\alpha\beta}q^\alpha\left[G_1(\nu,Q^2)S^\beta + \frac{G_2(\nu,Q^2)}{M^2}\left(S^\beta p\cdot q - p^\beta S\dot{q}\right)\right] \tag{2.13}$$

where $W_1(\nu,Q^2)$ and $W_2(\nu,Q^2)$ are the unpolarized response functions, $G_1(\nu,Q^2)$ and $G_2(\nu,Q^2)$ are the polarized response functions and $S^\mu = \overline{u}(p)\gamma^\mu\gamma_5 u(p)/2M$ is the nucleon spin vector. Thus the physics of the nucleon structure that is accessible in inclusive lepton scattering is all encapsulated in W_1, W_2, G_1 and G_2.

2.2.4 The Structure Functions

Normally, the cross section is not described in terms of the response function, but a set of structure functions displayed here:

$$F_1(x,Q^2) = MW_1(\nu,Q^2), \tag{2.14}$$

$$F_2(x,Q^2) = \nu W_2(\nu,Q^2), \tag{2.15}$$

$$g_1(x,Q^2) = M\nu G_1(\nu,Q^2), \tag{2.16}$$

$$g_2(x,Q^2) = \nu^2 G_2(\nu,Q^2). \tag{2.17}$$

From these structure functions, the relevant forms of the differential cross section can be written.

For the case of an unpolarized beam and target the differential cross section written in terms of lab frame parameters is

$$\frac{d^2\sigma}{d\Omega dE'} = \frac{\alpha^2}{4E^2\sin^4\frac{\theta}{2}}\left(\frac{F_2(x,Q^2)}{\nu}\cos^2\frac{\theta}{2} + \frac{2F_1(x,Q^2)}{M}\sin^2\frac{\theta}{2}\right). \tag{2.18}$$

It is of additional interest that $F_1(x,Q^2)$ and $F_2(x,Q^2)$ are related through the function $R(x,Q^2)$ defined as:

$$R(x,Q^2) \equiv \frac{\sigma_L}{\sigma_R} \tag{2.19}$$

where σ_L and σ_R are the longitudinal and transverse virtual photo-absorption cross sections [11][12]. The relation between $F_1(x,Q^2)$ and $F_2(x,Q^2)$ is:

$$F_1(x,Q^2) = \frac{1+\frac{Q^2}{\nu^2}}{2x\left[1+R(x,Q^2)\right]}F_2(x,Q^2). \tag{2.20}$$

The only spin-dependent terms that survive in the cross-sections are ones that have both electron and target polarization. The electron beam can either be polarized along or opposite to the direction of the electron beam path. The electron beam can be polarized perpendicular to the beam path, but that is not relevant to the physics presented in this thesis. The target polarization can either be in the direction of the electron beam, referred to as longitudinal polarization or perpendicular to the electron beam, referred to as transverse polarization.

The spin-dependent part of the electron scattering cross-section for a longitudinally polarized cross-section is

$$\left(\frac{d^2\sigma}{d\Omega dE'}\right)_{\text{long.pol.}} = \frac{1}{2}\left(\frac{d^2\sigma^{\downarrow\Uparrow}}{d\Omega dE'} - \frac{d^2\sigma^{\uparrow\Uparrow}}{d\Omega dE'}\right) \tag{2.21}$$

$$= \frac{2\alpha^2 E'}{Q^2 E M \nu}\left[(E + E'\cos\theta)\, g_1(x,Q^2) - 2xMg_2(x,Q^2)\right] \tag{2.22}$$

where $\uparrow$ and $\downarrow$ refer to the direction of the electron beam polarization, either along or opposite the beam path, and $\Uparrow$ means a target polarized along the electron momentum direction. When the target is transversely polarized, the spin-dependent part of the cross section can be written

$$\left(\frac{d^2\sigma}{d\Omega dE'}\right)_{\text{trans.pol.}} = \frac{1}{2}\left(\frac{d^2\sigma^{\downarrow\Leftarrow}}{d\Omega dE'} - \frac{d^2\sigma^{\uparrow\Leftarrow}}{d\Omega dE'}\right) \tag{2.23}$$

$$= \frac{2\alpha^2 E'}{Q^2 E M \nu} E' \sin\theta \left[g_1(x,Q^2) + \frac{4xEM}{Q^2} g_2(x,Q^2)\right] \tag{2.24}$$

where $\Leftarrow$ refers to a transversely polarized target. Both polarized cross sections change sign when the target is polarized in the opposite direction (*i.e.* when the target is polarized opposite the electron momentum direction or transversely polarized at 90° rather than 270° when the electron momentum direction is 0°).

2.3 Types of Inclusive Electron Scattering

2.3.1 General Description of Electron Scattering on a Nucleus

The cross-sections described by equations 2.18, 2.21 and 2.23 are quite general and are good for all x and Q^2; however, it is useful to separate different kinematic regions from one another for analysis purposes. The three scattering types that will be described are *elastic*, *quasi-elastic* and *inelastic*.

Elastic scattering occurs in the region where energy transfer (ν) from the electron to target is not large enough to excite the target into higher nuclear or hadronic states, but simply accelerates the nucleus to a new momentum. This means for a

given incident electron energy and scattering angle there is a unique electron scattering momentum. In Fig. 2.2, one can see that the elastic peak in the structure function F_2^A (the superscript A referes to the number of nucleons in the nucleus) is a delta function in x for a single Q^2. Excited nuclear states occur in F_2^A when energy from the probing electron creates a higher-energy configuration of the target nucleus.

Quasi-elastic scattering is elastic scattering off a nucleon (proton or neutron) that is part of a nucleus. It can be approximated as elastic scattering off a nucleon that has some Fermi motion (due to the nuclear binding). This Fermi motion causes the peak to be distributed in x as can be seen in Fig. 2.2 [13].

The resonance region begins where the energy transfer is large enough to create new hadrons. The lower limit is defined at the pion threshhold since pions are the lightest hadrons. At high energy and momentum transfer ($W > 2.0$ GeV) the probing electron behaves as if it were only scattering off a point-like quark. This is known as deep inelastic scattering.

2.3.2 Polarized Elastic Scattering on the Nucleon

Elastic scattering can be seen as a special case of Eq. 2.18 where $W^2 = M^2$ which implies $\nu = Q^2/2M$. Because of this the scattered electron energy for a certain beam energy and scattering angle in the lab frame will always be

$$E' = \frac{E}{1 + \frac{2E}{M}\sin^2\frac{\theta}{2}}. \tag{2.25}$$

This means that cross sections will be expressed in terms of $\frac{d\sigma}{d\Omega}$ instead of $\frac{d\sigma}{dE'd\Omega}$.

The usual formalism of polarized elastic scattering introduces a vector $\vec{S}_A$ to describe the unit target polarization direction as shown in Fig. 2.3 and written [14]

$$\vec{S}_A = \hat{x}\cos\phi^*\sin\theta^* + \hat{y}\sin\phi^*\sin\theta^* + \hat{z}\cos\theta^* \tag{2.26}$$

where θ^* and ϕ^* are the spherical coordinates of the momentum transfer vector $\vec{q}$.

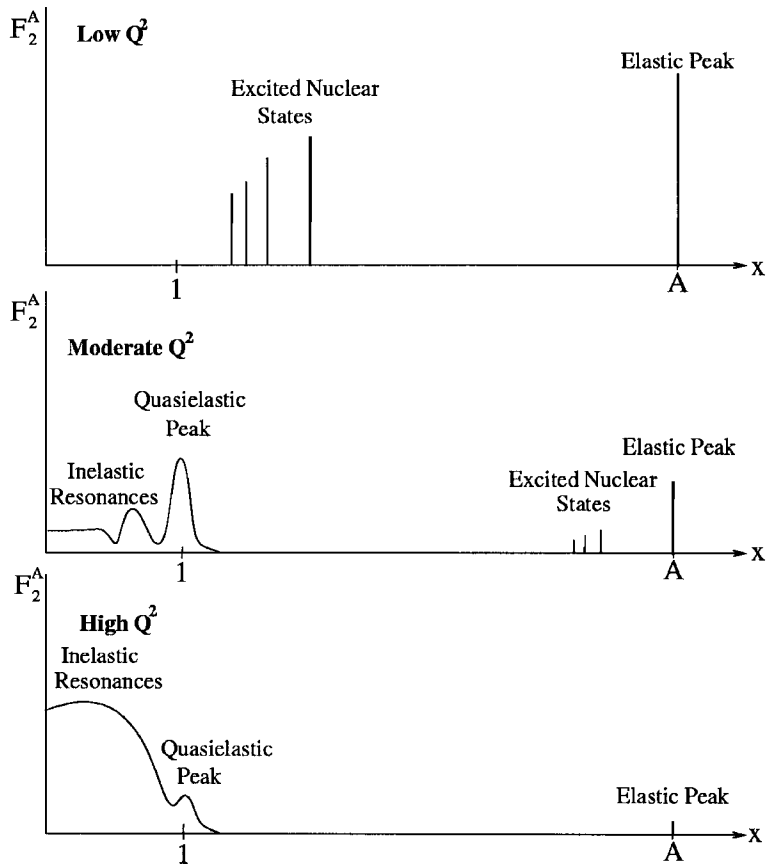

Figure 2.2: *A qualitative description of the unpolarized structure function F_2^A of a nucleus with A nucleons as a function of Bjorken x for different Q^2.*

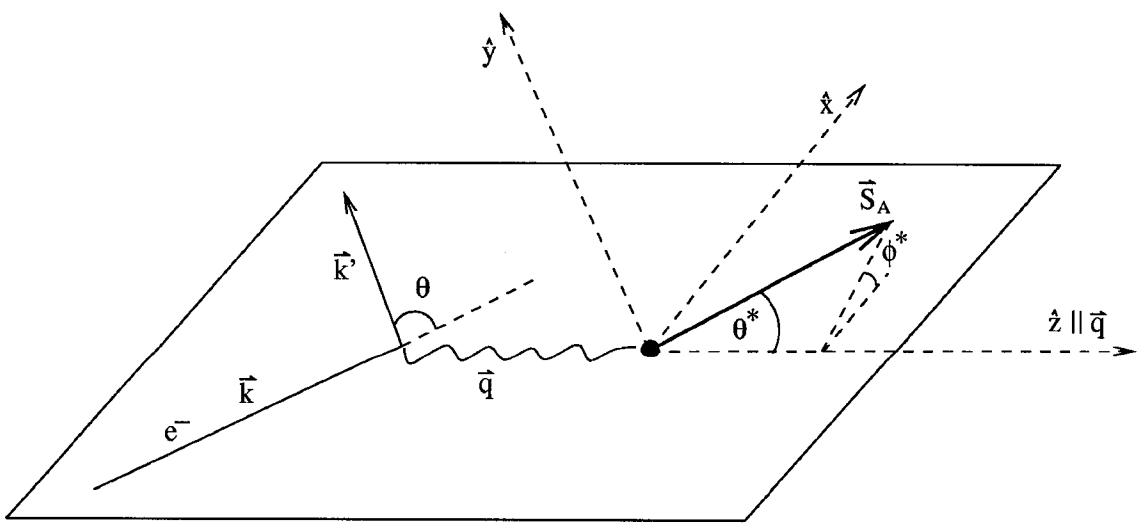

Figure 2.3: *Coordinate system for polarized elastic scattering.*

Substituting this polarization vector in for S and assuming $W^2 = M^2$ one can make the following substitutions into Eqs. 2.12 and 2.13 [15]:

$$W_1(\nu, Q^2) = \frac{1}{2} R_T(Q^2) \delta\left(\nu - \frac{Q^2}{2M}\right) \tag{2.27}$$

$$W_2(\nu, Q^2) = \frac{R_L(Q^2) + \frac{1}{2} R_T(Q^2)}{1+\tau} \delta\left(\nu - \frac{Q^2}{2M}\right) \tag{2.28}$$

$$G_1(\nu, Q^2) = \frac{1}{2}\frac{M^2}{Q^2}\left(\frac{Q^2}{M|\vec{q}^2|}\frac{R_{TL'}(Q^2)}{\sqrt{2}}\right)\delta\left(\nu - \frac{Q^2}{2M}\right) \tag{2.29}$$

$$G_2(\nu, Q^2) = -\frac{1}{2}\frac{M^2}{Q^2}\left(\frac{\nu}{|\vec{q}|}\frac{R_{TL'}(Q^2)}{\sqrt{2}} + R_{T'}(Q^2)\right)\delta\left(\nu - \frac{Q^2}{2M}\right) \tag{2.30}$$

where

$$|\vec{q}|^2 = \nu^2 + Q^2 \tag{2.31}$$

$$\tau = \frac{Q^2}{4M^2} \tag{2.32}$$

and where R_L, R_T, $R_{TL'}$ and $R_{T'}$ are the elastic response functions that depend on the type of target. For nucleon scattering the response functions are written in terms of the elastic and magnetic form factors G_E and G_M:

$$R_T(Q^2) = (1+\tau) G_E^2(Q^2) \tag{2.33}$$

$$R_L(Q^2) = 2\tau G_M^2(Q^2) \tag{2.34}$$

$$R_{T'}(Q^2) = 2\tau G_M^2(Q^2) \tag{2.35}$$

$$R_{TL'}(Q^2) = -\sqrt{2\tau(1+\tau)} G_E(Q^2) G_M(Q^2). \tag{2.36}$$

The differential cross section for unpolarized elastic scattering in the lab frame can be written

$$\left(\frac{d\sigma}{d\Omega}\right)_{\text{unpol.}} = \left(\frac{d\sigma}{d\Omega}\right)_{\text{Mott}} \left[\frac{G_E^2(Q^2) + \tau G_M^2(Q^2)}{1+\tau} + 2\tau G_M^2(Q^2) \tan^2\frac{\theta}{2}\right] \tag{2.37}$$

where

$$\left(\frac{d\sigma}{d\Omega}\right)_{\text{Mott}} = \frac{\alpha^2 \cos^2\frac{\theta}{2}}{4E^2 \sin^4\frac{\theta}{2}(1 + \frac{2E}{M}\sin^2\frac{\theta}{2})}. \tag{2.38}$$

The differential cross section for polarized elastic scattering in the lab frame can be expressed as

$$\left(\frac{d\sigma}{d\Omega}\right)_{\text{pol.}} = -h\left(\frac{d\sigma}{d\Omega}\right)_{\text{Mott}}\left[\cos\theta^* v_{T'}R_{T'}(Q^2) + 2\sin\theta^*\cos\phi^* v_{TL'}R_{TL'}(Q^2)\right] \quad (2.39)$$

where

$$v_{T'} = \tan\frac{\theta}{2}\sqrt{\frac{Q^2}{|\vec{q}|^2} + \tan^2\frac{\theta}{2}} \quad (2.40)$$

$$v_{TL'} = -\frac{1}{\sqrt{2}}\left(\frac{Q^2}{|\vec{q}|^2}\right)\tan\frac{\theta}{2} \quad (2.41)$$

and h is the incident electron helicity and is equal to either $+1$ or -1. To get a longitudinal and transverse target comparable to those in Eq. 2.21 and Eq. 2.23, one must set θ^* to the angle between the target polarization and the $\vec{q}$ direction. Because this experiment only dealt with in-plane scattering, ϕ^* is always 0 or π here.

2.3.3 Polarized Elastic Scattering on ^{3}He

The previous section described elastic scattering on a nucleon which, in principle, applies to the neutron as well as the proton. However, the form factors from the neutron must be extracted from nuclear targets since no practical pure neutron target exists. Similarly, the structure functions for the neutron must be extracted from nuclear targets. This experiment extracts the neutron structure functions from polarized ^{3}He; therefore, it is useful to describe the formalism for polarized ^{3}He elastic scattering.

The unpolarized cross section for elastic scattering on ^{3}He [16]:

$$\left(\frac{d\sigma}{d\Omega}\right)_{\text{unpol.}} = Z^2\frac{1}{\eta}\left(\frac{d\sigma}{d\Omega}\right)_{\text{Mott}}\left[\frac{Q^2}{|\vec{q}|^2}F_c^2(Q^2) + \frac{\mu^2Q^2}{2M_T^2}\left(\frac{1}{2}\frac{Q^2}{|\vec{q}|^2} - \tan^2\frac{\theta}{2}\right)F_m^2(Q^2)\right] \quad (2.42)$$

where Z is the charge of the nucleus, μ is the magnetic moment, $\eta = 1 - Q^2/4M_T^2$ is a factor taking into account the target recoil and M_T is the mass of the ^{3}He

nucleus. $F_c(Q^2)$ and $F_m(Q^2)$ are the charge and magnetic form factors for ^{3}He and are analogous to $G_E(Q^2)$ and $G_M(Q^2)$ for the nucleon.

The polarized cross section for polarized ^{3}He follows the same form as Eq. 2.39 except with new response functions:

$$R_{T'}(Q^2) = \frac{2\tau E'}{E}(\mu_A F_m)^2 \tag{2.43}$$

$$R_{TL'}(Q^2) = -\frac{E'\sqrt{2\tau(1+\tau)}}{E}(ZF_c)(\mu_A F_m) \tag{2.44}$$

where μ_A is the magnetic moment of the nucleus.

2.3.4 The Effective Polarization of the Neutron in the ^{3}He Nucleus

Before describing the details of polarized quasi-elastic and inelastic scattering, one must confront a complication resulting from use of a nucleus rather than a nucleon as a target. To be able to extract information about the nucleon from polarized nuclei, one must understand what fraction of the total nuclear polarization comes from each nucleon.

In a polarized ^{3}He nucleus, almost all the polarization comes from the neutron. The Pauli exclusion principle ensures that the polarization from the two protons cancel each other in the lowest energy state of the nucleus. Of course, the nucleus can be in other angular momentum states due to nucleon-nucleon interactions. The most important higher states are shown in Fig. 2.4.

Calculations of the effective polarization of a nucleon based on different models of the ^{3}He nucleus has been done by several groups and is summarized by Bissey *et al.* [17].

2.3.5 Polarized Quasi-elastic Scattering on ^{3}He

A rough approximation of the quasi-elastic scattering cross-section of the nucleus is the sum of the elastic scattering from each nucleon in the nucleus. However,

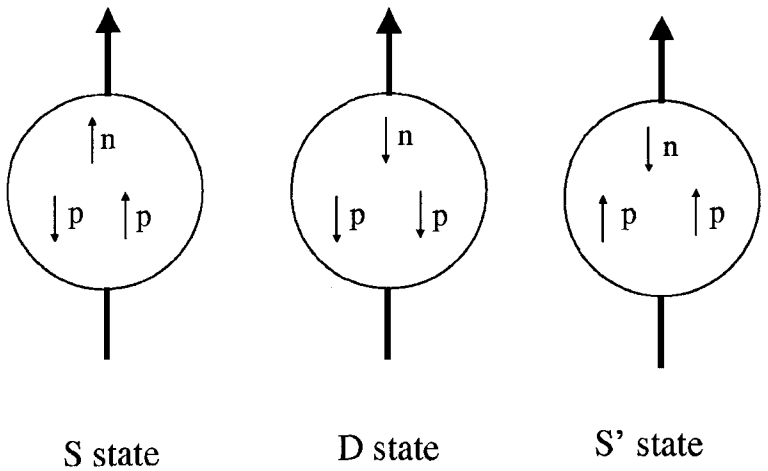

Figure 2.4: *A cartoon description of the three most populated ^{3}He nucleus polarization configurations.*

effects like Fermi motion, final state interactions and meson exchange distort the elastic scattering picture.

One description of the cross section for unpolarized quasi-elastic scattering comes from a model by Lightbody and O'Connell [18]. In this description, the quasi-elastic cross section is represented by a Gaussian peak written as

$$\sigma_{qe}^{^3\mathrm{He}}(\nu, Q^2) = Ae^{-\frac{(\nu - Q^2/2M)}{2|\vec{q}|^2 k_F^2/M^2}} \tag{2.45}$$

where k_F is the Fermi momentum of the nucleus and the constant A is defined by the relation

$$2\sigma_{qe}^{p} + \sigma_{qe}^{n} = \int_0^{E_{\mathrm{beam}}} Ae^{-\frac{(\nu - Q^2/2M)}{2|\vec{q}|^2 k_F^2/M^2}} d\nu \tag{2.46}$$

where σ_{qe}^{p} and σ_{qe}^{n} are the elastic cross sections for the proton and neutron respectively with form factors modified to fit quasi-elastic data.

The polarized quasi-elastic cross-section is more complicated, but in principle can be derived from similar techniques (*i.e.* broadening modified elastic cross sections into a Gaussian peak). A straight-forward description by Leidemann et al [19], uses the elastic formalism with the following substitutions :

$$R^{T'}(Q^2) = -2\tau\{G_M^{n\,2}(Q^2) - \frac{2}{3}P_D\left[G_M^{p\,2}(Q^2) + 2G_M^{n\,2}(Q^2)\right]$$

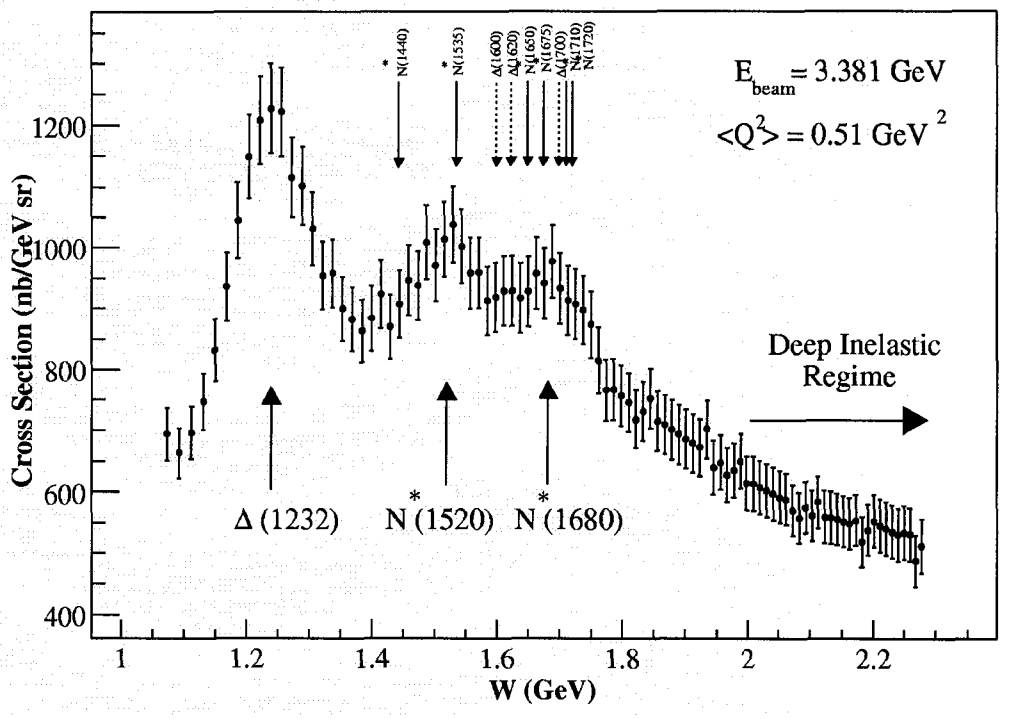

Figure 2.5: *Unpolarized ^{3}He cross section data in the resonance region from Jefferson Lab experiment E94-010 with some major and minor resonances labeled [20]*

$$+\frac{2}{3}P_{S'}\left[G_M^{p\,2}(Q^2) - G_M^{n\,2}(Q^2)\right]\} \tag{2.47}$$

$$\begin{aligned} R^{TL'}(Q^2) &= \sqrt{2\tau(1+\tau)}\{G_E^n(Q^2)G_M^n(Q^2) - \frac{2}{3}P_D\left[G_E^pG_M^p + 2G_E^n(Q^2)G_M^n(Q^2)\right] \\ &\quad +\frac{2}{3}P_{S'}\left[G_E^p(Q^2)G_M^p(Q^2) - G_E^n(Q^2)G_M^n(Q^2)\right] \\ &\quad +2G_E^pG_M^nT(Q^2)\} \end{aligned} \tag{2.48}$$

where P_D and $P_{S'}$ is the effective polarization of the excited states of ^{3}He and $T(Q^2)$ is the Fourier transform of the two-body density matrix. The new elastic cross sections with these substitutions then can be broadened into a Gaussian peak in a similar manner as the unpolarized cross section.

2.3.6 Scattering in the Resonance and Deep Inelastic Region

Pions, the lightest hadrons, can be created in hadronic final states from electron scattering on a nucleon at $W \geq 1.072$ GeV $= M_{\text{proton}} + m_{\text{pion}}$. Beyond the pion threshhold lies the resonance region and the deep inelastic scattering region. The resonance region is characterized by distinct hadronic final states whose cross-sections have a strong Q^2 dependence. The deep inelastic region is characterized by a slow, logarithmic dependence of the cross-section on Q^2 which is evidence of incoherent scattering off of individual quarks. The boundary between these two regions is usually defined as $W > 2.0$ GeV.

The resonance region is most acutely marked by the presence of the Δ resonance at $W = 1.232$ GeV as shown in Fig. 2.5. However, there are a number of other resonances and a non-resonant background that contribute to the cross section. In inclusive scattering one sees only the sum of all these transitions; therefore, the overall cross section is smoothed out. Also, the use of a nuclear target (like ^{3}He) smears resonance peaks even more, due to Fermi motion.

The deep inelastic region is characterized by the structure function's weak dependence on Q^2 for a constant value of x. This phenomena is known as *Bjorken scaling* and can be seen in the F_2^p data from the NMC experiments displayed in Fig. 2.6 [21]. Scattering off an object that had a finite size would lead to a much stronger Q^2 dependence; therefore, Bjorken scaling is the result of scattering off of point-like objects, *i.e.* quarks.

The region where Bjorken scaling is valid can be described by the structure functions in the limit

$$Q^2 \to \infty, \nu \to \infty, \text{with fixed } x. \tag{2.49}$$

This is known as the Bjorken limit and in this limit the structure functions become one-dimensional functions of x. One interesting feature of this limit is that $R(x, Q^2)$

vanishes and F_2 can be expressed (*c.f.* Eq. 2.20)

$$F_2(x) = 2xF_1(x) \tag{2.50}$$

which is known as the Callan-Gross relation.

One can also see from Fig. 2.6 [21] that Bjorken scaling is only an approximation. This is because of the radiation of gluons by the quark before and after the electron scattering process which are analogous to QED radiative effects. These processes cannot be separated from a single vertex process and therefore must be included in the structure functions. Because of this the structure function gains a logarithmic dependence on Q^2. However, there are clear set of procedures (known as DGLAP evolution) which can be used to evolve the structure functions to different Q^2 in the deep inelastic regime [7].

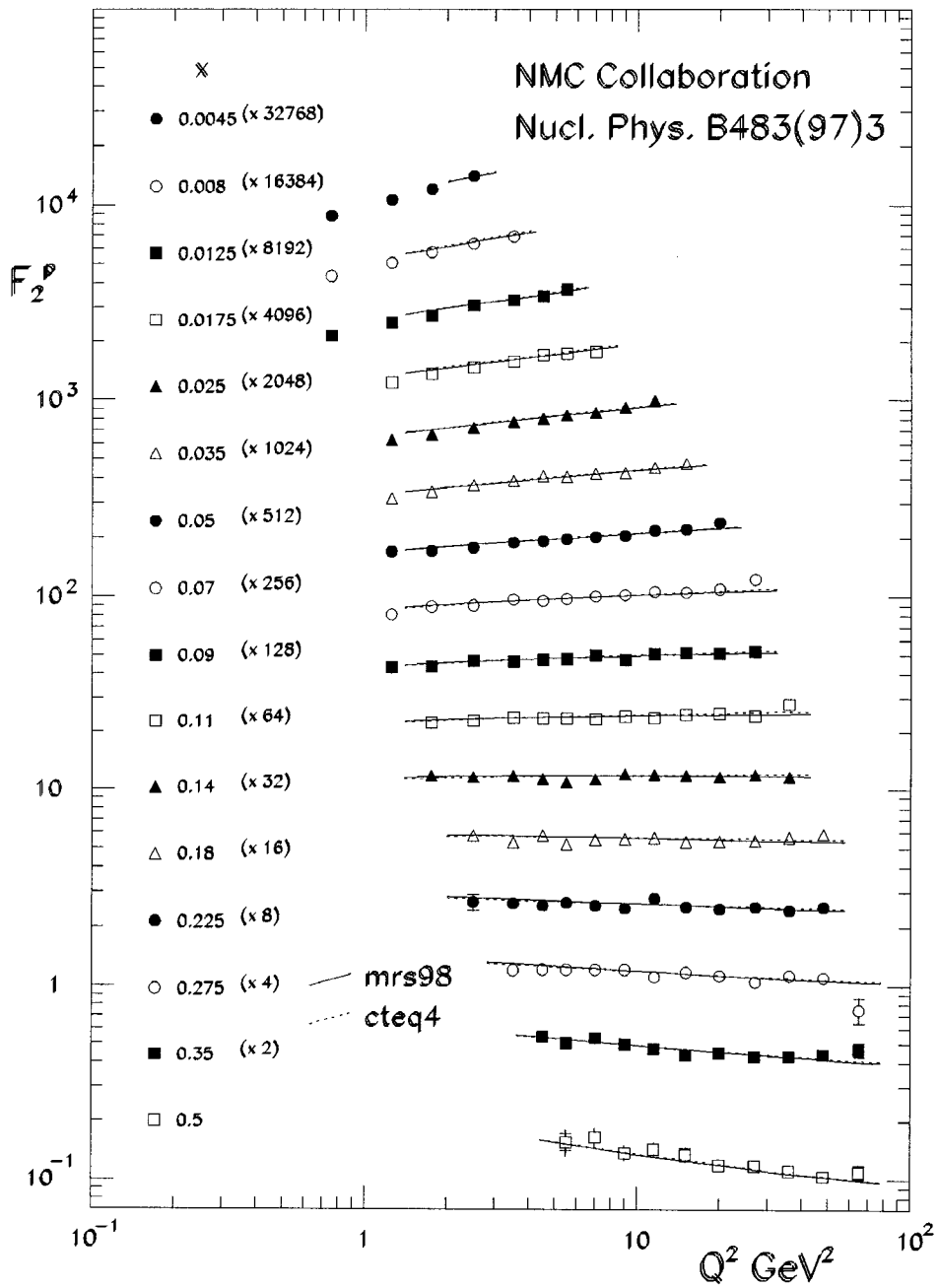

Figure 2.6: F_2^p from the NMC Collaboration experiments vs. Q^2 for various values of x [21].

CHAPTER 3

g_2 and Higher Twist Effects

3.1 Why Measure g_2?

Quantum Chromodynamics (QCD), the theory of the strong interaction, has two features which are essential to describing hadrons. The first is that the effects of the strong interaction, though many orders of magnitude stronger than the other fundamental forces, cannot be felt far outside of a hadron. This feature is known as *confinement.* The second feature of QCD is that when probing the nucleon at high momentum or, equivalently, short distances the coupling constant for the strong interactions goes to zero. This is known as *asymptotic freedom.*

These properties of QCD complicate direct measurements of the strong interaction. Using low momentum electrons to study nucleons, one sees the quarks in the confinement regime where they are enmeshed in dense gluon fields. Using high momentum electrons to study nucleons, one is in the regime of asymptotic freedom where the gluon fields are so weak that the quarks can be considered non-interacting, the strong force noticeable only through their momentum distributions. To isolate gluon exchanges between quarks, one must study the nucleon in a kinematic regime where the strong coupling constant is large enough for a single gluon exchange to be measured, but not so large that higher order terms begin to dominate.

What makes the structure function g_2 especially interesting is, because of a relation from Wandzura and Wilczek [22], the asymptotically-free quark part of the structure function can be calculated from the data on g_1 and subtracted from g_2. The remaining part of the structure function will be dominated by physics beyond simple

quark models, such as quark-gluon coupling. This means if precise measurements of g_1 and g_2 are made one can directly extract the magnitude of gluonic interactions between two quarks. This magnitude is represented theoretically by the so-called higher twist terms in the framework of the operator product expansion, which will be explained below.

There is at present little definite knowledge, from experiment and theory, about the size of the higher twist terms. Prior to E97-103, there were no precise measurements of the structure functions in the right kinematic region to allow an accurate estimate of the higher twist terms. Lattice QCD can be used to calculate sum rule integrals of g_2 over x, but theoretical predictions of $g_2(x, Q^2)$ itself are limited to simple Bag Models. It is the goal of E97-103 to provide measurements of g_2 in a kinematic region which will allow us to isolate and quantify these higher-twist effects and by doing so improve the quantitative understanding of QCD in the non-perturbative region.

3.2 Deriving the Wandzura-Wilczek Relation

3.2.1 A Description of the Operator Product Expansion

The structure functions can be deconstructed directly from the formalism of QCD with the operator product expansion. This method replaces a product of operators with a single local operator. The physical consequences of the original product of operators is revealed by working out the QCD rescaling of this new operator [23]. This approach has the advantages of being model-independent and having coefficients of the expansion that are calculable using perturbation theory.

To illustrate the operator product expansion, one can consider the product of two local operators with the space-time separation z [24]:

$$\mathcal{O}_a(z)\mathcal{O}_b(0). \tag{3.1}$$

The operators can be considered to be at nearly the same point in the limit $z \to 0$. In this limit, one can then calculate the product of operators with an expansion of local operators with a series of corresponding coefficients [24] :

$$\lim_{z\to 0} \mathcal{O}_a(z)\mathcal{O}_b(0) = \sum_k c_{abk}(z)\mathcal{O}_k(0). \tag{3.2}$$

This relation holds as long as z is small compared to the distance scale probed. This substitution can be used in the computation of matrix elements where the coefficients $c_{abk}(z)$ will be independent of the matrix element being calculated [24]. Because of asymptotic freedom, the coupling constant of QCD is small at short distances. Therefore it is possible that these coefficient functions can be calculated using perturbation theory, which requires a small coupling constant [24].

The operator expansion also works in momentum space as follows:

$$\lim_{q\to\infty} \int d^4z e^{iq\cdot z}\mathcal{O}_a(z)\mathcal{O}_b(0) = \sum_k c_{abk}(q)\mathcal{O}_k(0). \tag{3.3}$$

This works provided q, the momentum transfer from the probe, is much larger than the characteristic momentum of the external states [24].

3.2.2 Twist Two Operators in the Operator Product Expansion

In QCD, the operator product expansion can be applied to the time-ordered quark electromagnetic currents in the forward Compton scattering amplitude [7]:

$$T_{\mu\nu} = i \int d^4z e^{iq\cdot z}\langle N|\mathcal{T}(j_\mu(z)j_\nu(0))|N\rangle \tag{3.4}$$

where $\mathcal{T}$ represents the time-ordering operator. This amplitude will be connected to the hadron tensor from Eq. 2.9 by dispersion relations. It is necessary to work with the Compton scattering amplitude so that Wick's theorem can be used.

In this case, the product is expanded into quark and gluon operators with mass dimension d and spin n. These can be written:

$$\mathcal{O}_{d,n}^{\mu_1\cdots\mu_n} \tag{3.5}$$

where the operator $\mathcal{O}$ is symmetric and traceless under the indices $\mu_1 \ldots \mu_n$. The matrix element of $\mathcal{O}_{d,n}$ in the hadron target is proportional to [24]:

$$M^{d-n-2}\mathcal{S}[p^{\mu_1} \ldots p^{\mu_n}] \tag{3.6}$$

for a vector operator, and to

$$M^{d-n-2}\mathcal{S}[s^{\mu_1} p^{\mu_2} \ldots p^{\mu_n}] \tag{3.7}$$

for an axial operator. $\mathcal{S}$ acts on a tensor to project out the symmetric and traceless component. The power of M is derived from dimensional analysis of the conventional relativistic hadron state [24] where M has the unit of mass.

One can use this information to tell which terms in the expansion are most important and how the other terms are suppressed. This is done by analyzing the q dependence of the terms of the expansion. The coefficient functions $c_{abk}(q)$ are only functions of q. Therefore the free indices of $\mathcal{O}$ must be either μ, ν (the indices of the hadron tensor) or must be contracted with q^α. Every index on $\mathcal{O}$ contracted with q^α produces a factor of $p \cdot q$ (or $s \cdot q$ in the case of axial vector) which is of order Q^2/M. An index μ or ν is contracted with the lepton tensor $L_{\mu\nu}$ and results in a factor of $p \cdot k$ or $p \cdot k'$, both of which are of order Q^2/M [24]. Since the hadronic tensor has a dimension two, the coefficient of $\mathcal{O}$ must have dimension Q^{2-d}. The dimensions of the expansion terms can be summarized as follows:

$$c_{\mu_1 \ldots \mu_n} \mathcal{O}_{d,n}^{\mu_1 \ldots \mu n} \rightarrow \frac{q_{\mu_1}}{Q} \ldots \frac{q_{\mu_n}}{Q} Q^{2-d} \langle \mathcal{O}_d^{\mu_1 \ldots \mu_n} \rangle \tag{3.8}$$

$$\rightarrow \frac{q_{\mu_1}}{Q} \ldots \frac{q_{\mu_n}}{Q} Q^{2-d} M^{d-n-2} p^{\mu_1} \ldots p^{\mu_n} \tag{3.9}$$

$$\rightarrow \frac{(p \cdot q)}{Q^n} Q^{2-d} M^{d-n-2} p^{\mu_1} \ldots p^{\mu_n} \tag{3.10}$$

$$\rightarrow \left(\frac{1}{x}\right)^n \left(\frac{Q}{M}\right)^{2+n-d} = \left(\frac{1}{x}\right)^n \left(\frac{Q}{M}\right)^{2-t} \tag{3.11}$$

where t is known as the twist of the expansion term and is defined as:

$$t = d - n. \tag{3.12}$$

	ψ	$G_{\mu\nu}$	D^{μ}
d	3/2	2	1
n	1/2	1	1
t	1	1	0

Table 3.1: *The dimension (d), spin (n) and twist (t) of the operators for quarks (ψ), gluons ($G_{\mu\nu}$) and covariant derivatives (D^{μ}).*

With this dimensional analysis, one can group the operators into terms by twist using table 3.1. Any gauge invariant operator must contain at least two quark fields or two gluon strength tensors; therefore the lowest possible twist for such an operator is two [24]. For example, a twist two operator has either two quark fields ψ or two gluon operators $G_{\mu\nu}$ and an arbitrary number of covariant derivatives.

Twist two quark operators can be written:

$$\mathcal{O}_{V,a}^{\mu_1\ldots\mu_n} = \frac{1}{2}\left(\frac{i}{2}\right)^{n-1} S\{\overline{\psi_a}\gamma^{\mu_1}D^{\mu_1}\ldots D^{\mu_n}\psi_a\} \tag{3.13}$$

$$\mathcal{O}_{A,a}^{\mu_1\ldots\mu_n} = \frac{1}{2}\left(\frac{i}{2}\right)^{n-1} S\{\overline{\psi_a}\gamma^{\mu_1}D^{\mu_2}\ldots D^{\mu_n}\gamma_5\psi_a\} \tag{3.14}$$

where the index a represents the quark flavors (u, d, s). Twist two gluon operators are similar:

$$\mathcal{O}_{g,V}^{\mu_1\ldots\mu_n} = -\frac{1}{2}\left(\frac{i}{2}\right)^{n-2} S\left\{G_a^{\mu_1\alpha}D^{\mu_2}\ldots D^{\mu_{n-1}}G_{a\alpha}^{\mu_n}\right\}. \tag{3.15}$$

3.2.3 QCD Coefficients in the Operator Product Expansion

The next step in the operator product expansion is to determine the coefficient functions of the operators. As stated before, this can be done using perturbative QCD. The generic term in the operator product expansion can be written:

$$jj \sim c_q\mathcal{O}_q + c_g\mathcal{O}_g \tag{3.16}$$

where jj is the product of the hadron currents, c_q and c_g are the coefficients for the quark and gluon operators respectively. One can then take the matrix elements of both sides:

$$\langle q|jj|q\rangle \sim c_q\langle q|\mathcal{O}_q|q\rangle + c_g\langle q|\mathcal{O}_g|q\rangle. \tag{3.17}$$

The left hand side of Eq. 3.17 and the first term on the right hand side contain no factors of g, the strong coupling constant. The term with the gluon operator has a factor of g^2 in it and is a higher order term. When deriving the Wandzura-Wilczek expression, one is only interested in only the lowest order terms; therefore the second term will be dropped.

A detailed description of deriving the left hand side of Eq. 3.17 can be found in Ref. [24]. The spin-dependent part of the left hand side is revealed to be:

$$\mathcal{M}^{[\mu\nu]} = \sum_{n=0,2,4}^{\infty} 2\frac{2^{n+1}q^{\mu_2}\dots q^{\mu_n}}{(-q^2)^{n+1}} ih\epsilon^{\mu\nu\alpha\mu_1} q_\alpha p_{\mu_1}\dots p_{\mu_n}. \tag{3.18}$$

Notice that the matrix element only contains even spin terms. This is because even spin axial current vectors are even under charge conjugation. The odd spin are odd. Since electro-production is even under charge conjugation, the odd spin terms are dropped.

To compute the spin-dependent part of the right hand side of Eq. 3.17 one needs to evaluate the hadronic matrix elements of the operator in Eq. 3.14. Unfortunately, the matrix elements of the operators for a nucleon are not known. However, the matrix elements can be written :

$$\langle p,s|\mathcal{O}_A^{\mu_1\dots\mu_n}|p,s\rangle = a_n\mathcal{S}[s^{\mu_1}\dots p^{\mu_n}]. \tag{3.19}$$

where a_n is a scaler factor and $\mathcal{S}$ is defined as:

$$\mathcal{S}[s^{\mu_1}\dots p^{\mu_n}] = s^{\mu_1}\dots p^{\mu_n} + \mathcal{R}^{\mu_1\dots\mu_n} \tag{3.20}$$

and where :

$$\mathcal{R}^{\mu_1\dots\mu_n} = \frac{n}{n+1}s^{\mu_1}p^{\mu_2}\dots p^{\mu_n} + \frac{1}{n+1}p^{\mu_1}s^{\mu_2}\dots p^{\mu_n} + \dots + \frac{1}{n+1}p^{\mu_1}p^{\mu_2}\dots s^{\mu_n} \tag{3.21}$$

It is an important point that the tensor $\mathcal{R}^{\mu_1\dots\mu_n}$ has no completely symmetric part and is therefore spin n-1, instead of spin n. Thus the tensor contribution of $\mathcal{R}$ is

twist three *even though it came from a twist two matrix element.* This is an essential point in deriving the Wandzura-Wilczek relation.

If one equates Eq. 3.18 and Eq. 3.19 one arrives at:

$$\sum_{n=0,2,4}^{\infty} 2\frac{2^{n+1}q^{\mu_2}\dots q^{\mu_n}}{(-q^2)^{n+1}} ih\epsilon^{\mu\nu\alpha\mu_1} q_\alpha p_{\mu_1\dots\mu_n} = \sum_{n=0,2,4}^{\infty} c_n a_n \mathcal{S}[s^{\mu_1}\dots p^{\mu_n}]. \tag{3.22}$$

One can then calculate the c_q coefficient, with the knowledge that a_n is still not known. Thus the anti-symmetric part of the Compton scattering matrix $T^{\mu\nu}$ is:

$$T^{[\mu\nu]} = \sum_{n=0,2,4}^{\infty} 2C_n i\epsilon^{\mu\nu\alpha\mu_1} q_\alpha \frac{2^{n+1}q^{\mu_2}\dots q^{\mu_n}}{(-q^2)^{n+1}} a_n \mathcal{S}[s^{\mu_1}\dots p^{\mu_n}] \tag{3.23}$$

where C_n is a term to take into account the charge of the quark flavor (which previously has been ignored).

3.2.4 Extracting Relations for g_1 and g_2

If one ignores the $\mathcal{R}$ tensor contribution to Eq. 3.23 and combines terms with matching indices one has:

$$T^{[\mu\nu]} = \sum_{n=0,2,4}^{\infty} -\frac{4}{q^2} C_n i\epsilon^{\mu\nu\alpha\mu_1} q_\alpha s_{\mu_1} a_n \left(\frac{1}{x}\right)^n. \tag{3.24}$$

One can see this is similar to the $\tilde{g}_1$ term in the scattering amplitude:

$$T^{[\mu\nu]} = \sum_{n=0,2,4}^{\infty} i\epsilon^{\mu\nu\alpha\lambda} s_\lambda \frac{\tilde{g}_1}{p\cdot q} \tag{3.25}$$

where $\tilde{g}_1$ is the spin structure function of Compton scattering. One then equates the previous equations to get:

$$\tilde{g}_1 = \sum_{n=0,2,4}^{\infty} -\frac{4p\cdot q}{q^2} C_n a_n \left(\frac{1}{x}\right)^n \tag{3.26}$$

$$\tilde{g}_1 = \sum_{n=0,2,4}^{\infty} 2C_n a_n \left(\frac{1}{x}\right)^{n+1}. \tag{3.27}$$

Already this is a remarkable result. The operator product expansion has allowed one to express the spin structure function $\tilde{g}_1$ in terms of a power series of $1/x$.

However, it is necessary to relate $\tilde{g}_1$ to the physical region. One can do this by calculating the contour integral [24]:

$$2C_n a_n = \frac{1}{2\pi i}\oint_C \tilde{g}_1(\omega)\frac{d\omega}{\omega^{n+2}} \tag{3.28}$$

and using the optical theorem:

$$\tilde{g}_1(\omega + i\epsilon) - \tilde{g}_1(\omega - i\epsilon) = 4\pi i g_1(\omega) \tag{3.29}$$

where $\omega = 1/x$ and $g_1(\omega)$ is the measurable spin structure function. The result of this integral is:

$$2C_n a_n = 2[1 - (-1)^{n+1}]\int_1^\infty g_1(\omega)\frac{d\omega}{\omega^{n+2}}. \tag{3.30}$$

The translation of this equation into x instead of ω is:

$$2\int_0^1 dx x^n g_1(x) = C_n a_n,\ n = 0, 2, 4, \ldots \tag{3.31}$$

This is a calculation of the twist two moment for g_1.

Up to this point, the $\mathcal{R}$ tensor in Eq. 3.21 has been ignored. If the $\mathcal{R}$ tensor is inserted into Eq. 3.23 then one gets:

$$T^{[\mu\nu]} = \sum_{n=0,2,4}^{\infty} -\frac{n}{n+1}\left[s^{\mu_1}\frac{2^{n+1}(p\cdot q)^n}{(-q^2)^{n+1}} - p^{\mu_1}\frac{2^{n+1}(p\cdot q)^{n-2}q\cdot s}{(-q^2)^{n+1}}\right] 2C_n a_n i\epsilon^{\mu\nu\alpha\mu_1}q_\alpha. \tag{3.32}$$

This kinematic structure is the same as the Compton scattering spin structure function $\tilde{g}_2$ which can be written:

$$\tilde{g}_2(\omega) = \sum_{n=0,2,4}^{\infty} 2C_n a_n\left[\frac{1}{n+1} - 1\right]\omega^{n+1}. \tag{3.33}$$

Substituting Eq. 3.26 into the above equation one gets the relation:

$$\tilde{g}_2(\omega) = \tilde{g}_1(\omega) + \int_0^\omega \tilde{g}_1(\omega')\frac{d\omega'}{\omega'}. \tag{3.34}$$

This can be translated into the physical regime using the optical theorem:

$$g_2(x) = g_2^{\mathrm{WW}}(x) = -g_1(x) + \int_x^1 g_1(x')\frac{dx'}{x'}. \tag{3.35}$$

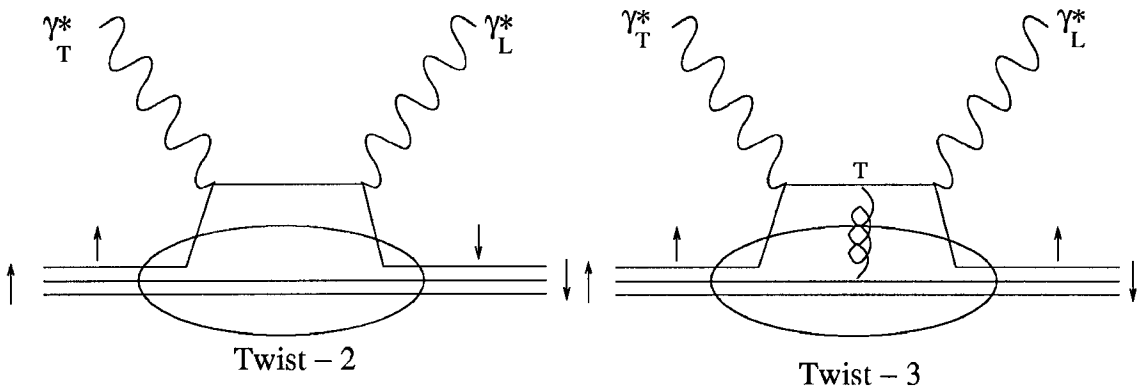

Figure 3.1: *Compton scattering diagrams for twist two and twist three operators. The arrows label the spin of the quarks and nucleon.*

This is the Wandzura-Wilczek relation [22]. It is derived by using the operator product expansion and cutting off terms with twist higher than two. It shows that the contribution to g_2 from the twist two operator is purely a function of g_1. This part that can written in terms of g_1 is usually written g_2^{WW}.

3.2.5 Twist Three Operators

The structure functions $g_1(x, Q^2)$ and $g_2(x, Q^2)$ have been calculated from their equivalents in Compton scattering and using the optical theorem. An interpretation of $g_2(x, Q^2)$ can be made by looking at its Compton scattering counterpart. $g_2(x, Q^2)$ is the imaginary part of the process [25]:

$$\gamma^\star(+1) + N(1/2) \rightarrow \gamma^\star(0) + N(-1/2) \tag{3.36}$$

where $\gamma^\star$ and N represent the virtual photon and nucleon, respectively, and the numbers in parenthesis are their helicities. This process is illustrated by the right diagram in Fig. 3.1.

Because of the vector coupling, the helicity of massless quarks cannot be flipped in perturbative processes. There are two processes which can perform the helicity exchange : first, single quark scattering in which the quark absorbs the helicity through its transverse momentum and, second, through quark scattering where the

quark also absorbs a transversely polarized gluon from another quark. Both of these processes form twist three operators.

As seen from the dimensional analysis of Eq. 3.8 terms with twist higher than two are suppressed by increasing powers of M/Q. This is not the case in the confinement region where higher twist terms dominate. Nevertheless, in the deep inelastic scattering region, where the measurements of E97-103 take place, the twist three terms can be expected to dominate the higher twist terms.

The twist three operators with two quark fields and a gluon field can be written [26]:

$$R_l^{\sigma\mu_1\ldots\mu_n} = \frac{i^{n-3}}{4} g\mathcal{S}\left[\overline{\psi}(0)D^{\mu_1}\ldots D^{\mu_{l-1}}G^{\sigma\mu_1}D^{\mu_{l+1}}\ldots D^{\mu_{n-1}}\gamma^{\mu_n}\gamma^5\psi(0)\right] \quad (3.37)$$

$$S_l^{\sigma\mu_1\ldots\mu_n} = \frac{i^{n-2}}{4} g\mathcal{S}\left[\overline{\psi}(0)D^{\mu_1}\ldots D^{\mu_{l-1}}\tilde{G}^{\sigma\mu_l}D^{\mu_{l+1}}\ldots D^{\mu_{n-1}}\gamma^{\mu_n}\psi(0)\right]. \quad (3.38)$$

There is also an explicit quark mass-dependent operator that is twist three:

$$O_m^{\sigma\mu_1\mu_2\ldots\mu_n} = \frac{i^{n+1}}{4}\mathcal{S}[\overline{\psi}(0)m_q[\gamma^\sigma,\gamma^{\mu_1}]\gamma^5 D^{\mu_2}\ldots D^{\mu_n}\psi(0)] \quad (3.39)$$

where m_q is the quark mass.

In g_1, the twist three terms are suppressed by an additional M/Q term compared to the twist two term [27]. However, in g_2 the twist three enter at the same order of M/Q as the twist two term. To leading order in M/Q, the moments of the structure functions up to twist three can be written [26]:

$$\int_0^1 x^n g_1(x,Q^2)dx = \frac{1}{2}\sum_i a_i^n(\mu^2)C_{2,i}^n(Q^2,\mu^2),\ n=0,2,4,\ldots \quad (3.40)$$

$$\int_0^1 x^n g_2(x,Q^2)dx = \frac{n}{2(n+1)}[\sum_i a_i^n(\mu^2)C_{2,i}^n(Q^2,\mu^2) - \sum_i d_i^n(\mu^2)C_{3,i}^n(Q^2,\mu^2)],\ n=2,4,\ldots \quad (3.41)$$

where the $a_i^n(\mu^2)$ is the twist two matrix element coefficient with its dependence on renormalization scale (μ^2) made explicit, $d_i^n(\mu^2)$ is the twist three matrix element

coefficient and $C^n_{2,i}(Q^2,\mu^2)$ and $C^n_{3,i}(Q^2,\mu^2)$ are the operator product expansion coefficients for twist two and twist three operators.

Looking at these moments of g_1 and g_2, the value of measuring g_2 again becomes evident. If the only leading order terms om M/Q are kept in the expansion, one can write g_2 as:

$$g_2(x,Q^2) = g_2^{\mathrm{WW}}(x,Q^2) + \overline{g_2}(x,Q^2) \tag{3.42}$$

where $g_2^{\mathrm{WW}}(x,Q^2)$ is the contribution to g_2 from twist two terms in the operator expansion and $\overline{g}_2(x,Q^2)$ represents the contribution from twist three operators. Therefore, if one knows $g_1(x,Q^2)$, accurately and one believes the terms beyond twist two are suppressed sufficiently, then $g_2^{\mathrm{WW}}(x,Q^2)$ can be calculated. The twist two part of g_2 can then be subtracted from $g_2(x,Q^2)$ and the term $\overline{g_2}(x,Q^2)$ can be isolated. The function $\overline{g_2}(x,Q^2)$ is expected to be dominated, even when the full expansion is included, by the twist three gluon operators and there is no reason it should be small [26].

3.3 Models of g_2

3.3.1 The Parton Model

The parton model begins with the assumption hadrons are made up of free infitesimally small particles called 'partons'. The hadron tensor can then be formed by combinations of the distributions functions of these partons. This assumption has considerable validity in the deep inelastic scattering region because of the asymptotic freedom of the quarks. It is useful because of its straight-forward interpretation for the structure functions, F_1 and g_1. However, complex modifications to these assumptions are necessary to get a physical description of g_2.

To lowest order in QCD, virtual photons only scatter off of quarks because gluons have no electric charge. The interaction is pictured in Fig. 3.2. Within the framework of inclusive electron scattering, this makes the hadron tensor $W_{\mu\nu}$ very

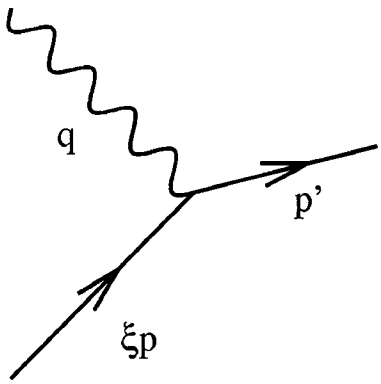

Figure 3.2: *Feynman diagram of a parton with momentum fraction ξ absorbing a virtual photon.*

similar to the lepton tensor $L_{\mu\nu}$. An additional subtlety of the parton scattering case is that the parton's momentum is only a fraction, ξ of the observed hadron momentum. By making the substitutions $k \to \xi p$, $k' \to p'$ and $q \to -q$, multiplying by the square of quark electric charge $\mathcal{Q}$ and assuming massless partons one can transform the lepton tensor $L_{\mu\nu}$ into the hadron tensor [24]:

$$\begin{aligned} W_{\mu\nu} &= \frac{1}{4\pi}\int \frac{d^3p'}{(2\pi)^3 2E_{p'}}\frac{1}{\xi}(2\pi)^4\delta^4(\xi p + q - p') \\ &\quad \times 2\left[\xi p^\mu p'^\nu + \xi p^\nu p'^\mu - g^{\mu\nu}\xi p\cdot p' + i\epsilon^{\mu\nu\alpha\beta}q_\alpha s_\beta\right]. \end{aligned} \tag{3.43}$$

This integral can be performed using the identity:

$$\int \frac{d^3p'}{(2\pi)^3 2E_{p'}} = \int \frac{d^4p'}{(2\pi)^4}(2\pi)\delta\left((\xi p + q - p')^2\right) = \int \frac{d^4p'}{(2\pi)^4}\frac{(2\pi)}{2p\cdot q}\delta\left(\xi + \frac{q^2}{2p\cdot q}\right). \tag{3.44}$$

Since the partons are massless one can write $s_\beta = h\xi p_\beta$ where h is the helicity of the parton. Then one can write the hadron tensor as:

$$W_{\mu\nu} = \frac{\mathcal{Q}^2}{2\xi p\cdot q}\left[\xi p^\mu p'^\nu + \xi p' p'^\mu - g^{\mu\nu}\xi p\cdot p' + ih\xi e^{\mu\nu\alpha\beta}q_\alpha p_\beta\right]\delta(\xi - x) \tag{3.45}$$

$$= \frac{\mathcal{Q}^2}{2\xi p\cdot q}\left[2\xi^2 p^\mu p^\nu - g^{\mu\nu}\xi p\cdot q + ih\xi\epsilon^{\mu\nu\alpha\beta}q_{alpha}p_\beta\right]\delta(\xi - x). \tag{3.46}$$

Because of Eq. 3.44, p' can be replaced with $\xi p + q$ and the q^μ and q^ν terms can be dropped. The total target spin s_h can be replaced with $\mathcal{H}p$, where $\mathcal{H}$ is the

helicity of the target and p is the total target momentum. Using this substitution and the kinematic structure of Eq. 2.12 and Eq. 2.13 one can calculate the structure functions:

$$F_1 = \frac{\mathcal{Q}^2}{2}\delta(\xi - x),\ F_2 = \mathcal{Q}^2\xi\delta(\xi - x),\ g_1 = \frac{\mathcal{Q}^2}{2}h\mathcal{H}\delta(\xi - x),\ g_2 = 0. \tag{3.47}$$

However, this is only the structure function for a single quark with a known helicity. Nucleons will contain a distribution of quarks and anti-quarks with different helicities. The total structure function is obtained by sums of probabilities to find a quark (or anti-quark) with that helicity as shown here:

$$F_1(x,Q^2) = \sum_i \frac{\mathcal{Q}_i^2}{2}(q_+(x) + q_-(x) + \overline{q}_+(x) + \overline{q}_-(x)) \tag{3.48}$$

$$F_2(x,Q^2) = \sum_i \mathcal{Q}_i^2 x(q_+(x) + q_-(x) + \overline{q}_+(x) + \overline{q}_-(x)) \tag{3.49}$$

$$g_1(x,Q^2) = \sum_i \frac{\mathcal{Q}_i^2}{2}(q_+(x) - q_-(x) + \overline{q}_+(x) - \overline{q}_-(x)) \tag{3.50}$$

$$g_2(x,Q^2) = 0 \tag{3.51}$$

where q_+ is the probability of a quark having the helicity of the nucleon, q_- is the probability of a quark having the opposite helicity of the nucleon and $\overline{q}_+$ and $\overline{q}_-$ are the anti-quark probabilities with same and opposite helicity respectively.

From this set of equations one can already seen some physical behavior of the structure functions. First, the structure functions depend only on x and not on Q^2. This result reflects the Bjorken scaling present in experimental data at high Q^2. Secondly, the Callan-Gross relation, seen in Eq. 2.50, is satisfied.

Also, one can see clear interpretations of some of the structure functions. F_1 is the probability of finding a quark with momentum fraction x. g_1 is the difference in probabilities between quarks with momentum x with spin parallel to the nucleon spin and quarks with momentum x with spin anti-parallel to the nucleon spin.

Whatever useful qualities the parton model has, it completely fails to describe g_2. This is because the parton model assumes all the quarks have collinear mo-

mentum and are non-interacting. As has been explained earlier, g_2 is the result of transverse momentum and quark-gluon interactions; therefore, it is not surprising to find $g_2(x, Q^2) = 0$.

One way to extend the parton distribution to describe g_2 is to include transverse momentum, $\vec{p}_\perp$ in the model. Then one can write the g_2 from above as [7]:

$$g_2(x, Q^2) = \sum_i \frac{\mathcal{Q}^2}{2} \left(\frac{m_q}{xM} - 1 \right) (q_+(x) - q_-(x) + \overline{q}_+(x) - \overline{q}_-(x)) \tag{3.52}$$

where m_q is the quark mass and M is the nucleon mass. Clearly, if $m_q = xM$, an initial assumption in the parton model, then $g_2(x, Q^2) = 0$ again. However, if $m_q \neq xM$ then the quark is said to be off-mass-shell and $g_2(x) \neq 0$. Therefore, g_2 measures the degree the quarks in the nucleon are off-mass-shell.

Another approach is to define new parton distributions corresponding to the transverse momentum [28]. In terms of these newly distributions one can write g_2 as:

$$g_2(x, Q^2) = \sum_i \frac{\mathcal{Q}^2}{2} \left(q_{T+}(x) - q_{T-}(x) + \overline{q}_{T+}(x) - \overline{q}_{T-} \right) \tag{3.53}$$

where q_T is the transverse parton distribution.

However, even this approach reveals the difficulty of describing g_2 with a parton model. q_T does not evolve autonomously under scale transformation; therefore, one has to separate the transverse parton distribution into two two-parameter parton distributions [25]:

$$\Delta q_T(x) = \frac{2}{x} \int_{-1}^{1} dy (K_1(x, y) + K_2(x, y)) \tag{3.54}$$

where $K_1(x, y)$ and $K_2(x, y)$ are defined in such a way that the scale transformation is autonomous. A summary of the various approaches to the parton distributions can be found in Ref. [25]. In any case, most of the work on these parton distributions goes into predicting the matrix elements d_n and not $g_2(x, Q^2)$ for particular x and Q^2.

3.3.2 Bag Models of g_2

Bag models try to improve on the parton model by building a framework that incorporates the confinement phenomenology of QCD. In general, a bag model does this by separating the nucleon into two spaces : an interior, where the quarks have small masses and weakly interact, and an exterior, in which the quarks are not allowed to propagate and have a different vacuum energy [7]. Since confinement interactions are built in, these models potentially could describe the quark-gluon interaction part of g_2 in a more straight-forward manner.

While there are several types of bag models, the one given here will be the modified center-of-mass bag model which has been used to calculate $g_2(x, Q^2)$ [29]. This model makes a series of assumptions. First, the virtual photon interacts with one quark at a time and the other two are spectators. Secondly, the nucleon is assumed to be in a Fock state with three valence quarks. Finally, the effect of quark confinement is described in terms of a bound state quark spatial wave function.

Based on these assumptions the hadron current can be written:

$$\begin{aligned}\int d^4y e^{iq\cdot y}\langle p'|J_\mu(y)|p\rangle &= (2\pi)^4\delta^4(p+q-p')\langle p'|J_\mu(0)|p\rangle \\ &= (2\pi)\delta^4(p+q-p') \\ &\times \sum_{1\to 2,3}\int\left(\prod_{i=1}^{3} d^3\mathbf{r}_i\right) e^{i\mathbf{q}\cdot\mathbf{r}_1}\overline{q}_{p',\alpha'}(\mathbf{r}_1,\mathbf{r}_2,\mathbf{r}_3)[\hat{e}_q\gamma_\mu]_1 q_{p,\alpha}(\mathbf{r}_1,\mathbf{r}_2,\mathbf{r}_3).\end{aligned} \tag{3.55}$$

where $\mathbf{r}_i$ is the position of the quark with respect to the center of mass, $\hat{e}_q$ is the charge operator of the struck quark and $q_{p,\alpha}$ is the nucleon wave function. The subscript 1 of the operator $[\hat{e}_q\gamma_\mu]_1$ denotes that the operator appears in the terms concerning the quark that is struck by the virtual photon and not the two other quark terms. The nucleon wave function can be written in further detail:

$$q_{p,\alpha}(\mathbf{r}_1,\mathbf{r}_2,\mathbf{r}_3) = \prod_{i=1}^{3} q_{p,m}(\mathbf{r}_i)\alpha_N \tag{3.56}$$

where α_N is the wave function of the nucleon and $q_{p,m}$ is the wave function of a

bound quark.

Using Eq. 3.55, one can then write the hadronic tensor as [29]:

$$W_{\mu\nu}(P,q,S) = \sum_{1\to 2,3}\sum_{\alpha_1,m_1} b_{\alpha_1,m_1}(1;23)\frac{M}{(2\pi)^6 R_1^3} \times \int\prod_{i=1}^{3}\frac{d^3\mathbf{k}_i}{2k_i}\delta^4(q+P-\sum_i k_i) I_{m_1\mu\nu}(\mathbf{k}_1-\mathbf{q}) I_{m_2}(\mathbf{k}_2) I_{m_3}(\mathbf{k}_3) \tag{3.57}$$

where $b_{\alpha_1,m_1}(1;23)$ is the matrix element of $\hat{e}_q^2$, $\mathbf{k}_i$ and m_i are the three-momentum and spin projections of the ith quark and R_i are the parameters which determine the radius of the quark distribution. The integral :

$$I_{m_1,\mu\nu}(\mathbf{k}_1-\mathbf{q}) \equiv \int d^3\mathbf{r}_1' \int d^3\mathbf{r}_1 e^{i(\mathbf{k}_1-\mathbf{q})\cdot(\mathbf{r}_1-\mathbf{r}_1')}\overline{q}_{m_1}(\mathbf{r}_1)\gamma_\mu \not{k}_1\gamma_\nu q_{m_1}(\mathbf{r}_1') \tag{3.58}$$

denotes the contribution from the struck quark where:

$$I_{m_j}(\mathbf{k}_j) \equiv \int d^3\mathbf{r}_j \int d^3\mathbf{r}_j' e^{i(\mathbf{k}_j)\cdot(\mathbf{r}_1-\mathbf{r}_1')}\overline{q}_{m_j}(\mathbf{r}_j)\gamma_\mu \not{k}_j\gamma_0 q_{m_j}(\mathbf{r}_j') \ (j=2,3) \tag{3.59}$$

denotes the contribution from the spectator quarks. These quark wave functions can be calculated using the cavity solution to the MIT bag model or other bound quark wave function in relativistic quark model. A summary of these approaches can be found in Ref. [29].

Two calculations have been made at $Q^2 = 1.0$ GeV^2 using bag models for $g_2^n(x)$ one by X. Song [30] and one by M. Stratmann [31]. These are shown in Fig. 3.4.

3.4 Experimental Data on g_2

While polarized spin structure function measurements in the deep inelastic regime have been on-going since the late 1980's, the data on g_2 for both the proton and the neutron are sparse. This is because most of these measurements put an emphasis on $g_1(x,Q^2)$. The E155X experiment at the Stanford Linear Acclerator Facility (SLAC) is the only previous dedicated $g_2(x,Q^2)$ measurement in the deep

Experiment	x range	Q^2 range	number of g_1^p points	Ref.
E143	0.027-0.749	1.17-9.52	28	[32]
HERMES	0.028-0.660	1.13-7.46	39	[33]
E155	0.015-0.750	1.22-34.72	24	[34]
SMC	0.005 - 0.480	1.30-58.0	12	[35]
EMC	0.015 - 0.466	3.50-29.5	10	[36]

Table 3.2: *Description of the DIS world data set on* g_1^p.

Experiment	target	x range	Q^2 range	number of g_1^n points	Ref.
E143	^{2}H	0.027-0.729	1.17-9.52	28	[37]
E155	^{2}H	0.015-0.750	1.22-34.79	24	[34]
SMC	^{2}H	0.005-0.479	1.30-54.8	12	[35]
E142	^{3}He	0.035-0.466	1.10-5.50	8	[38]
HERMES	^{3}He	0.033-0.464	1.22-5.25	9	[39]
E154	^{3}He	0.017-0.564	1.20-15.0	17	[40]
E99-117	^{3}He	0.327-0.601	2.709-4.833	3	[41]

Table 3.3: *Description of the previous DIS world data set on* g_1^n.

inelastic scattering region. The Jefferson Lab experiment E99-117, while focused on measuring A_1^n, also performed a precise measurement of g_2^n.

The data taken on g_1 and g_2 are summarized in the Tables 3.2, 3.3, 3.4 and 3.5. Also in Fig. 3.3 and Fig. 3.4 the best data on g_2^p and g_2^n are presented. The rest of the world data for g_2 for both proton and the neutron is much less precise and is not included in the tables and in the plots.

Even though higher twist effects should be present in both the proton and the neutron, E97-103 made the choice of searching for higher twist effects in g_2^n over g_2^p for two reasons. First, g_1^p is 3-5 times larger than g_1^n in the kinematic region of interest, even though g_2^p and g_2^n are roughly the same size. Since measurements of g_2 always have a g_1 background contribution, the smaller g_1 is, the cleaner the measurement of g_2. Secondly, there are certain practical advantages of a polarized ^{3}He target for measuring g_2 rather than a polarized proton target. In any case, one can see that more measurements of g_2 are warranted.

Experiment	x range	Q^2 range	number of g_2^p points	Ref.
E155X	0.021-0.780	0.8-0.780	10	[34]

Table 3.4: *Description of DIS world data set on g_2^p.*

Experiment	target	x range	Q^2 range	number of g_2^n points	Ref.
E155X	^{2}H	0.021-0.780	0.8-8.20	10	[34]
E99-117	^{3}He	0.327-0.601	2.709-4.833	3	[41]

Table 3.5: *Description of DIS world data set on g_2^n.*

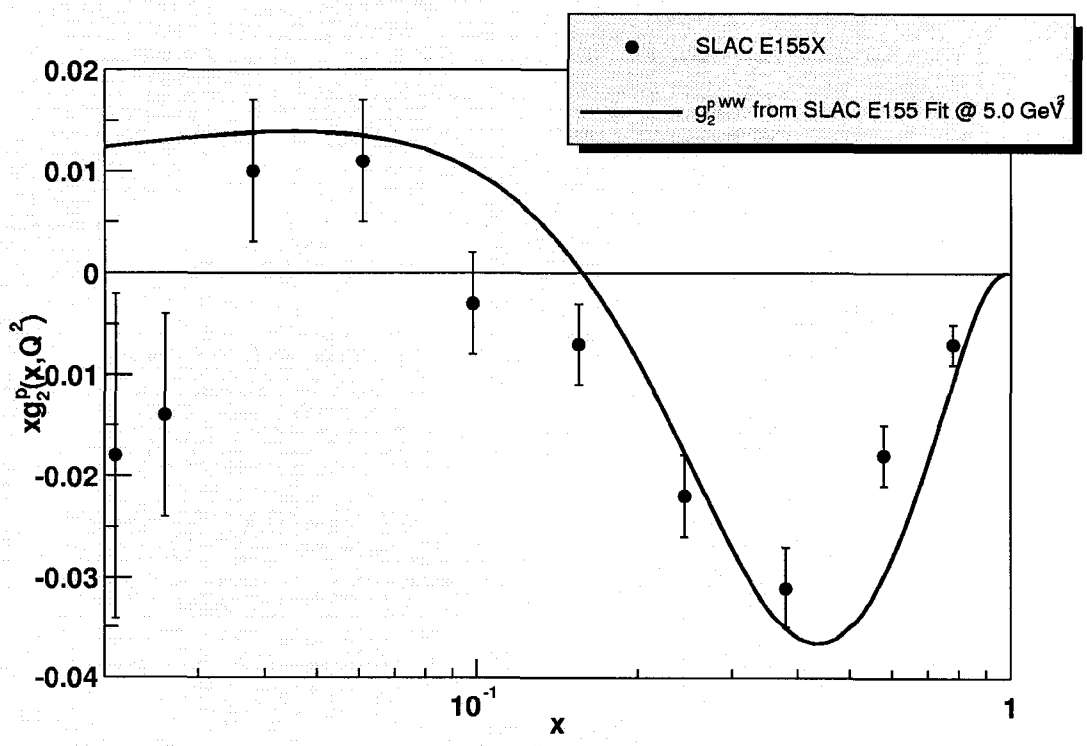

Figure 3.3: *A plot of xg_2^p from SLAC E155X*

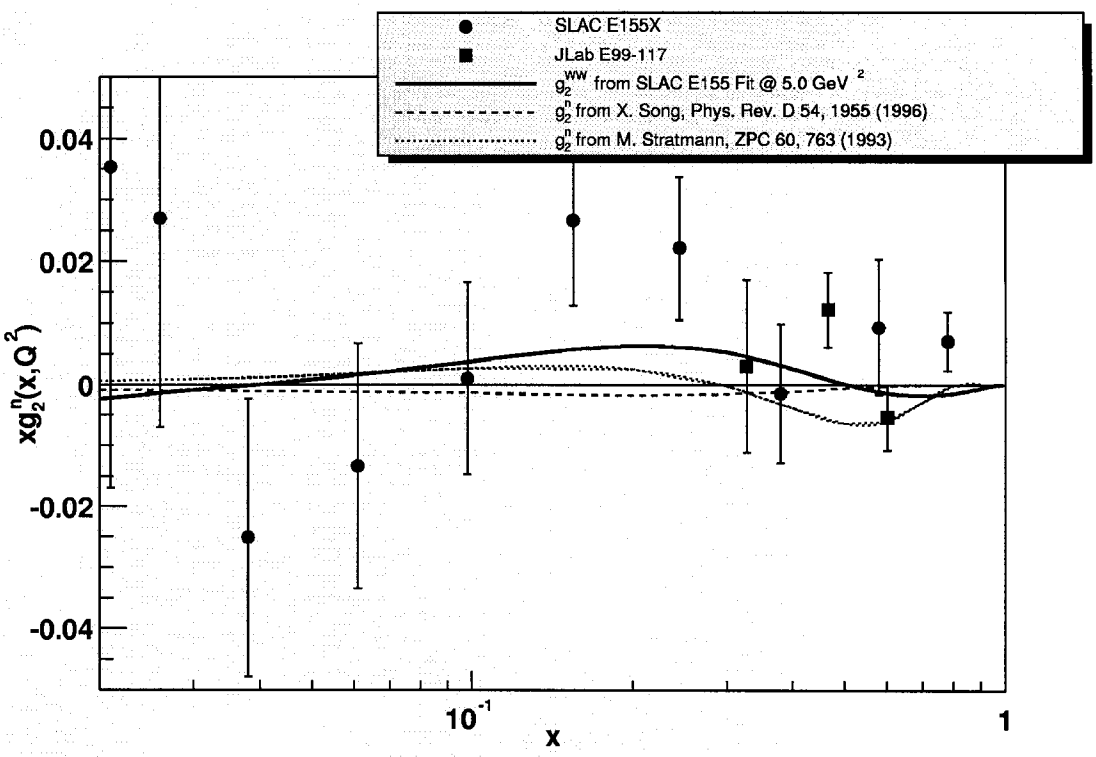

Figure 3.4: *A plot of xg_2^n from SLAC E155X and JLab E99-117*

CHAPTER 4

Experimental Overview

4.1 Goals of E97-103

4.1.1 Physics goals

The goal of Jefferson Lab experient E97-103 was to measure the spin-structure function g_2^n at five points in the deep inelastic scattering region. The five kinematic points are given in Table 4.1. The points were chosen to be at an $x \approx 0.2$ and centered at a $Q^2 \approx 1.0$ GeV^2. The value of x was chosen because of the large value of g_2^{WW} and it was kept nearly constant to be able to isolate the Q^2 dependence. The Q^2 was chosen so that it would be in the deep inelastic scattering regime, but at low Q^2 so that the higher twist effects would be larger.

The most obvious way to measure g_2 is to measure the polarized cross section differences in Eq. 2.21 and Eq. 2.23 with a polarized beam and polarized target. However, cross section measurements are complicated by the need to understand the spectrometer acceptance and detector efficiencies. It is also possible to measure asymmetries and use the world unpolarized data to circumvent this problem.

E (GeV)	E' (GeV)	θ (degrees)	Q^2 (GeV)^2	x	W (GeV)
3.465	1.600	18.6	0.571	0.163	1.95
4.598	2.290	15.8	0.781	0.188	2.10
4.598	1.990	18.6	0.942	0.192	2.20
5.727	2.630	15.8	1.127	0.194	2.36
5.727	2.270	18.6	1.341	0.202	2.46

Table 4.1: *A listing of the acceptance-averaged kinematics for E97-103*

If one defines the cross section differences as:

$$\Delta\sigma_{\parallel} = \frac{1}{2}\left(\frac{d\sigma^{\uparrow\Uparrow}}{dEd\Omega} - \frac{d\sigma^{\downarrow\Uparrow}}{dEd\Omega}\right), \Delta\sigma_{\perp} = \frac{1}{2}\left(\frac{d\sigma^{\uparrow\Rightarrow}}{dEd\Omega} - \frac{d\sigma^{\downarrow\Rightarrow}}{dEd\Omega}\right) \tag{4.1}$$

and the sum:

$$\sigma_0 = \frac{1}{2}\left(\frac{d\sigma^{\uparrow\Uparrow}}{dEd\Omega} + \frac{d\sigma^{\downarrow\Uparrow}}{dEd\Omega}\right) = \frac{1}{2}\left(\frac{d\sigma^{\uparrow\Rightarrow}}{dEd\Omega} + \frac{d\sigma^{\downarrow\Rightarrow}}{dEd\Omega}\right) \tag{4.2}$$

the longitudinal and transverse asymmetries are defined as

$$A_{\parallel} = \frac{\Delta\sigma_{\parallel}}{\sigma_0}, \; A_{\perp} = \frac{\Delta\sigma_{\perp}}{\sigma_0}. \tag{4.3}$$

Measuring asymmetries is easier than measuring cross sections since the acceptance, and often the efficiencies, cancel in the asymmetries. While the structure functions can't be extracted directly from the asymmetries, the unpolarized data taken on the proton and deuterium cover a large kinematic range and can be used to calculate σ_0. By combining σ_0, $A_{\parallel}$ and $A_{\perp}$, one can extract the structure functions g_1 and g_2.

Experiment E97-103 was performed in such a way that the structure functions could be extracted either by measuring just the asymmetries or by doing the full cross section analysis. This dissertation is limited to the asymmetry analysis.

An additional complication is that E97-103 measures the spin structure functions of polarized ^{3}He and not the neutron. The method of measuring the cross section or asymmetry is the same, but one must make the additional step of making a correction for the nuclear effects.

It should be mentioned that these are the physics asymmetries mentioned in Eq. 4.3 assume a pure ^{3}He target, 100% beam polarization and 100% target polarization. Of course, this is not the case in a real experimental situation. The physics asymmetries are derived from the raw experimental asymmetries using

$$A_{\parallel} = \frac{A_{\parallel}^{\text{raw}}}{f P_t P_b}, A_{\perp} = \frac{A_{\perp}^{\text{raw}}}{f P_t P_b} \tag{4.4}$$

where f is the fraction of the total number of events that came from ^{3}He (known as the dilution factor), P_t is the average target polarization and P_b is the average beam polarization.

The measured asymmetries are calculated from the number of events within certain acceptance cuts normalized to the number of incident electrons for each helicity using

$$A^{\text{raw}} = \frac{(N^+/\zeta^+Q^+) - (N^-/\zeta^-Q^-)}{(N^+/\zeta^+Q^+) + (N^-/\zeta^-Q^-)} \tag{4.5}$$

where $N^\pm$ is the number of events within acceptance cuts with helicity ± 1, $Q^\pm$ is the accumulated beam charge for helicity ± 1, and $\zeta^\pm$ is a dead-time correction defined as:

$$\zeta = \frac{\text{Number of events recorded by the DAQ}}{\text{Number of events that trigger the detector electronics}}. \tag{4.6}$$

The dead-time correction is necessary since the detector electronics can take data much faster than the data acquisition system (DAQ) can record it.

Finally, $g_2^{^3\text{He}}$ needs to be converted to g_2^n. This is done using the nuclear correction from [17] :

$$g_2^n = \frac{1}{P_n + 0.056}\left[g_2^{^3\text{He}} + (0.014 - 2P_p)g_2^p\right] \tag{4.7}$$

where P_n and P_p are the effective neutron and proton polarizations in ^{3}He. The structure function g_2^p is another quantity that must be acquired from world data.

A summary of all the experimental quantities that are needed to measure g_2^n is provided in Table 4.2. The rest of this dissertation will explain how these quantities were measured and their uncertainties were determined and present and discuss the results for g_2^n.

4.2 Experimental Setup

Experiment E97-103 took place at Jefferson Lab in experimental Hall A from 1 Aug 2001 to 17 Sep 2001. It used a polarized ^{3}He gas target and two symmet-

Quantity	Description	Source of Measurement
N^+,N^-	number of electrons in acceptance cuts	HRS detector packages
Q^+,Q^-	Accumulated charge	BCMs
ζ^+,ζ^-	Dead time correction	DAQ and scalers
f	dilution factor	reference cell data and cell fill data
P_t	target polarization	NMR,EPR
P_b	beam polarization	Møller and Compton polarimeters
E	beam energy	Arc and Ep measurements
E'	scattered electron energy	spectrometer settings
θ	scattering angle	spectrometer survey

Table 4.2: *Experimental quantities needed for measurements of* g_2^n.

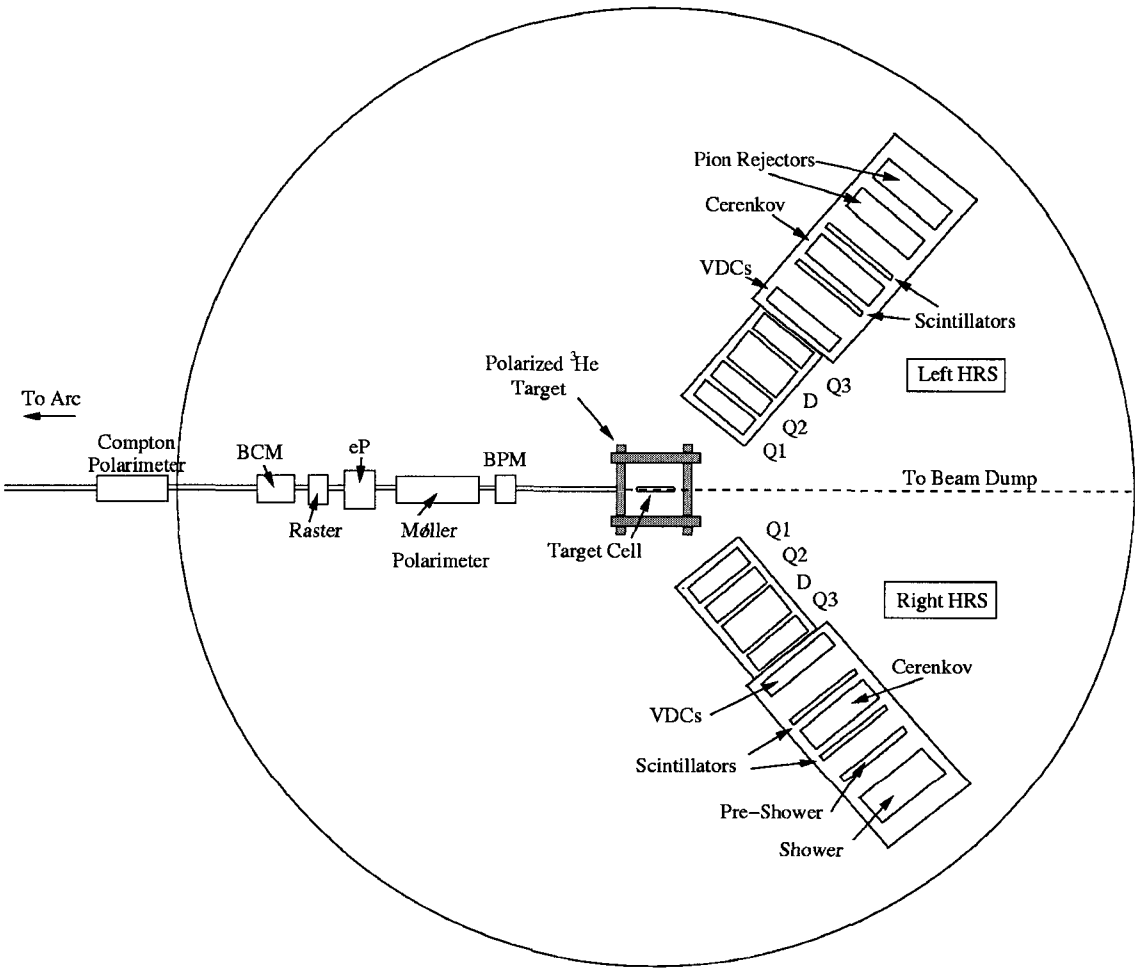

Figure 4.1: *A schematic of the spectrometer, target and beam line apparatus in Hall A.*

ric high-resolution spectrometers (HRS). Each spectrometer was equipped with the standard Hall A detector package used here for identifying and characterizing scattered electrons. The Hall A beam line was used with the standard set of equipment for measuring beam energy, polarization and position. A diagram of the Hall A set-up is shown in Fig. 4.1.

The details of the beam line apparatus, the polarized ^{3}He target and spectrometers will be given in the following chapters.

CHAPTER 5

The Electron Beam and Beam line Apparatus

5.1 Jefferson Lab and CEBAF

5.1.1 The Accelerator Facility

The experiment E97-103 took place in experimental Hall A at Jefferson Laboratory in Newport News, VA. The continuous electron beam accelerator facility (CEBAF) at Jefferson Laboratory is a polarized electron accelerator specifically designed to study strong interaction physics. It is capable of sending electron beams simultaneously to three experimental end stations, known as Hall A, Hall B and Hall C. Jefferson Lab was a natural choice for E97-103 since the experiment required high luminosity, high beam polarization and enough beam energy to reach the deep inelastic scattering region.

The accelerator, shown in Fig. 5.1, consists of an injector, two linear accelerators (known as linacs) and two sets of recirculation (ARC) magnets. The injector transports electrons from the injector source to the north linac, accelerating them to 45 MeV in the process. The north linac then can accelerate the electrons up to 600 MeV. After passing through the north linac the electrons are transported by a set of recirculation magnets where they enter the south linac. The electrons are given an additional acceleration of up to 600 MeV. After the south linac, the electrons can either enter another set of recirculating magnets and be given an additional acceleration by the linacs or enter one of the experimental halls. The electrons can be circulated through the linacs 1-5 times for a energy range of 0.6-5.7 GeV [42].

Each of the cryomodules that make up the linacs consist of eight super-conducting

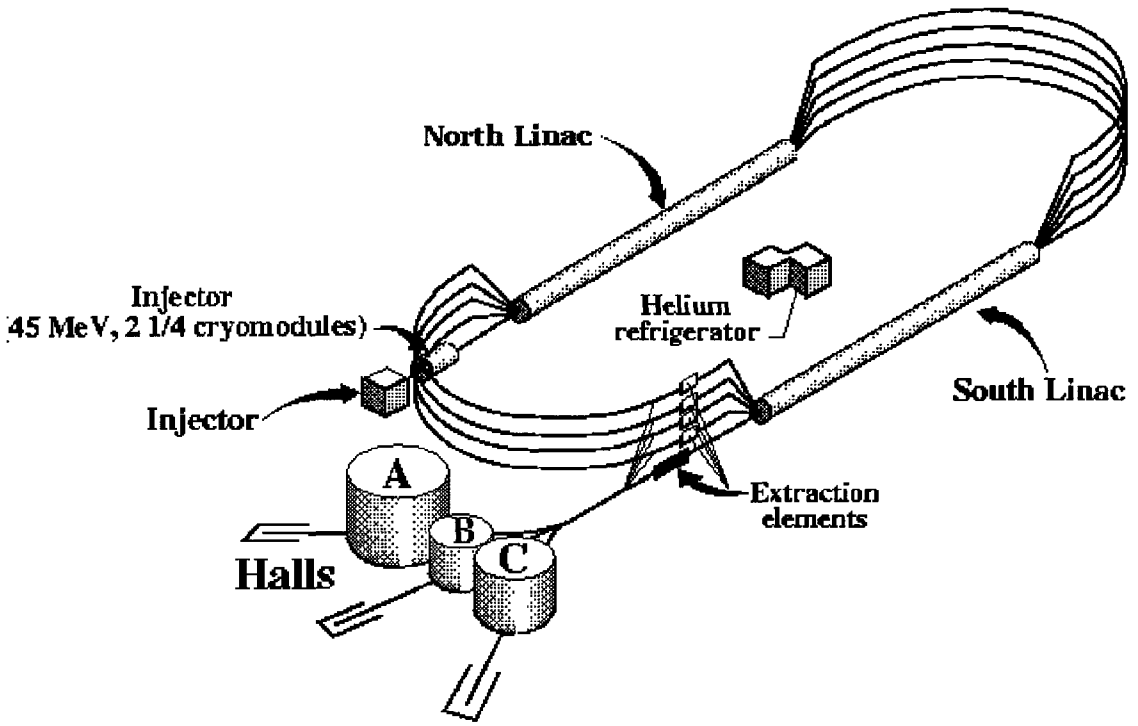

Figure 5.1: *The electron accelerator facility at Jefferson Lab.*

niobium cavities. The niobium cavities are maintained in a 2.0 K liquid helium bath to maintain their superconducting properties. The superconductivity allows more power to be applied the cavity without heat loss due to resistance. The electrons are accelerated by 1497 MHz RF oscillations in the cavities. The accelerator divides these oscillations into three 499 MHz bunches, one for each experimental hall [42]. The bunches are separated after the south linac by an RF separator and sent to the appropriate hall. Because of this system, each hall can operate at different beam energy and current.

5.1.2 The Polarized Source

Polarized eletrons are produced by photo-emission from a photo-cathode using circularly polarized laser light. The injector optical source consists of a laser, a linear polarizer, a removable half-wave plate, a Pockels cell, a rotatable half-wave plate and the photocathode. A diagram of these components is shown in Fig. 5.2. The laser is

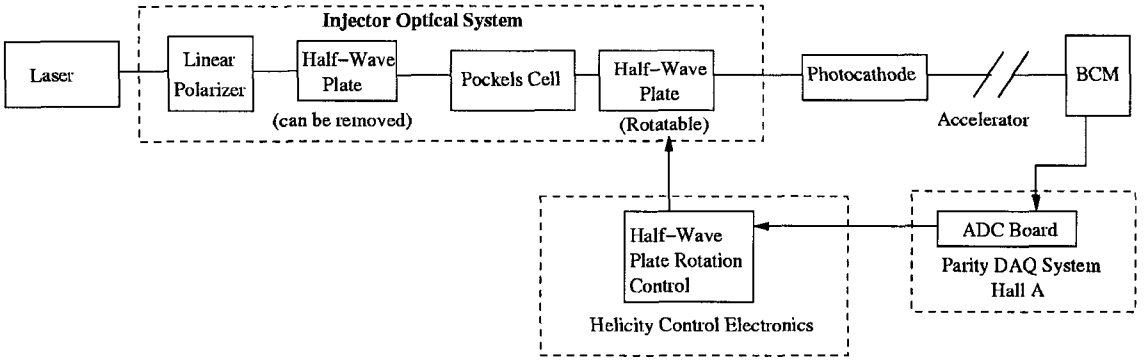

Figure 5.2: *A diagram of the polarized source optics and helicity feedback system used to produce polarized electron beam and control charge asymmetry.*

the source of photons needed to excite the electrons at the photocathode. The linear polarizer converts the unpolarized light to linearly polarized light. The removable half-wave plate is occasionally inserted in the system to change the sign of the helicity (positive helicity bunches become negative helicity bunches and vice versa). By running with and without the removable half-wave plate, many systematic errors cancel.

The Pockels cell is a voltage-controlled crystal used to convert the linearly polarized light to circularly polarized light. The helicity of the polarized light is controlled by voltage inputs to the Pockels cell which are in turn controlled by the helicity electronics. A rotatable half-wave plate is used to compensate for charge asymmetries due to residual linear polarization that can be analyzed by the photocathode. Finally, the polarized light illuminates the photocathode.

Polarized electrons for CEBAF are created from a GaAs cathode. This cathode is built on a GaAs substrate. Layers of different materials containing GaAs are grown on the substrate as shown in Fig. 5.3. The top layer is made of pure GaAs. The layer directly below it is made of $GaAs_{0.72}P_{0.28}$ (a GaAs crystal with 28% of the arsenic replaced with phosphorus). The lattice spacing of the $GaAs_{0.72}P_{0.28}$ is shorter (5.5968 Å) than pure GaAs (5.6533 Å). This causes a strain on the pure GaAs layer and induces an energy gap between electrons in the $P_{3/2}$,m_j=$\pm$3/2 states

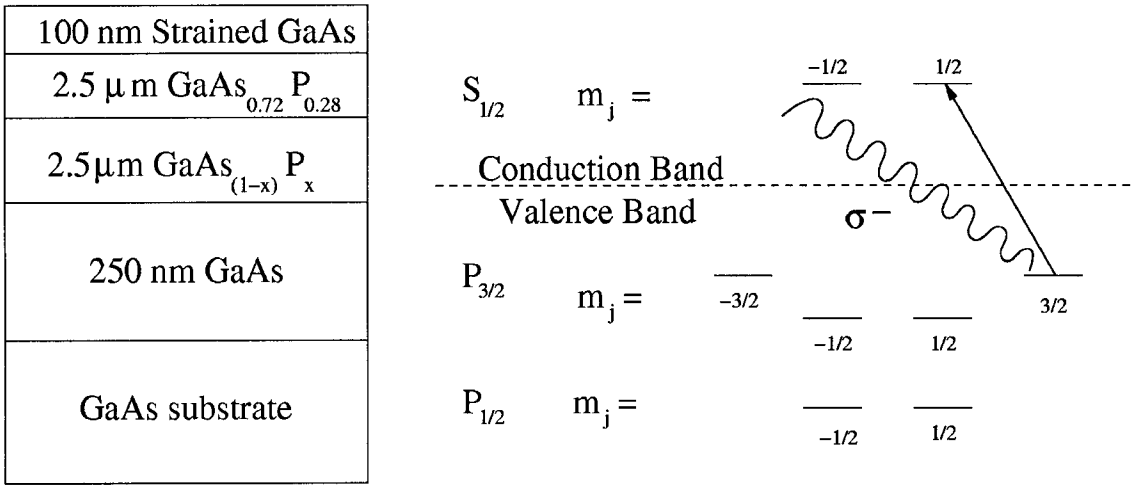

Figure 5.3: *Two diagrams of the GaAs cathode used as a source of polarized electrons at CEBAF. The boxes on the left represent the different GaAs combinations that make up the photo-cathode. The diagram on the right shown circularly polarized light exciting an electron in the layer of strained GaAs.*

and the $P_{3/2}$,m_j=$\pm$1/2 states [43].

The seperation of the electron states allows excitation of electrons in a speciific m state. By applying left-handed circularly polarized laser light (helicity = -1), electrons from the $P_{3/2}$,m_j=3/2 state can be excited to $S_{1/2}$, m_j=1/2 state of the conduction band. From there the polarized electrons can escape through the surface into the surrounding vacuum. The electrons that escape by this process will all have the same polarization since only electrons from the $P_{3/2}$, m_j=3/2 can be excited by the circularly polarized light. The same is true of right-handed circularly polarized laser light (helicity = +1) and electrons in the $P_{-3/2}$,m_j=-3/2 state.

The polarized source can produce 200 μA of current split between the three halls. The beam polarization is regularly about 75% and often exceeds 80%. The maximum beam into Hall A is over 100 μA, but the beam current for E97-103 never exceeded 15 μA due to constraints arising from the polarized ^{3}He target.

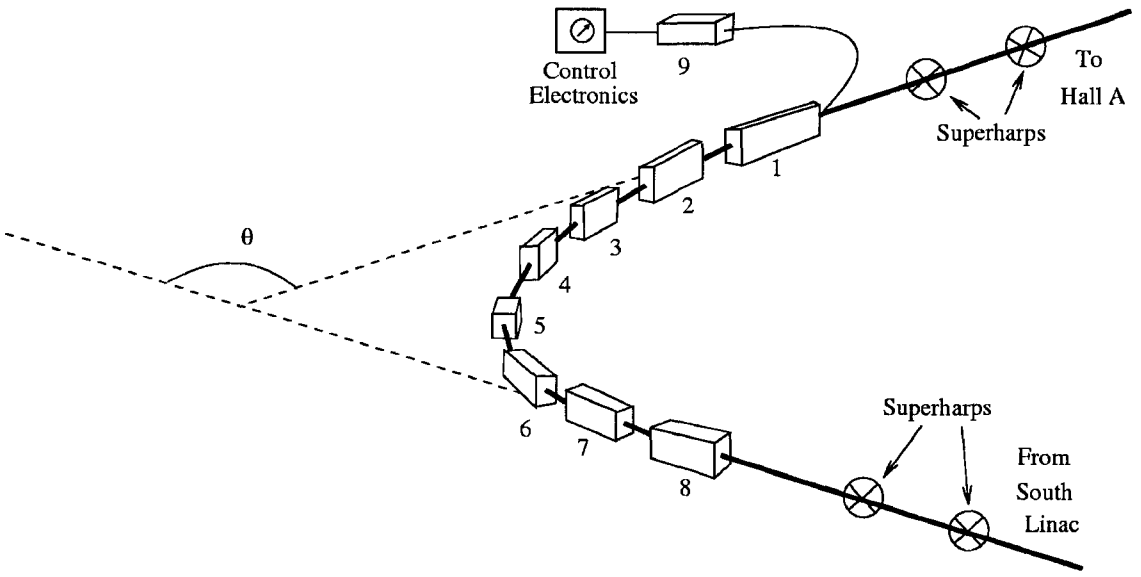

Figure 5.4: *The diagram of the equipment used for the Arc energy method.*

5.2 Measuring the Beam Energy

5.2.1 Arc Energy Measurements

The Arc energy measurement is one of two independent methods of measuring the electron beam energy in Hall A. The method extracts the beam energy by measuring its deflection in a known magnetic field. Therefore, the technique requires a simultaneous measurement of the deflection of the beam and the integrated magnetic field ($\int \vec{B} \cdot \vec{dl}$) in the arc section of the beam line entering Hall A.

The nominal bend angle of the beam line in this section is θ =34.3° [44]. Deviations from this bend angle are measured by a series of wire scanners known as "superharps". The superharps move a thin wire across the beam. Scattering from the wire is measured by nearby ion chambers. Since the position of the wire is well-known during the beam crossing, the position of the beam can be determined precisely.

The magnetic field is prodced in the 8 dipole magnets in the arc, and their field is calibrated by a ninth dipole connected in series, which is not directly in the beam line, as shown in Fig. 5.4. The beam energy can then be calculated using the

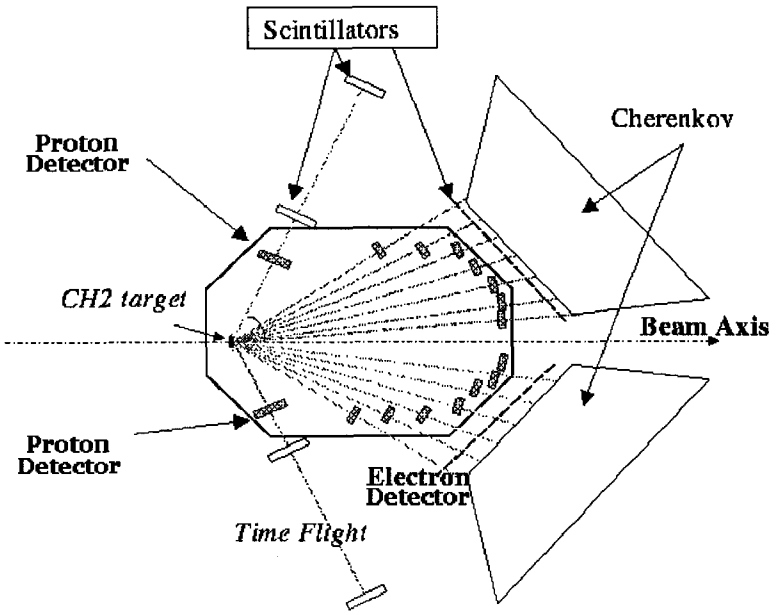

Figure 5.5: *A diagram of the eP measurement target and detectors.*

formula:

$$p = c\frac{\int \vec{B} \cdot \vec{dl}}{\theta} \tag{5.1}$$

where c is the speed of light.

5.2.2 eP Energy Measurements

The other method used in Hall A for beam energy measurements is the eP method. This method determines the beam energy by measuring the scattering electron angle θ_e, and the recoil proton angle θ_p, from the ^{1}H$(e, e'p)$ elastic reaction. The following kinematic formula is used to extract the beam energy [44]:

$$E = M_p \frac{\cos(\theta_e) + \sin(\theta_e)/\tan(\theta_p) - 1}{1 - \cos(\theta_p)} + O(m_e^2 + E^2). \tag{5.2}$$

where M_p is the mass of the proton and m_e is the mass of the electron. The second term, $O(m_e^2 + E^2$ represent higher order terms which are small and ignored in the final calculation.

The diagram in Fig. 5.5 shows the setup of the eP measurement target and

Date of Energy Change	Arc Method (MeV)	eP Method (MeV)	Tiefenback Method (MeV)	Average (MeV)
4 Aug 2001	-	1197.27±0.47	1196.87	1197.27±0.47
9 Aug 2001	3465.0±3.0	-	3463.57	3465.0±3.0
19 Aug 2001	-	4598.25±1.37	4596.98	4598.25±1.37
15 Sep 2001	5728.1±2.0	5726.0±1.1	5727	5727.1±1.1

Table 5.1: *List of energy measurements made for E97-103. The Tiefenback method is included only for comparison and is not used in the average.*

detectors. The target is a thin piece of CH_2 film. There are two arms that each contain a proton detector and a series of electron detectors. The proton detectors consist of a silicon micro-strip detector for determining position and two scintillators to calculate time of flight. The electron detectors each have a series of 7 micro-strip detectors for covering a wide range of energies. The electron detectors also each have a Cerenkov detector that improves electron identification.

5.2.3 Beam Energy Used for E97-103

Both the Arc method and eP method for measuring the beam energy were used in E97-103. The values measured for the beam energies used in the experiment are listed in table 5.1. This table also lists an on-line energy measurement known as the "Tiefenback energy" (named after Jefferson Lab accelerator physicist Michael Tiefenback). This measurement is made using the Hall A Arc $\int B \cdot dl$ value and Hall A Arc beam position monitors. This value can be calculated on-line and is compared to the calibrated values of the Arc measurement.

5.3 Measuring the Beam Polarization

5.3.1 Møller Polarimeter

E97-103 used two systems to measure the beam polarizations on three orthogonal axes. The Møller polarimeter measures the scattering of polarized electrons from the beam off of polarized atomic electrons in a magnetized foil [44]. The cross

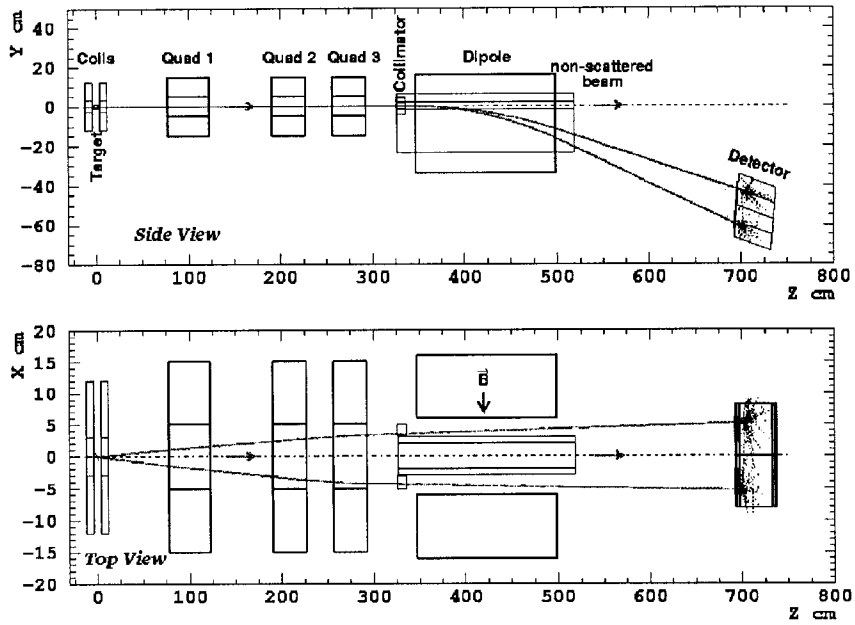

Figure 5.6: *A diagram of the Møller polarimeter.*

section for this scattering depends on the beam and target polarizations P^b and P^t as shown here:

$$\sigma \propto \left[1 + \sum_{i=X,Y,Z} (A_{ii} \cdot P_i^t P_i^b)\right] \tag{5.3}$$

where $i = X, Y, Z$ are the projections of the polarizations. The analyzing power A depends on the scattering angle in the center-of-mass frame, θ_{CM}. [44]. If the beam direction is defined as traveling along the Z axis and the electron scattering happens in the ZX plane then the analyzing power can be written:

$$A_{ZZ} = -\frac{(7 + \cos^2\theta_{CM})\sin^2\theta_{CM}}{(3 + \cos^2\theta_{CM})^2} \tag{5.4}$$

$$A_{XX} = -\frac{\sin^4\theta_{CM}}{(3 + \cos^2\theta_{CM})^2} \tag{5.5}$$

$$A_{YY} = -A_{XX} \tag{5.6}$$

It can be seen from these equations that at $\theta_{CM} = 90°$ the analyzing power has its maximum value of $7/9$.

The Hall A Møller polarimeter uses a ferromagnetic foil in a 24 mT field as a target of polarized electrons. The target can be tilted at various angles to the

beam in the horizontal plane to measure both the longitudinal and transverse components of the beam polarization. The asymmetry at angles of $\pm 20°$ is measured by two detectors. The target polarization is obtained from offline foil polarization measurements [44], and for the supermendur foil used in E97-103 the polarization was $7.95 \pm 0.24\%$. Knowledge of the target polarization is the largest systematic error in Møller scattering.

The Møller polarimeter uses a magnetic spectrometer consisting of three quadrupole magnets and a dipole magnet as shown in Fig. 5.6. The spectrometer can select electrons from a scattering range of $75° < \theta_{CM} < 105°$ in the horizontal plane and $-5° < \phi_{CM} < 5°$ where ϕ_{CM} is azimuthal angle [44]. The polarimeter can be used with beam energies from 0.8 GeV to 6.0 GeV.

The detectors of the Møller polarimeter are two lead-glass calorimeter modules. The beam-helicity correlated asymmetries measured in the detectors determine the polarization of the beam. The detectors work in both coincidence mode (only counting electron hits when they strike both detectors simultaneously) and singles mode (measuring electron rates independently). A comparison of the asymmetries measured in coincidence and singles mode reveals that 30% of the singles events came from a source other than the Møller target. The background in coincidence mode is less than 5%.

5.3.2 Compton Polarimeter

The second method used in E97-103 for measuring the beam polarization was the Compton polarimeter. Circularly-polarized photons from a laser scatter off the polarized electron beam, and the scattered electrons and scattered photons are detected [44]. The polarization is extracted from the measurement of the counting rate asymmetry of electrons and photons for opposite beam helicities of the electron beam. The Compton measurement, unlike that with the Møller polarimeter, is an

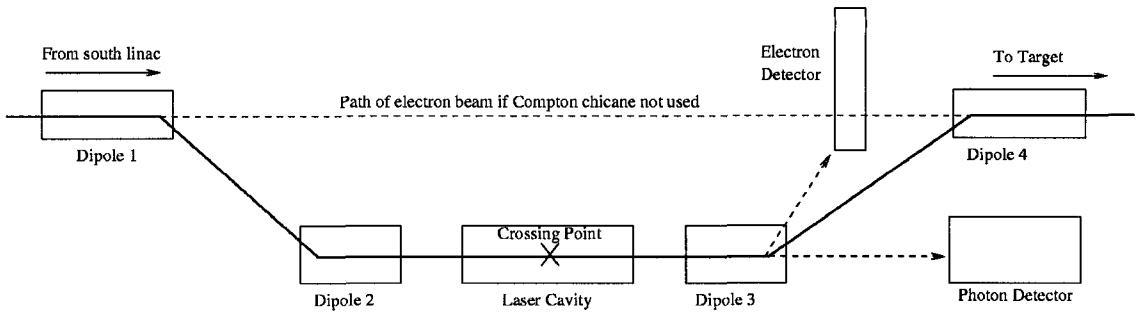

Figure 5.7: *Schematic of the Compton apparatus*

effectively passive measurement and can be done while taking production data on the main target.

The Compton polarimeter, as pictured in Fig. 5.7, consists of a magnetic chicane, a photon source, an electromagnetic calorimeter and an electron detector. The chicane bends the beam vertically using four dipole magnets so that the photon beam provided by the laser can cross the electron beam and the scattered electrons and photons can be detected. The photons from the laser are backscattered into a calorimeter. A silicon strip electron detector is used to detect the scattered electrons. Electrons that did not interact with the photon beam exit the polarimeter and reach the target.

A resonant Fabry-Pérot cavity is used the amplify the photon beam [45]. The resonance cavity uses two mirrors to amplify a primary 230 mW CW Nd:YaG laser ($\lambda = 1064$ nm). An amplification factor of 7300 has been measured corresponding to a photon beam power of 1680 W inside the cavity [44]. The circular polarization of light has been measured to be $> 99\%$ for both positive and negative helicity states. The helicity of the polarized laser light can be changed by using a rotatable half-wave plate.

To maximize the number of scattered photons, the angle at which the photon beam crosses the electron beam must be as small as possible. The nominal crossing angle is 23 mrad. The position of the electron beam and the photon beam are

Beam Energy (GeV)	Polarization (%)
1.19727	83.1±3.3
3.4650	-69.3±2.8
4.59825	76.6±3.1
5.7271	-81.6±3.3

Table 5.2: *The values used for the polarization for each beam energy are based on a combination of Møller and Compton polarimeter measurements.*

adjusted until the maximum rate of Compton events in the detectors is acheived. The measurement can be done using photon singles events, electron singles events or a coincidence measurement of photon and electrons. Measurements taken with the laser beam off reveal a background/signal ratio of as good as 0.05 [44].

Using the position of the electrons in the micro-strip planes and from the amount of light collected, one can calculate the energy of the scattered particles. In coincidence mode this is especially useful, since the photon energies can be determined allowing a calibration of the response functions of the calorimeter to be made. These type of coincidence measurements have the smallest systematic errors.

5.3.3 Beam Polarization for E97-103

The values used for the polarization are listed in Table 5.2. A plot of the average values compared with the individual Compton and Møller polarimeter measurements is shown in Fig. 5.8.

The error on the polarization is estimated to be 4% (relative). This error is based on results of the Spin Dance 2000 measurement [46] and recent experience in Hall A. In the Spin Dance measurements, polarimetry results from all three halls were compared to each other for the same beam. The results in Fig. 5.9 are shown with the expected systematic errors for each polarimeter, normalized to the polarization value given by the injector Mott polarimeter. The results show that there is significant discrepancy between the Hall A Møller and the Hall A Compton polarimeters. The "Hall A Average" shown in Fig. 5.9 is the value of the polarization

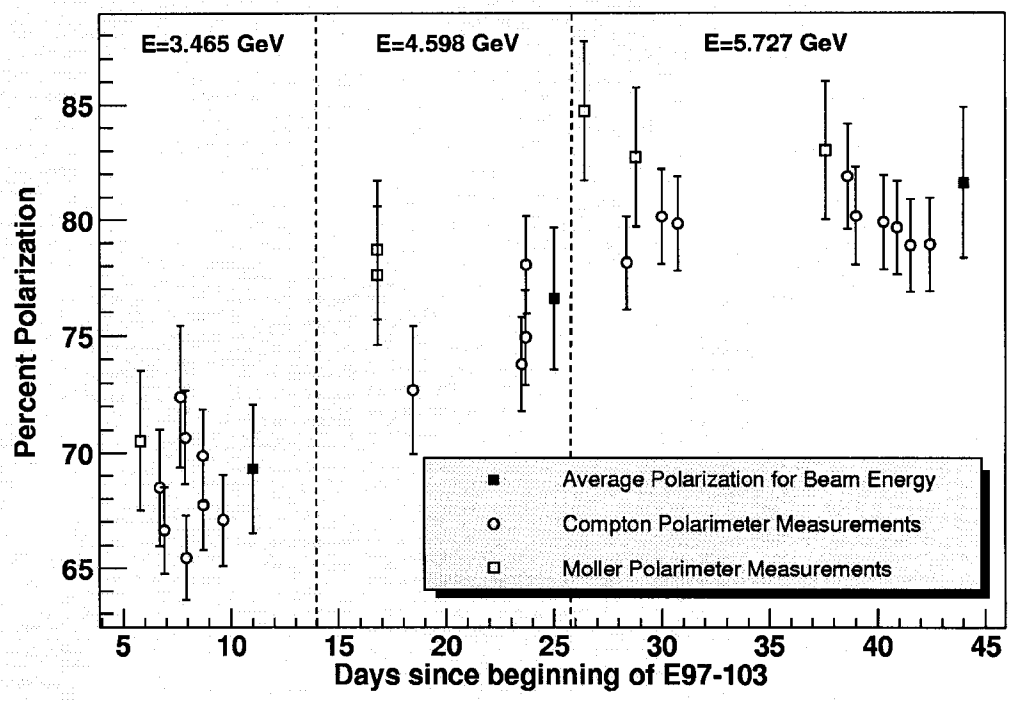

Figure 5.8: *A plot of the different beam polarization measurements and their average for each beam energy.*

using the average of the Hall A Compton and Hall A Møller and a 4% relative error. The average of the Hall A Compton measurements and Hall A Møller measurements are computed separately and averaged.

5.4 Beam Helicity, Charge and Position

5.4.1 Beam Helicity

As can be seen in Eq. 2.21 and Eq. 2.23, the spin-dependent structure functions can be isolated by measuring the difference in cross section correlated with changing beam helicity. The helicity is flipped by a Pockels cell that changes the handedness of the circularly polarized laser light that excites the electrons from the photocathode. The Pockels cell design allows the helicity to be changed pseudo-randomly at a rate of 30 Hz.

An example of the helicity pattern is shown in Fig. 5.10. This plot shows

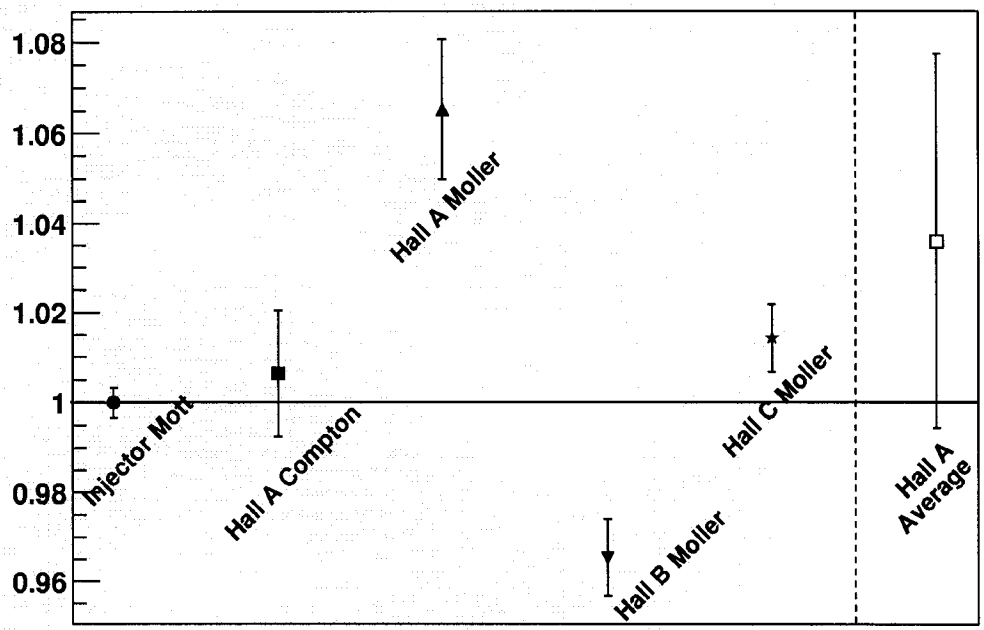

Figure 5.9: *The results for a comparison of Jefferson Lab beam polarimeters performed in 2000. The polarization is normalized to the Mott polarimeter. The "Hall A Average" is the value of the polarization using the method used in E97-103 [46].*

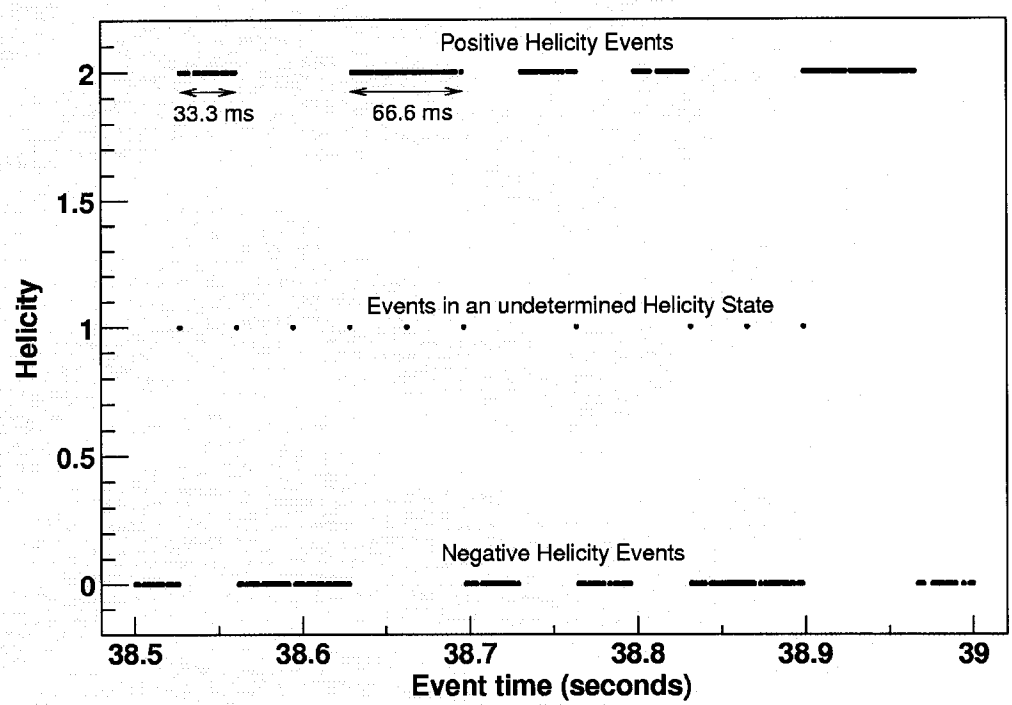

Figure 5.10: *A plot of the beam helicity in a half second time span as extracted from reconstructed data. See text for details.*

the beam helicity in a 0.5 second time span as extracted from reconstructed data. Each point represents an event that triggered the detector system. The events with helicity '0' occurred during period of negative beam helicity and helicity '2' events occurred during periods of positive beam helicity. The helicity '1' events occurred during periods of undetermined helicity. These periods are usually caused by a 0.2 ms "blank off" that is set up in the electronics system to occur every 33.3 ms to cover up periods when the helicity is changing. This eliminates the number of events assigned the wrong helicity.

The helicity pattern does not simply alternate between positive and negative helicity states regularly (as it would in "toggle" mode). Instead the length of each state is determined randomly between periods of 33.3 ms and 66.6 ms in each helicity state (known as "pseudo-random" mode). This technique eliminates systematics

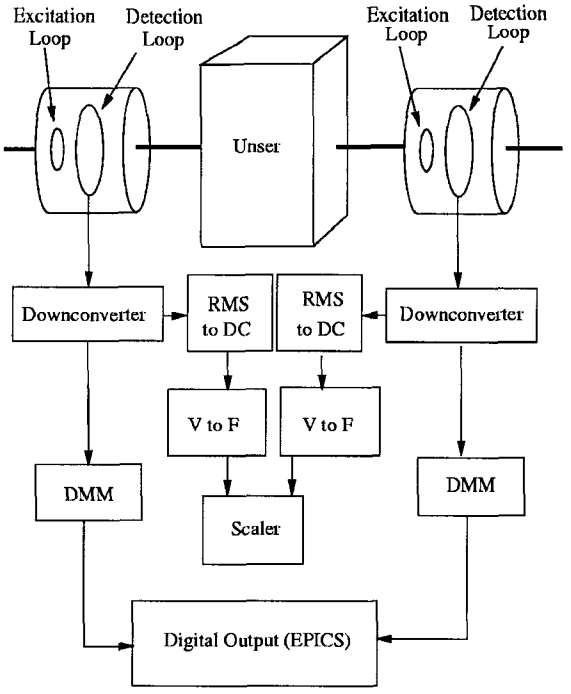

Figure 5.11: *Beam charge montioring system*

that could be associated with 30 Hz noise in the system.

5.4.2 Measuring Beam Charge

The amount of charge delivered to the target is an important normalization factor in both the cross section and asymmetry measurements. In Hall A the charge is measured by a passive beam current monitor (BCM). The BCM consists of an Unser monitor, two RF cavities, associated electronics and a data-acquisition system. The setup is displayed in Fig. 5.11 [47].

The Unser monitor is a Parametric Current Transformer which provides an absolute reference for the calibration of the beam [44]. The monitor is calibrated by passing a known current through a wire inside the beam pipe. To maintain this calibration, extensive magnetic shielding and temperature stabilization is required to reduce noise and baseline drift. However, since the Unser monitor's output signal drifts if used for a period of more than several minutes, it cannot be used to

continuously monitor the beam current.

The two RF resonance cavity monitors are stainless steel waveguides tuned to the frequency of the charge oscillation of the accelerator cavities (1497 MHz). The voltage output of these monitors is proportional to the current in the beam [44]. The output data from the cavities is sent to two output channels: a sampled channel and an integrated channel.

The sampled channel is sent to a digital multimeter which produces a digital signal that represents the root-mean-square (RMS) of the signal over one second. These signals are sent via GPIB ports to a computer where the RMS values for both cavities are stored in the EPICS database (this is part of the data acquisition system the will be discussed in a later chapter). The integrated values are sent to an RMS to DC converter followed by a voltage to frequency converter (V to F). The integrated readings are sent to a scaler which is read by the data acquisition (DAQ) system and inserted into the data stream every four seconds [44].

The RF cavities are calibrated regularly by running the current from zero to the maximum current several times, dwelling at each setting for 60 to 90 s. The output from the Unser is used to calibrate the output of the RF cavities. The calibration can be determined down to a current of 1 μA with an accuracy of $\leq$0.5% [44].

The calibration used for E97-103 was performed in January 2001 and is given in Table 5.3. The accumulated charge can be derived from these calibration constants and values from the scalers. The scaler values needed are the helicity-gated clock values (t_h) (the helicity-gated clock times the amount of time in each helicity state measured with a 1024 Hz clock) and the helicity-gated BCM scaler reading for the upstream cavity (N_h^u) and for the downstream cavity (N_h^d). In the case of t_h, N_h^u and N_h^d there are three types of helicity : positive, negative and ungated, which is the sum of positive and negative. In addition to this, for each helicity of t_h, N_h^u and N_h^d there are three levels of amplification (x1,x3,x10) that can be used for different

Upstream Cavity				
Ampli-	Offsets			Constant
fication	ungated	positive	negative	
1	92.072596	92.21067	92.069586	1345
3	167.05737	167.0949	166.95239	4114
10	102.62361	102.62498	102.46542	12515
Downstream Cavity				
Ampli-	Offsets			Constant
fication	ungated	positive	negative	
1	72.190291	72.309803	72.176298	1303
3	91.080796	91.145456	90.984981	4114
10	199.50698	199.57484	199.34949	12728

Table 5.3: *Table of constants used for calculating accumulated charge sent to the target.*

ranges of beam current.

This creates a total of 18 possible values for the accumulated charge (2x for 2 cavities, 3x for three helicities and 3x for three levels of amplification). All 18 values can be calculated using the following formula with the correct constants from table 5.3:

$$Q^i_{h,a} = \frac{N^i_{h,a}/t_h - f_{a,h}}{c_a} t_h \tag{5.7}$$

where h refers to the helicity, a refers to the amplification, i refers to the cavity (upstream or downstream), $f_{a,h}$ refers to the corresponding offset in Table 5.3, $c_{a,h}$ refers to the corresponding constant in Table 5.3, $Q^c_{h,a}$ is the accumulated charge in time period t_h and $N^c_{h,a}$ is the accumulated scaler reading for time period t_h.

For E97-103 the charge was calculated using the 3x amplifier scaler because it is appropriate for current values from 1-20 μA. The charge vales for the upstream and downstream cavities were averaged. The formula used to calculate the positive and negative accumulated charge is given by the equations:

$$Q_+ = \frac{1}{2}\left(Q^u_{+,3} + Q^d_{+,3}\right) \tag{5.8}$$

$$Q_- = \frac{1}{2}\left(Q^u_{-,3} + Q^d_{-,3}\right) \tag{5.9}$$

where $+$ and $-$ refer to positive and negative helicity respectively.

5.4.3 Beam Charge Asymmetry Feedback System

Due to helicity-dependent differences in the injector or in the helicity gating, there can be significantly different amounts of charge in each helicity state. These differences result in a charge asymmetry which is defined by:

$$A_Q = \frac{Q^+ - Q^-}{Q^+ + Q^-}. \tag{5.10}$$

Q^+ and Q^- are the accumulated charge given by the BCMs. However, these can be broken down further, for purposes of studying the charge asymmetry, into $Q^+ = I^+t^+$ and $Q^- = I^-t^-$ where $I^\pm$ is the beam current during $\pm$ helicity states and $t^\pm$ is the time interval of the helicity pulses [41].

The two general categories for sources of beam charge asymmetry are when $t^+ \neq t^-$ and when $I^+ \neq I^-$. $t^+ \neq t^-$ is caused by unequal timing in the helicity generation circuitry. $I^+ \neq I^-$ is caused by various sources in the injector source. These include incomplete polarization of the injector laser, and imperfections in the Pockels cell or half-wave plate.

The charge asymmetry from either of these categories can be corrected, when calculating the cross section or asymmetry, by normalizing the charge for the positive and negative helicity states independently. However, the charge asymmetry can only be measured confidently to 1% because of non-linear effects in the BCMs. Also a beam intensity asymmetry may affect the beam transport in the accelerator. Therefore, a helicity feedback system was created to minimize the effect of charge asymmetry on the production physics data.

The timing differences in the helicity gates was expected to be small enough not to need significant improvement; therefore the helicity feedback system focused on controlling the intensity differences at the source. A separate data-acquisition system, called the "parity DAQ", was set up to control the rotatable half-wave plate. The parity DAQ would record values from the BCM and calculate the charge

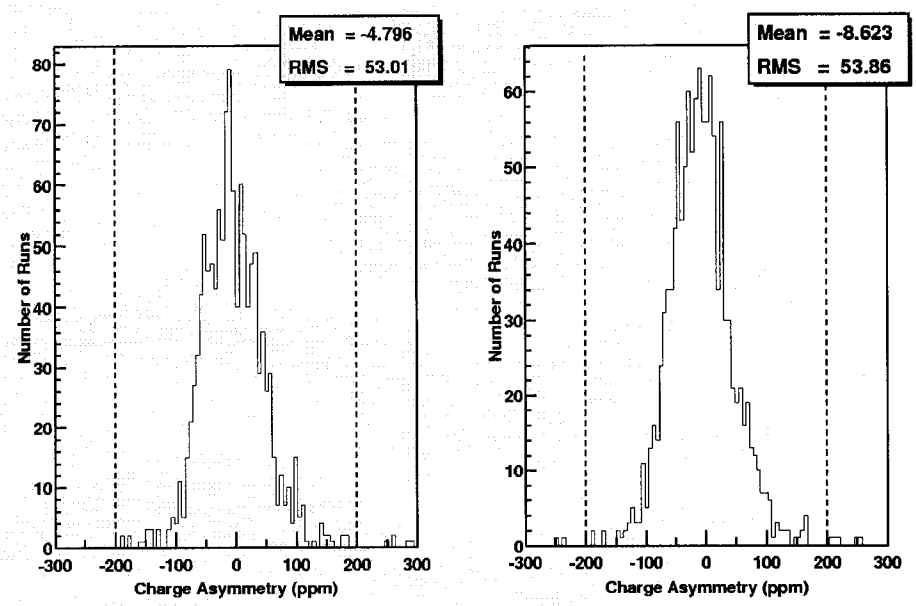

Figure 5.12: *The distribution of charge asymmetry for each run. The left histogram is the charge asymmetry with the beam trips and the right histogram is the charge asymmetry with the beam trips cut out.*

asymmetry every five minutes. A new setting for the rotatable half-wave plate would be entered into an EPICS database on an ADC board in Hall A (the one used for the target controls). This database could be read by control systems at the injector which would make the proper rotation of the half-wave plate. The system is illustrated in fig:charge.

This system exceeded the necessary requirements for the experiment. A charge asymmetry of less than 200 ppm would have been sufficient to suppress the charge asymmetry as a source of systematic error. One concern for this experiment is that the beam asymmetry would occasionally be large during periods when the beam was ramping up to the nominal current after a beam trip. This procedure could last up to 30 seconds with an average of 3-4 beam trips per run. These periods can be cut out of the data when calculating the charge asymmetry. Histograms of the charge asymmetry for each run are shown in Fig. 5.12. The left histogram is with the beam trips included in the data and the right histogram is the charge asymmetry

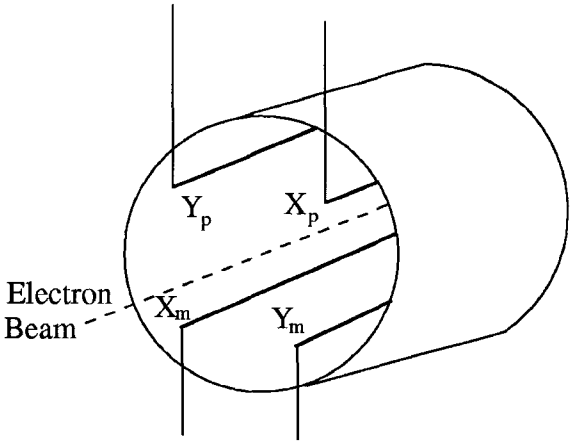

Figure 5.13: *A diagram of the beam position monitor.*

distribution with these beam asymmetries cut out. Both show a distribution width around 53 ppm, which more than satisfied the design requirements of the experiment.

5.4.4 Beam Position Monitors

Careful measurement of the beam position is necessary to make sure the beam stays on the target and because it can change the values of important kinematic values. Determination of the beam position is made by two beam position monitors (BPMs) located at 7.5 m (BPMA) and 2.4 m (BPMB) upstream of the target. The BPMs each consist of four antennae that are tuned to the 1497 MHz oscillation of the accelerator. The voltage output of each antenna increases as the beam gets closer to it [48]. A schematic of one the BPMs is shown in Fig. 5.13.

The BPMs are calibrated with wire scanners or "harps". These are located adjacent to the BPMs. Just like the superharps, used in the Arc energy measurement, the harp measurement moves a wire across the beam line and measures where the wire crosses the beam by scattering into ion chambers. The wire scanners used for the BPMs are regularly surveyed with respect to the coordinate system in Hall A.

The beam position at the target can be calculated using the coordinates derived

from the BPMs and the following formulas:

$$x_{\text{beam}} = \frac{1}{z_B - z_A}(x_A z_B - x_B z_A) \tag{5.11}$$

$$y_{\text{beam}} = \frac{1}{z_B - z_A}(y_A z_B - y_B z_B) \tag{5.12}$$

$$\theta_{\text{beam}} = \frac{x_B - x_A}{z_B - z_A} \tag{5.13}$$

$$\phi_{\text{beam}} = \frac{y_B - y_A}{\sqrt{(x_B - x_A)^2 + (z_B - z_A)^2}} \tag{5.14}$$

where x_A and x_B are the x coordinates determined by the BPMA and BPMB BPMs respectively, y_A and y_B are the y coordinates determined by the BPMA and BPMB BPMs respectively, z_A is -7.345 m and z_B is -2.214 m.

5.4.5 Raster

Since the beam size from the accelerator is quite small ($\approx$ 100 microns), the polarized ^{3}He target used in E97-103 requires constant beam movement or rastering, to avoid cell ruptures as a result of localized heating. The system used in Hall A for E97-103 is a circular raster made by a pair of dipole magnets located 24 m upstream of the target [41].

The magnets are driven at 18 kHz with a 90° phase difference between the two so that it makes a circular pattern. The radius of the circular pattern is cycled from 0.2 mm to 2 mm at a frequency of 1 kHz. Fig. 5.14 shows the raster pattern and the distribution in x_{beam} and y_{beam}. Fig. 5.15 shows the average beam position in x_{beam} and y_{beam} and the raster RMS for the first experimental kinematic ($Q^2 = 0.54$ GeV^2). There was a coordinate shift in y_{beam} because of physical adjustments of the target.

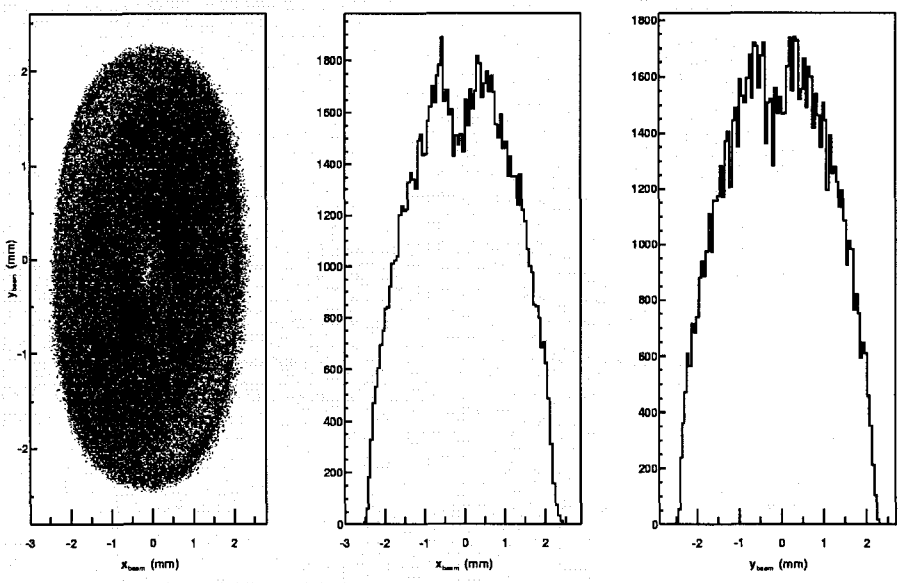

Figure 5.14: *The left histogram is a 2-D histogram of the raster position for a 100000 events. The center histogram is just the x axis distribution for the same 100000 events. The right histogram is the y axis distribution.*

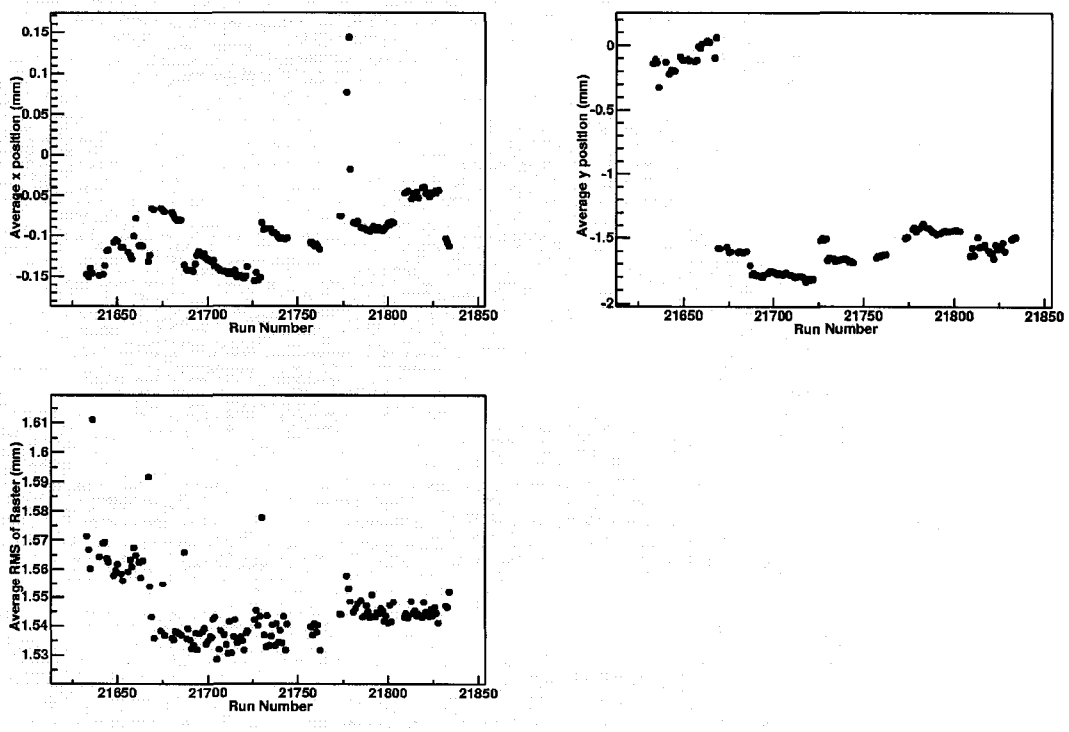

Figure 5.15: *The upper-left hand plot is the average x_{beam} position for the right spectrometer runs for the first kinematic setting. The upper-right hand plot is the average y_{beam}. The lower-right hand plot is the average RMS beam spot of each run.*

CHAPTER 6

The Polarized ^{3}He Target System

6.1 Why a Polarized ^{3}He Target?

The ideal target for measuring neutron spin-structure functions would be a high-density collection of polarized neutrons. Unfortunately, the finite half-life of the neutron (885.7 ± 0.8 s [49]) and the difficulty of manipulating neutral particles make a free polarized neutron target impractical for precise spin-structure function measurements. A suitable substitute is a polarizable nuclear target.

Deuterium was used as an effective polarized neutron target in spin-structure function measurements at SLAC (E143 [32], E155 [34] and E155X [50]) and at Jefferson Lab (E93-009, E91-023 and E01-006). These experiments use solids like ^{6}LiH or $^{15}NH_3$ with the hydrogen replaced with deuterium for target material. The target systems use a process known as dynamic nuclear polarization to achieve a typical deuterium polarization of 22% [50]. While this type of target has a high neutron density, its polarization deteriorates in electron-beam currents above 100 nA [51]. In addition, the 5 Tesla holding field in this type of target causes serious difficulties due to electron beam deflection when polarized perpendicular to the electron beam.

Polarized ^{3}He has also been used to study spin-structure functions by experiments at SLAC (E142 [38] and E154 [52]), at Jefferson Lab (E94-010, E95-001, E99-117 and this experiment) and in the HERMES experiment at DESY [39]. The HERMES experiment used a low-density (areal density of 3.3×10^{14} atoms/cm^2 [39]) internal target designed for the HERA storage ring at DESY and not appropriate

for fixed-target accelerators like SLAC and Jefferson Lab. The SLAC and Jefferson Lab experiments instead have used optically polarized rubidium to polarize ^{3}He gas in sealed glass cells. While this results in a much lower neutron density (2.7×10^{20}cm^3) than the solid targets, it has the benefits of high average polarization (35-40%) and the ability to maintain that performance in electron beam currents up to 15μAmps [53]. In addition, changing target field direction is simple and the relatively small holding field results in insignificant beam deflection.

Because it could be operated using Jefferson Lab's high electron-beam current and could be easily switched from longitudinal to transverse polarization, the Jefferson Lab polarized ^{3}He target best suited the physics goals of E97-103. The target performed well during E97-103, with a 40% average polarization and minimal complications.

6.2 Other ^{3}He Polarization Techniques

The Jefferson Lab polarized ^{3}He target is based on the transfer of polarization from polarized rubidium vapor to ^{3}He nuclei. It should be noted that this is not the only way to polarize ^{3}He. A common technique, known as 'Meta-stability Exchange Optical Pumping', polarizes the ^{3}He nucleus by hyperfine exchange with excited ^{3}He atoms. It can achieve very high polarizations ($\approx$70%), but unfortunately meta-stability exchange only occurs efficiently at pressures below 1 atmosphere, a density much lower than possible with alkili metal optical polarization. Compression techniques, in principle, can be used, but have not been implemented at Jefferson Lab. References on applying meta-stable optical pumping to electron scattering physics can be found in [54] and [55].

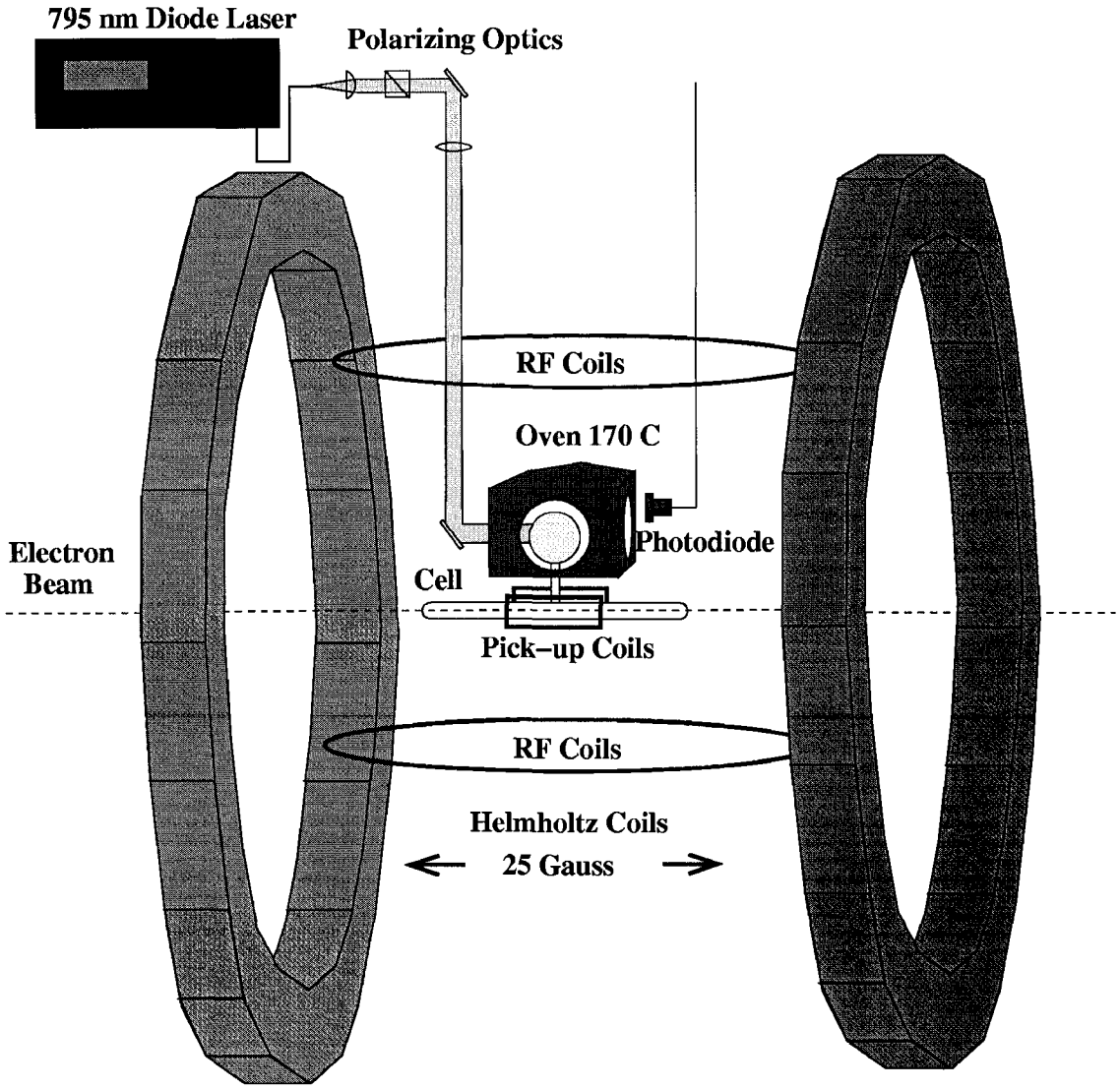

Figure 6.1: *A diagram of the polarized ^{3}He target system. The transverse Helmholtz coils are not shown for clarity.*

6.3 Jefferson Lab Polarized ^{3}He Target Overview

The Jefferson Lab polarized ^{3}He target, pictured in Fig. 6.1, uses optically polarized rubidium to polarize high-pressure ^{3}He gas sealed in double-chambered glass cells. The cells are located in two orthogonal sets of 25 Gauss Helmholtz coils whose combined fields determine the polarization direction. The rubidium is polarized using 795 nm circularly-polarized light from three 30 W diode lasers. The polarized rubidium then polarizes the ^{3}He in a spin-exchange process.

The glass cells used to contain the target material have two chambers : a spherical pumping chamber where the optically-polarized rubidium polarizes the ^{3}He nuclei and a cylindrical target chamber where the electron beam scatters off the target material. The pumping chamber is maintained at a temperature of at least 170° C degrees to maintain sufficient rubidium vapor density for optimum spin-exchange.

The polarization of the target material is determined by two independent polarimetry systems. The first uses the amplitude of the signal produced by the nuclear magnetic resonance (NMR) of ^{3}He nuclei to measure the polarization of the ^{3}He in the target chamber. This signal is calibrated by the known NMR signal of water. The second method extracts the polarization of ^{3}He by measuring the change in the electron paramagnetic resonance (EPR) of rubidium when the polarization direction of the ^{3}He nuclei is reversed. Using two polarimetry methods reduces the systematic uncertainty in the target polarization.

6.4 Polarizing ^{3}He Using Rubidium

6.4.1 Polarizing Rubidium

The energy levels of the atomic spin orbitals of rubidium electrons separate in a magnetic field. Because of this splitting, and because of spin conservation, circularly polarized laser light can excite valence electrons of a specific spin state.

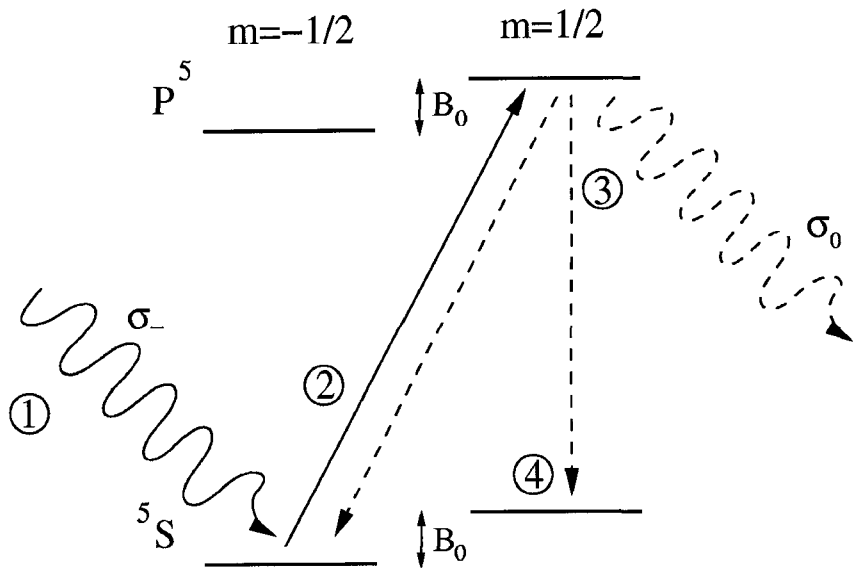

Figure 6.2: *A diagram explaining optical pumping. (1) Rb atoms in a magnetic field are exposed to circularly polarized laser light (2) The valence electron is excited from the* $^5S_{-1/2}$ *state to the* $^5P_{1/2}$ *state (3) The electron decays by emitting a photon into either the* $^5S_{-1/2}$ *where it repeats steps (2) and (3) or into the* $^5S_{1/2}$ *state where (4) it remains.*

Left circularly polarized 795 nm photons can be used to excite electrons of the m=1/2 ^{5}S state to the m=-1/2 ^{5}P state, while right circularly polarized light of the same wavelength can be used to excite electrons in the m=-1/2 ^5S state to the m=1/2 ^{5}P state. In this experiment only right-handed circularly polarized light is used.

The excited electron will decay, by emitting a photon, into either the m=1/2 or m=-1/2 ^{5}S state. Since the light is only exciting the electrons from the m=-1/2 state, all the valence electrons of the exposed rubidium atoms will eventually occupy the opposite spin orbital. This process is commonly known as "optical pumping" and results in polarized rubidium atoms. A diagrammatic explanation of optical pumping is shown in Fig. 6.2.

The emitted photon from the electron decays is unpolarized and can be re-absorbed by other rubidium atoms. This process makes high rubidium polarization impossible. Fortunately, this effect can be reduced by introducing nitrogen into

the system. Nitrogen allows photon-less de-excitation by absorbing energy into its rotational and vibrational motion during a collision.

The average polarization of the rubidium vapor can be expressed by the equation:

$$\langle P_{\mathrm{Rb}} \rangle = \frac{R}{R + \Gamma_{\mathrm{SD}}} \tag{6.1}$$

where Γ_{SD} is the spin-destruction rate of the rubidium vapor and R is defined by the equation:

$$R = \int \Phi(\nu)\sigma(\nu)d\nu \tag{6.2}$$

where $\Phi(\nu)$ is the photon flux per unit frequency from the laser light and $\sigma(\nu)$ is the light absorption cross-section. It is obvious from the above equations that the key factors to high rubidium polarization are the laser flux, Φ, and the spin-destruction rate Γ_{SD}. The laser flux is simply a function of laser power at the absorption frequency and can be increased as needed. The spin-destruction rate is determined by several factors which are worth exploring in detail.

The spin-destruction rate of rubidium is dominated by rubidium transferring spin angular momentum to the rotational angular momentum of other atoms. In the E97-103 system, the rubidium collisions of significant concern are : Rb-Rb, Rb-^{3}He and Rb-N_2. (Collisions with the glass walls of the system are in principle a concern, but because of the high ^{3}He pressure in the E97-103 cells, the diffusion rate of rubidium amongst high-pressure ^{3}He is small. According to Wagshul and Chupp [56], only rubidium within $\approx$ 0.1 mm of the cell walls are affected by this spin-destruction process.) The total spin-destruction rate from these process can be written:

$$\Gamma_{\mathrm{SD}} = k_{\mathrm{Rb-He}}\left[^3\mathrm{He}\right] + k_{\mathrm{Rb-N_2}}\left[\mathrm{N_2}\right] + k_{\mathrm{Rb-Rb}}\left[\mathrm{Rb}\right] \tag{6.3}$$

where $k_{\mathrm{Rb-i}}$ is the spin-destruction rate constant for collision Rb $-$ i. The constants

for these have been calculated by Wagshul and Chupp [56]:

$$k_{\mathrm{Rb-Rb}} = 8 \times 10^{-13}\mathrm{cm}^3/\mathrm{s} \tag{6.4}$$

$$k_{\mathrm{Rb-^3He}} \leq 2 \times 10^{-18}\mathrm{cm}^3/\mathrm{s} \tag{6.5}$$

$$k_{\mathrm{Rb-N_2}} = 8 \times 10^{-18}\mathrm{cm}^3/\mathrm{s} \tag{6.6}$$

These numbers have a strong temperature dependence and should be treated as factor of "2" estimates [57].

For the E97-103 experiment, the approximate densities of the components ($[^3\mathrm{He}] = 2 \times 10^{20}\mathrm{cm}^{-3}$, $[\mathrm{N_2}] = 1.8 \times 10^{18}\mathrm{cm}^{-3}$, $[\mathrm{Rb}] = 4 \times 10^{14}\mathrm{cm}^{-3}$) gives the following [57]:

$$\Gamma_{\mathrm{SD}} = 400_{\mathrm{Rb-^3He}} + 14_{\mathrm{Rb-N_2}} + 320_{\mathrm{Rb-Rb}} = 734\mathrm{s}^{-1} \tag{6.7}$$

One can see from this result that the Rb-^{3}He and Rb-Rb collision rates are similar. It should be noted that Rb-Rb collisions do not depolarize the rubidium sample since spin is conserved in the collision process. It should also be noted that the Rb-^{3}He collisions mentioned here absorb the rubidium spin into their angular momentum and are not the spin exchange collisions with the ^{3}He nuclei which are needed for polarized ^{3}He.

6.4.2 Polarizing ^{3}He With Polarized Rubidium

Rubidium can transfer its electron polarization to the nucleus of a ^{3}He atom through a hyperfine-like interaction. This spin-exchange process between Rb and ^{3}He has a small contribution ($\Gamma_{\mathrm{SE}} = 24\mathrm{s}^{-1}$) to Γ_{SD} compared to the total number of Rb-He collisions; consequently, only approximately 3% of polarized rubidium atoms lose their polarization through a spin-exchange process with ^{3}He. This makes the polarization of ^{3}He through rubidium spin-exchange an inherently inefficient process.

The polarization of ^{3}He with respect to time can be described by

$$P_{^3\mathrm{He}}(t) = \langle P_{\mathrm{Rb}} \rangle \frac{\gamma_{\mathrm{SE}}}{\gamma_{\mathrm{SE}} + \Gamma} \{1 - \exp[-(\gamma_{\mathrm{SE}} + \Gamma)\, t]\} \tag{6.8}$$

where $\gamma_{\mathrm{SE}} = k_{\mathrm{SE}}[\mathrm{Rb}]$, Γ is the ^{3}He polarization destruction rate and $\langle P_{\mathrm{Rb}} \rangle$ is the average rubidium polarization in the system.

Γ is the quantity which best describes the level of ^{3}He polarization a system will achieve. This quantity is can be broken into its four most important sources of depolarization:

$$\frac{1}{\Gamma} = \frac{1}{\Gamma_{\mathrm{Dipole}}} + \frac{1}{\Gamma_{\mathrm{Wall}}} + \frac{1}{\Gamma_{\nabla B}} + \frac{1}{\Gamma_{\mathrm{BeamDepol.}}} \tag{6.9}$$

where Γ_{Dipole} is depolarization from ^{3}He-^{3}He collisions, Γ_{Wall} is depolarization from interactions with the glass walls, $\Gamma_{\nabla B}$ is depolarization from magnetic field gradients and $\Gamma_{\mathrm{BeamDepol.}}$ is depolarization by the electron beam.

Γ_{Dipole} is the dominant factor in high-density ^{3}He system like the one used in E97-103. It is a result of spin-destructive ^{3}He-^{3}He collisions. This term can be expressed by

$$\Gamma_D = \frac{[^3\mathrm{He}]}{744} \mathrm{hrs}^{-1} \tag{6.10}$$

where $[^3\mathrm{He}]$ is in amagats [58]. . (An Amagat is the dimensionless ratio of the number density of a gas over the number density of an ideal gas at 0°C and 1 atm. A gas at 1 Amagat has a number density of 2.689×10^{19} atoms/cm^3).

Another important process in polarization relaxation is ^{3}He interactions with the glass cell walls. There are multiple reasons that the cell walls cause depolarization. One is the out-gassing of paramagnetic gases like O_2 or NO from the walls when the cell is heated. Another is paramagnetic material like Rb_2O on the surface of the cell walls. A third reason is increased sticking time of ^{3}He to the surface of the walls due to microscopic fissures in the glass. It is uncertain which effect is the dominant source of spin-destruction. Γ_{Wall} varies significantly from cell to cell, depending

on the conditions of its manufacture. A good cell can have a $\Gamma_{\text{Wall}} < 1/200\text{hrs}^{-1}$. A bad cell can have a $\Gamma_{\text{Wall}} > 1\text{hrs}^{-1}$.

Magnetic field gradients can also contribute to depolarization. The relevant formula is

$$\Gamma_{\nabla \text{B}} = D_{^3\text{He}} \frac{|\nabla B_x|^2 + |\nabla B_y|^2}{B_z^2} \tag{6.11}$$

where $D_{^3\text{He}}$ is the self-diffusion constant of ^{3}He and B_z is the magnitude of the holding field. ∇B_x and ∇B_y are the field gradients perpendicular to the holding field. The self-diffusion constant in the case of a high-density system is small ($D_{^3\text{He}} = 0.28\text{cm}^2/\text{s}$). The gradient in the Jefferson Lab Polarized ^{3}He system is usually kept below 10 mGauss/cm which translates to a negligible $\Gamma_{\nabla \text{B}} = 6000\text{hr}^{-1}$.

The target, of course, is subjected to a high-current electron beam. The electrons from this beam ionize ^{3}He atoms. The single electron from the ionized ^{3}He can depolarize the nucleus by hyperfine interaction with the nucleus. $^3\text{He}^+$ ions can also form $^3\text{He}_2$ molecules which can depolarize the nucleus by spin-rotation interaction; however, this is a much less frequent process since the molecule is quickly broken up by collisions with ^{3}He and N_2. As described in [59] and [60], the beam depolarization can be be written

$$\Gamma_{\text{BeamDepol.}} = (n_{\text{a}} + n_{\text{m}})\Gamma_i \tag{6.12}$$

where n_{a}+n_{m} is the number of ^{3}He atoms depolarized over the number ionized, where n_{a} is the contribution from ionized atoms and n_{m} is the contribution from ionized $^3\text{He}_2$ molecules. This fraction can range from close to zero to many thousands. Γ_i is the mean ionization rate per atom and is defined by:

$$\Gamma_{\text{i}} = i_{\text{b}} \left(\frac{\text{d}E}{\text{d}x} \right)^{^3He} \frac{L}{E_{\text{ion}}^{^3He} V} \tag{6.13}$$

where i_{b} is the beam current in particles per second, $(\text{d}E/\text{d}x)^{^3He}$ is the energy loss per incident electron per ^{3}He atom per area, $E_{\text{ion}}^{^3He}$ is the mean energy required to

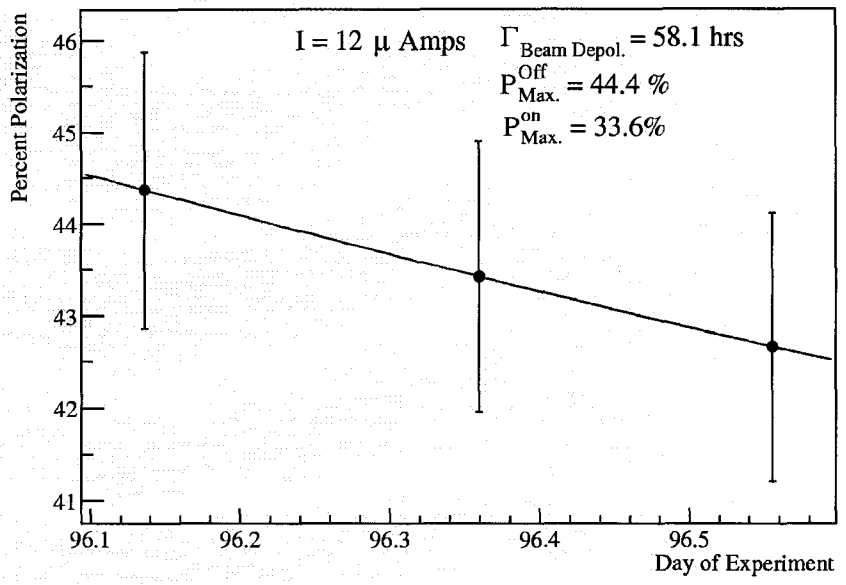

Figure 6.3: *The effect of the electron beam on the polarization of a polarized ^{3}He target.*

produce an ion pair from a target atom, L is the target length and V is the target volume. According to Bonin *et al.* [60] n_m is suppressed by the presence of N_2 and can be neglected.

A calculation of $\Gamma_{\text{BeamDepol.}}$ was made for this system by Ioannis Kominis in his dissertation [61]. His calculation was based on the formalism discussed above. The predicted value for $\Gamma_{\text{BeamDepol.}}$ was $\leq 1/30$ hrs for a current of 10 μA. The error on this measurement is difficult to determine. The error bars presented on the polarization are mostly systematic errors from the calibration. The individual signals have error bars of 0.5%.

The effect of beam depolarization on the ^{3}He target can be measured empirically. During an experiment, it is complicated to get a good data set because for the most accurate measurement, the target must be at its highest polarization, the beam must be at nearly constant current for a long period of time and the laser power on the pumping chamber must be constant. Unfortunately, these three conditions are rarely met simultaneously. The target rarely gets to its highest polarization due to

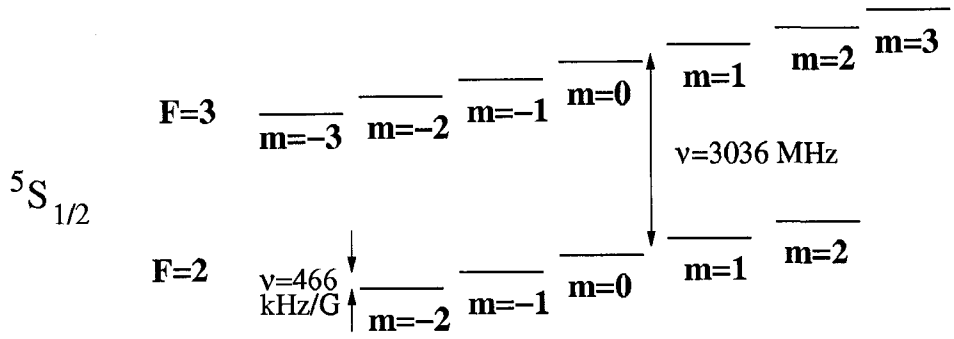

Figure 6.4: *The electron states of the $^5S_{1/2}$ orbital of rubidium.*

time constraints. The beam rarely goes through long periods of constant current without being off on the order of an hour or two. In E97-103, the constant configuration changes between longitudinal and transverse and the unequal laser power of the two, made extraction of this quantity problematic. However, it was extracted for a short period during the ^{3}He elastic commissioning using the formula:

$$P(t) = \left(P_{\text{Max}}^{\text{off}} - P_{\text{Max}}^{on}\right) e^{-\Gamma_{\text{BeamDepol.}} t} + P_{\text{Max}}^{\text{on}} \tag{6.14}$$

where $P_{\text{Max}}^{\text{off}}$ is the maximum polarization with the electron beam off and $P_{\text{Max}}^{\text{on}}$ is the maximum polarization with the electron beam on. For the data set presented in Fig. 6.3 the $1/\Gamma_{\text{BeamDepol.}} = 58_{29}^{+42}$ hrs with a significant amount of uncertainty from 29 hrs to 100 hrs.

6.4.3 Hyperfine Splitting from the Nucleus

While optical polarization of rubidium can be explained using simple Zeeman splitting of the electron states, explanations of more complicated phenomena such as collisional mixing and electron-paramagnetic resonances (EPR) one must pay attention to the additional level splitting caused by hyperfine interaction spin coupling. In general, the eigenstates of the total angular momentum projected on the axis of the magnetic field can be represented by the equation:

$$F_z = I_z + S_z \tag{6.15}$$

where F_z is the total angular momentum along the holding field direction, I_z is the spin of the rubidium nucleus and S_z is the of the electron. F_z determines the energy level of the electron state.

Because the spin of the ^{85}Rb nucleus is 5/2 (^{87}Rb has I=3/2), the eigenvalue m_I goes from -5/2, to 5/2 by increments of 1 (-5/2,-3/2,-1/2, etc.). The eigenvalue corresponding to the spin, m_S, of the electron can either be 1/2 or -1/2. When not in a magnetic field the valence electron has two states $F = 2$ or $F = 3$, corresponding to when the electron's angular momentum is parallel or anti-parallel to nuclei. However, when the atom is in a magnetic field, a direction preference emerges and the different nuclear spins become distinguishable. In a magnetic field, the F_z states split into $2F + 1$ levels as shown in Fig. 6.4 corresponding to different combinations of nucleus and valence electron spin states.

A phenomena associated with these nucleus-electron hyperfine spin states is *collisional mixing*. Because of spin-conserved Rb-Rb collisions, electrons in ^{5}P states or ^{5}S states are distributed in the hyperfine states. Because of this distribution electrons will have different excitation and photon emission energies. Because of collisional mixing means that the photons emitted from excitation of the electron paramagnetic resonance will have a broad range of frequencies rather than just one. This allows separation of these photons from the intense background of the laser light.

6.5 Polarized ^{3}He Cell Construction

6.5.1 The Fabrication of the Glass Target Cells

The use of glass cells for polarized ^{3}He targets began in the late 1980's with the form factor experiments at the MIT-Bates laboratory [54]. The technology was transfered first to SLAC for the E142 [38] and E154 [40] experiments and then to Jefferson Lab for experiments E94-010 [62] and E95-001 [63]. Consequently, by the

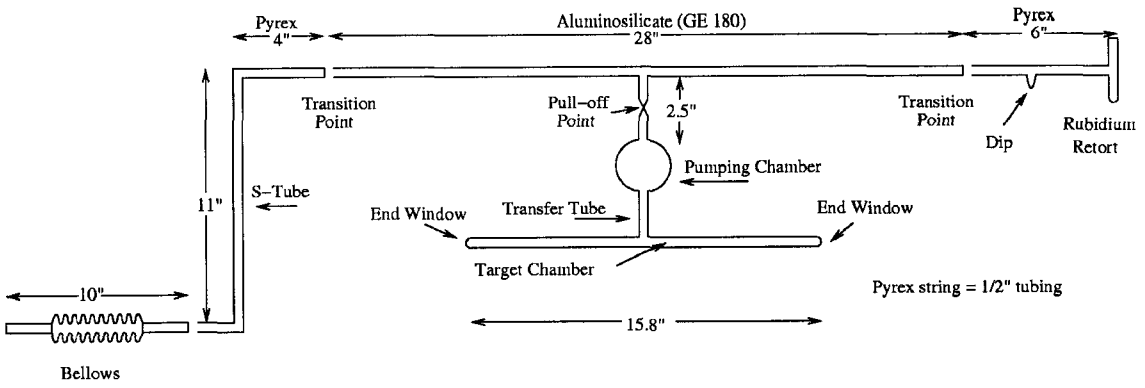

Figure 6.5: *Diagram of the glass cell assembly created by the glass-blower.*

time of E97-103, a set of techniques for creating high-quality glass cells for polarizing ^{3}He had been established.

The procedures for cell construction, based on the experience of these past experiments, focus on two factors that affect the quality of the cell : the presence of paramagnetic materials on the cell walls and the smoothness of the interior walls. Paramagnetic materials are mostly eliminated by starting with clean glass, avoiding processes that could add paramagnetic material and baking the cell extensively before filling it. The smoothness of the cell walls is largely depends on techniques used by the glass-blower when constructing the cell. Since both of these qualities are difficult to monitor during the cell-making process, there is still considerable variation in the quality of the cells.

Because of these demands, cell construction is done by a professional glass worker. Mike Souza at Princeton, who did the pioneering work for the SLAC experiments, and William Shoup at the University of Virginia did the glass blowing for this experiment. The glass blower constructs the cell and a glass assembly (or string) as shown in Fig. 6.5. The cell consists of a spherical pumping chamber and a cylindrical target chamber. These chambers are connected by a short transfer tube. The ends of the target chamber are capped by thin walled end-windows. The glass assembly serves two purposes: to connect the cell to the gas filling system and to

connect the retort where the rubidium enters the system. The cell is then sent to a lab where it is filled with the requisite amounts of ^{3}He, N_2 and rubidium.

The cells start off as 1/2" diameter GE 180 aluminosilicate glass tubing. Aluminosilicate glass is chosen because it holds up well in a radiation environment, contains very few magnetic or paramagnetic compounds and has sufficiently low porosity to high-pressure ^{3}He to prevent leaks. In previous experiments the cells had been made of Dow Corning 1720 aluminosilicate glass. GE 180 was used because it is easier material to work with and because of the limited supply of Dow Corning 1720. However, the trade off in choosing GE 180 is that it has a shorter radiation length than Dow Corning 1720.

The stock tubing acquired from the manufacturer is first cleaned by the glass blower. The tubing is resized using a surface mix torch burning methane and oxygen and a glass-working lathe [64]. The outside diameter of the tubing is then adjusted using a fixed graphite block. This resizing of the tubing is done not only to match the dimensional specifications of the target cell, but it also seems to help with getting rid of paramagnetic materials and generally improves the smoothness of the surface.

The pumping chamber is shaped to specifications by heating a sealed end of a piece of tubing then blowing it into a sphere. Then another piece of tubing is inserted into the still molten glass so that the pumping chamber can be connected to the rest of the assembly. Once cool, the pumping chamber is pressure tested to 300 psi for 20 minutes [64].

There are rather strict requirements for the end windows of the target chamber. The windows must be 100$\pm$20 microns thick. This is to reduce energy loss by the electron beam and to reduce background scattering into the detector acceptance. The glass blower makes a series of these end windows. He then uses a digital indicator (Mitutoyo digimatic) with a resolution of 2 microns to see if the windows match specifications [64]. A good end window will then be attached to the end of

the target chamber. The end window thickness is re-measured again using a laser system after the cell is filled.

Once the cell is assembled, it is annealed in a 785°C oven for 10 minutes. This relieves any stress in the glass that may have formed during its construction. Once annealed, the cell is attached to the rest of the assembly. The rubidium retort and the S-tube piece shown in Fig. 6.5 are constructed out of Pyrex. The S-tube connects the cell assembly to the cell-filling system through a bellows tube. The bellows tube is flexible and allows adjustments to be made to the cell position when attached. The bellows are also crucial for removing the cell from the string during the pull-off procedure. The rubidium retort consists of an open-ended cylinder where a rubidium ampoule is inserted and a dip where the rubidium is moved to during the filling procedure. Both the rubidium retort and the S-tube are connected to the cell using a transition glass of Corning 3320 since GE 180 and Pyrex can't be connected directly. The bellows are also connected with a glass-to-metal transition.

Once the cell is assembled it is transported to a filling lab. Cork or rubber stoppers are put in the open ends of the glass assembly to keep the interior clean. Sometimes the assembly is filled with argon gas for additional cleanliness.

6.5.2 The Cell Filling System

Once the cell is constructed it must be filled with the target material, plus the rubidium and nitrogen required to polarize the ^{3}He. This is done by a gas filling system specifically designed for polarized ^{3}He cells. The procedures to fill the cell are as important to creating a good cell as the glass construction.

The filling system shown in Fig. 6.6 consists of several systems. The first is a set of pumps that create a vacuum throughout the system and the cell assembly. There is a roughing pump used when the pressure is above 1×10^{-3} Torr. The turbo pump can be used when the pressure is below 1×10^{-1} Torr and can pump down to

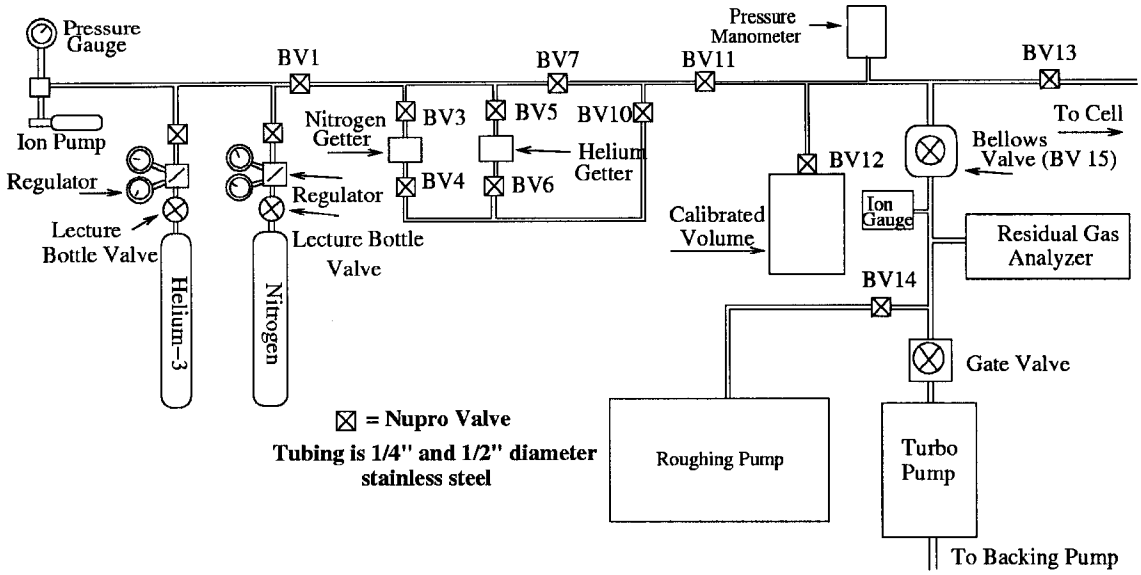

Figure 6.6: *Cell filling system. 'BV' refers to the name of the valve.*

pressures in the 1×10^{-8} to 1×10^{-9} Torr range. There is also an ion pump which is used to maintain good vacuum near the lecture bottles.

The next part of the cell filling system are the lecture bottles and their regulators. The lecture bottles are bought from Spectra Gases and contain 99.99% pure ^{3}He and nitrogen gas. Each bottle contains 25 L. The ^{3}He is very expensive ($\approx$\$140 a liter) and considerable effort is made to conserve it. Spectra Gases attached valve stems to the bottles which could then be attached to regulators which control the flow of gas from the bottles.

In addition to those devices, there are several smaller sections. There are two heated getters, one for helium and one for nitrogen. These getters act as filters, absorbing impurities into materials inside the getter and letting the desired gas flow through. The ion gauge is used to measure pressure below 1×10^{-3} Torr. A pressure manometer is used for pressures above that. The calibrated volume is used to measure gas in the cell filling process. The residual gas analyzer is used for diagnostics when cleaning the system, but is turned off when a cell is attached to the system.

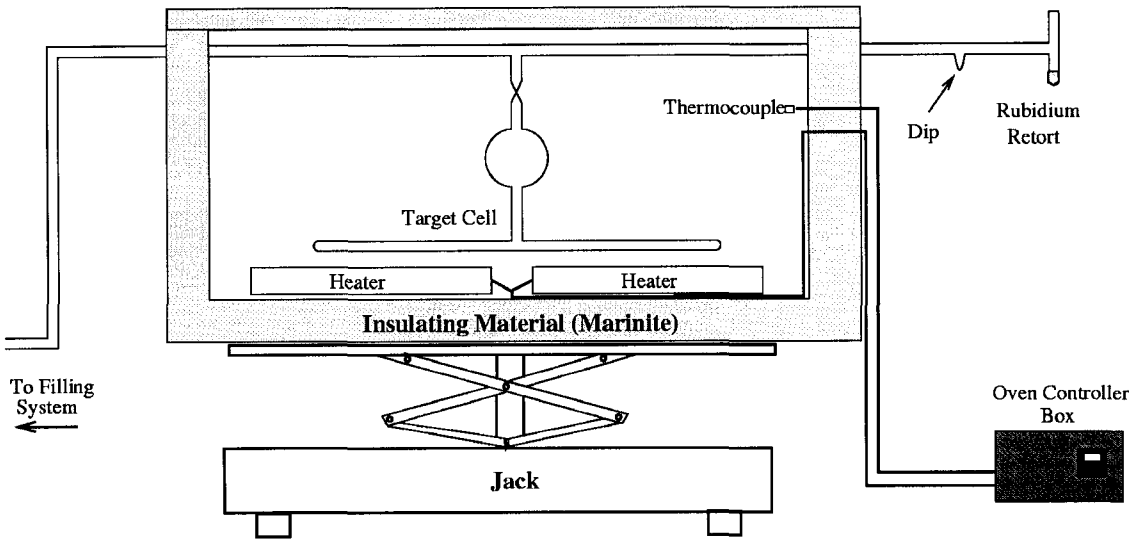

Figure 6.7: *Cell baking configuration*

6.5.3 Preparing for Cell Filling

The first step of the cell filling procedure is to attach the glass assembly to the cell filling system pictured in Fig. 6.6. The bellows on the cell assembly have a Swagelok fitting on it that can be attached to the filling system. The cell assembly is supported by aluminum rods held together by clamps.

The next step is to insert the rubidium into the cell assembly. Rubidium is highly reactive with air and comes sealed in an ampoule. The retort on the cell assembly shown in Fig. 6.5 is a cylindrical tube that is open at the top. Before inserting the rubidium, BV11 (a Nupro Valve), BV12 and the gate valve are closed. The rubidium ampoule is opened and inserted into the retort. The open end of the retort is sealed by a methane/oxygen torch. The system is then rapidly evacuated by the roughing pump through BV14.

At this point, the cell and the cell assembly need to baked at high temperature to remove any impurities on the surface. The filling system and cell assembly are first evacuated by the turbo pump. This will get the pressure down to $\approx 1 \times 10^{-7}$ Torr. The cell is then placed in an oven as shown in Fig. 6.7. The oven is made

of marinite which is a type of calcium silicate board. It is light weight and a good insulator. The heat of the oven is generated by two sets of heating elements that sit at the bottom. They are controlled by an Omega autotune controller that uses a thermocouple in the oven to read the temperature. The oven is heated to 420 °C and that temperature is maintained for three or four days.

It is important when baking the cell, to occasionally heat the rest of the assembly that is not in the oven. This is done with a methane/oxygen torch with a cooler, bushy flame to avoid melting the glass assembly (flamebaking). The procedure is to heat the S-tube portion and the rubidium retort except for where the rubidium is, two to three times a day for about 10 minutes each time. The rubidium will be heated later in the procedure when the cell is cleaner. Generally, when this is done the pressure in the system will rise to 1×10^{-6} Torr temporarily, but will soon fall to an even lower pressure than before the heating. This procedure is repeated until the vacuum is consistently on the order of 10^{-9} Torr or below.

Usually after several days of baking the cell, the rubidium is moved from the bottom of the retort to a dip, shown in Fig. 6.7 farther into the cell assembly. The purpose of this is to move the rubidium to place where the glass has been heated thoroughly from a place of questionable cleanliness. Also, mild heating of the rubidium helps remove gas impurities that may have been in the ampoule at the time of sealing. Rubidium vaporizes easily when heated by a methane/oxygen flame. The key to moving rubidium from one place to another is keeping the part where the rubidium needs to go cool, and heating everything else. A cooler flame seems to keep the rubidium from forming impurities by reacting with the glass. After the rubidium is moved to the dip, the retort is removed from the glass assembly with a torch.

Once the vacuum has stopped improving (typically 5-7 days), the oven is turned off and the turbo pump is left on for a period of time to achieve the best vacuum

possible. The oven takes a long time to cool, so generally the oven is turned off the night before the cell fill. The vacuum system typically achieves pressures $< 5 \times 10^{-9}$ Torr. The oven is then removed from around the cell. The getters must be turned on at this point so they will be at operating temperature when the cell is filled.

The next step is to move the rubidium from the dip to the cell. This must be done with extreme care since the quality of the cell is strongly affected by this process. The torch should be about the same as when flamebaking, but should not be so hot to melt the glass or course Rb to react. Again, the key to moving rubidium in the cell assembly is to leave the area where the rubidium should collect cool, and heat everything else. Making sure the rubidium is vaporized repeatedly during this process helps cleans the rubidium of impurities. This process continues until the rubidium that collects on the pumping chamber walls becomes visible. There does not need to be a lot of rubidium in the pumping chamber. The rubidium shoud be shiny, indicating a general lack of impurities. Oxidized rubidium is paramagnetic and appears black usually indicating a bad cell.

6.5.4 Measurement of the Cell Assembly Volume

Once the rubidium is in place, a procedure to measure the cell string volume is performed. The cell filling process requires a reasonably accurate value for the volume of the string, which is the volume of the cell assembly minus the volume of the cell. This can be done because the cell volume can be estimated to reasonable accuracy using only its external dimensions.

The calibrated volume is first filled with a known pressure (referred to as P_1 here) of nitrogen. The volume of the calibrated volume (V_{CV}) is known very precisely (1.064±0.001 L) from mechanical measurements. This volume of gas is then released first into the small area, referred to as the manifold, between the calibrated volume and the valve to the cell assembly (BV13) with the bellows and BV11 valves closed.

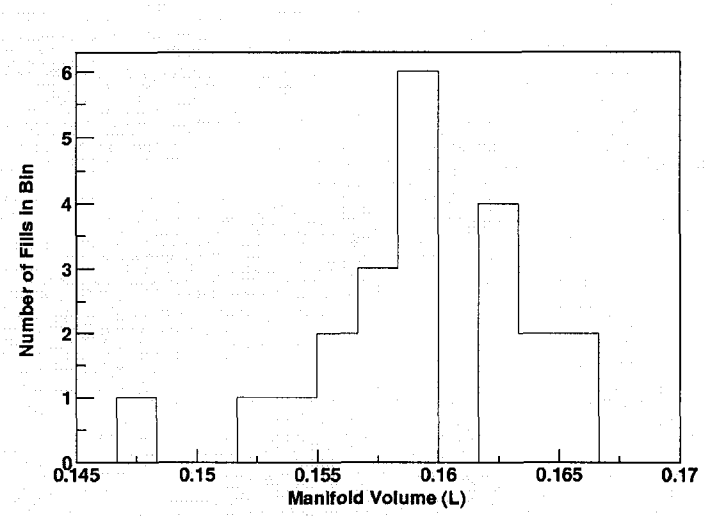

Figure 6.8: *A plot of the manifold volume measured during the cell filling process.*

The pressure is read (P_2) and then the valve to the cell assembly is opened. The pressure is then read again (P_3).

The ideal gas law can be used to calculate the volume of the cell assembly with the results of this procedure. If one assumes that the entire system is at the measured room temperature, then

$$V_{\mathrm{M}} = \frac{P_1 - P_2}{P_2} V_{\mathrm{CV}} \tag{6.16}$$

$$V_{\mathrm{S}} + V_{\mathrm{C}} = \frac{(P_1 - P_3)V_{\mathrm{CV}} - P_3 V_{\mathrm{M}}}{P_3} \tag{6.17}$$

where P_1, P_2 and P_3 are the pressures at various steps in the procedure, V_{CV} is the volume of the calibrated volume, V_{M} is the volume of the manifold section, V_C is the volume of the cell and V_{S} is the volume of the string. The V_{C} and V_{S} can't be separated by this procedure, but V_{C} can be estimated accurately using external measurements of the cell and then V_{S} can be extracted from the results of this procedure.

A useful piece of information in estimating the error from this procedure is to look at the consistency of the measurement of the volume of the manifold section. These data are plotted in Fig. 6.8. The data was taken for fills where the manifold

volume was the same (the same tubing and valve sections were used each time). This procedure is done before and after a cell fill and it seems that the volume measurements done after the cell fills are systematically larger. This is likely due to temperature changes from nearby cryogens used in the filling procedure. The overall error is estimated to be $\pm$ 5 ml.

6.5.5 Filling the Cell with Nitrogen and ^{3}He

Nitrogen, necessary for radiationless quenching of the optically polarized rubidium, is put into the cell at room temperature. The procedure is to fill the manifold with nitrogen that has been purified by the nitrogen getter. The pressure in the manifold required to get 65 Torr of nitrogen (a reasonable amount) in the final cell can be calculated using:

$$P_{N_2} = (65\text{torr})\frac{V_C(V_M + V_S + V_C)}{V_M(V_S + V_C)}. \tag{6.18}$$

This equation assumes the following procedure: the manifold is filled to pressure P_{N_2} with the valve to the calibrated volume (BV12) closed , this gas is then released into the cell assembly by opening BV13. BV13 is then closed. When the cell is cooled to 4 K, as will be done in the next step, the nitrogen in the cell assembly will all condense into the bottom of the target chamber.

The next step is to cool the lower chamber of the cell to 4 K using liquid helium. This is done because the cell pressure must be below 1 atm while removing the cell from the cell assembly. Removing the cell, known as the pull-off, requires the use of a methane/oxygen torch to melt the glass tubing between the cell and the cell assembly. Keeping the cell pressure below 1 atm ensures that the atmospheric pressure will collapse the molten glass in a self-sealing manner, keeping out atmospheric gases. Failure to do this, will cause the high-pressure helium to punch a hole at the point of the pull-off and the ^{3}He gas will leak out into the atmosphere.

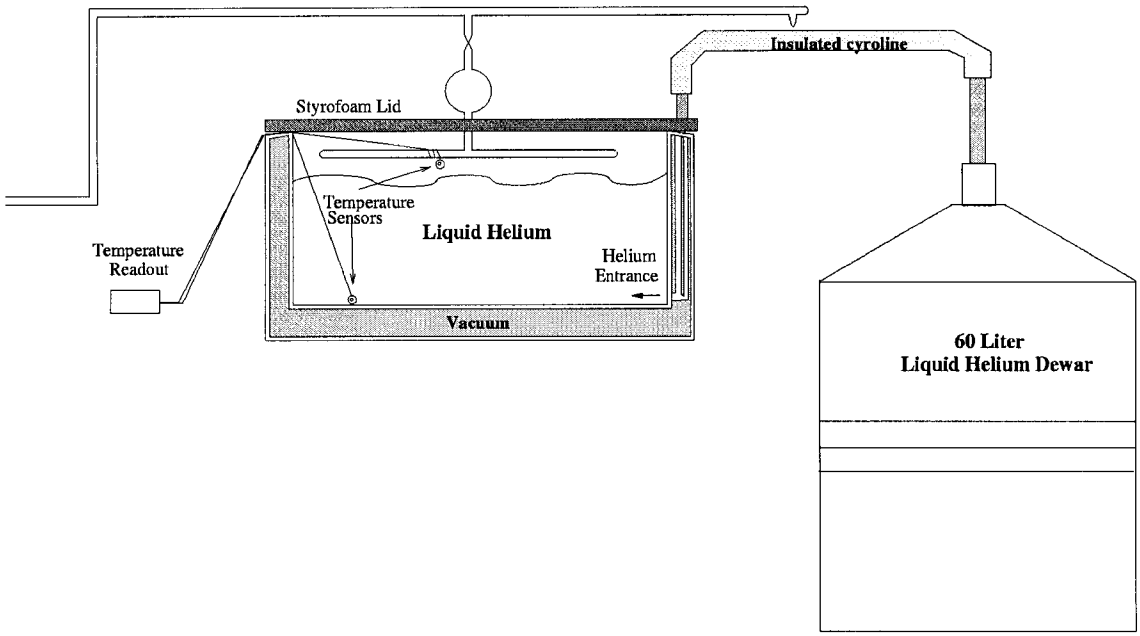

Figure 6.9: *Cyrocooling Configuration*

A stainless steel dewar filled with liquid helium is used to cool the cell as shown in Fig. 6.9. The dewar, custom-made for this system, is basically a cylindrical bucket that is designed to hold liquid helium. The walls of the dewar are superinsulated and are evacuated to minimize thermal contact with the environment. The lid of the dewar is made of a non-descript piece of Styrofoam which helps insulate the helium liquid, though it is not air-tight and leaks quite a bit of cold gas.

The dewar has a tube inside of it which allows an insulated cryoline to be inserted and the helium from the cryoline to enter the bottom of the dewar. This cryoline is connected to a 60 L storage dewar of liquid helium. The flow of liquid helium to the target dewar is increased by back pressure from a gaseous helium line into the storage dewar.

It usually takes from 10-20 minutes to fill the dewar with liquid depending on the flow of helium. The temperature is measured by a pair of cryogenic temperature sensors, one placed on the cell and one placed at the bottom of the dewar. Once the helium reaches 4 K, the temperature is rather stable and the dewar can maintain

that temperature for an hour or more.

The ^{3}He gas is then put into the cell assembly in a manner similar to the nitrogen. The gas is filtered through a heated getter into the manifold. Because higher pressures are necessary, the calibrated volume is opened which allows the manifold pressure to remain below what our pressure gauges can read. The goal of E97-103 was to create cells with a number density of 8.5 Amagats (see section 6.4.2 for definition of Amagat). The cells were filled with two charges of ^{3}He so that the pressure did not become too high for the instrumentation. The formula for calculating the final number density is:

$$n_{^3\mathrm{He}} = \frac{273.16}{T_{\mathrm{M}} V_{\mathrm{C}}} \left[(P_i^1 - P_f^1 + P_i^2 - P_f^2)(V_M + V_{CV}) - V_S P_f^2 \right] \tag{6.19}$$

where $n_{^3\mathrm{He}}$ is the ^{3}He density in Amagats, P_i^1 and P_i^2 are the manifold pressures before opening the valve (BV13) to the cell assembly for the first and second charges respectively, P_f^1 and P_f^2 are the manifold pressures after the valve (BV13) to the cell assembly and T_M is the temperature of the manifold.

Once the proper amount of ^{3}He is in the cell, it can be separated from the assembly using the methane/oxygen torch. The tubing at the pull-off point has been narrowed by the glass blower to make the separation easier. The person melting the glass must be sure to heat the glass evenly and to anneal the glass around the pull-off point on the cell after it has been separated. Both of these steps help to prevent cracking that can occur when it cools. The liquid helium lines are removed from the dewars, the cell is covered and generally is left over night to warm up. Then the cell is ready to be characterized and tested.

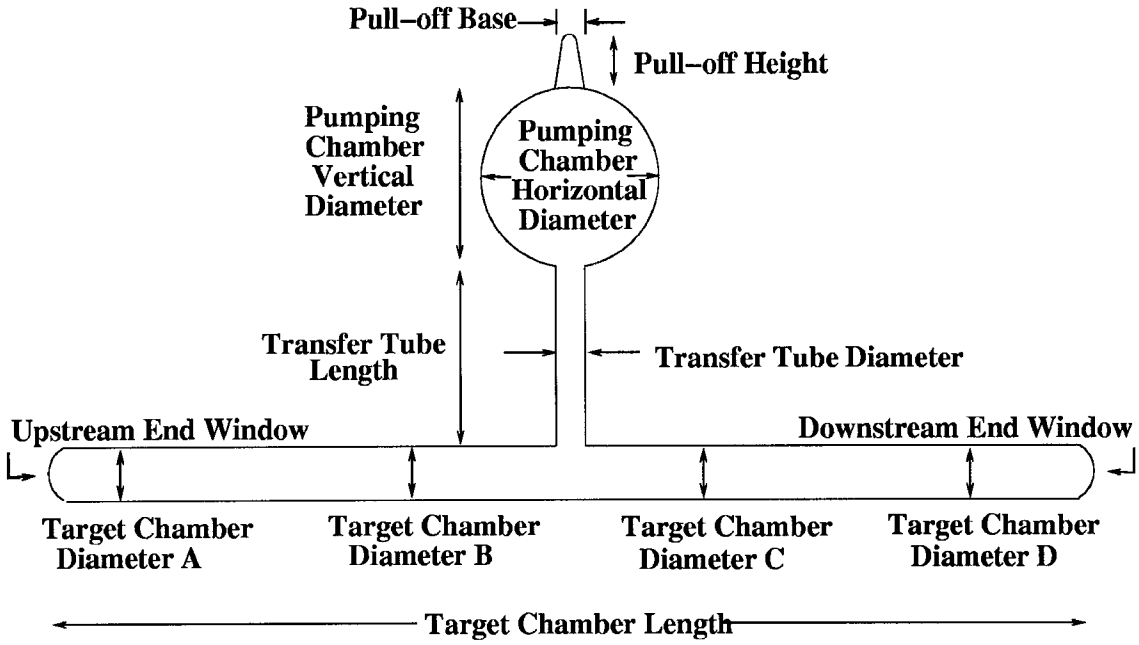

Figure 6.10: *Names for the cell dimensions*

6.6 Characterizing Target Cells

6.6.1 The Purpose of Characterizing Cells

The cell geometry has to been known in detail because it enters into the calculation of the structure functions in many places. The density and volume of gas are both parameters in extracting absolute polarization from the two polarimetry systems. The density of ^{3}He and N_2 has to be known accurately to calculate the nitrogen dilution factor. Also the density enters any calculation of the cross-section. Finally, energy loss of the incoming and outgoing electrons in the cell walls and windows make knowledge of the glass thickness important for radiative corrections. Therefore specific knowledge about cell shape and size are necessary to reduce systematic errors in structure function measurements with this target system.

6.6.2 External Dimensions of Cells Used During E97-103

There were two ^{3}He cells used during E97-103, named Shapiro and Virginia One. Also, two other cells filled with water were used to calibrate the NMR system.

Dimension	Shapiro	Virginia One	25cm H_2O	40cm H_2O	Uncertainty
Pull-Off Height	2.86	3.62	1.59	1.54	0.16
P. C. V. Diam.	6.52	6.74	6.62	6.72	0.18
P. C. H. Diam.	6.48	6.34	6.233	6.505	0.020
T. Tube Diam.	1.11	1.06	1.111	1.254	0.026
T. Tube Len.	6.46	6.52	6.380	6.46	0.020
T. C. Diam. A	1.91	1.85	1.880	1.871	0.010
T. C. Diam. B	1.88	1.92	1.865	1.946	0.010
T. C. Diam. C	1.88	1.91	1.867	1.927	0.010
T. C. Diam. D	1.93	1.92	1.878	1.928	0.010
T. C. Length	39.7	39.4	24.9	40.0	0.16

Table 6.1: *A list of external cell dimensions and their uncertainties. All values in centimeters.*

The external dimensions of each cell was measured with a caliper. For the most part, this is an accurate method since the caliper can make accurate measurements at the 10-20 micron level. However, some of the dimensions have to be estimated (for instance where the top of the pumping chamber turns into the pull-off) and measurement error contributes to the uncertainty. The other source of uncertainty is variation along the surface of the glass, for instance in the case of the target chamber diameter. Fig. 6.10 displays the position of measurements. Table 6.1 lists all the measurements and their uncertainties.

6.6.3 Measuring the Total Internal Cell Volume

Archimede's principle says that the buoyant force on an object in water is equal to the gravitational force of the water it displaced. Using the density of water, one can calculate the displacement volume from the buoyant force and this volume is equal to the volume of the object. This method is used to determine the external volume of the cell.

The buoyant force in this case is the difference in weight of the cell sitting on a scale and the weight of the cell submerged in water. Since the cell floats in water, one must attach a weight to sink the cell. The buoyancy of this weight and the wire

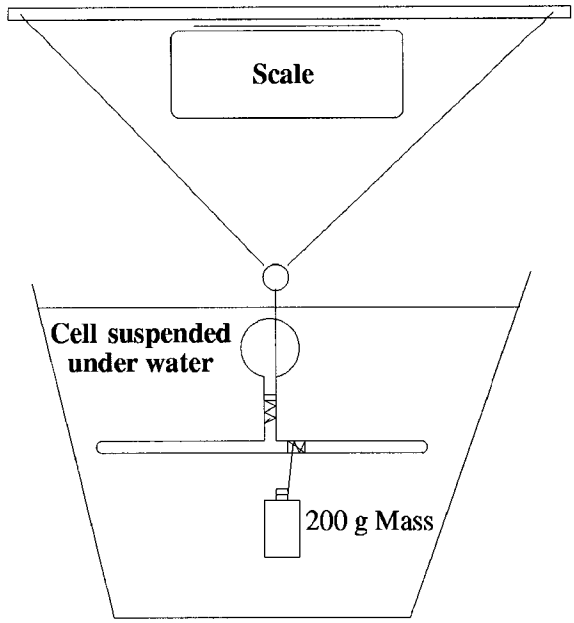

Figure 6.11: *The setup for volume measurement using the Archimedes method*

used to support the cell and weight, must be measured separately. The buoyant force can be calculated using the following formula:

$$F_B = g(m_{\text{cell}} + m_{\text{app}} - m_{\text{sub}}) \tag{6.20}$$

where F_B is the buoyant force, m_{cell} is the mass of the cell, m_{app} is the mass of the submerged weight and wire not including the cell, m_{sub} is the mass of the submerged cell plus apparatus and g is gravitational acceleration [53].

Since the density of water and the density of the aluminosilicate glass are well known, to get the internal cell volume one uses the formula:

$$V_{\text{in}} = \frac{F_B}{\rho_{\text{water}} g} - \frac{m_{\text{cell}} - m_{\text{Rb}} - m_{^3\text{He}}}{\rho_{\text{GE180}}} - \frac{m_{\text{Rb}}}{\rho_{\text{Rb}}} \tag{6.21}$$

where V_{in} is the internal volume of the cell, F_B is the buoyant force, ρ_{water} is the density of water (0.9984 g/cm^3), m_{Rb} is the estimated mass of the rubidium in the cell (typically 0.3 g), $m_{^3\text{He}}$ is the mass of the helium gas inside the cell (typically 0.2 g), ρ_{GE180} is the density of the glass (2.76 g/cm^3, acquired from a combination of GE literature and Archimedes measurements on just the glass) and ρ_{Rb} is the

Cell Name	UVa Volume (cm^3)	W & M Volume (cm^3)
Shapiro	201.6	201.1
Virginia One	195.0	194.4

Table 6.2: *The Archimedes volume measurements done at the University of Virginia and the College of William and Mary.*

density of solid Rb [53].

Two sets of measurements were done: one at the University of Virginia and one at the College of William and Mary. Results are given in Table 6.2, and show a systematic difference of $\approx$0.5 ml.

6.6.4 The External Volumes of the Cell Chambers

The external volumes of the different chambers can be used to determine their corresponding internal volumes. The internal volumes need to be known so that the density differences in the cell when it is being polarized can be determined. For each cell there are three chambers of interest: the target chamber, the pumping chamber and the transfer tube. The volume of the pumping chamber can be estimated with the formula:

$$V_{pc\ ext} = \frac{\pi d_{\text{pc vert}} d^2_{\text{pc horiz}}}{6} \tag{6.22}$$

where $V_{\text{pc ext}}$ is the external volume of the pumping chamber, $d_{\text{pc vert}}$ is the vertical diameter of the pumping chamber, $d_{\text{pc horiz}}$ is the horizontal diameter of the pumping chamber.

The external volume of the transfer tube is just a cylinder and can be easily calculated. The target chamber is mostly cylindrical, but because the end windows are curved at the end and the diameter of the cylinder is non-uniform, the following formula is used:

$$V_{\text{tc ext}} = \frac{\pi d^2_{\text{avg}}(L - 2l_{\text{ew}})}{4} + \frac{3\pi d^2_{\text{avg}} l_{\text{ew}}}{8} \tag{6.23}$$

where $V_{\text{tc ext}}$ is the external volume of the target chamber, d_{avg} is the average di-

Chamber	Shapiro	Virginia One	25cm Water	40cm Water	Uncertainty
Pumping	143.3	141.9	134.7	148.9	4.0
Transfer	6.25	5.75	6.18	7.98	0.35
Target	111.4	110.6	67.1	114.0	1.4
Total Vol.	261.0	258.3	208.8	271.4	4.3
Meas. Vol.	262.5	257.5	-	-	1.0

Table 6.3: *External volumes of the cells' chambers. All values in milliliters.*

Chamber Name	Nitric Acid	Water	Methanol	Average	Uncertainty
Target Chamber	50.07	49.87	49.87	49.94	0.10
Transfer Tube	3.34	3.33	3.68	3.45	0.10
Pumping Chamber	106.57	106.75	107.30	106.87	0.3

Table 6.4: *Volume of the three chambers of the 25cm water cell. All values are in milliliters.*

ameter of the target chamber and l_{ew} is the approximate length of the curved end windows (usually around 0.8 cm). The first term is the volume from the cylindrical part of the target chamber. The second term is an approximation to the volume of the end windows. It is 3/4 of the volume of the cylinder of the length and diameter of the end windows. This is a crude approximation, but the error is less than a half a milliliter so a more refined model is unnecessary.

The volume of the pull-off varies from half a milliliter to one milliliter. It is ignored for this purpose. The external volumes of each cell are given Table 6.3. The calculated values are compared to the measured external volume acquired from the Archimedes method.

6.6.5 The Dimensions of the 25cm Water Cell

The 25cm water cell is unique because it had the volumes of its chambers measured carefully before being sealed. This is useful in determining which methods of estimating the internal volumes of the other cells is the most accurate.

The volumes were determined by first weighing the empty cell. Then enough liquid would be added to fill the target chamber. The cell would then be weighed

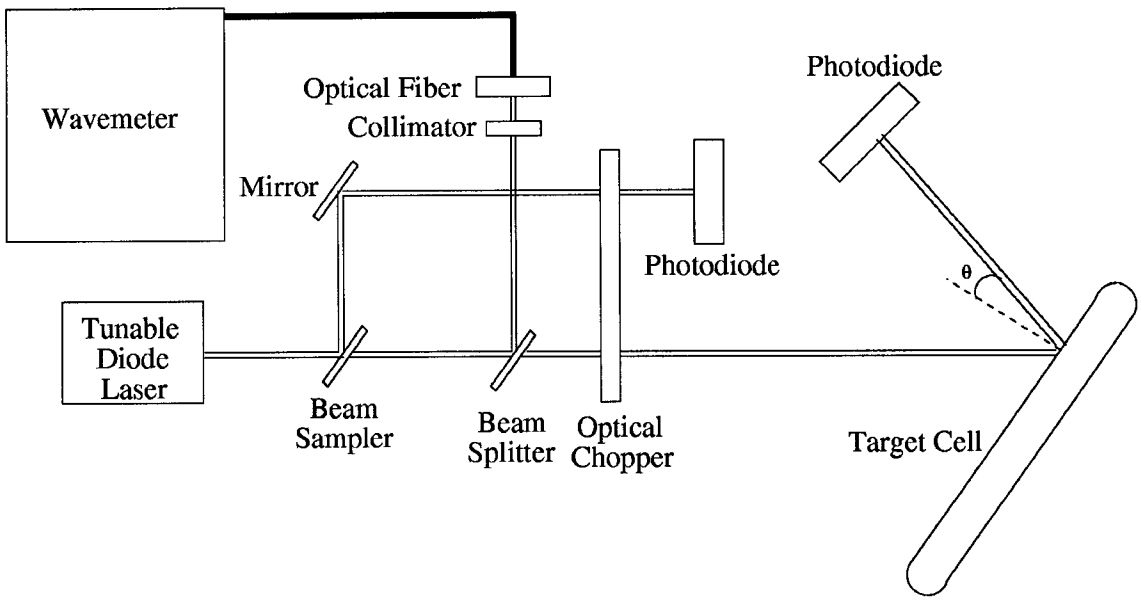

Figure 6.12: *Set up for wall thickness measurements at Jefferson Lab*

again. While keeping the previous amount of liquid in the target chamber, the transfer tube would be filled with additional liquid and weighed. Finally, the cell would be filled completely and weighed again. Three liquids were used, all with well known densities. The average result of these liquids are used as the volume. The results are shown in Table 6.4.

6.6.6 Target Chamber Wall Thicknesses

The wall thickness of the target chambers used in the experiments was measured using an interferometric method using a tunable laser and a photo-detector. The intensity of reflected light off of a flat plate is given by [53]:

$$I_r = \frac{\eta}{1+\eta} I_o \tag{6.24}$$

where

$$\eta = \frac{4\left(\frac{n-1}{n+1}\right)^2}{1-\left(\frac{n-1}{n+1}\right)^2} \sin^2\left(\frac{2\pi n t \cos\theta}{\lambda}\right), \tag{6.25}$$

n is the index of refraction, λ is the wavelength of the incident laser light, θ is the angle of the reflected light and t is the thickness of the plate.

Section	Shapiro	Virginia One	25cm H_2O	40cm H_2O	Uncertainty
A Left	0.141	0.138	0.152	0.119	0.003
A Right	0.142	0.163	0.139	0.111	0.003
B Left	0.145	0.142	0.156	0.115	0.003
B Right	0.140	0.142	0.138	0.114	0.003
C Left	0.145	0.141	0.131	0.119	0.003
C Right	0.143	0.141	0.132	0.113	0.003
D Left	0.132	0.138	0.132	0.121	0.003
D Right	0.140	0.142	0.154	0.110	0.003

Table 6.5: *Wall thicknesses by section. A is the upstream end, D is the downstream. Left is on the side of the left spectrometer. Right is the on the side of the right spectrometer. All measurements are in centimeters.*

To measure the wall thickness with a tunable diode laser, the laser is separated into three beam paths as shown in Fig. 6.12. The first beam path is split by a beam sampler (which is a beam splitter that removes only 10% of the beam), through an optical chopper and into a photodiode. This beam is used to monitor the power of the laser. The optical chopper makes the signal from the photodiode oscillate at 1 kHz so that a lock-in amplifier can cleanly read the signal. The second laser path goes to an optical fiber which leads to a Burleigh wavemeter. The wavemeter measures the laser wavelength to ± 0.0015 nm. It is is always difficult to get enough light to the wavemeter with a low power laser so a collimator has been added to increase the quantity of light into the wavemeter. The third path goes through an optical chopper, reflects off the cell and into a photodiode. The intensity of this light will vary as the laser changes wavelengths.

The side walls of the target chamber were measured optically both at Jefferson Lab and the University of Virginia. Four to six measurements were done on each side of the cell. Because the window sections of the cells are made of a different tube than the middle part it is useful to describe the target chamber in four sections. Two represent the two window pieces on the end and two represent the middle sections separated by the transfer tube. It is found the wall thickness is uniform within an

Cell Name	Upstream Window Mark	Thickness	Downstream Window Mark	Thickness
Shapiro	19	127	7	117
Virginia One	4	154	9	124

Table 6.6: *The window thicknesses in microns and their window markings.*

uncertainty of 30 μm within each section, but sections can differ by 300 μm.

The measurements were not necessarily done at the same places on the cell for both Jefferson Lab and UVa measurements nor were the measurements done symmetrically (the same point on both sides). Nevertheless, the sets of measurements agreed well with a final uncertainty of 30 microns in the average wall thickness in each section of the cells. The results are given in Table 6.5.

6.6.7 Target Chamber End Window Measurement

The target chamber end window measurements were done at the University of Virginia using a method described in the doctoral dissertation of Ioannis Kominis [61]. This method is similar to the measurement of the wall thickness. The thicknesses are listed in Table 6.6 for convenience and to document the window orientation during the experiment.

6.6.8 Estimating the Interior Volumes of Target Cells

The interior volumes of the targets must be accurately estimated for two reasons: to accurately estimate the target density when the cell is being polarized and to calculate the electromagnetic flux for the NMR polarimetry measurement. The method used for E97-103 uses a simple geometrical calculation for the target chamber based on the wall thicknesses and external measurements:

$$V_{\text{Int Vol Section}} = \frac{\pi \left(d_{\text{ext}} - t_{\text{right}} - t_{\text{left}}\right)^2 L}{16}. \tag{6.26}$$

Chamber	Shapiro	Virginia One	Uncertainty
Pumping Chamber	116.5	110.8	1.5
Transfer Tube	3.5	3.21	0.25
Target Chamber	81.2	80.6	1.0
Total Volume	201.2	194.6	1.8

Table 6.7: *The estimated chamber volumes in milliliters*

where $V_{\text{Int Vol Section}}$ is the internal volume for one section, D_{ext} is the external diameter of that section of the target chamber, t_{right} and t_{left} are the right and left wall thicknesses of the section and L is the length of the target chamber. This calculation was in agreement at the level of 0.5 ml with the 25cm water cell chamber. The uncertainty is set at 1.0 ml due to lack of statistics.

The volume of the transfer tube is estimated by using external measurements, the ratio of the external to internal volume of the 25 cm water cell and then calculating:

$$V_{\text{tt int}} = \frac{V_{\text{tt water cell int}}}{V_{\text{tt water cell ext}}} V_{\text{tt ext}} \tag{6.27}$$

where $V_{\text{tt int}}$ is the interior volume of the transfer tube, $V_{\text{tt water cell int}}$ is the interior volume of the transfer tube of the 25 cm water cell, $V_{\text{tt water cell ext}}$ is the external volume of the 25cm water cell and $V_{\text{tt ext}}$ is the external volume of the transfer tube whose interior volume is being estimated.

The pumping chamber volume is estimated by subtracting these two volumes from the total internal volume estimated by the Archimedes method. The internal volumes of the chambers are presented in Table 6.7.

6.6.9 Measuring the Cell Density

There are two methods used in E97-103 for measuring the ^{3}He number density in the cells. The first is to use the density given by Eq. 6.19 with improved volume numbers from the Archimedes method. This second is to measure the pressure broadening of the wavelength of light absorbed by rubidium in the cell. The results

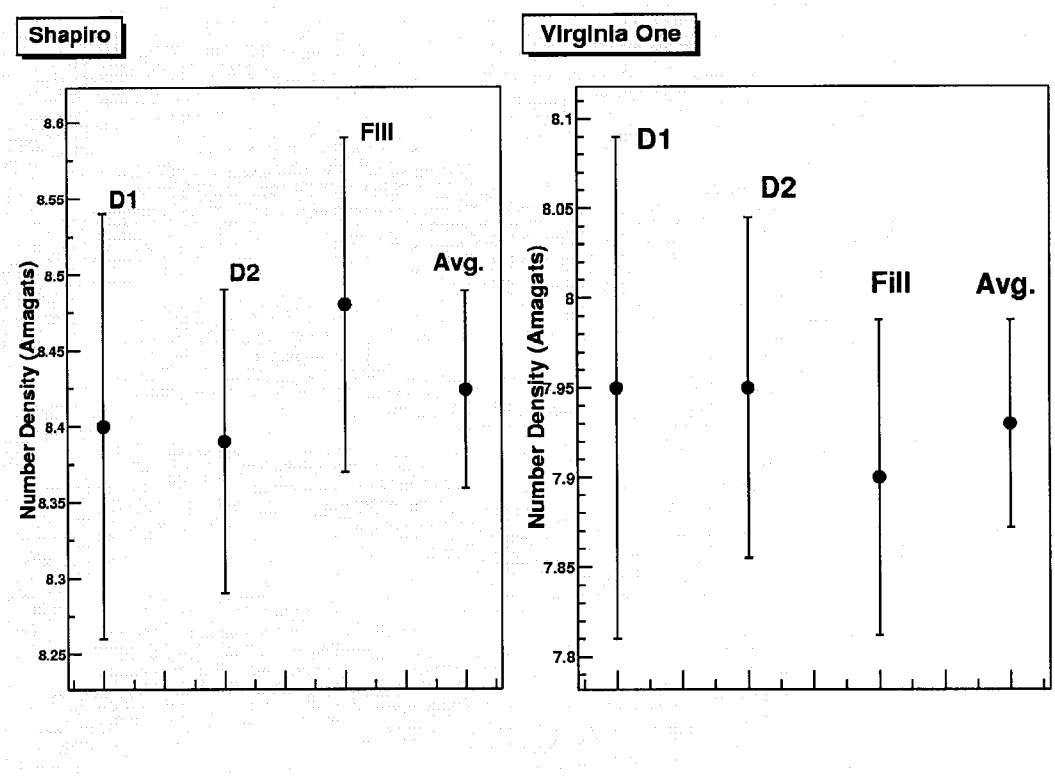

Figure 6.13: *The density of the two cells used in E97-103.*

of both of these methods are shown in Fig. 6.13, and are in good mutual agreement. D1 and D2 indicate the results from pressure broadening with D1 (795 nm) laser light and with D2 (785 nm) laser light. Details of the density measurement using pressure broadening is found in Ioannis Kominis' thesis [61].

6.7 Lasers and Optics

6.7.1 Polarizing Optics

Optical polarization of rubidium requires circularly polarized laser light. In E97-103 the laser light is provided by three Coherent diode laser systems. A diode laser produces monochromatic photons by exciting an electron transition between a p-n semi-conductor junction [65]. The light from each diode is then channeled into a fiber optic line. Since each diode provides a limited amount of power, the output fibers of many diodes are bundled into a fiber-array package (FAP). Each

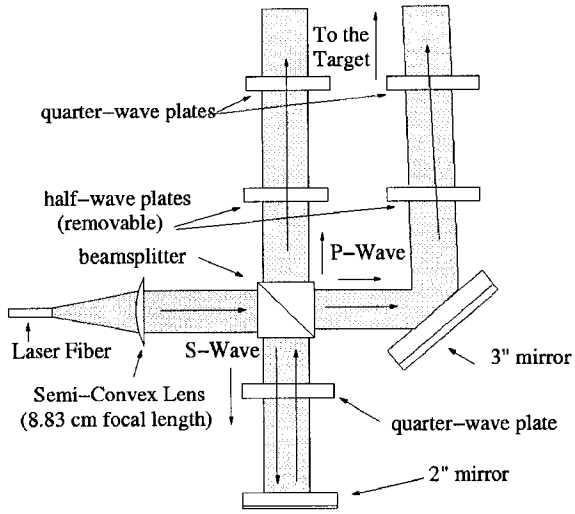

Figure 6.14: *Polarizing optics for Jefferson Lab polarized ^{3}He target.*

FAP system provides thirty watts of power and the frequency spectrum is centered at 795 nm, with a full-width half-max of 2 nm at operating temperature through a single 800 μm diameter output optical fiber.

The technique used in E97-103 to generate circularly polarized light uses a series of optics as shown in Fig. 6.14. The light emitted by the fiber-optic is divergent, but can be made parallel by a semi-convex lens. This lens determines the size of the laser spot, typically a 3-4 cm diameter circle. This spot continues to get larger and isn't this size at the cell.

The light then enters a beam-splitter which reflects the S-wave light (light polarized perpendicular to the bottom of the beam splitter) to the right while the P-wave light (light polarized parallel to the bottom of the beam splitter) is allowed to pass through and bounce off a mirror towards the target. The reflected S-wave light is converted to P-wave light by traveling through a quarter-wave plate, bouncing off a mirror and returning through the same quarter-wave plate. The first trip through the quarter-wave plate converts the S-wave to circularly polarized light. The second trip converts it to P-wave light. This P-wave light can travel straight through the beam-splitter. However, this process is not 100% efficient and up to 10% remains

S-wave and is reflected, unfortunately, back towards the laser fiber! Consequently, one has to be careful when aligning these optics since back reflection can not only damage the fiber, but also travel down the fiber and damage the diode. (A solution is to tilt the beam splitter a little.)

Both sets of P-wave light are then rotated to circularly polarized light by two quarter wave plates. This light can be converted to an opposite circular polarization by inserting half-wave plates either before the quarter-wave plates or after. The laser light is then ready to polarize rubidium.

6.7.2 Optics Configuration

Increasing the efficiency of these optics is important for maximum rubidium polarization with minimal laser power. The dominant cause of inefficiency is caused by the spatial profile of the light which is divergent and does not have a point-like source. This means that all the light cannot be made perfectly parallel with just one semi-convex lens and will eventually diverge on the path to the target (which can be up to 5 meters with this target). Another important source of power loss comes from the surfaces of the optics which produce small (1%) power losses due to reflection. These losses can be diminished, but not eliminated, by coatings. The converted S-wave light will therefore generally have lower power output in a well-optimized system.

Another source of inefficiency is the orientation of the quarter- and half-wave plates. Quarter- and half-wave plates are made of crystals whose transmission velocity depends on the polarization of the normally incident light entering the crystal [65]. The axes of maximum and minimum transmission velocity are known as the fast and slow axes, respectively. To create left circularly polarized light from linearly polarized light, a quarter-wave plate needs to have its slow axis -45° from the linear polarization plane and its fast axis 45° from the linear polarization plane

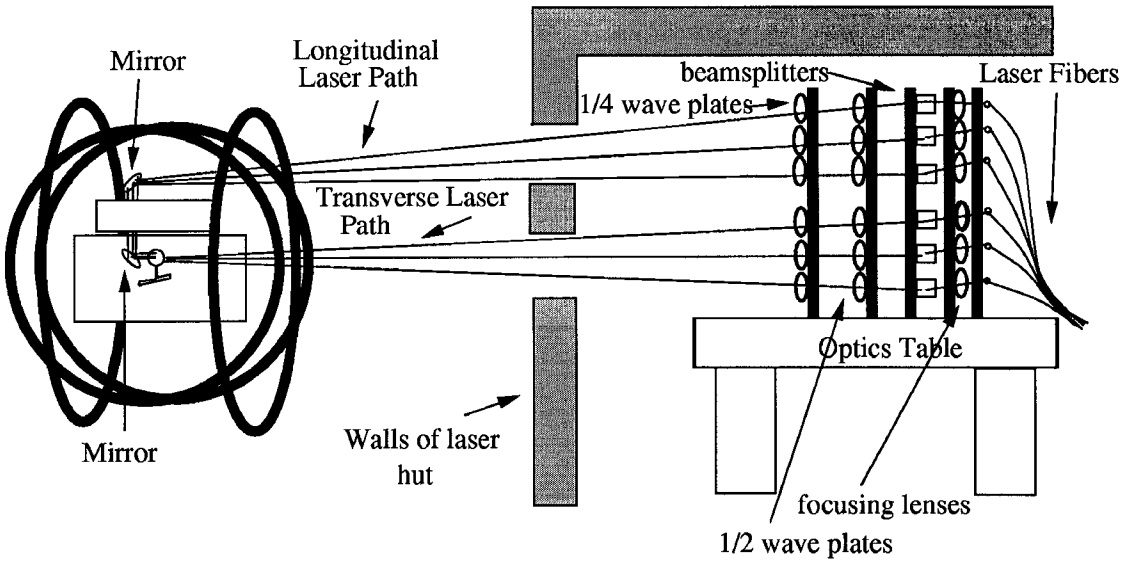

Figure 6.15: *A diagram of Laser Optics Configuration in Hall A.*

viewing the optics towards the target. For right circularly polarized light, the fast axis is at -45° while the slow axis is at 45°. When using the half-wave plate, its axis must also be at a 45° angle from the plane of linear polarization. Deviations from this alignment of the quarter and half-wave plates will reduce the polarization of the laser light, potentially reducing the rubidium polarization.

The optics configuration in Hall A used six beam lines: three for the lasers used for longitudinal target polarization and three lasers for transverse target polarization, as shown in Fig. 6.15. There was also a spare beam line which was not used. The polarizing optics and the optical fibers from the lasers are mounted in parallel on three-foot tall 2" diameter metal poles. The longitudinal laser paths are on top and use two mirrors at the target to align the light along the longitudinal holding field. The transverse laser paths are the bottom set of optics and travel straight into the pumping chamber through a hole in the side of the target cover.

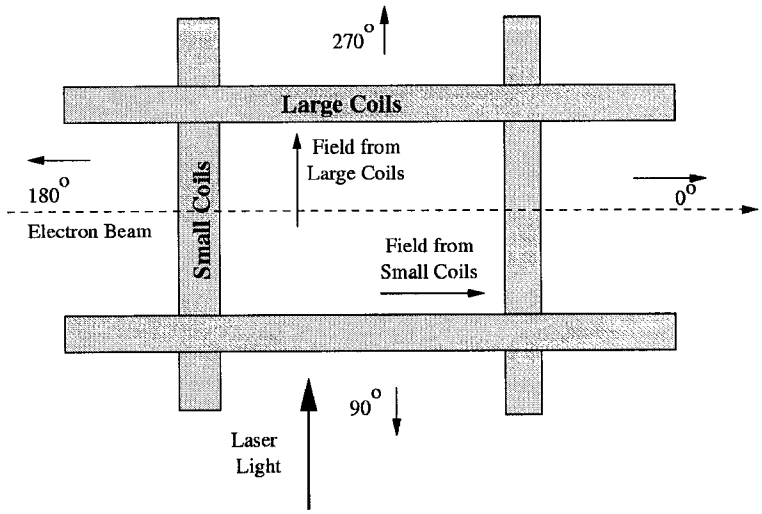

Figure 6.16: *Helmholtz coils configuration with respect to beam line and lasers. The electron beam arrives from the left.*

6.8 The Magnetic Fields

6.8.1 The Helmholtz Coils

The Helmholtz coils provide the holding field for the polarized ^{3}He target. There are two sets of coils that can be used in combination to form a uniform holding field around the target cell that can be in any direction in the scattering plane. In E97-103 the coils were arranged so that the smaller coil's field was along the path of the electron beam and the larger coil's field was perpendicular to it, as shown in Fig. 6.16.

The smaller coils have an interior radius of 63.3 cm and are made of 256 windings of wire in each coil. The larger coils have an interior radius of 72.4 cm and are made of 272 windings [66]. Each set of coils is powered by a KEPCO Model BOP 36-12D power supply. The maximum current of the power supply is 10 A with a maximum voltage of 32 V. The power supplies are run in voltage mode which means the power supply provides constant voltage with slightly fluctuating current. It would be better to run in current mode, but these particular power supplies create a high-frequency noise when in current mode making NMR polarimetry measurements impossible [67].

Calibration	α_I (Amps/V)	β_I (Amps)	α_B (G/V)	β_B (G)	α_{BI} (G/Amps)	β_{BI} (G)
Cold Small Coils	-1.164	0.078	4.123	-0.277	-3.542	-0.001
Warm Small Coils	-1.156	0.180	4.026	-0.633	-3.483	-0.007
Cold Large Coils	-1.202	0.084	4.018	-0.558	-3.343	-0.278
Warm Large Coils	-1.152	0.124	3.962	-0.718	-3.439	-0.292

Table 6.8: *A list of the constants used to calibrate the Helmholtz coils in E97-103.*

The voltage output in each KEPCO power supply is controlled by a SRS DS345 function generator. These two function generators are in turn controlled through a GPIB interface to a Windows-based PC running LabVIEW. The output voltage of the DS345 must be calibrated to get a meaningful magnetic field out of the coils. It also useful to know the current calibration, so that a relation between the magnetic field and the current is known. This is useful for monitoring the magnetic field.

One set of coils is calibrated at a time. Since the coils are warmer when current has been running through them, the coils are calibrated at high current (warm coil calibration) and at low current (cold coil calibration). The warm coil calibration is used whenever the cuurent is above 1 A. The relations between the coils and their current and magnetic field are written:

$$I = \alpha_I V_{pp} + \beta_V \tag{6.28}$$

$$B = \alpha_B V_{pp} + \beta_V \tag{6.29}$$

$$B = \alpha_{BI} I + \beta_{BI} \tag{6.30}$$

where I is the current in the coils, α_I and α_B are the slope constants for the calibrations, β_I and β_B are the offset constants for the calibrations, α_{BI} and β_{BI} are the calibration constants between the current and voltage and V_{pp} is the voltage output of the DS345 function generator. The results of these calibrations are in the Table 6.8 and plots can be found in Appendix A.

The magnetic field measurements are done with two Gaussmeters. The cold

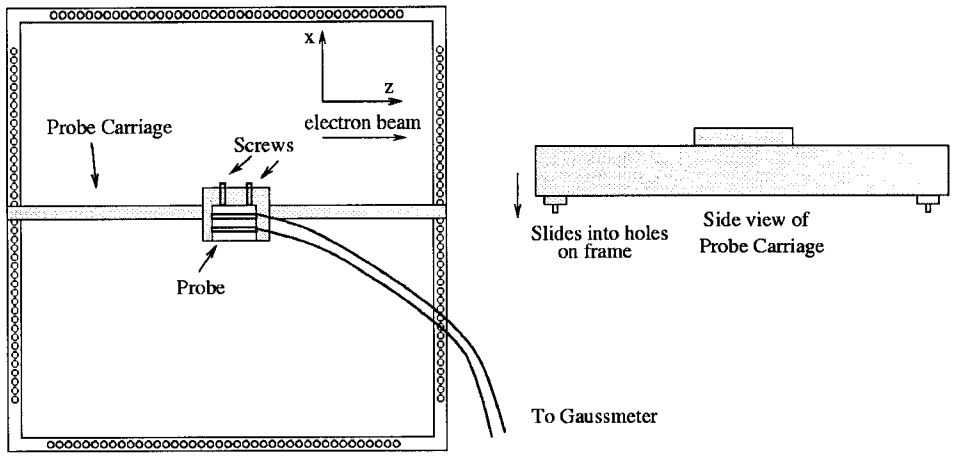

Figure 6.17: *Diagram of frame and probe carriage used to map holding field.*

coil measurements are done with an extremely sensitive Gaussmeter, but could only measure up to 1 Gauss. The other Gaussmeter, made by Lake Shore, could measure much higher fields than was necessary, but was only precise to 0.010 Gauss. It is unclear whether the difference in calibrations in warm and cold coils is due to the differences in the actual calibration or simply differences in the Gaussmeters.

6.8.2 Mapping of Helmholtz Coils

There are two reasons that make it important to control holding field gradients in a polarized ^{3}He target. The first and most important is that field gradients over 20 mGauss/cm for a 25 Gauss field will increase polarization losses during polarimetry measurements that depend on adiabatic fast passage (AFP). Both of the polarimetry methods used on the Jefferson Lab polarized ^{3}He target (NMR and EPR) depend on AFP. The second reason is that field gradients over 100 mGauss/cm for a 25 Gauss field will begin lowering the maximum polarization of the target cell. Obviously, this is a less important reason because performance is already affected at 20 mGauss/cm.

The field gradients are measured using the two Gaussmeters used to calibrate the field. The Lakeshore Gaussmeter is used to measure fields over 1 Gauss and the sensitive Gaussmeter is used for all other measurements. The probes for the

Gaussmeter are fastened to the probe carriage pictured in Fig. 6.17. The entire carriage sits on an aluminum frame that sits in the target chamber. The frame is centered where the target would be when it is in beam. The carriage can be positioned accurately on the frame by the precisely machined holes. There are 40 holes on each side of the frame with a 1 cm separation between them.

These field measurements could only be done in the x and z directions, though for a full measurement one would also like to do vertical measurements. When the probe is aligned perpendicular to the holding field it is particularly sensitive to small changes in angle. For the x direction only points in the center chamber matter since the cell is only <2 cm wide in x. However, the cell extends from -20 cm to 20 cm in z (in this coordinate system); therefore all the gradients in z are important.

The measured gradients for the small coil are presented in Appendix A. There seems to be a large gradient on the negative edge of $\frac{dB_z}{dz}$ for the small coil and $\frac{dB_x}{dx}$ for the large coil. Since these are along the axis of the holding field the field should be symmetric. It's unclear what is the source of this gradient is. Some data points on the edge of x have been ignored since they are outside the cell area and don't indicate a larger trend.

6.8.3 Field Direction of the Helmholtz Coils

To measure g_2^n, both longitudinal and transverse asymmetries must be measured. The expected physics asymmetries showed that the longitudinal asymmetry was an order of magnitude larger than the transverse asymmetry. Therefore, if the holding field direction was not exactly aligned with the electron beam then there could be a significant amount of longitudinal asymmetry mixed in with the transverse asymmetry.

To maximize the accuracy when setting the holding field direction, a set of measurements were done with a long compass and a survey team to measure the

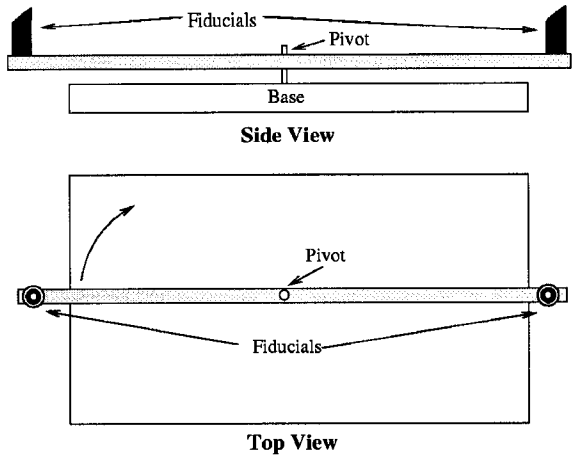

Figure 6.18: *Compass used to measure the holding field direction.*

holding field angle. The compass, shown in Fig. 6.18, is a rectangular iron rod. A set of fiducials are placed on either end of the rod. The rod of the compass is set on a pivot about which it can swing freely. The compass is placed inside the target scattering chamber. When the magnetic field is set to the desired direction, a survey team can measure the absolute position of the fiducial in reference to set locations in Hall A to 0.2 mm.

A summary of the surveys is presented in Table 6.9. A listing of all the survey information is provided in Appendix C. The measurements from the third survey were used to align the holding field. However, the calculated angles from the Helmholtz currents disagreed with the survey by 0.5° at the 270° setting and 1.0° in the 90° setting. Unfortunately, the measurements from the final survey (Survey 4) agree within $< 0.3°$ with the calculations from the Helmholtz coil currents, contradicting the previous measurement. The final survey also agrees well with the first survey done. It is unclear what is the source of the discrepancy. The effect of this discrepancy on E97-103's results will be discussed in the asymmetry analysis chapter.

Nominal Angle	Survey 3 Angle	Calculated Angle	Survey 4 Angle 1	Calculated Angle 2
0	0.02	0.218	-0.480	-0.262
90	89.92	88.93	89.09	88.93
180	180.17	179.96	180.15	179.96
270	270.02	269.44	269.59	269.46

Table 6.9: *Table of holding field angles given by two surveys and the holding field calibrations. Survey 3 was done just before E97-103 and Survey 4 was done just after. Calculated Angle refers to the angle calculated by the Helmholtz coil currents during Survey 3 and Survey 4 respectively. All angles are given in degrees.*

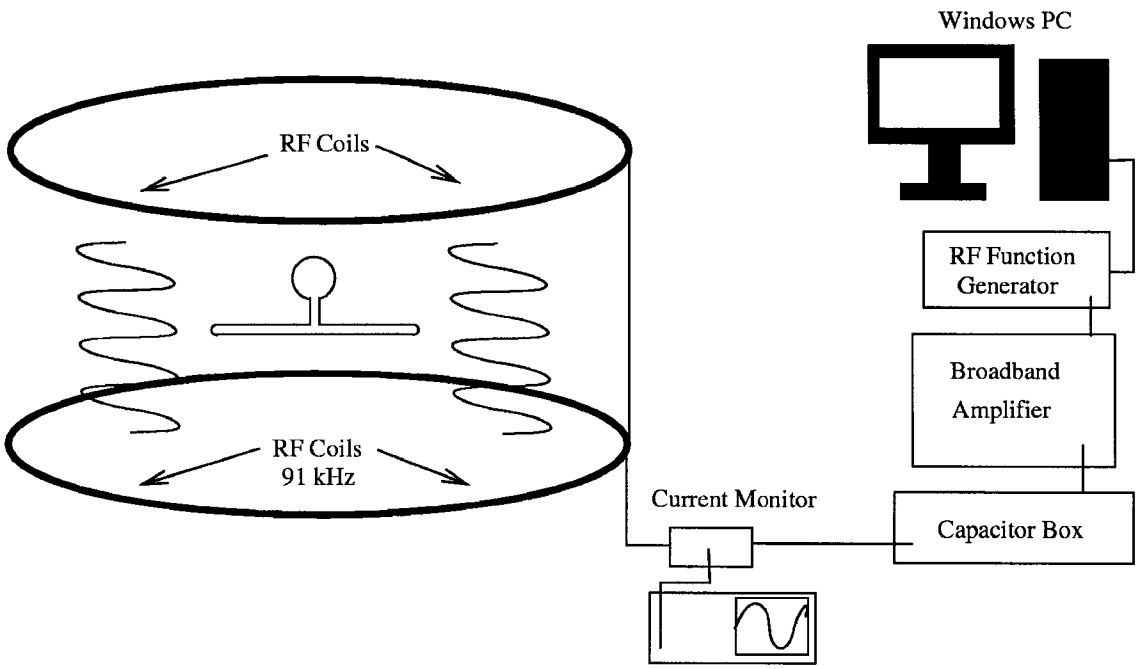

Figure 6.19: *Equipment used to power and monitor RF coils.*

6.8.4 Calibration of RF coils

There are two radio frequency (RF) coils that are used to create a high-frequency magnetic field of up to 100 mGauss for use in the target polarimetry. The coils are powered by a Hewlett Packard Model 355 D function generator and a ENI - 2100 L broadband power amplifier as shown in Fig. 6.19. A capacitor (inside the capacitor box) is added to the system to boost power in the coils by matching the impedance with the RF coilsr. The current in the RF coils is monitored by a loop current monitor made by Pearson. The signal from the current monitor is read by an oscilloscope.

The magnitude of the field created by the RF coils is usually referred to as H_1. H_1 is calibrated by inserting a small loop of wire perpendicular to the RF field and monitoring the amplitude of the voltage that comes out of it with an oscilloscope. The H_1 field can be calculated using the formula:

$$H_1 = \frac{V_{pp}(10^7 \text{ mGauss/T})}{8\pi^2 f N D^2} \frac{1}{|1 - R_c/Z|} \approx \frac{V_{pp}(10^7 \text{ mGauss/T})}{8\pi^2 f N D^2} \tag{6.31}$$

where H_1 is the RF field amplitude, V_{pp} is the peak-to-peak voltage read on the oscilloscope, f is the frequency of the RF field, N is the number of turns in the measurement loop, D is the diameter of the measurement loop, R_c is the resistance of the coil and Z is the impedance of the coil and the cable used to attach it to the oscilloscope. $|R_c/Z|$ in the system used in E97-103 was $\ll 1.0$ and ignored.

The H_1 calibration is shown in Fig. 6.20. The coil of wire used for the calibration had 47 turns and a diameter of 1.25 cm. The RF frequency used for the experiment was 91 kHz. The voltage setting on the RF function generator used for AFP measurements was 2.5 V rms which translates from this calibration to 57.93 mGauss.

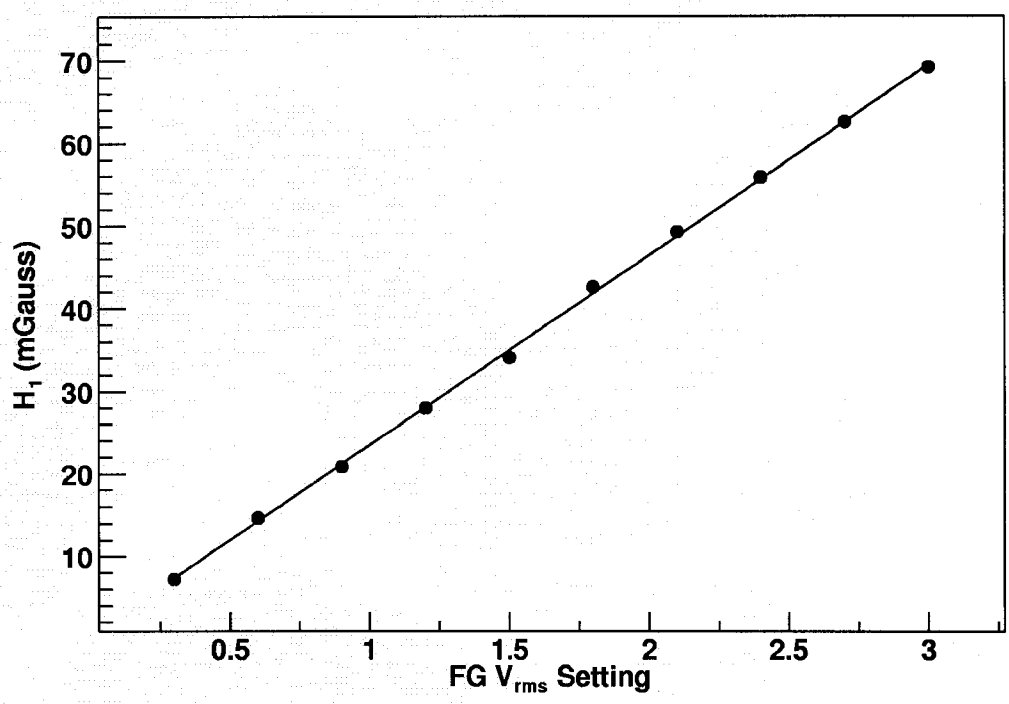

Figure 6.20: *The H_1 RF field versus the voltage on the HP Function Generator.*

6.9 Measuring Target Polarization

6.9.1 The Adiabatic Condition

Adiabatic Fast Passage (AFP) is a technique for reversing nuclear magnetization that is used in the two forms of polarimetry used by the polarized ^{3}He target. For AFP to work, the process of polarimetry must meet the adiabatic condition. To see how to define the adiabatic condition one must start with a free magnetization (like a ^{3}He nucleus) in a static magnetic field $\vec{H}_0 = H_0\hat{k}'$. The motion of the magnetization in a holding field is described classically (which is sufficient for describing the polarimetry systems) by [68]:

$$\frac{d\vec{M}}{dt} = \gamma\vec{M} \times \vec{H}_0 \tag{6.32}$$

where γ is the gyromagnetic ratio (3.24 kHz/Gauss for ^{3}He [69]).

Since this motion is obviously a precession around the holding field $\vec{H}$, it is

useful to describe the system in a rotating frame of reference S' that rotates around the holding field axis at the same frequency as the precession. Any vector, $\vec{A}$, in a rotating frame of reference can be described as [68]:

$$\frac{d\vec{A}}{dt} = \frac{\partial \vec{A}}{\partial t} + \vec{\omega} \times \vec{A} \tag{6.33}$$

where the first term on the right hand side is the motion in the rotating frame of reference and the second term is the motion of the frame defined by axis $\vec{\omega}$. With this relation one can define the motion of the magnetization as:

$$\frac{\partial \vec{M}}{\partial t} = \gamma \vec{M} \times \left(\vec{H}_0 + \frac{\vec{\omega}}{\gamma} \right). \tag{6.34}$$

Therefore if one picks the right frequency of rotation ω such that $\omega = -\gamma H_0$ the motion of the magnetization $\frac{\partial \vec{M}}{\partial t} = 0$. This frequency in a static holding field is known as the *Larmour frequency* and is usually denoted ω_0.

For AFP, a rotating field $\vec{H}_1 = H_1 \cos(\omega t)\hat{i} + H_1 \sin(\omega t)\hat{j}$ is added to the static field $\vec{H}_0$, where ω is the frequency of precession of the rotating frame, which is not necessarily w_0. In the rotating frame, once can define an effective field $\vec{H}_e$ which is static in this frame:

$$\vec{H}_e = \left(H_0 + \frac{\omega}{\gamma} \right) \hat{k} + H_1 \hat{i}. \tag{6.35}$$

The magnitude of this vector is

$$H_e = \left[\left(H_0 + \frac{\omega}{\gamma} \right)^2 + H_1^2 \right]^{\frac{1}{2}} \tag{6.36}$$

The next step in describing the adiabatic condition is to make the static holding field, a slowly varying field. It is useful to generalize this situation to a vector $\vec{H}$ whose time derivative can be written [68] :

$$\frac{d\vec{H}}{dt} = \vec{\Omega} \times \vec{H} + \Omega_1 \vec{H} \tag{6.37}$$

where the vector $\vec{\Omega}$ is an instantaneous axis constantly along the direction of H and Ω_1 is a scaler. A collection of spins with net magnetization $\vec{M}$ in a magnetic field H described above will change in time as:

$$\frac{\partial \vec{M}}{\partial t} = \gamma \vec{M} \times \left(\vec{H} + \frac{\vec{\Omega}}{\gamma} \right). \tag{6.38}$$

Looking at this equation carefully, the adiabatic condition becomes apparent. If the magnitude of $\vec{\Omega}$ is much smaller than the magnitude of $\gamma \vec{H}$ then the second term in Eq. 6.38 can be ignored and the components of magnetization can be written:

$$\frac{\partial M_z}{\partial t} = M_x \Omega_y - M_y \Omega_x \tag{6.39}$$

$$\frac{\partial M_x}{\partial t} = \gamma H M_y \tag{6.40}$$

$$\frac{\partial M_y}{\partial t} = -\gamma H M_x \tag{6.41}$$

which depends on $H_x = H_y = 0$ which is true by definition of the frame.

Over a long period of time the change in M_z will be:

$$\Delta M_z = M_z(t) - M_z(0) = \int_0^t \left[M_x(t') \Omega_y(t') - M_y(t') \Omega_x(t') \right] dt \tag{6.42}$$

Since M_x, M_y, Ω_x and Ω_y are all oscillatory and if Ω_x and Ω_y are small then M_z is constant with time. This means that the angle of the magnetization with the instantaneous direction of the field is a constant of the motion if the adiabatic condition, $\Omega \ll |\gamma H|$, is satisfied [68].

To derive the adiabatic condition more specifically for the purposes of the polarized ^{3}He target, one needs to go back to the effective field presented in Eq. 6.35. Assuming the holding field $\vec{H}_0$ changes linearly in time as $\dot{H}_0 t$, the change in the effective field $\vec{H}_e$ is [68]

$$\frac{d\vec{H}_e}{dt} = \cos\theta \frac{\dot{H}_0}{H_e} \vec{H}_e + \sin\theta \frac{\dot{H}}{H_e} (\hat{n} \times \vec{H}_e) \tag{6.43}$$

where θ is the angle between the effective field $\vec{H}_e$ and the holding field $\vec{H}_0$. The vector has been written in the frame of the normalized unit vectors $\vec{H}_e/H_e$ and $\hat{n} \times$

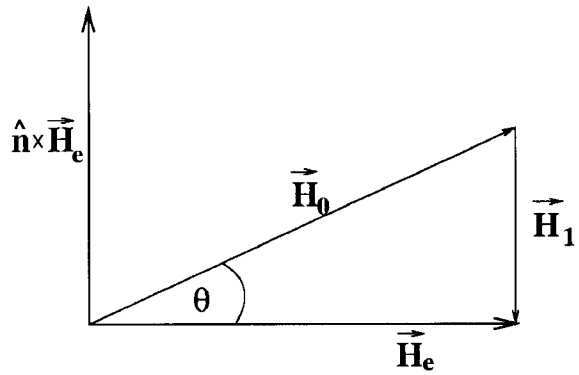

Figure 6.21: *The holding field $\vec{H}_0$ and rotating field $\vec{H}_1$ in the frame of reference defined by $\vec{H}_e$ and $\hat{n} \times \vec{H}_e$.*

$\vec{H}_e/H_e$, as shown in Fig. 6.21, where $\hat{n}$ is a unit vector in the direction perpendicular to H_0 and H_1. Comparing this equation and Eq. 6.37 one can see [68]:

$$\Omega = \sin\theta \frac{\dot{H}_0}{H_e} = H_1 \frac{\dot{H}_0}{H_e^2} \tag{6.44}$$

where $\sin\theta = H_1/H_e$ comes from the geometry in Fig. 6.21. So for the system of a changing holding H_0 and a rotating field H_1 the adiabatic condition is:

$$\dot{H}_0 \ll \frac{\gamma H_e^3}{H_1}. \tag{6.45}$$

Near the Larmour frequency where $H_1 \approx H_e$:

$$\dot{H}_0 \ll \gamma H_1^2. \tag{6.46}$$

This is the adiabatic condition for the polarized ^{3}He target. When this condition is met, the magnetization of the ^{3}He nucleus will follow the effective field. This is what allows a magnetization reversal during AFP.

6.9.2 The Bloch Equations

The derivation of the adiabatic condition assumed a free target in a homogeneous field. In reality, there are effects that must be added to the equation of motion presented by Eq. 6.32. A magnetization in a static field will tend towards its

equilibrium value $M_z = M_0 = \chi_0 H_0$, where χ_0 is the magnetic susceptibility, which can be described by the equation [68]:

$$\frac{dM_z}{dt} = -\frac{M_z - M_0}{T_1} \tag{6.47}$$

where T_1 is the longitudinal relaxation time. Similarly, if the magnetization is given a component, through an RF field for example, at right angles to the applied field H_0, this component will decay as [68]:

$$\frac{dM_x}{dt} = -\frac{M_x}{T_2}, \quad \frac{dM_y}{dt} = -\frac{M_y}{T_2} \tag{6.48}$$

where T_2 is called the transverse relaxation time. Finally, in the presence of an applied field that is made of a static holding field and a much smaller RF field, the motion due to relaxation, as described above, can be added directly to the motion of a free spin [68]:

$$\frac{d\vec{M}}{dt} = \gamma \vec{M} \times \vec{H} - \frac{M_x \hat{i}' + M_y \hat{j}'}{T_2} - \frac{(M_z - M_0)\hat{k}'}{T_1} \tag{6.49}$$

where $\hat{i}'$,$\hat{j}'$ and k' are the unit vectors in the laboratory frame of reference.

An additional modification is necessary because H_1 in the polarized ^{3}He system is sufficiently large that the magnetizations relax to $\vec{M}_0 = \chi_0(\vec{H}_0 + \vec{H}_1(t))$. This results in a set of modified Bloch equations [70]:

$$\frac{dM_x}{dt} = -\frac{M_x - \chi_0 H_1}{T_2} + \Delta\omega M_y \tag{6.50}$$

$$\frac{dM_y}{dt} = -\Delta\omega M_x - \frac{1}{T_2} M_y - \omega_1 M_z \tag{6.51}$$

$$\frac{dM_z}{dt} = \omega_1 M_y - \frac{M_z - M_0}{T_1} \tag{6.52}$$

where $\Delta\omega = \gamma(H(t) - H_0)$ where $H_0 = -\omega_0/\gamma$ where ω_0 is the Larmour frequency and $\omega_1 = -\gamma H_1$.

This can be translated into a polarization vector $\vec{P}$ that can be written [70]:

$$\frac{dP_x}{dt}(t) = -\frac{1}{T_2} P_x(t) + \gamma[H(t) - H_0]P_y(t) + \frac{1}{T_2}\chi H_1 \tag{6.53}$$

$$\frac{dP_y}{dy}(t) = -\gamma[H(t) - H_0]P_x(t) - \frac{1}{T_2}P_y(t) + \gamma H_1 P_z(t) \quad (6.54)$$

$$\frac{dP_z}{dt}(t) = -\gamma H_1 P_y(t) - \frac{1}{T_1}P_z(t) + \frac{1}{T_1}\chi H(t). \quad (6.55)$$

where $\chi = \mu/k_B T$ where μ is the magnetic moment of the nucleus, k_B is the Boltzmann constant (8.61739×10^{-5} eV/K) and T is the temperature. These equations are used to calculate the shape of the NMR signal when the ^{3}He (or water for water calibrations) nuclei undergo AFP.

6.9.3 Adiabatic Fast Passage

Adiabatic Fast Passage is a way of reversing the polarization of nuclei in a magnetic field. This is done by applying a perpendicular RF field H_1 with frequency ω_1 and increasing the holding field adiabatically until it goes through the Larmour resonance. At this resonance, the polarization direction of the nuclei will follow the effective field and change sign. Then the field is usually swept back to reverse the polarization back to the original direction.

The speed at which the holding field is changed has to be slow enough to meet the adiabatic condition, but fast enough so sweeping is faster than the relaxation times (T_1 and T_2). Polarized ^{3}He has T_1 of 435 s [57] making the adiabatic condition easily met with an $H_1 = 58$ mG, $\omega_1 = 91$ kHz and a $H_0 = 25.0$ Gauss. Water has a $T_1 \approx 3s$ and therefore relaxes quickly under the same conditions; therefore, careful modeling of the relaxation is needed to extract the signal height.

The nominal holding field for the polarized ^{3}He target is 25 Gauss. The sweep rate for AFP is 1.2 Gauss/s. The field is swept up to 32 Gauss and then back down to 25 Gauss. A plot of the magnetic field B, the polarization along the holding field (P_z) and perpendicular to the field (P_x) during an polarized ^{3}He AFP sweep is shown in Fig. 6.22.

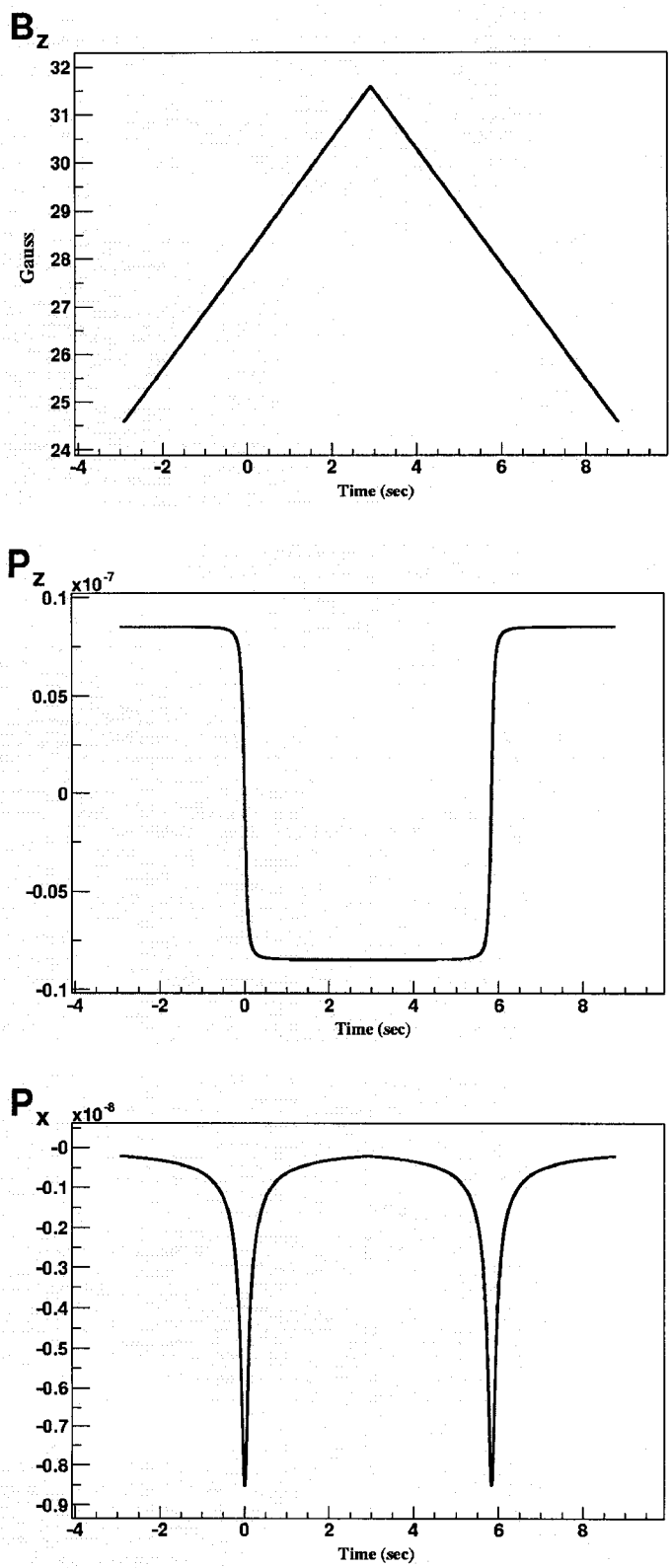

Figure 6.22: *Plots from a model of the Bloch equations for ^{3}He nuclei undergoing AFP. The top plot shows the increase and decrease of the holding field. The middle plot shows the polarization along the direction of holding field. The bottom plot is the transverse field from the ^{3}He nuclei.*

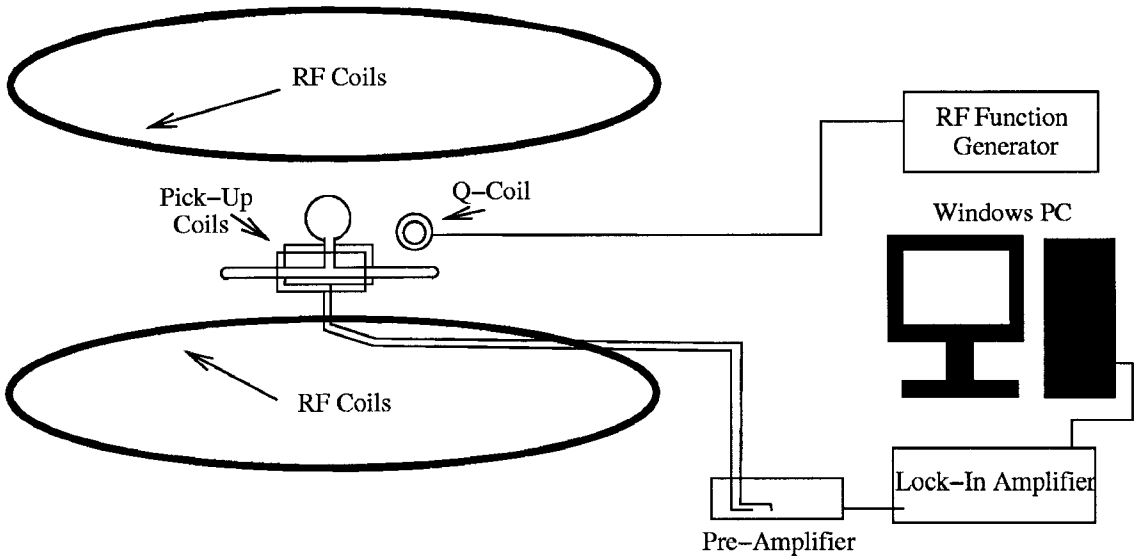

Figure 6.23: *The equipment used to monitor NMR signal.*

6.9.4 NMR Polarimetry Setup

The height of the transverse signal (P_x in Fig. 6.22) during AFP is proportional to the target polarization. This signal can be measured by a pair of coils (called "pick-up coils") placed near the target during AFP. In principle the polarization can be extracted directly from the signal height, but in practice it is better to calibrate with a known polarization. The known polarization used in the Jefferson Lab polarized ^{3}He target is the thermal polarization of water.

The NMR polarimetry system consists of three systems: the Helmholtz coils, the RF coils and the pick-up coils. The Helmholtz coils system and RF coils, described earlier in the chapter, work in tandem to perform AFP on the polarized ^{3}He. The RF coils create the oscillating H_1 field, while the Helmholtz coils sweep the holding field through the Larmour resonance.

The pick-up coil system, shown in Fig. 6.23, detects the transverse oscillating magnetic field. The signal is amplified and filtered by a pre-amplifier. The signal is then sent to a lock-in amplifier that measures the 91 kHz signal. The signal for the entire sweep is stored in the lock-in amplifier buffer then sent to a PC running

LabVIEW to be stored and analyzed.

The pick-up coils are simply two coils of 32 Gauge wire on plastic frames. The exact number of windings is not known, but it has been estimated by measuring the resistance of the coils to be about 96 turns. The shape of the pick-up coils is a 2cm by 11cm square. The coils on each side of the cell are wired oppositely (if one is wound clockwise, the other is wound counterclockwise) so that the signal in the coils add and the background cancels.

Because the water signal is small, a lot of work goes into the placement of the coils. The pick-up coils are aligned so that a minimum amount of signal from the RF coils gets into the pick-up coils in order to maximize the sensitivity of the system to the water signal. This is done by looking at the signal out of the pre-amplifier on an oscilloscope and adjusting the pick-up coil frame with plastic shims and placement screws. Some background from the RF coils is needed for the lock-in amplifier, but generally the less RF signal the better.

6.9.5 Extracting Polarization from the NMR Signal

The shape of either peak when the holding field is being swept up through resonance (the "up sweep") or the signal when the holding field is being swept down through resonance (the "down sweep") can be written as the square root of a Lorentzian [57]:

$$S(t) = \frac{hH_1}{\sqrt{H_1^2 + (H(t) - H_0)^2}} + bH(t) + c \tag{6.56}$$

where S is the signal in the pick-up coils, h is the signal height at resonance, H_0 is the value of the holding field at resonance and t is time. b and c are parameters used to subtract background in the lock-in amplifier. The information about the

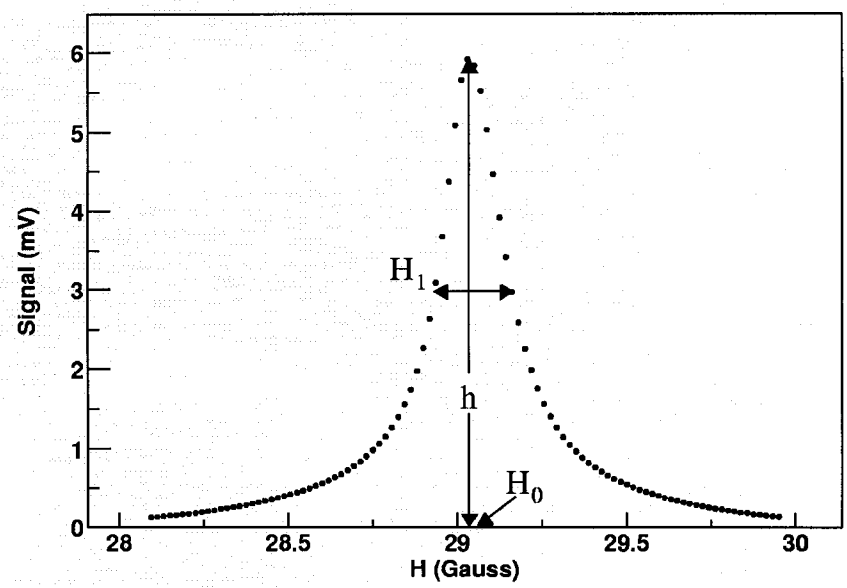

Figure 6.24: *A plot of a signal from a typical NMR measurement. h is the signal height, H_1 the amplitude of the RF field and H_0 is the holding field value at the Larmour resonance.*

polarization is contained in the value h. $H(t)$ for the polarized ^{3}He target is:

$$H(t) = \begin{cases} \alpha t + \beta & \text{if } t < t_{\text{sweep}} \\ \beta - \alpha t & \text{if } t_{sweep} < t < 2t_{sweep} \end{cases} \tag{6.57}$$

where α is the sweep rate (1.2 Gauss/s, in E97-103), β is the initial holding field (25 Gauss in E97-103) and t_{sweep} is the length of one sweep through resonance (5.8333 s in E97-103). Notice the Ht begins and ends at 25 Gauss with a maximum at 32 Gauss.

The polarization of the target can in principle be extracted from h using the formula [57]:

$$P_{^3\text{He}} = \frac{4\pi h}{\mu_0 \omega \mu_{^3\text{He}} (\Phi_{\text{pc}} n_{\text{pc}} + \Phi_{\text{tc}} n_{\text{tc}} + \Phi_{\text{tt}} n_{\text{tt}}) N_c G_c G_p G_l C_\nabla C_\tau C_a} \tag{6.58}$$

where μ_0 is permeablity of free space and the rest of the parameters are given in Table 6.10. This is generally not done since there are unknown systematic errors associated with most of these parameters. No attempt was made to do this for E97-103.

Parameter	Description
h	NMR signal height of ^{3}He
$\mu_{^3\mathrm{He}}$	magnetic moment of ^{3}He (1.155×10^{-13} MeV/T)
Φ_{pc}	Magnetic flux of pumping chamber through pick-up coils
n_{pc}	^{3}He density in pumping chamber
Φ_{tc}	Magnetic flux of target chamber through pick-up coils
n_{tc}	^{3}He density in target chamber
Φ_{tt}	Magnetic flux of transfer tube through pick-up coils
n_{tt}	^{3}He density in transfer tube
N_c	Number of windings in pick-up coils
G_c	Gain of the pick-up coils
G_p	Gain of the pre-amplifier
G_l	Gain of the lock-in amplifier
C_∇	Correction factor due to holding field gradients
C_τ	Correction factor due to lock-in time constant
C_a	Correction factor due to anntenuation in cables

Table 6.10: *Parameters used in extracting polarization from NMR signals.*

The method used to extract the polarization from the ^{3}He NMR signal is to perform an NMR measurement for calibration using a sample of water. The water sample used for this experiment was contained in a glass cell made as similar in dimensions to the helium cells as possible. The protons in water have a magnetic moment that can be aligned in a magnetic field which gives the water a small, but well-known polarization. This polarization can be described by $P_w = (\chi H)$ where $\chi = 3.4616 \times 10^{-10}$/Gauss at 22 °C [70]. The gyro-magnetic ratio for the proton is 2.67515×10^4/(Gauss s) therefore the resonance peak with a frequency of 91 kHz is 21.37 Gauss [70].

The polarization measured using the NMR can be extracted from a ratio of Eq. 6.58 for ^{3}He and water:

$$\frac{P_{^3He}}{P_w} = \left(\frac{h}{h_w}\right)\left(\frac{\mu_p n_p \Phi_{tot}}{\mu_{^3He}(\Phi_{\mathrm{pc}} n_{\mathrm{pc}} + \Phi_{\mathrm{tc}} n_{\mathrm{tc}} + \Phi_{\mathrm{tt}} n_{\mathrm{tt}})}\right)\left(\frac{G_p^w C_\nabla^w C_\tau^w}{G_p C_\nabla C_\tau}\right) \tag{6.59}$$

where the individual parameters are listed in Tables 6.10 and 6.11. Notice that some of the parameters cancel immediately. In most cases C_∇ and C_τ also cancel, but are kept in here because of special cases that occurred during the experiment. Since

Parameter	Description
h_w	NMR signal height of water
P_{th}	Thermal polarization of water (7.481×10^{-9})
μ_p	magnetic moment of ^{3}He (8.795×10^{-13} MeV/T)
$\Phi_{\rm tot}$	Total magnetic flux of cell through the pick-up coils
$n_{\rm tt}$	Density of protons in room temp water (2482 Amagats)
G_p^w	Gain of the pre-amplifier in water signal
C_∇^w	Correction factor due to holding field gradients in water signal
C_τ^w	Correction factor due to lock-in time constant in water signal

Table 6.11: *Additional parameters used in water calibrated NMR*

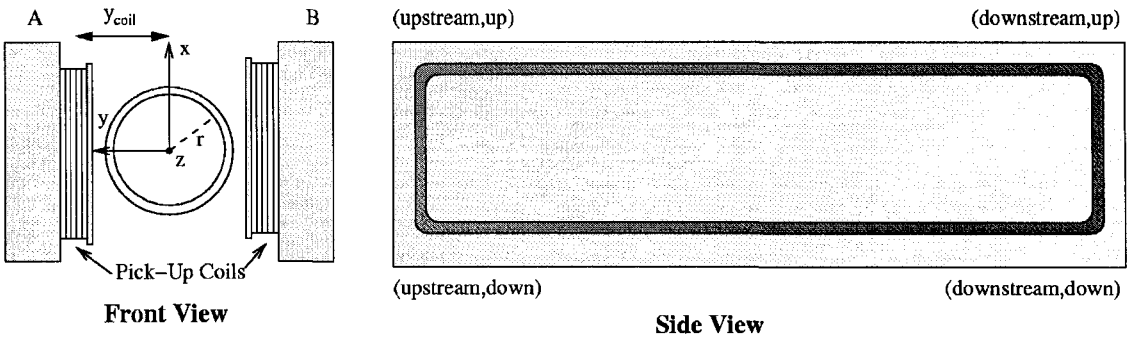

Figure 6.25: *The reference frame of the magnetic flux calculation with respect to the target chamber and the pick-up coils.*

P_w is known, after measurement of the water signal h_w a calibration constant c_w is calculated :

$$c_w = \left(\frac{P_w}{h_w}\right)\left(\frac{\mu_p n_p \Phi_{tot}}{\mu_{^3He}(\Phi_{\rm pc} n_{\rm pc} + \Phi_{\rm tc} n_{\rm tc} + \Phi_{\rm tt} n_{\rm tt})}\right)\left(\frac{G_p^w C_\nabla^w C_\tau^w}{G_p C_\nabla C_\tau}\right) \qquad (6.60)$$

then the polarization from a particular NMR polarization measurement on ^{3}He can be extracted with $P_{^3He} = c_w h$. Each of the parameters that go into c_w will be analyzed in the following subsections.

6.9.6 NMR Flux in the Pick-up Coils

The magnetic flux is the amount of magnetic field normal to an area multiplied by the area. In the context of the NMR polarimetry the field is from the ^{3}He nuclei or protons in water going through resonance and the area is the face of the pick-up coils. The amount of current in the coils is proportional to the flux. The magnetic

flux is written:

$$\Phi = \int \frac{\vec{B}}{B} \cdot d\vec{a} = \oint_{\text{coils}} \frac{\vec{A}}{A} \cdot d\vec{l} \tag{6.61}$$

where $\vec{B}$ is the magnetic field from the nuclei and $\vec{A}$ is the magnetic vector potential. The definition of flux here is normalized ($\vec{B}/B$ instead of just $\vec{B}$) to unit magnetization so that the flux is independent of the density and polarization of the cell, which enter the calibration constant independently. Using the reference frame defined by Fig. 6.25, the magnetic vector potential is:

$$\vec{A}(\vec{r}) = \int_{V_{\text{cell}}} d^3\vec{r} \frac{-\hat{y} \times \vec{r}}{|\vec{r}|^3} \tag{6.62}$$

where V_{cell} is the volume of the cell and $-\hat{y}$ is a unit vector in the -y direction representing the direction of magnetization during an AFP flip.

The code used to calculate the magnetic flux was written by Ioannis Kominis [61]; it divides the cell into small cubes of equal volume. $\vec{A}(\vec{r})$ at any $\vec{r}$ is the sum of the vector potential of all of these cubes. It then sums $\vec{A}(\vec{r}) \cdot d\vec{l}$ over the path of one of the pick-up coils. The target chamber, transfer tube and pumping chamber fluxes are calculated separately for both pick-up coils.

The results of these calculations are shown for the two cells in Table 6.13 using the cell and pick-up coil geometries in Table 6.12. The internal radius of the target chamber is calculated by subtracting the wall thickness from the external radius for the middle section of the cell (where the pick-up coils are). The pumping chamber volume is derived by using the internal volume and assuming it is spherical. The transfer tube internal radius is determined by assuming it is a cylinder. The placement of the pick-up coils assumes that the cell axis is along z=0 cm and the center of the cell is at x=0 cm and y=0 cm. The positions of the pick-up coil corners are determined by measuring the distance between the corners with the cell out of the pick-up coils and then inserting the cell and determining its position with a caliper.

The error caused by measurement of the cell position is a major systematic error

	Shapiro			Virginia One		
Corner Name	x	y	z	x	y	z
A, Down, Downstream	-1.023	1.567	5.510	-0.961	1.658	5.510
A, Up, Downstream	0.977	1.568	5.510	1.039	1.660	5.510
A, Up, Upstream	0.977	1.506	-5.510	1.039	1.585	-5.510
A, Down, Upstream	-1.023	1.502	-5.510	-0.961	1.578	-5.510
B, Down, Downstream	-1.023	-1.904	5.510	-0.961	-1.819	5.510
B, Up, Downstream	0.977	-1.908	5.510	1.039	-1.822	5.510
B, Up, Upstream	0.977	-1.803	-5.510	1.039	-1.731	-5.510
B, Down, Upstream	-1.023	-1.798	-5.510	-0.961	-1.720	-5.510
Cell Dimension						
Pumping Chamber Radius		3.03			2.98	
Transfer Tube Radius		0.398			0.396	
Transfer Tube Length		6.46			6.52	
Target Chamber Radius		0.796			0.819	
Target Chamber Length		40.0			39.4	

Table 6.12: *Values used for the flux calculation. All values are in centimeters*

Cell	Coil	Target Chamber	Pumping Chamber	Transfer Tube	Total
Shapiro	A	-25.15	1.84	0.04	-23.26
	B	19.12	-1.76	0.05	17.41
	B-A	44.26	-3.59	0.01	40.69
Virginia One	A	-24.78	1.74	-0.01	-23.04
	B	21.63	-1.70	0.05	19.97
	B-A	46.41	-3.45	0.05	43.01

Table 6.13: *Flux values for polarized ^3He cells. All values are in cm^2.*

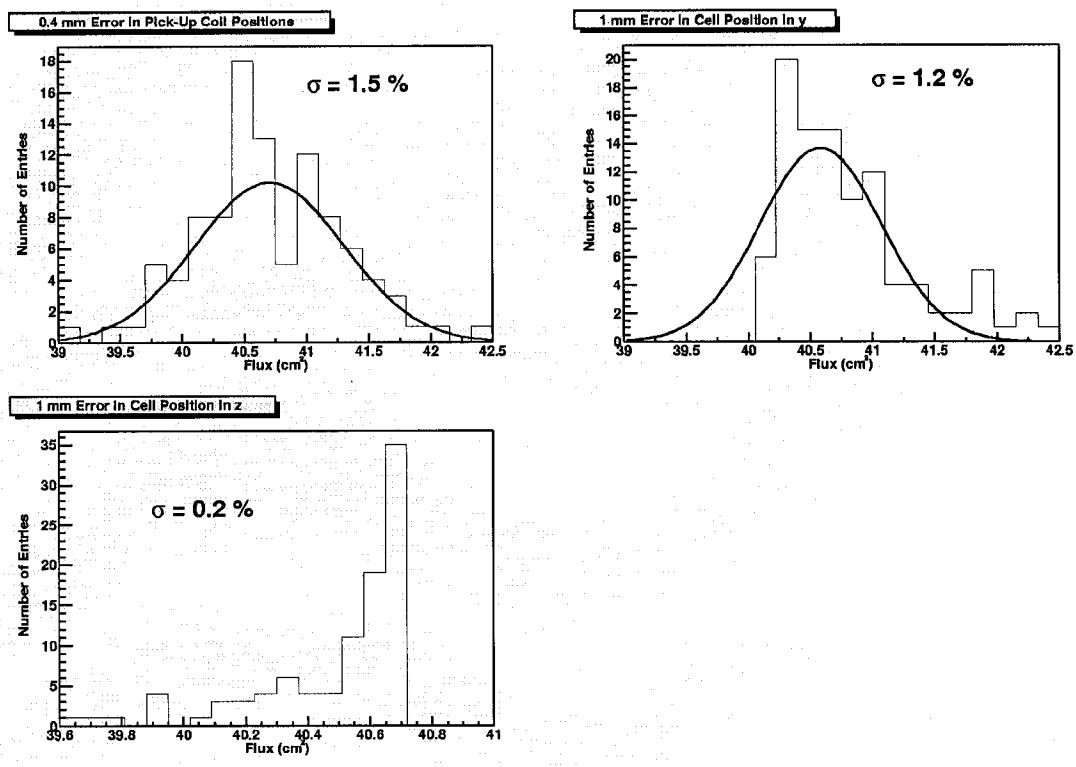

Figure 6.26: *Results of a simulation of the cell flux error due to mismeasurement of the pick-up coil positions.*

in our NMR measurement. The effect of mismeasurements on the total cell flux of a cell is shown in Fig. 6.26. These distributions were determined by running the flux calculation code 100 times while varying a set of parameters randomly within the error bars of the measurement. The uncertainties in measurements were chosen by looking at the distribution of measurement results (for instance the space between the top of the pick-up coils) repeated several times. The overall error in the flux due to mismeasurement is 2.0%.

A study was done to see how well the flux calculation used agreed with an absolute flux number. This was done by taking NMR measurements from a polarized ^{3}He cell with the pick-up coils in the same position, but moving the cell slowly upwards. Since the vertical motion on the target is done with a precision mechanical lifter it can be done very precisely. The goal was to change the flux and see if the

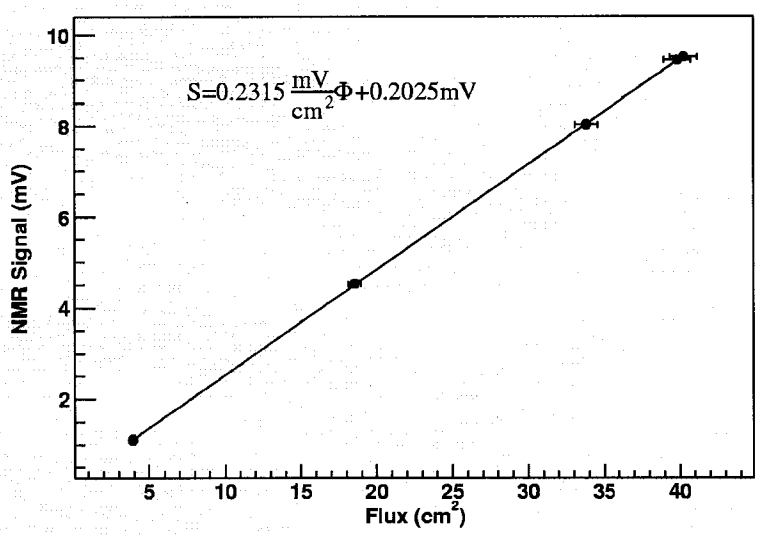

Figure 6.27: *A plot of the helium signal height vs. flux.*

model followed the expected trend. In this case, the ratio of flux to signal should be constant and when the signal is zero the flux should be zero. A plot of the data taken is shown in Fig. 6.27.

The signal is clearly linear, but the y-intercept is non-zero. The shift, while large at low flux, is about 2% of the flux at the place where the cell usually sits. The source of this shift is unknown, though there are a number of factors that could contribute to it. There could be a calculation error in the flux calculation code. Another reason could be that error bars on the low flux points are being underestimated. Using an absolute error of 0.85 cm^2 on all the data points allows the a line going through zero to be fit with a $\chi^2 = 1$. In both cases, an absolute shift affects the small flux data more than the high flux data. Therefore, an additional error of 1.3% of systematic error was added to the 2.0% of measurement error to the flux. This allows one to plot the points with a flux > 15 cm^2 with a line forced to go through zero and a $\chi^2 = 1$. This should be a reasonable estimate of the uncertainty due to this effect in these measurements.

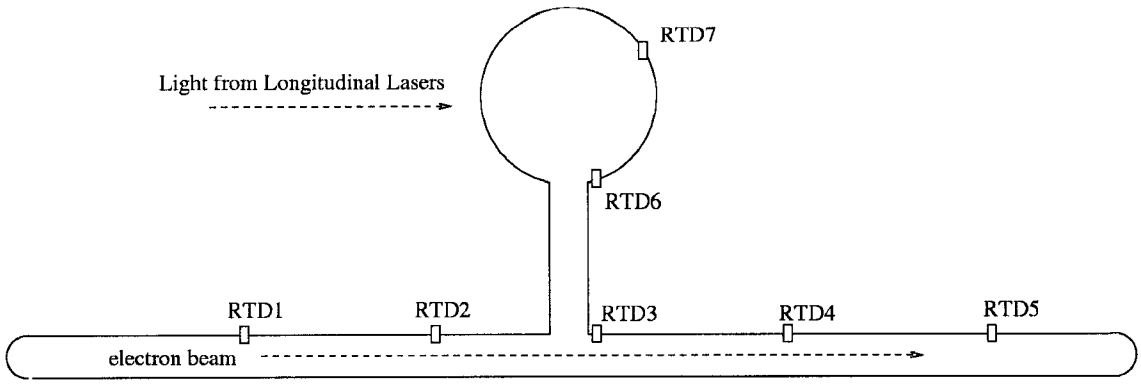

Figure 6.28: *The placement of the temperature sensors in E97-103.*

6.9.7 Measuring Cell Temperature and Density

Using the ideal gas law, the number density of the target chamber during an NMR measurement is determined by :

$$n_{tc} = n_0 \left[1 + \frac{V_{pc}}{V_{tot}} \left(\frac{T_{tc}}{T_{pc}} - 1\right)\right]^{-1} \tag{6.63}$$

where n_0 is the room temperature number density of the cell, V_{pc} is the internal volume of the cell pumping chamber, V_{tot} is the total internal volume of the cell, T_{tc} is the average target chamber temperature and T_{pc} is the average temperature of pumping chamber. Similarly, the number density of the pumping chamber can be calculated:

$$n_{pc} = n_0 \left[1 + \frac{V_{tc}}{V_{tot}} \left(\frac{T_{pc}}{T_{tc}} - 1\right)\right]^{-1} \tag{6.64}$$

where V_{tc} is the internal volume of the target chamber.

The cell temperature is measured with a series of high-temperature resistive temperature devices (RTDs) made by Omega. The RTD placement is shown in Fig. 6.28. The target chamber temperature, T_{tc}, was calculated by simply taking an average of RTDs 1-5. More sophisticated analysis yielded average temperatures within 1% of this temperature. This is because the temperatures were more or less the same along the target chamber. Normally, because the pumping chamber is at a much higher temperature, RTD3 is 20 °C higher than the RTD1 and RTD5. In

the case of E97-103, there were helium jets blowing on the ends of the cells (for protecting the cell from ruptures) and that made the thermal gradient smaller in the target chamber, where RTD3 $< 5.0°$ C different from RTD1 and RTD5.

The pumping chamber also has RTDs on it and plot of the temperatures during the experiment are listed in Fig. 6.29; however, these RTDs only reflect the interior temperature of the cell when the lasers are off. When the lasers on, there is a large thermal gradient between the inner part of the cell and the edge of the pumping chamber. To measure the average pumping chamber temperature, a separate measurement using the NMR system is made.

This measurement compares the NMR signal height when the lasers are on and when the lasers are off. The procedure is to take an NMR measurement and record the RTD temperatures with the lasers on and the temperature stable. Then the lasers are turned off and when the temperature stabilizes (about 15-20 minutes) take another NMR and record the RTD temperature. The lasers are then turned back on and when the temperature stabilizes (another 15-20 minutes) another NMR measurement is done and the RTD temperatures are recorded. The NMR signal height from the two NMR measurements done when the lasers are on are averaged as well as their temperatures. Then the following formula can be used to calculate the average pumping chamber temperature:

$$T_{\rm pc} = V_{\rm pc} T_{\rm tc}^{on} \left\{ \frac{S^{\rm off}}{S^{\rm on}} \frac{T_{\rm tc}^{\rm on}}{T_{\rm tc}^{\rm off}} \frac{T_{\rm coils}^{\rm off}}{T_{\rm coils}^{\rm on}} \left[V_{\rm tot} + V_{\rm pc} \left(\frac{T_{\rm tc}^{\rm on}}{T_{\rm pc}^{\rm off}} - 1 \right) \right] - V_{\rm tot} + V_{\rm pc} \right\}^{-1} \tag{6.65}$$

where $T_{\rm tc}^{\rm on}$ and $T_{\rm tc}^{\rm off}$ is the temperature of the target chamber when the lasers are on and off respectively, S^{on} and S^{off} is the height of the NMR signal with the lasers on and off respectively and T_{coils}^{on} and T_{coils}^{off} is the temperature of the part of the target chamber between the pick-up coils. T_{coils} can be calculated by:

$$T_{\rm coils} = \frac{1}{2} \left[T_3 + \frac{1}{2} (T_2 + T_4) \right] \tag{6.66}$$

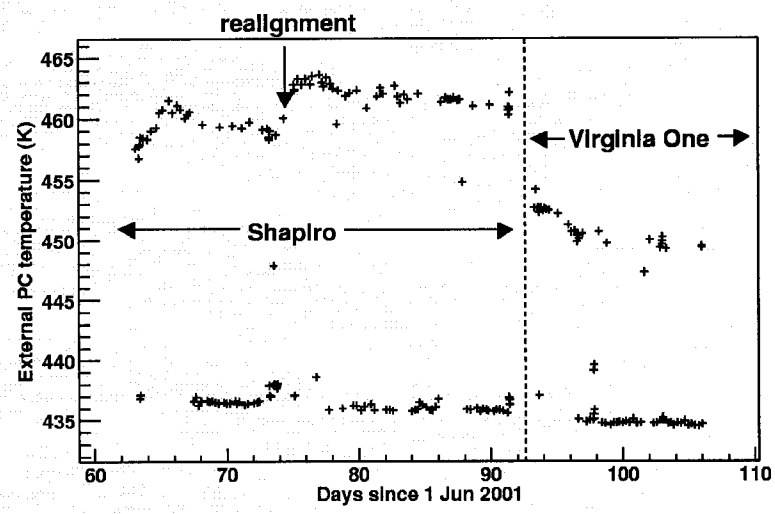

Figure 6.29: *The external pumping chamber temperatures during NMR measurements in E97-103.*

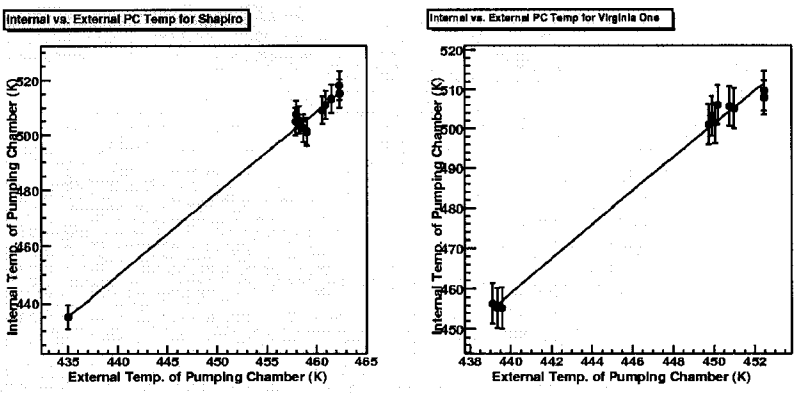

Figure 6.30: *The relationship between the average reading of RTD6 and RTD7 and the average internal temperature of the pumping chamber.*

where T_2, T_3 and T_4 are the temperatures from RTD 3, 4 and 5 respectively.

Once this measurement has been done several times, the pumping chamber internal temperature (T_{pc}) versus the pumping chamber external temperature (as measured by the RTDs) can be plotted, as it has been in Fig. 6.30. The measurements have been separated for the two cells as the exterior RTDs had different placement and different levels of thermal contact with the cell. This data is from specific temperature measurements. To calculate T_{pc} for a specific NMR measurement the values of RTD6 and RTD7 and a fit to this data were used to calculate the internal pumping chamber density. The calibrations used are:

$$T_{pc}^{Shapiro} = 1.464(T_6 + T_7) - 838.7 \quad (6.67)$$

$$T_{pc}^{VirginiaOne} = 2.111(T_6 + T_7) - 1398.3 \quad (6.68)$$

where T_6 and T_7 are the temperatures from RTD 6 and RTD 7. The uncertainty in these measurements was estimated to be 8°C.

Its useful to know the average density when running taking production data. The average target chamber density of Shapiro with the three lasers on was 10.72 Amagats. The average target chamber density of Virginia One with three lasers on was 10.01 Amagats.

6.9.8 The Gain of the Pick-Up Coils

The gain of the pick-up coils is monitored throughout the experiment. This is done by a small coil of wire, known as the Q-coil, that is glued to the side of the target chamber with the magnetic field of the Q-coil pointing at the pick-up coils. The Q-Coil is connected directly to the RF function generator as shown in Fig. 6.23. The coil is run slowly through a series of frequencies from 65 kHz to 300 kHz at a constant amplitude. This measures the relative pick-up coil response as a function of frequency.

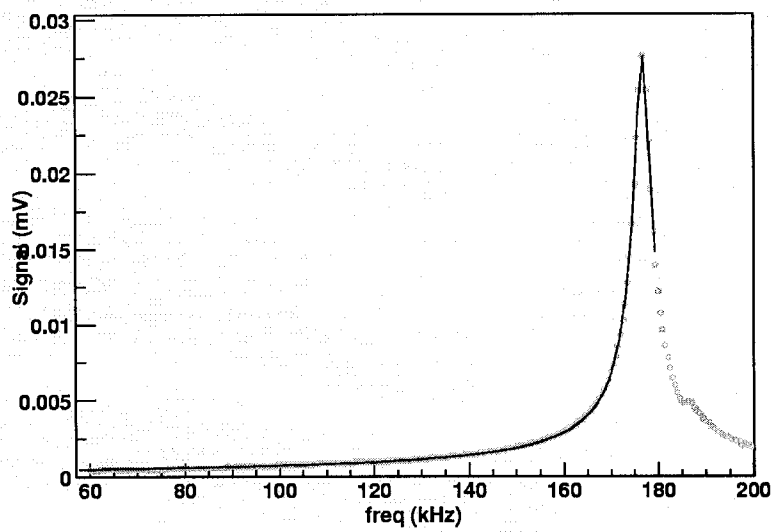

Figure 6.31: *An example of a resonance curve created by the Q-coil.*

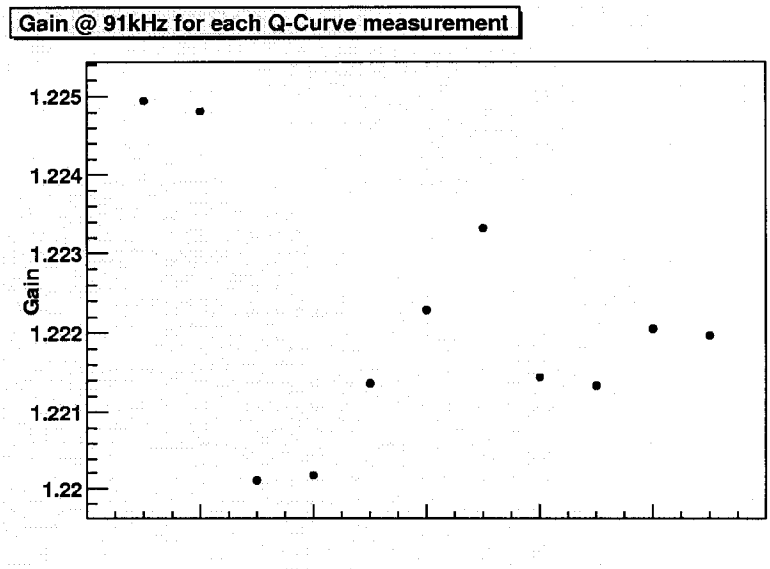

Figure 6.32: *Measurementss of the gain of the pick-up coils throughout the experiment.*

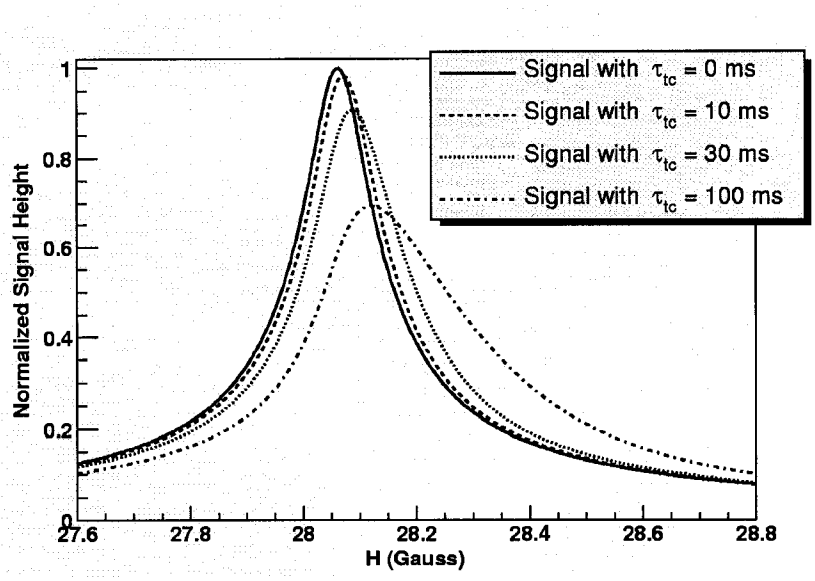

Figure 6.33: *The effect of the lock-in amplifier time constant on a normalized NMR signal with an H_1 of 58 mG.*

The data from this measurement can be fit with [71]:

$$V(f) = \frac{kf}{\sqrt{\frac{1}{Q^2}\frac{f^2}{f_0^2} + \left(\frac{f^2}{f_0^2} - 1\right)^2}} + c \tag{6.69}$$

where $V(f)$ is the voltage output of the pick-up coils, f is the frequency of the Q-Coil and k, Q, f_0 and c are fitted parameters. The relative gain can be extracted for any frequency once these parameters are known:

$$G(f) = \frac{1}{\sqrt{\frac{1}{Q^2}\frac{f^2}{f_0^2} + \left(\frac{f^2}{f_0^2} - 1\right)^2}} \tag{6.70}$$

where $G(f)$ is the relative gain of the circuit. The gain for the frequency 91 kHz is presented in Fig. 6.32. There is a less than 0.3% variation in gain throughout the experiment.

6.9.9 Modifications to the NMR signal shape

There are two important modifications to the NMR signal shape. The first is the time constant from the lock-in amplifier that reads in the voltage from the pick-up coils. The time constant tells the lock-in how long to integrate the data before

outputting a value. Increasing the time constant suppresses noise, but distorts the signal. Fortunately, the signal distortion is predictable. The differential equation representing the effect of the lock-in time constant on the NMR signal is [72]:

$$\frac{dS_{\text{lock-in}}(t)}{dt} = \frac{1}{\tau_{\text{tc}}}(S_{\text{raw}}(t) - S_{\text{lock-in}}(t)) \tag{6.71}$$

with initial condition:

$$\frac{dS_{\text{lock-in}}(0)}{dt} = 0.0 \tag{6.72}$$

where $S_{\text{lock-in}}$ is the signal in the lock-in, S_{raw} is the raw signal out of the pick-up coils and τ_{tc} is the lock-in time constant. The lock-in time constant used for this experiment was 30 ms. It was chosen to reduce noise in the water signal, but not to be so large as to distort the signal significantly. The effect of the lock-in time constant on the shape of an NMR signal is illustrated in Fig. 6.33.

The second source of distortion is from holding field gradients. The gradients distort the signal because different parts of the cell will resonate at different times with the result being a broadening of the signal. These became especially critical for analyzing the helium signal for Virginia One since its data was taken with a set of coils intentionally causing a gradient. (These coils were used to stop the masing effect described later). The signal can be modeled numerically using the formula:

$$S_{\text{corr}}(H) = \frac{1}{L\Phi_{\text{tot}}} \sum_{i=0}^{N} \Phi(i\Delta z - L/2)\Delta z S_{\text{tc}}\left(H + \frac{dB_z}{dz}(i\Delta z - L/2)\right) \tag{6.73}$$

where S_{corr} is the corrected signal, L is the length of the cell, Φ_{tot} is the total flux from the target chamber, N is the number of divisions of the target chamber in the calculation, Δz is L/N, $\Phi(z)$ is the amount of flux for a section Δz of the target chamber, $S_{\text{tc}}(H)$ is the NMR signal corrected for the lock-in time constant and dB_z/dz is the field gradient along the target chamber axis. $\Phi(z)$ was calculated with the flux code and is shown in Fig. 6.34.

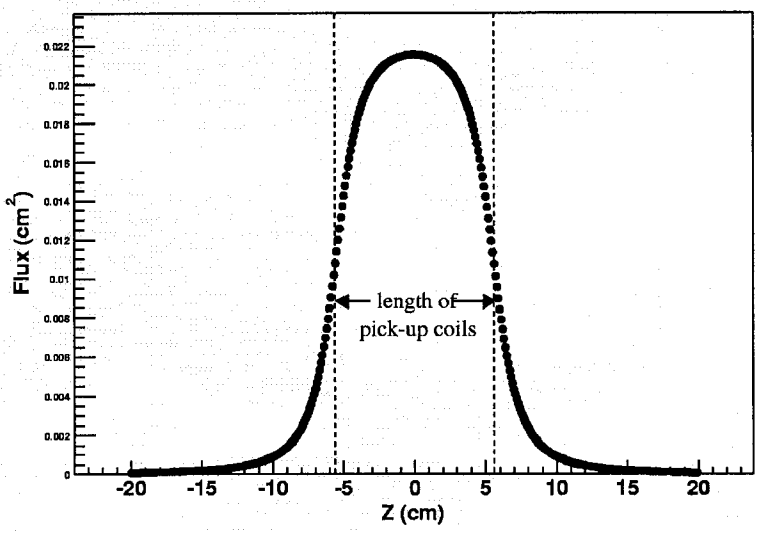

Figure 6.34: *The amount of calculated flux from a section of target chamber as a function of z.*

The procedure for creating a model of the signal shape for NMR in E97-103 was to first numerically integrate Eq. 6.71 with a S_{raw} from Eq. 6.56 using a 4th order Runge-Kutta from *Numerical Recipes in C* [73]. The signal is broken into sections along H and the mean value of the signal for the section is placed in an array. Then the signal is summed by using the elements of the array. Examples of signals with gradients are shown in Fig. 6.35.

The models of the signal shape are used to calculate correction factors to the signal. While the model works well for the lock-in time constant and for smaller gradients, it doesn't work especially well for signals taken under high gradients. High gradient fields only occurred when a set of coils, known as gradient coils, were used to intentionally create gradients to break up the masing effect. No gradient coils were used during Shapiro's running period, but the gradient coils were used throughout Virginia One's running period.

The gradient coils were placed parallel to both sets of Helmholtz coils. The set on the small coils (along the longitudinal direction) were twenty windings of

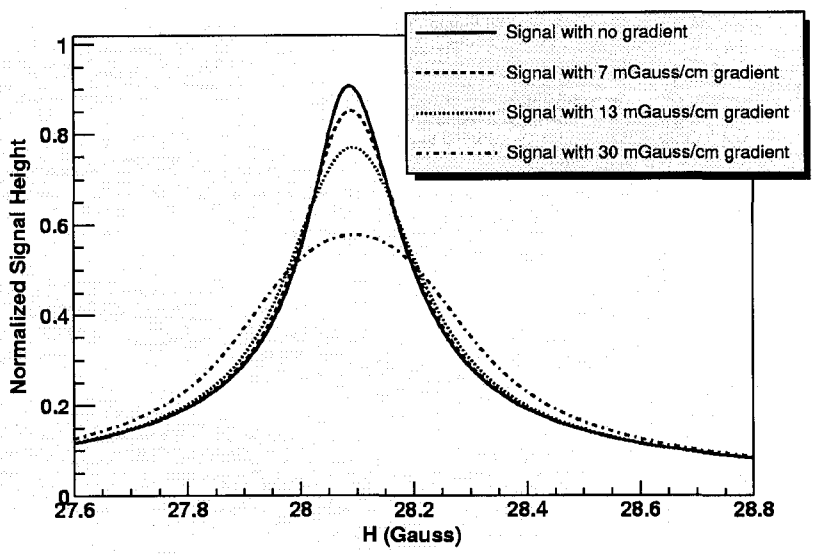

Figure 6.35: *Examples of different sizes of gradients on the ^{3}He NMR signal.*

18 gauge wire. The set on the large coils (along the transverse direction) were 10 windings of 10 gauge wire. They were powered by a power supply that could deliver a maximum of 7 A of current. Virginia One used them with 2 A on the longitudinal gradient coils and 7 A on the transverse gradient coils. The correction to the NMR signal from these gradient coils were measured empirically. After the experiment was finished a study was done to compare the NMR signal with and without the gradient coils. To do this a NMR signal was taken with no cuurent in the gradient coils. The gradient coil was turned up to a certain cuurent. Another NMR was taken. The gradient coil was turned off again and another NMR was taken. This was done for the entire range of currents for both the longitudinal and transverse gradient coils.

All the signals in this study were fit with Eq. 6.56. The ratio of the heights of the signal when the gradient coils were on to the average heights of the two signals around it that had the gradient coils off are plotted in Fig. 6.36 and Fig. 6.37. The transverse gradient coils had almost no effect on the NMR signal. A comparison of the shape used to fit the signal compared to the shape from a model is shown in

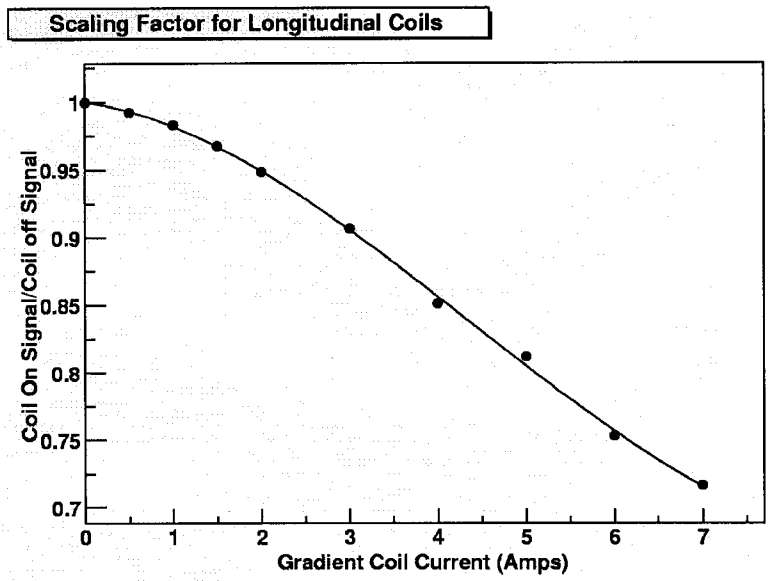

Figure 6.36: *The effect on NMR signal height of the longitudinal gradient coil.*

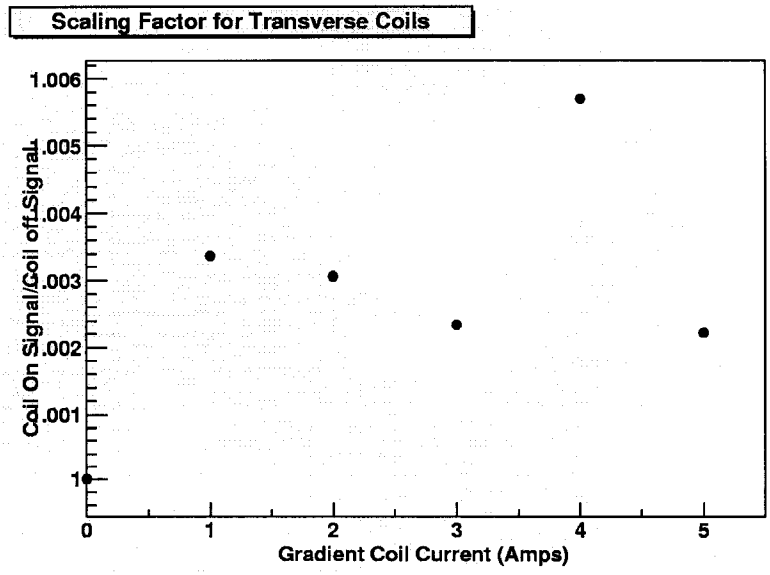

Figure 6.37: *The effect on NMR signal height of the transverse gradient coil.*

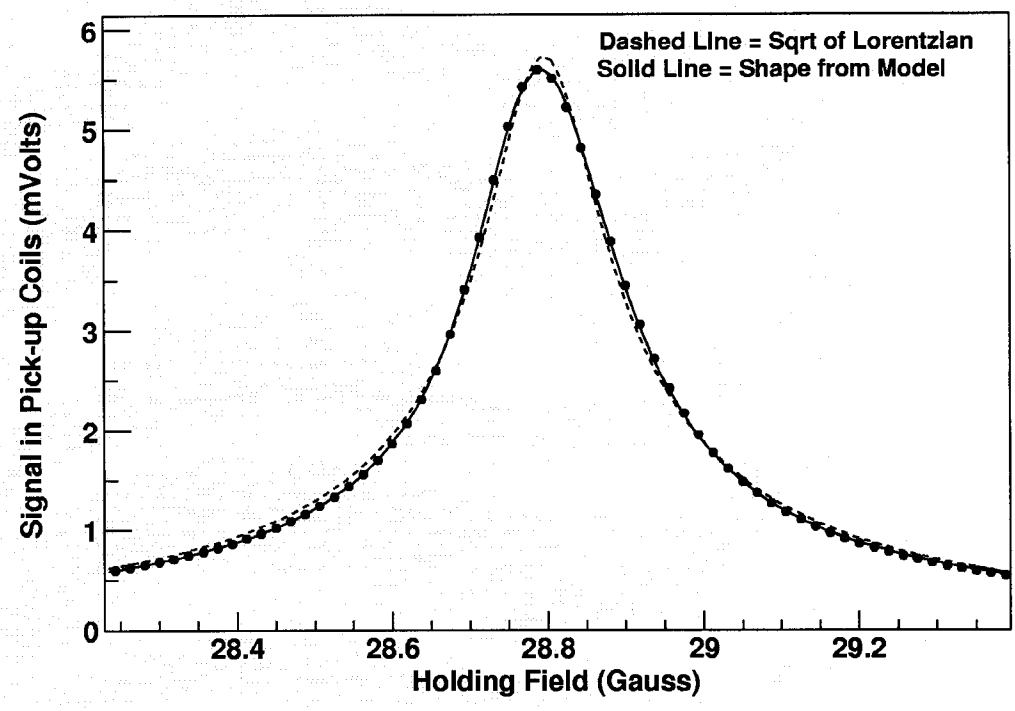

Figure 6.38: *NMR data fit two different ways : a square root of a Lorentzian and one with a shape corrected for time-constant effect and holding field gradients.*

Fig. 6.38.

6.9.10 Polarization Loss due to AFP Measurements

Small polarization losses are inevitable during AFP measurements. The AFP loss is measured by simply taking several NMR measurements back-to-back. Usually, a time span of 3-5 minutes between measurements is used, though this may not be necessary. The average loss per measurement is calculated assuming no other source of polarization loss occurs during the data taking. The polarization loss for a cell with no gradient coils on is shown in Fig. 6.39. The polarization loss for Shapiro was $\approx 0.5\%$ per NMR measurement. The polarization loss for Virginia One was about $\approx 1.0\%$ per NMR measurement due to the increase in AFP loss due to the gradient coils. The loss fraction can vary by 30% depending on the amount of polarization.

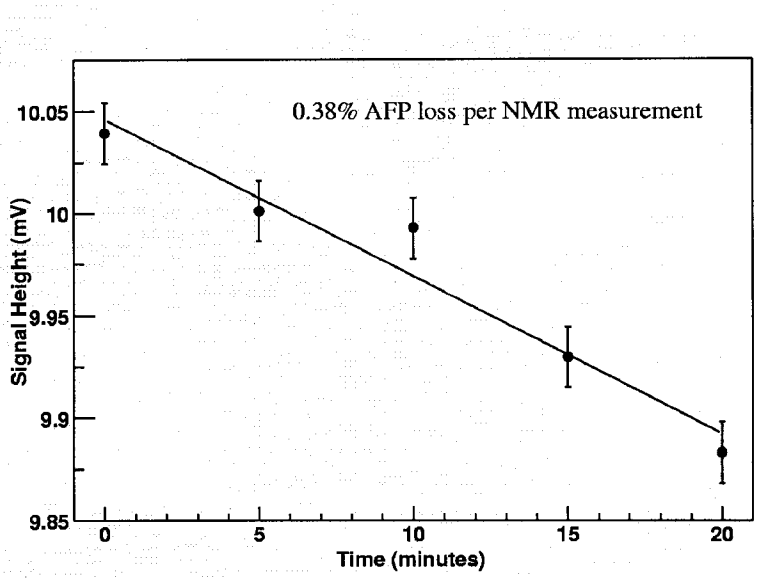

Figure 6.39: *A plot of the effects of polarization loss due to AFP during NMR.*

6.9.11 Analysis of the NMR Signals from Water Cells

As stated previously, the polarizations of the ^{3}He cells are calibrated with the NMR signal from water. Unfortunately, the water signals are quite small (10000 times smaller than a typical helium signal) and are taken in a noisy environment. However, since the polarization doesn't change from sweep to sweep, the measurements can be taken thousands of times and averaged. Another complication of the water signal is that the relaxation times of water, T_1 and T_2, are on the order of the sweep time for an NMR measurement. This results in a slightly more complicated signal shape than the signals from the polarized ^{3}He cells. This signal shape is plotted from a model in Fig. 6.40.

In E97-103 there were 4 water calibrations done with a 40 cm water cell. The number of sweeps used and signal height of these calibrations are shown in Table 6.14. The holding field for the water calibration is swept from 18 Gauss to 25 Gauss rather than when the 25 Gauss to 32 Gauss used for the polarized ^{3}He signal. This is to be able to use the same frequency for the RF coils, since the gyro-magnetic ratios are different for ^{3}He and water. There is also a 5.833 s hold when the field

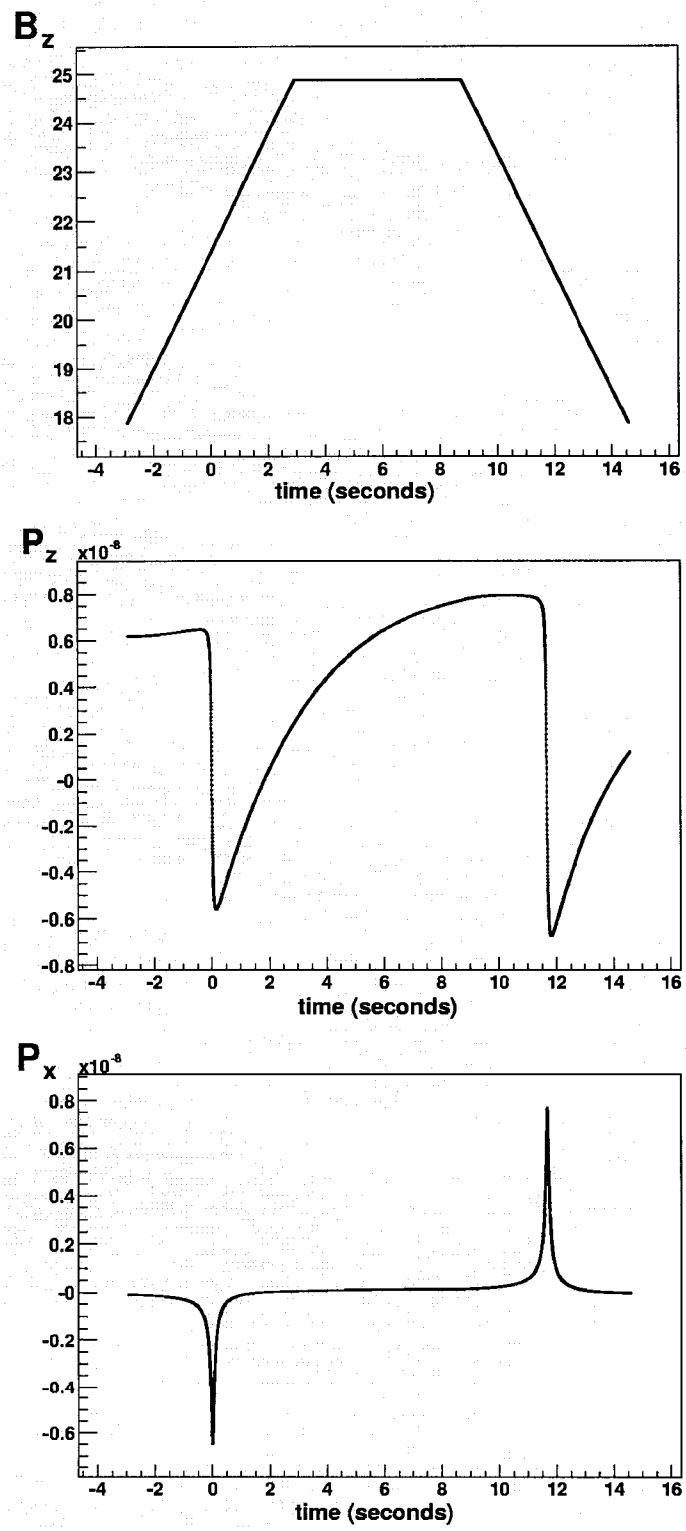

Figure 6.40: *The magnetic field and the z and x component of the polarization from a water cell undergoing AFP. These plots were made from a model of the water signal.*

Date	Num. Sweeps	Up Sig. (μ V)	Down Sig. (μ V)	Flux (cm^2)
1 Aug	350	9.24±0.35	11.11±0.30	46.69
31 Aug	966	9.38±0.28	9.78±0.53	46.73
1 Sep	600	8.76±0.41	11.19±0.45	46.73
17 Sep	600	9.53±0.30	10.01±0.56	46.97

Table 6.14: *The date, signal heights, the number of sweeps and the flux for each water calibration.*

reaches 25 G to wait for the water sample to relax. Because the water polarization is proportional to the holding field, the resonance when the field is being swept down will be larger than the field is being swept up because the starting field is larger.

As with the polarized ^{3}He NMR, the data files created by the LabVIEW software that runs the water calibrations separates the water into four files : X Up, Y Up, X Down and Y Down. The "Up" and "Down" refer to whether the field was being increased or decreased through resonance. The "X" and "Y" refer to the X channel and Y channel in the lock-in amplifier. The X channel is generally locked on the signal, but sometimes the phase isn't set correctly so there is some signal in the Y channel. These can be easily combined by averaging and fitting each channel separately then combining the signal heights with $S = \sqrt{X^2 + Y^2}$.

Because so many sweeps are averaged together, one has to worry about magnetic field drift in the signals. Since the magnetic field is not recorded during the water calibrations and the voltage of the power supply drifts a little bit, the resonance of the water signal will not appear at the same H for every sweep. This can be corrected by recording the currents and using the current-magnetic field calibrations shown earlier to correct each sweep.

Once the sweeps are field corrected, a calculation is made to determine the amount of noise in each sweep. This is done by fitting a line to each sweep and measuring the standard deviation of the data points around this line. The value produced by this process can then be put into a histogram as shown in Fig. 6.41.

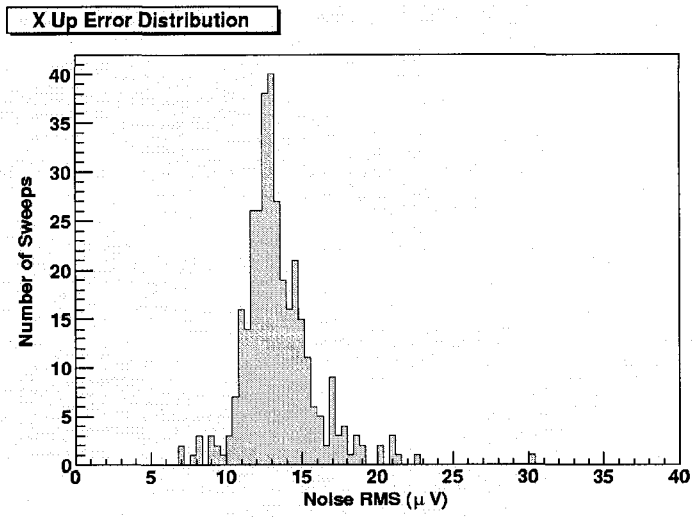

Figure 6.41: *Distribution of noise levels in the X channel of the lock-in amplifier for each sweep of a water calibration.*

Exceptionally noisy sweeps can then be cut by cutting all the sweeps above a certain RMS level. In the case of this water analysis, no cuts were made for particularly noisy sweeps.

The sweeps are then averaged for all four files. The shape of the signal can be derived from Eq. 6.53. This set of equations can be approximated by [70]:

$$P_{\text{eff}} = k\sqrt{P_x^2 + P_y^2 + P_z^2} \tag{6.74}$$

where $k = \pm 1$ and P_{eff} is the polarization in the direction of the effective field. This can only be done if $T_1 = T_2$ which is approximately the case ($T_1 = 3.0$ s, $T_2 = 2.7$ s [70]). With this approximation the solution to the differential equations in Eq. 6.53 can be written:

$$P_{\text{eff}} = e^{-(t-t_i)/T_1}\left[P_{eq}(t_i) + \frac{1}{T_1}\int_{t_i}^{t} e^{(u-t_i)/T_1} P_{eq}(u)du\right] \tag{6.75}$$

where t_i is the starting time of the sweep and

$$P_{eq} = \chi\frac{H_1^2 + \alpha t(H_0 + \alpha t)}{\sqrt{H_1^2 + \alpha^2 t^2}} \tag{6.76}$$

where α is the sweep rate. The term $e^{(u-t_i)/T_1}$ in the integral can be expanded and

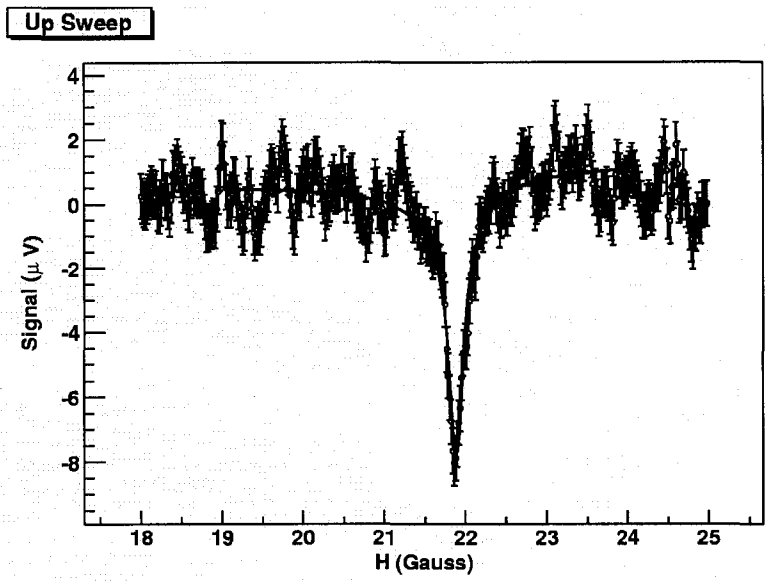

Figure 6.42: *A fit of the Up sweep in the X channel of the 1 Aug 2001 water calibration.*

Parameter	Value	Uncertainty	Source
$P_w C_\nabla C_\tau$	5.510×10^{-9} (Up), 6.611×10^{-9} (Down)	1.7 %	Model of Bloch Eq.
μ_p/μ^3He	1.313	neg.	[57]
G_p^w	200	0.5 %	Gain Measurements
Φ_{tot}	46.69-46.97 cm^2	2.3%(stat.)$\pm$1.0%(sys.)	Table 6.14
n_p	2482 Amagats	0.1 %	[57]

Table 6.15: *List of parameters used to calculate c'_w.*

only the first few terms kept, so that the final form of $P_{\text{eff}}(t)$ is analytical. This function is used to fit the water signals as shown in Fig. 6.42.

After fitting the functions, the quantity c'_w from these fits can be plotted, where c'_w is defined as:

$$c'_w = \left(\frac{P_w}{h_w}\right)\left(\frac{\mu_p n_p \Phi_{tot} G_p^w C_\nabla^w C_\tau^w}{\mu_{^3He}}\right). \tag{6.77}$$

The average of c'_w is plotted in Fig. 6.43. The values used for the parameters in Eq. 6.77 are listed in Table 6.15.

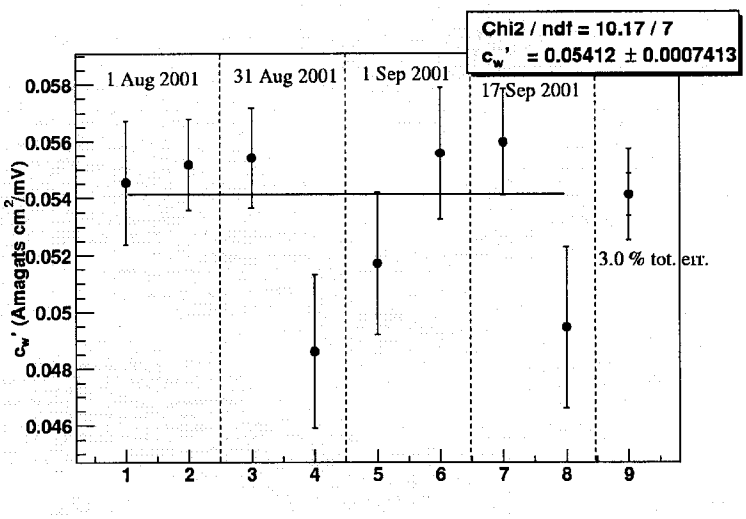

Figure 6.43: *Average of the 4 water calibrations done in E97-103.*

6.9.12 EPR polarimetry

The second polarimetry system on the polarized ^{3}He target measures the shift of the electron paramagnetic resonance (EPR) in the rubidium electron states when the polarization direction of the polarized ^{3}He nuclei is reversed. Specifically, what is being measured is the width of the Zeeman splitting between electron state $F = 3, m = -3$ to $F = 3, m = -2$ in Fig. 6.4. The width of this splitting depends on the total magnetic field. The total magnetic field is the sum of the holding field plus a much smaller contribution from the polarized ^{3}He nuclei. Changing the direction of polarization of the nuclei will also change the width of the Zeeman splitting.

The width of Zeeman splitting is measured by measuring the frequency at which electrons in the $F = 3, m = -3$ state can absorb photons and be transfered to the $F = 3, m = -2$ state. This is done with a excitation coil near the pumping chamber of the target cell. The frequency of excitation is quite high $\approx$ 11.6 MHz. However, the transition is quite narrow so it can be measured precisely.

Of course, one needs to know when the electron is making this electron state transition. The technique for doing this takes advantage of the method of optical polarization of rubidium. When the electron makes the transition from $F = 3, m = -3$

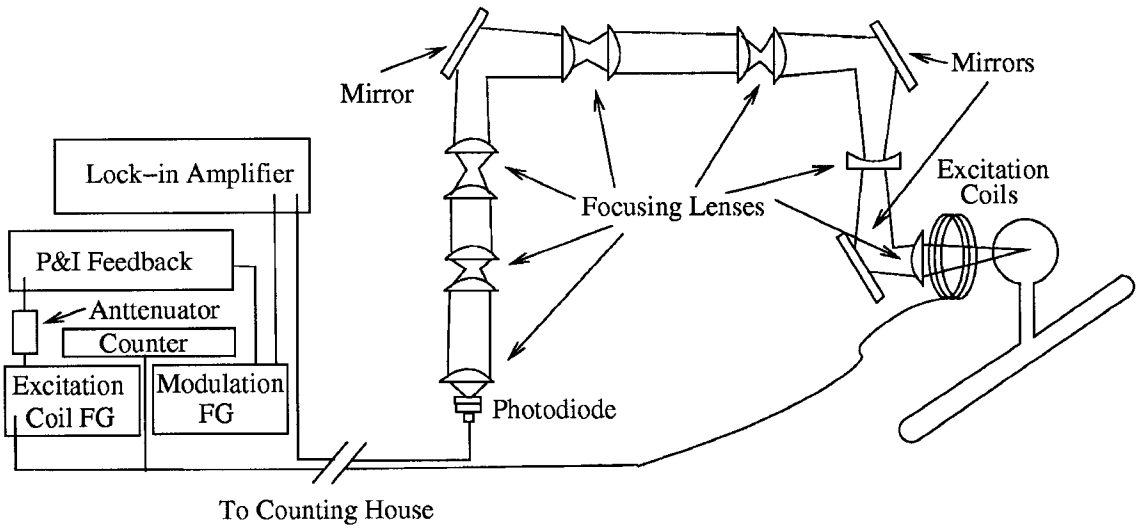

Figure 6.44: *The equipment setup for EPR polarimetry.*

to $F = 3, m = -2$, it can then absorb circularly polarized laser light and be excited to the ^5P state. Electrons in the $F = 3, m = -3$ cannot be excited by circularly polarized light. Therefore, when electrons are successfully making this transition there will be an immediate increase in outgoing photons from electrons dropping from the ^5P to ^5S state, as these excited electrons decay. Because of collisional mixing, which results in electron state transition due to rubidium-rubidium collisions, there will be an increased amount of photons at a range of frequencies. The two photon frequencies that indicate the resonance most strongly are the D1 (795 nm) and the D2 (785 nm) transitions. For EPR polarimetry, the D2 resonance is the one detected since the D1 resonance is lost in the huge intensity of laser light at 795 nm.

The setup for EPR polarimetry is shown in Fig. 6.44. The normal procedure for performing a measurement is to set the excitation function generator (Wavetek 80) to the frequency where the EPR transition is expected. This will power the excitation loops near the pumping chamber. The frequency to the excitation loops is modulated by another function generator (SRS DS345) at 200 Hz. This helps to separate the signal being caused by the excitation coils from background. The frequency from the excitation coil function generator is monitored precisely by an

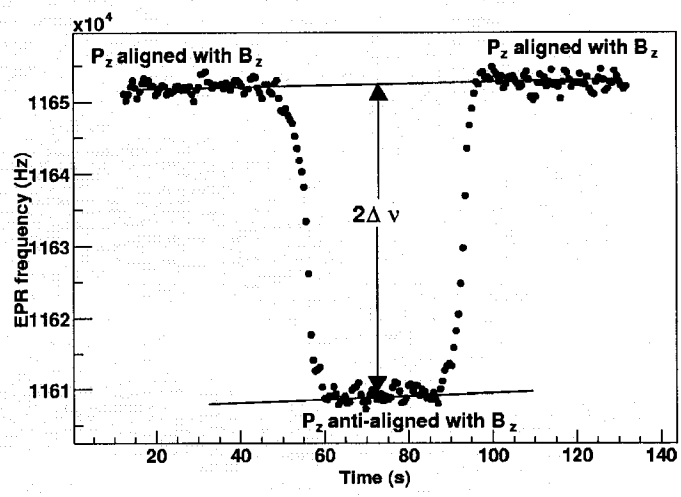

Figure 6.45: *The EPR resonance plotted vs. time during AFP.*

electronic counter (SRS SR620).

Light from the pumping chamber of the cell is focused through a series of lenses to a photodiode which produces a signal which is proportional to the intensity of light that it absorbs. In principle, the lenses are unnecessary and the photodiode can be place directly next to the pumping chamber; however, the target area is a high-radiation environment when the electron beam is on and radiation damages the photodiodes. Therefore, a series of lenses is necessary to keep the photodiode working.

The photodiode signal is directed to a lock-in amplifier which is locked into a frequency of 200 Hz. When the excitation loop is not at the right frequency for the EPR transition to occur there is no signal in the lock-in amplifier. When the frequency is found there will be a small signal. However, when the polarization of the ^{3}He nuclei is reversed the frequency of this signal will move rapidly. Therefore, a set of electronics is used to lock-into the EPR signal and adjust the frequency of the excitation coil function generator so that it is always exciting the EPR transition. This set of electronics is known as the P&I feedback box. Further details about the electronics set-up can be found in [41] and [57].

Once the signal is locked on by the P&I feedback system the polarization of the ^{3}He is reversed using AFP. Unlike NMR where the holding field was ramped through resonance, the holding field is held constant and the RF coil frequency is ramped through resonance. This is because the resonance is very sensitive to the magnitude of the holding field, but not sensitive at all to the RF field. Once the polarization is reversed, the new EPR frequency is recorded for a period of 20-30s. Then the polarization is flipped back to the original orientation. An example of this process is shown in Fig. 6.45.

The frequency difference ($2\Delta\nu$) is proportional to the polarization as shown here:

$$2\Delta\nu = \frac{4\mu_0}{3}\frac{d\nu_{\mathrm{EPR}}}{dB}\kappa\mu_{^3He}n_{\mathrm{pc}}P_{^3\mathrm{He}} \tag{6.78}$$

where $\mu_{^3He}$ is the magnetic moment of ^{3}He, n_{pc} is the number density of the pumping chamber, $P_{^3\mathrm{He}}$ is the polarization of the ^{3}He in the pumping chamber and the derivative $d\nu_{\mathrm{EPR}}/dB$ and the κ are constants from atomic physics experiments. Detailed analysis of $d\nu_{\mathrm{EPR}}/dB$ and κ can be found in [57] and [41].

6.9.13 Combining Data from EPR and NMR

For E97-103, every time a polarimetry measurement was needed, usually every 4-6 hours, both an NMR and EPR measurement was done. The results from these calibrations are shown in Fig. 6.46.

The method of combining these two set of data was to use the EPR measurements as a constant calibration of the NMR measurements. This was done because the NMR signal can be measured much more precisely (0.5% for each measurement) than the EPR signal (1-4% for each measurement). However, the EPR measurements give an absolute value for the polarization whereas the NMR measurements need to be calibrated. There is a value for the calibration from the water signal, but it can be improved by including information from the EPR signal.

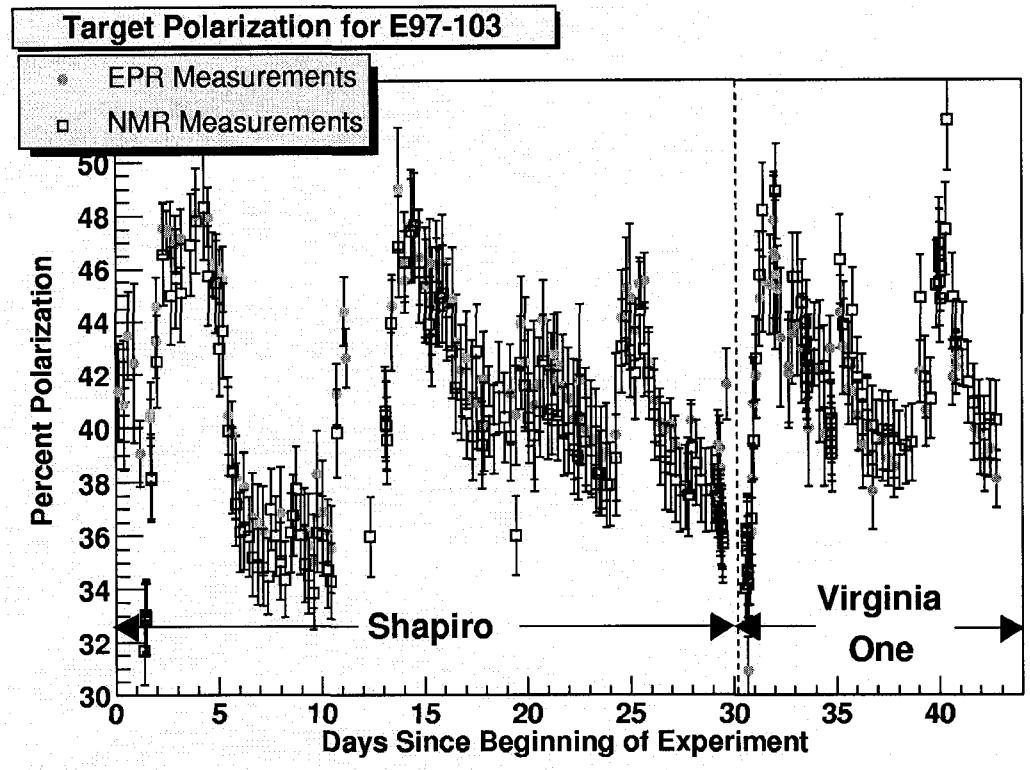

Figure 6.46: *The NMR and EPR polarimetry measurements in E97-103.*

Cell	Constant (Amagats cm^2/mV)	Uncertainty (Amagats cm^2/mV)
Shapiro	0.05220	0.00155
Virginia One	0.05602	0.00168
Average	0.05400	0.00157

Table 6.16: *EPR calibration constants for NMR.*

Parameter	Error	Note
$S_{\rm NMR}/P_{\rm EPR}$	0.6%	Statistical Error
$S_{\rm NMR}/P_{\rm EPR}$	1.5%	Systematic Error
n	1.0%	Systematic Error
Φ	2.4%	Systematic Error

Table 6.17: *List of errors associated with NMR calibration from EPR.*

Calibration Method	Constant	Uncertainty
Water NMR	0.05412	0.00161
EPR	0.05400	0.00157
Average	0.05406	0.00112

Table 6.18: *Calibration Constants for NMR signals. Values in Amagats cm^2/mV*

To extract an NMR calibration from EPR signal one can calculate the EPR calibration constant $c'_{\rm EPR}$ for each pair of NMR-EPR measurements:

$$c'_{\rm EPR} = \frac{S_{\rm NMR}}{P_{\rm EPR}(n_{\rm pc}\Phi_{\rm pc} + n_{\rm tc}\Phi_{\rm tc} + n_{\rm tt}\Phi_{\rm tt})C_\nabla C_\tau} \tag{6.79}$$

where $S_{\rm NMR}$ is the NMR signal from polarized ^{3}He, $P_{\rm EPR}$ is the polarization extracted from the EPR measurement, $n_{\rm pc}$, $n_{\rm tc}$ and $n_{\rm tt}$ are the densities of the various chambers, $\Phi_{\rm pc}$, $\Phi_{\rm tc}$ and $\Phi_{\rm tt}$ are the fluxes from the various parts of the cell, and C_∇ and C_τ are the NMR signal correction factors from the gradient and lock-in time constant. c'_{EPR} is a constant for all NMR measurements and can be compared directly to c'_w from the water calibration. The average values of c'_{EPR} for E97-103 is presented in Table 6.16. The errors associated with $c'_{\rm EPR}$ are presented in Table 6.17.

The two calibration constants and their weighted average are shown in Table 6.18 . A list of systematic errors that go into every polarization value is shown in Table 6.19. The polarizations using this method are assigned to each data-taking run using a linear interpolation between polarimetry measurements.

Description	Parameter	Uncertainty
Calibration Constant	c'	2.1 %
NMR Signal Height	S_{NMR}	0.5 %
Flux (all chambers)	Φ	2.4 %
Density	n	1.0 %
Corrections	$C_{\nabla}C_{\tau}G_p$	1.0 %
Total	P_{NMR}	3.7%

Table 6.19: *List of systematic errors in the polarization measurements in E97-103.*

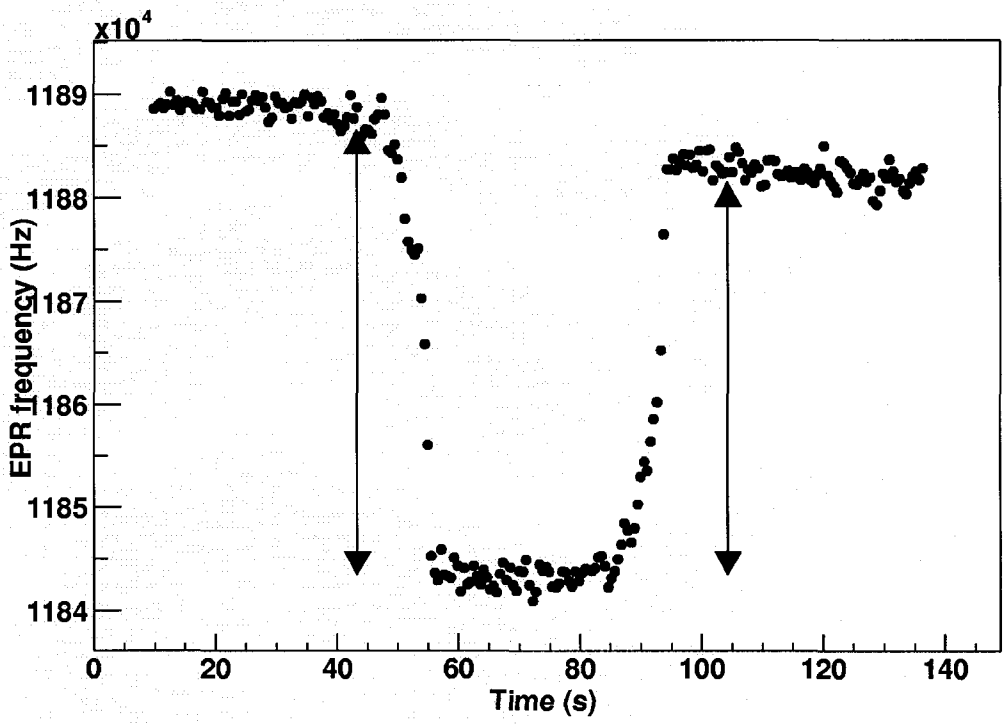

Figure 6.47: *An example of masing occurring during an EPR measurement.*

6.10 The Masing Phenomena

A phenomenon associated with the polarized ^{3}He target, often referred to as "masing", has two characteristics: a sudden loss of polarization during AFP and a polarization threshold where this masing phenomena is not seen [57]. The results of masing can be seen in Fig. 6.47. In this figure, the first value of $2\Delta\nu$ from the first magnetization reversal shows a high polarization, but when the magnetization is in the reversed state it begins to lose polarization until the magnetization is flipped again. This behavoir continues until the system reaches a certain polarization at which this masing behavior stops.

The source of this phenomena has been linked to the resonance frequency of the pick-up coils [57]. In the case of E97-103, the resonance frequency is 180 kHz where the RF coil frequency is 91 kHz. The pick-up coil placement and configuration was the same for both cells. However, Virginia One showed strong masing at high polarization, whereas Shapiro showed none. It is unknown why one cell would show this phenomena and not the other. It has been speculated that the rubidium inside the pumping chamber plays a part in this phenomena. The amount of rubidium in Shapiro and Virginia One were about the same.

In the case of Virginia One, the gradient coils were turned on for the duration of its use. The higher gradients suppress the masing effect, by causing a wider distribution of AFP resonances, and allow the cell to get to high polarizations, at the cost of higher AFP losses. Masing has been an ongoing problem with this system and requires further study.

6.11 Reference Cell

In addition to the polarized ^{3}He cells, the Jefferson Lab target also provides for electron scattering from a carbon foil target and a reference cell target that can be filled with nitrogen, ^{4}He or ^{3}He. These targets, plus the polarized ^{3}He target, are

included on the same target ladder, which can be moved in and out of the beam by a vertical lifter.

The carbon foil target has a series of five thin carbon graphite foils that are used for spectrometer optics studies and measurements of false asymmetries. The reference cell is used to measure the yield ratio of nitrogen to ^{3}He for the dilution factor. The reference cell is connected to a series of pumps and valves that allow gas to be pumped in and out of the cell remotely. Unfortunately, the reference cell system leaked throughout the experiment and approximations had to be made for the actual pressure in the cell.

CHAPTER 7

The Hall A Spectrometers and Detector Package

7.1 Spectrometer Magnets

Hall A is equipped with two high-resolution spectrometers (known as the left and right spectrometers) which are nearly identical in design. The spectrometers transport charged particles covering a narrow range in scattering angle and momentum into a detector package. The use of these spectrometers minimizes background and allows precise cross-section measurements. The spectrometers can be positioned around the target at angles from 12.5° to 130° (the left spectrometer can go to 150°). For E97-103, the spectrometers were set at symmetrical angles and used as independent single-arm detectors to double the rate of data taking of scattered electrons.

Each spectrometer has four magnets, as shown in Fig. 7.1. The first two magnets are superconducting quadrupole magnets that focus the scattered electrons before the entrance of the dipole magnet. The first quadrupole, Q1, focuses the electrons vertically at the focal plane and the second quadrupole, Q2, focuses the electrons horizontally at the focal plane [74]. The third magnet is a superconducting dipole which bends the electrons 45° vertically. The current setting in the dipole magnet determines the momentum of the electrons which make it into the detector package. The fourth magnet is another superconducting quadrupole magnet which does additional horizontal focusing at the focal plane. The characteristics of the spectrometers are given in Table 7.1 [74].

The spectrometers also have a tungsten collimator which can be inserted before

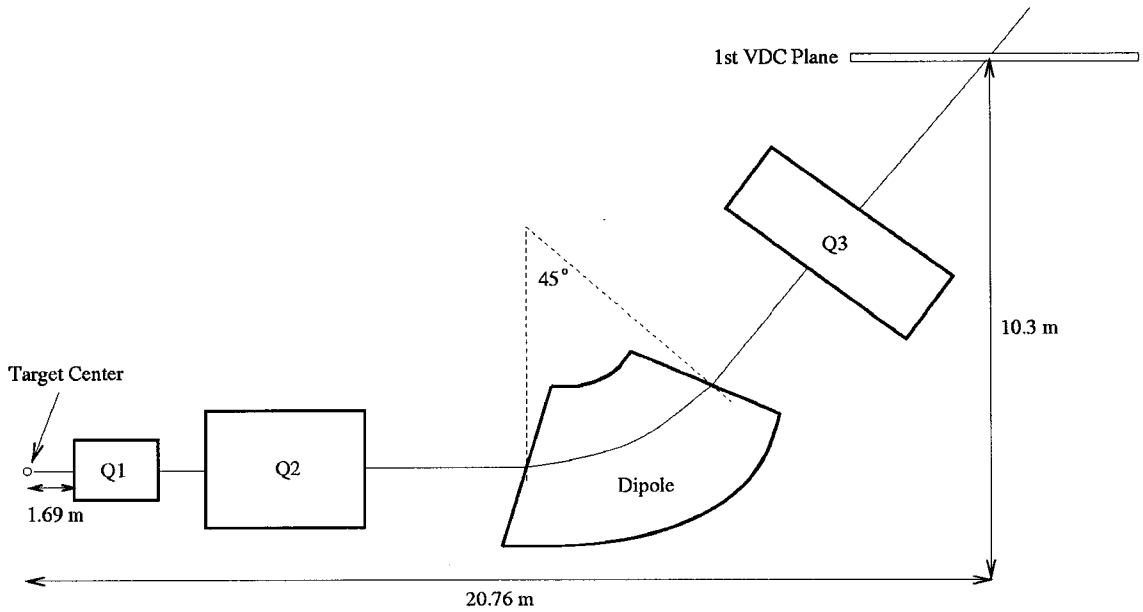

Figure 7.1: *A schematic diagram of the magnets of the Hall A high resolution spectrometers.*

Characteristic	Value
Momentum range	0.3-4.0 GeV
Target to detector length	23.4 m
Momentum acceptance	±4.5%
Horizontal angular acceptance	±28 mr
Vertical angular acceptance	±60 mr

Table 7.1: *Characteristics of the Hall A spectrometers.*

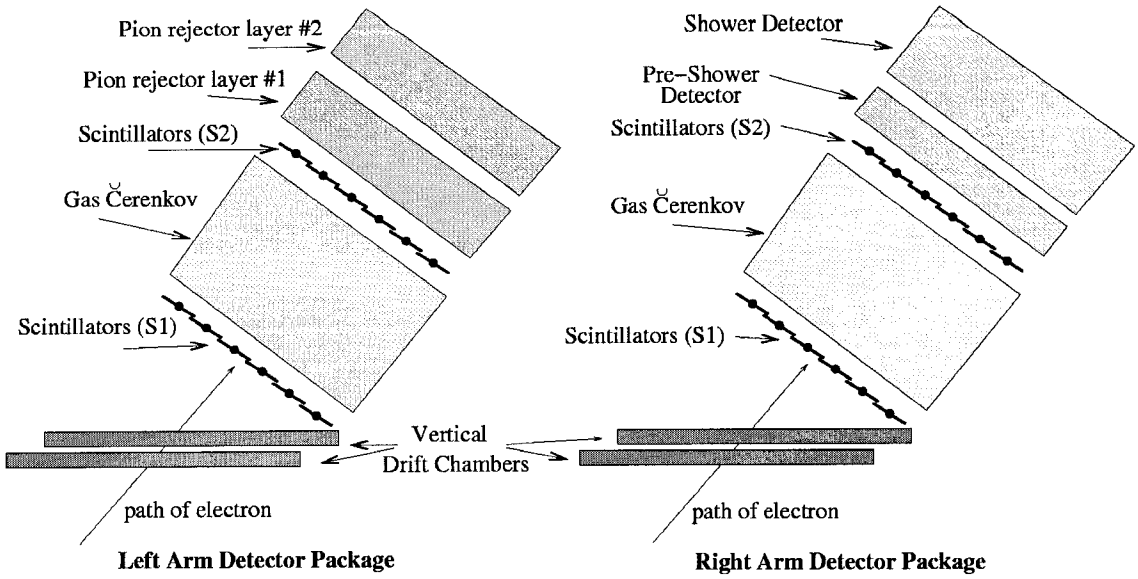

Figure 7.2: *A diagram of the detector package used in the Hall A spectrometers.*

the first quadrupole which limits the angular acceptance of the spectrometer. It is machined and positioned to have a 6 msr acceptance. It was used for most of the elastic runs described later and was removed for the DIS runs to maximize statistics.

7.2 Detector Package

7.2.1 Overview

Once the scattered electrons exit the spectrometer magnets, they enter a set of devices known as the detector package. In E97-103, the detector package's purpose was to identify scattered electrons and to characterize their momentum and direction. This was done with four types of devices: vertical drift chambers (VDCs), scintillators trigger planes, a gas Čerenkov detector and lead-glass shower detectors. These devices are shown in Fig. 7.2. The detector packages in the left and right spectrometers are almost identical. The major difference between the two is the configuration of the lead-glass shower detectors. The left arm has two layers of lead-glass detectors of equal thickness ("pion-rejector") and the right arm also has two layers, but with one layer ("shower detector") thicker than the other

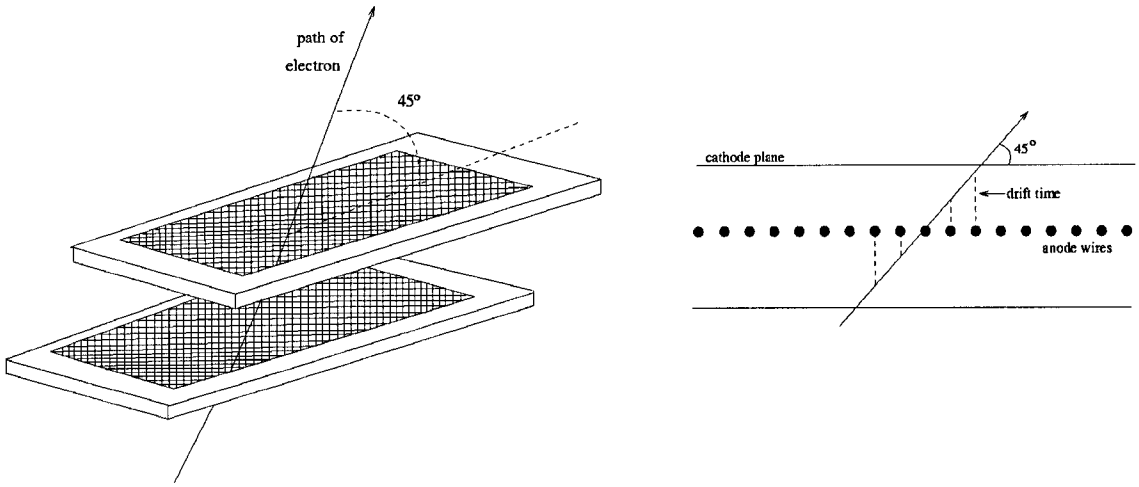

Figure 7.3: *Two diagrams of the vertical drift chambers. The left diagram shows the path of an electron through the two VDCs. The right diagram shows an electron path firing five wires.*

("pre-shower detector").

7.2.2 Vertical Drift Chambers

The purpose of the vertical drift chambers (VDCs) is to determine the position and direction of charged particles that pass through them. VDCs can measure position by using planes of wires where each wire will create a signal if a charged particle passes near it. By using multiple planes of these wires, the direction of the particle can be reconstructed.

There are two identical VDCs in each spectrometer placed at 45° to the central electron path [44]. Each VDC is a closed chamber filled with gas (62% argon and 38% ethane gas) and two parallel planes of 400 gold-plated wires. Each plane of wires is enclosed in a layer of aluminized mylar that is kept at high negative voltage, while the wire planes are grounded. The wires in the two planes run perpendicular to each other in the plane of the VDCs, as shown in Fig. 7.3.

Charged particles that pass through the VDCs ionize the gas in the chamber. The newly formed ions will head towards the negatively charged mylar. The electrons freed in the process move towards the grounded wires. If a charged particle

passes near a wire, the positive ions moving away from it will induce a detectable negative signal in the wire [75]. Because of the 45° angle and the close spacing of the wires (4.243 mm spacing), a particle passing through a VDC plane will typically create a signal in 5 wires [74]. Because of occasional inefficiencies in the wire signals, only 3 wire signals are needed to be considered a good track in that plane.

The amount of time it takes for the effects of ionization to reach a wire from the particle path is known as the drift time. The distance from the wire to the particle path can be accurately determined from the drift time. Drift time is measured by a Time to Digital Converter (TDC) [76] which is a electronic device that acts like a clock. The TDCs are started by an event in the scintillators and the TDCs are stopped by a wire hit. The position of the charged particle can be deduced from the difference in signal times from the TDCs from each wire of the VDCs.

The VDC efficiency can be measured by looking at the quality of the path reconstruction from its output. This is done by going through a set of events and counting the number the possible paths it could have had going through the VDCs. Ideally, each electron will have only one possible reconstructed path. However, if there is wire noise or an inefficient wire then there can be multiple paths the particle could have taken.

Fig. 7.4 shows the VDC efficiency for each kinematic. The conditions for this analysis were to look only at events that have a signal in either the shower and pre-shower detectors in the right arm or both pion-rejectors in the left arm. This made sure that most of the events were scattered particles and not noise or cosmic rays. For each kinematic, six sets of events (or runs as they are called) were chosen, three from the left arm and three from the right arm. There were no zero track events from events that had shower and pre-shower (or both pion rejector) signals. As expected, the efficiency of VDCs is correlated to the rates, as the elastic kinematic had a significantly higher rate than the rest. The deep inelastic scattering kinematics all

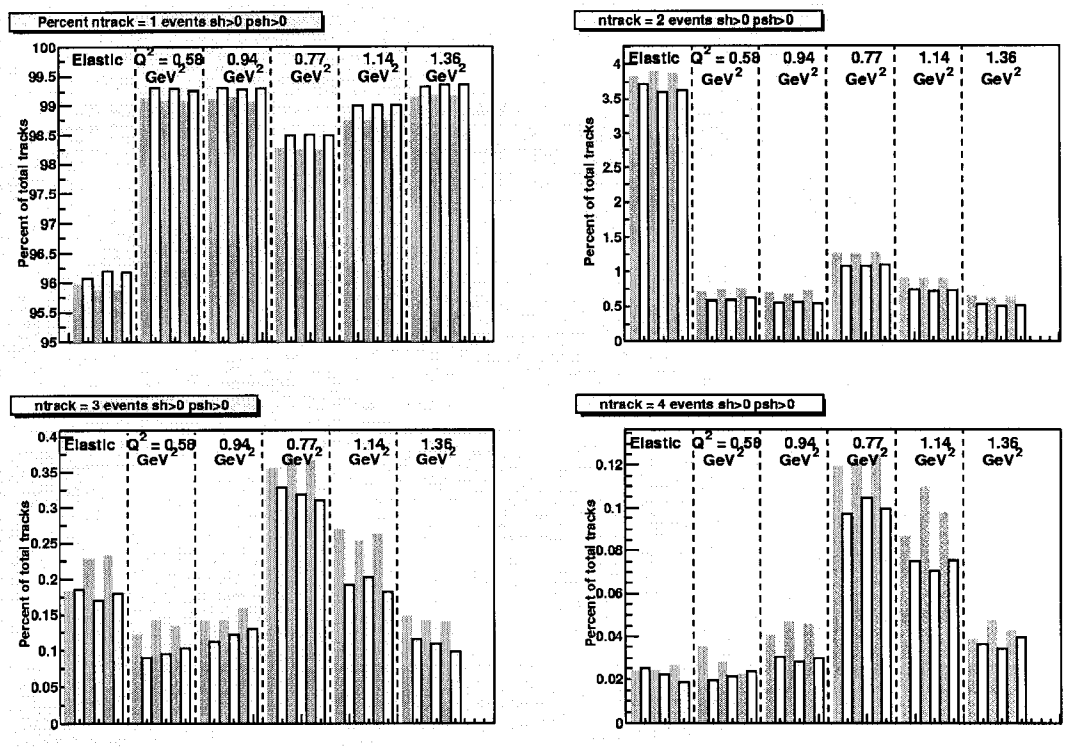

Figure 7.4: *A plot of the percentage of events assigned to one, two, three and four track events by reconstructing the TDC information from the VDCs. Six runs are plotted for each kinematic, three for the left spectrometer (solid bars) arm and three for the right (unfilled bars). The runs were chosen at random from the kinematics.*

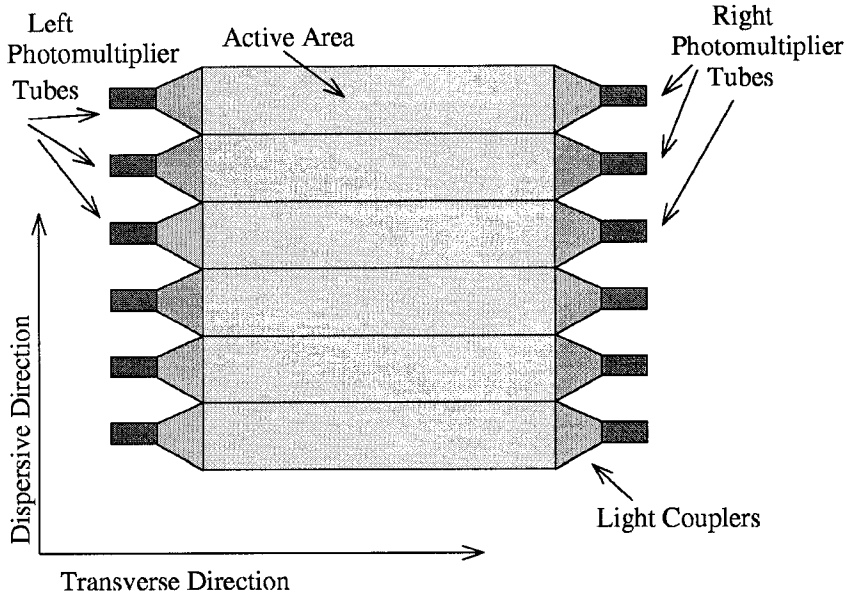

Figure 7.5: *A diagram of the scintillator paddles.*

had tracking efficiencies higher than 98%. All events with more than one track were rejected in the asymmetry analysis.

7.2.3 Scintillator and Trigger Electronics

The scintillator planes S1 and S2 are used to trigger the data acquisition system and as an additional method of tracking charged particles through the spectrometer. The scintillators, shown in Fig. 7.5, are made of Bicron BC-408 plastic and are 1.27 cm thick [74]. There are six scintillators paddles in each plane and each scintillator paddle has a photo-multiplier tube at each end.

Charged particles generate light as they pass through a scintillator. The light travels through the scintillator to the photo-multipler tubes. The intensity and timing of the light is monitored by ADC (Analog to Digital Converter) and TDC electronics. Both photo-multiplier tubes have to register a signal for an event to be considered good.

The scintillators are used to identify and classify events. The paddles in the S2 planes in both arms are used to trigger events. There are four types of events labeled

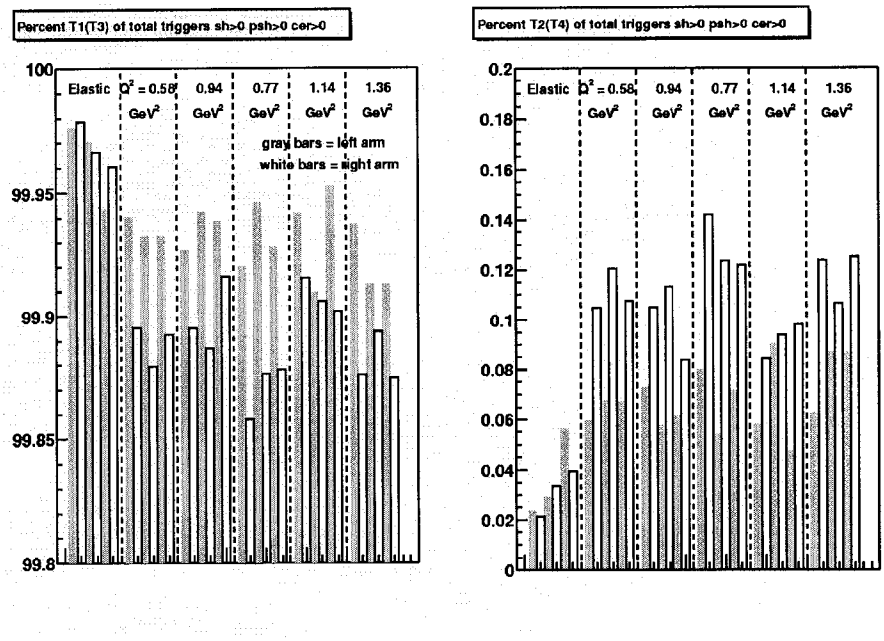

Figure 7.6: *A plot of the scintillator efficiencies in the left and right spectrometers. Six runs are chosen for each kinematic, three from the left arm and three from the left arm. The runs are chosen at random.*

T1, T2, T3 and T4. T1 and T3 events are from particles that cause signals in a paddle in the S2 plane as well as the corresponding paddle in the S1 plane (or the paddle right above or below to account for the particle traveling at an angle to the scintillator plane). T1 events are for the scintillator planes in the right spectrometer arm and T3 are for the scintillator planes in the left spectrometer arm. T2 and T4 events are from two sets of particles. The first set are events that cause signals in a combination of S1 and S2 paddles that do not correspond to a T1 or T3 event. The second are for particles which cause a signal in a paddle in the S2 plane and have a Čerenkov signal, but did not cause a signal in any S1 paddle. T2 events are for the right spectrometer arm, while T4 events are for the left spectrometer arm.

Unless the rates are high, T2 and T4 events are considered bad events. This is because the events were likely caused by particles on the edge of the acceptance or from cosmic rays. The scintillator efficiency can be measured by:

$$\eta = \frac{T_1}{T_1 + T_2} \text{ for the right HRS}, \eta = \frac{T_3}{T_3 + T_4} \text{ for the left HRS} \qquad (7.1)$$

where T_n is the number events of type n in the sample. This has been done for E97-103 and is plotted in Fig. 7.6. The scintillator efficiency was measured by counting T1, T2, T3 and T4 events that had a signal in the Čerenkov and lead glass detectors. Again, the Čerenkov and lead glass detectors are to make sure almost all the events are coming from scattering particles.

7.2.4 Gas Čerenkov Detector

The gas Čerenkov detector is used for separating electrons from other types of charged particles, in particular pions. Čerenkov light is created when a charged particle, traveling in a medium, is traveling faster than the speed of light in that medium. The threshold for this Čerenkov light is determined by the index of refraction of the medium. If the particle is not traveling fast enough to exceed this threshold then no Čerenkov light is emitted.

The principle of the Čerenkov detector is to separate particles that are traveling fast enough to create Čerenkov light from slower particles. Electrons and pions coming out of the spectrometer will have the same momentum, but different velocities because of their mass difference. If the Čerenkov detector has a properly chosen index of refraction, then electrons will generate a measurable amount of Čerenkov light, while the heavier pions won't.

In the Hall A Čerenkov detectors, shown in Fig. 7.7, the medium used is CO_2 held at 1 atmosphere. The threshold for this type of detector is 17 MeV for electrons and 4.87 GeV for pions [74]. The Čerenkov light created by the electrons is focused onto set of ten photo-multiplier tubes. The signals from these phototubes are sent to ADCs and summed. The sum of the ADC signals is the total measured light generated by the particle.

There is a significant background caused by electrons knocked out of material by pions before reaching the Čerenkov detector. These knocked out electrons are

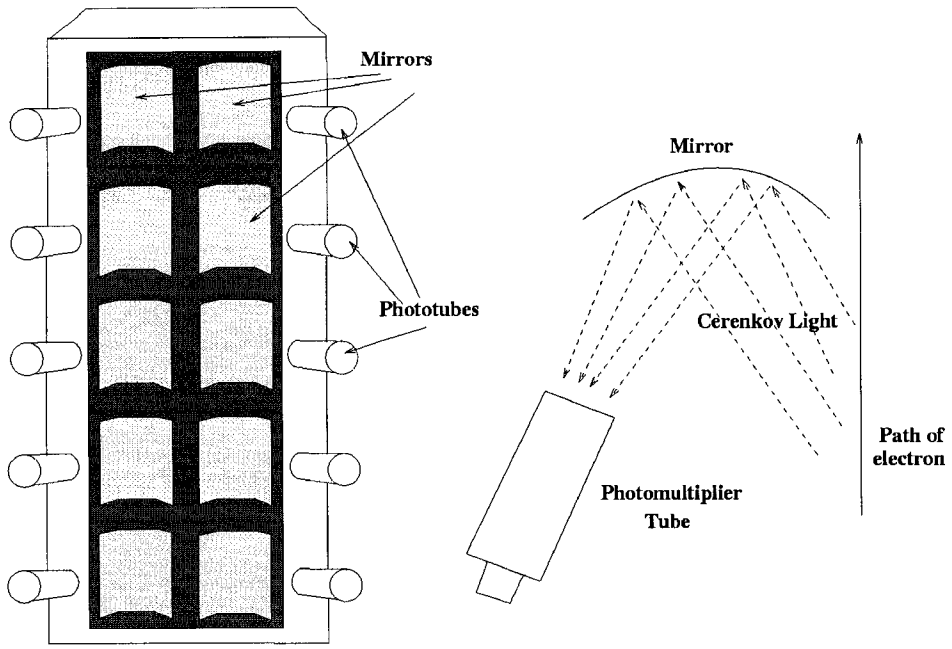

Figure 7.7: *Two diagrams of the gas Černkov detector. The left shows the front of the detector with the cover off. The right is a schematic depicting the mirror collecting Čerenkov light and reflecting it into a phototube.*

known as δ-electrons [77], and can produce Čerenkov light and thus create ADC signals. Generally, δ-electrons aren't traveling in the same direction as the scattered electrons and, as a result, will create less Čerenkov light. Additional help identifying δ-electrons comes from the lead-glass detectors.

7.2.5 Lead-Glass Shower Detectors

Lead-Glass detectors are another way of separating scattered electrons from other types of particles. High-energy charged particles will create bremsstrahlung radiation when traveling through the lead glass. The bremsstrahlung will in turn create e^-/e^+ pairs which will also bremsstrahlung and create new particles [74]. The photomultiplier tubes detect the Čerenkov light from the e^-/e^+ pairs. This process is known as an electromagnetic shower and the energy of the particle is proportional to intensity of the bremsstrahlung photons from the e^-/e^+. Bremsstrahlung intensity decreases with increased mass as $1/m^2_{\text{particle}}$. Therefore, the intensity of the

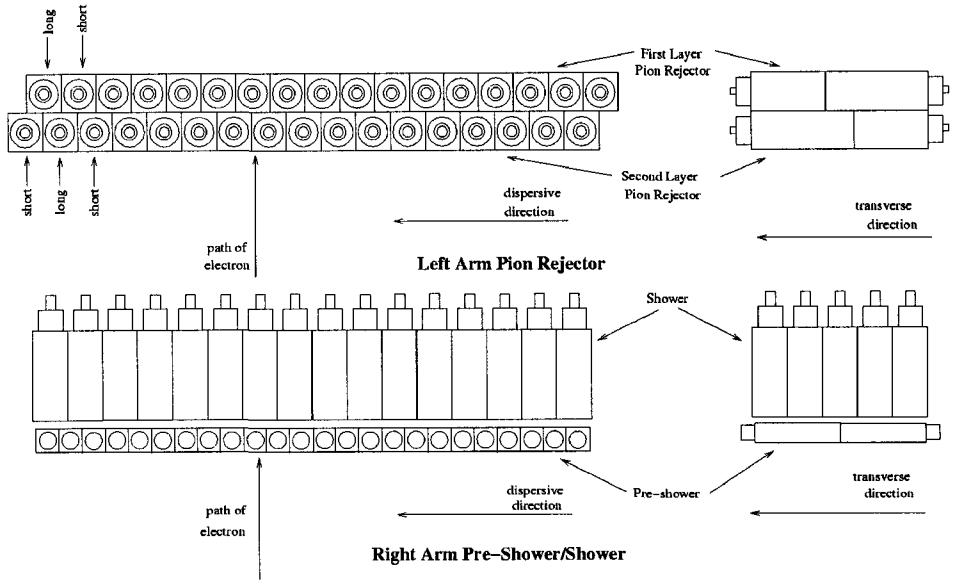

Figure 7.8: *A diagram of the phototube and lead glass configurations in the pre-shower, shower and pion rejectors.*

light created by pions and heavier particles will be significantly less than electrons. It should be noted that the photo-multiplier tubes can't measure bremsstrahlung directly, but instead measure the Čerenkov genereated by the e^-/e^+ pairs in the lead-glass.

A lead-glass detector consists of a rectangular chunk of lead-glass with a photo-multiplier tube glued to the end. The lead-glass detectors are assembled differently in each spectrometer arm. In the left arm, there are 17 long block ($14.5 \times 14.5 \times 35$ cm) detectors and 17 short block ($14.5 \times 14.5 \times 30$ cm) detectors assembled into two layers as shown in Fig. 7.8. The photo-multipliers are perpendicular to the path of the particles through the spectrometers. This assembly is known as the 'pion-rejector'. The lead-glass detectors in the right arm, are made of two types of lead-glass blocks. The smaller blocks that make up the 'pre-shower' are made of 48 blocks, each $10 \times 10 \times 35$ cm assembled with the photo-multiplier tubes perpendicular to the path of the electron beam. The larger blocks consist of 100 blocks, each 100 $14.5 \times 14.5 \times 35$ cm arranged into a 5×20 rectangle with the photo-multiplier tubes

aligned with the particle path, as shown in Fig. 7.8.

The photo-multiplier tubes are connected to ADCs so that the intensity of light corresponding to each event is recorded. In E97-103, there were two distinct peaks corresponding to electrons and pions. The two layers help to separate the tail of the pion peak from the electron peak. At higher energies the separation between the peaks becomes larger and easier to differentiate [41].

7.2.6 Combined Particle Identification Efficiency

A significant amount of pions from photoproduction from the electron beam's bremsstrahlung are created at the kinematics of this experiment. The photoproduction of pions from a polarized electron beam has a strong helicity-dependence; therefore these pions will have their own asymmetry that is not associated with electron scattering asymmetry that is the focus of the experiment This asymmetry is larger than the electron asymmetry and since the pion/electron ratio is $\approx$1, good particle identification was necessary for this experiment. A thorough analysis of the efficiencies of the Čerenkov and lead-glass detectors was done by Xiaochao Zheng for scattered electron momenta of $0.8 < p < 2.0$ GeV and is detailed in her thesis [41]. The scattered electron momenta for E97-103 are slightly above this, but this analysis still applies.

The particle identification efficiencies are characterized by two variables. The first, η_e, is the electron efficiency and is defined as the percentage of electrons that enter the detector that are properly detected. This is necessary to know when calculating cross sections. The second, η_π, is the pion rejection factor, the ratio of pions properly identified as pions to pions mis-identified as electrons. The larger this number is, the smaller is the error from mis-identified pions contributing to the electron asymmetry. The measured values for these efficiencies for the left and right spectrometer are summarized in Table 7.2.

Left Spectrometer Arm			
Detector	η_e (%)	η_π	Cuts
Gas Čerenkov	99.9	> 770	ADC sum > 400
Pion Rejectors	98	≈ 38	$E_{PR1} > 0.42p$, $E_{PR2} > 100$, $0.75E_{PR1} + E_{PR2} > 0.8p$
Combined	98	$> 3 \times 10^4$	
Right Spectrometer Arm			
Detector	η_e (%)	η_π	Cuts
Gas Čerenkov	99	900	ADC sum > 342
Pre-Shower, Shower	98	≈ 182	$E_{psh} > 0.14p$, $E_{sh} > 100$, $E_{psh} + E_{sh} > 0.75p$
Combined	97	$> 1.6 \times 10^5$	

Table 7.2: *The electron efficiencies and pion rejection factors for the left and right arm spectrometers, where p refers to the central electron momentum of the spectrometer.*

7.3 Data Acquisition System

The ADC and TDC information from the detectors, helicity information and information from the beam-line apparatus, such as those presented in 5, are stored in data files by the Hall A data acquisition system (Hall A DAQ). The DAQ is built on CODA, which is a software package designed specifically for nuclear physics applications. There were actually three DAQ systems running: one for each spectrometer arm and one for the helicity feedback system known as the Parity DAQ.

The data files recorded by the DAQ contained three types of information. The first were events resulting from triggers of the S2 scintillator planes. These store information about the detectors and helicity information and are known as CODA events. The CODA event rate in the experiment for the DIS data was limited to < 2 kHz. The second type of event stored contains information from the EPICS database. This database contains a large quantity of information about the spectrometer magnets, beam line apparatus, target information and other "slow control" information about the experiment. The third type of event put into the data files is scaler information. Scalers record the number of triggers and accumulated charge of the run. Because the scalers are read directly from the detector electronics, there

are no missing events in the scalers, unlike the DAQ, which can't keep up with the data rate being produced by the detectors. The typical computer deadtime for the DAQ was around 10%.

The data is first written to a local disk and then it is moved to the Jefferson Lab Mass Storage System (MSS). The MSS stores the data on tape from where it can be retrieved at any time in the future for analysis.

CHAPTER 8

Asymmetry Analysis

8.1 Extracting Raw Asymmetries

8.1.1 Overview

The longitudinal and transverse raw asymmetries presented in Eq. 4.5 are extracted from the data files recorded by the detector package and data acquisition system. There is a data file for every run taken during the experiment. The run length is limited either by the number of events (< 3 million events) if the rates are high or by time if the rates are low (no runs longer than an hour). Each spectrometer arm has its own data file for each run.

The data files are analyzed using the software presented in Fig. 8.1 and are converted to N-tuples by ESPACE. The scaler information is also extracted from the raw data files. Information from the scalers and the N-tuples are then combined to produce charge and dead-time corrected asymmetries.

8.1.2 Creating N-tuples with ESPACE

ESPACE (Event Scanning Program for Hall A Collaboration Experiments) is a software application specifically written to take data files from the data acquisition system and turn them into manageable physics information. Some of the many useful tasks that ESPACE does are particle track reconstruction using the VDC and scintillator information, creating histograms of the lead-glass and Čerenkov detector signals and constructing N-tuples which store this information [78]. N-tuples are sequential arrays, where each element of the array is an event with an associated

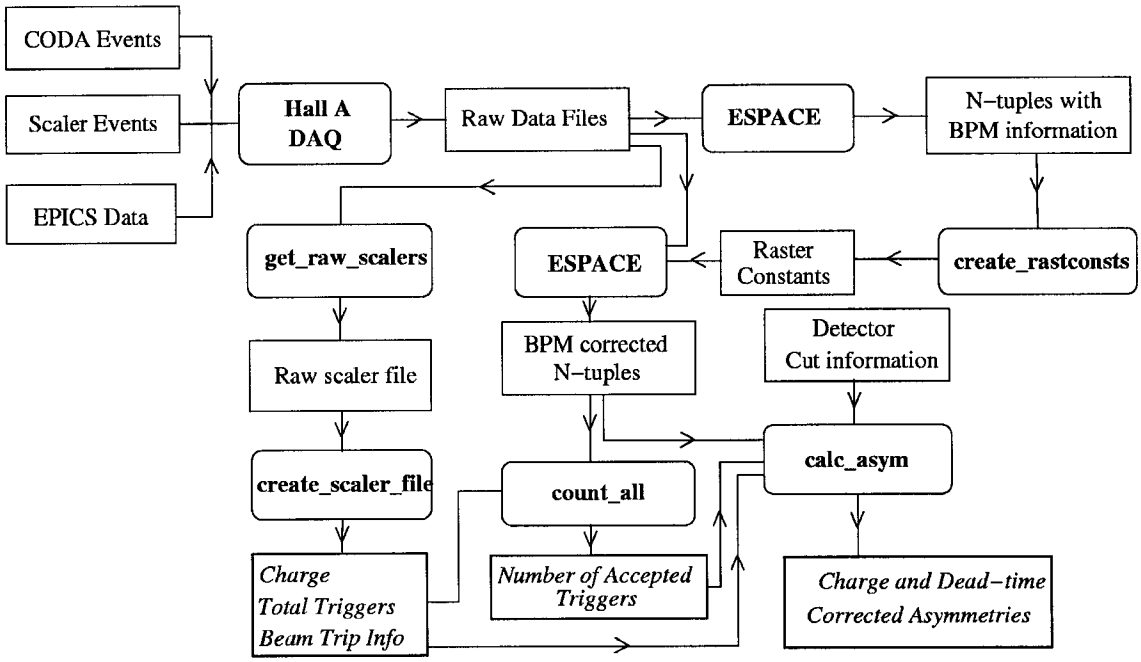

Figure 8.1: *A flowchart of the various data files and analysis programs used to calculate the charge and dead-time corrected asymmetries.*

set of variables. These N-tuples are created in CERNLIB HBOOK format, but are converted to a ROOT file for the purposes of this analysis.

For the E97-103 analysis, an N-tuple was made for each good run. The criteria for a good run was that it surpassed a minimum length and no comments were made concerning instability in the log books. The N-tuple was made in a series of stages. The first N-tuple made from `ESPACE`, as shown in Fig. 8.1, was made to extract raster and BPM information from the raw data files. The reconstruction of the scattering location requires average values of the spot position and raster size and this can only be done by making a complete pass through the data file. This N-tuple containing the correct BPM and raster information is analyzed using a ROOT C++ code known as `create_rastconsts`. The output of `create_rastconsts` creates the necessary input file for `ESPACE` to do the scattering point reconstruction correctly.

After the beam position input files are created, `ESPACE` is re-run and the new N-tuples contain information about the reconstructed momentum, scattering point

and direction, values for the Čerenkov and lead-glass detectors and the event time. Though ESPACE is capable of doing elaborate cuts on the data, all events recorded by the DAQ are included in this N-tuple.

8.1.3 Extracting Charge and Dead-time Information

The scaler information used to calculate the helicity-correlated charge and dead-time corrections is extracted from the raw data files. The scaler data is sent to the DAQ every four seconds. The information from the scalers relevant to this analysis are the total number of T_1, T_2, T_3 and T_4 triggers for the positive and negative helicity states, the charge accumulated in BCM with the 3x amplification for both positive and negative helicity states, and the accumulated time from the 1024 Hz clock for positive, negative and ungated helicity. In the experiment preceding E97-103, the T_1 and T_3 trigger scaler that was normally used started to show signs of multiple triggers for one event. Another set of scalers were created called T_1 clean and T_3 clean that did not have this problem [79]. Whenever the total number of triggers is mentioned, these quantities are what is used. A ROOT C++ program was written called `get_raw_scalers` that reads every scaler event in the raw data file and outputs a text file with the scaler values for each scaler event.

Since the scalers are normally cleared at the beginning of the run, the last reading of the scalers can be used to represent the accumulated values of the scaler variables over the run. However, there are two reasons the scalers aren't treated this way in this analysis. The first reason was that there were times, specifically during the carbon quasi-elastic data taking, that the scalers were not being cleared at the beginning of the run [80]. The second reason is that there was concern about large charge asymmetries during the ramping of the beam current. To study the effect of this beam ramping, it was useful to be able to cut out parts of the run. This meant that one had to be able to subtract the proper amount of triggers and charge that

occured during the removed periods from each of the accumulated scalers.

The scaler information was summed by a ROOT C++ program known as `create_scaler_file`. This program calculated the total scaler values by calculating the increase in the accumulated value of each variable for each 4 second interval between scalers. This can be described by:

$$s_{\text{sum}} = \sum_{i=2}^{N} \Delta s_i \tag{8.1}$$

where s_{sum} is the accumulated value for a particular scaler variable s, N is the number of scaler events and Δs_i is defined by:

$$\Delta s_i = \begin{cases} s_i - s_{i-1} & \text{if } I_i \geq I_{\text{min}} \\ 0 & \text{if } I_i < I_{\text{min}} \end{cases} \tag{8.2}$$

where s_i is the value of scaler s for scaler event i, I_{min} is the minimum current and I_i is defined as:

$$I_i = \frac{Q_i^+ + Q_i^- - Q_{i-1}^+ - Q_{i-1}^-}{t_i^u - t_{i-1}^u} \tag{8.3}$$

where $Q_i^{\pm}$ is the charge scaler value for event i and helicity $\pm$ and t_i^u is the value of the ungated helicity clock value for event i. The values for $Q^{\pm}$ must be calculated using the calibration constants in Eq. 5.7. The value for I_{min} is arbitrary and the change in the raw asymmetry due to a the change in the choice of I_{min} will be discussed later. Whenever an interval of the scaler information is cut out, the clock times are recorded for that interval relative to the first clock time. This is done so that the events in the N-tuples from that interval can be removed as well.

The charge values and total triggers have been acquired from the scaler information in the raw data file. The only other information needed is the total accepted triggers by the data acquisition system. This number is extracted by counting all events in the N-tuple output from ESPACE with the ROOT C++ program `count_all`. If beam ramping cuts are made, the events corresponding to

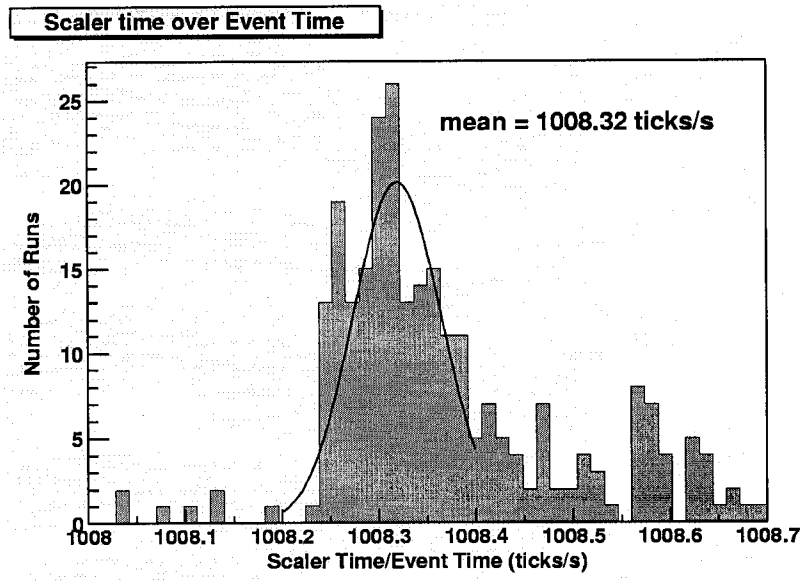

Figure 8.2: *A histogram of the ratio of total scaler clock time to event clock time of a run.*

these times are removed. This is done by looking at the `event_time` variable in each event. However, the scaler clock's unit is a tick of the 1024 Hz clock where event time from the N-tuple is in seconds. To convert from one to the other, one can use:

$$t_{\text{scaler}} = (1008.32 \text{ ticks/s}) t_{\text{event}} \tag{8.4}$$

where t_{scaler} is the time on the scaler clock in clock ticks and t_{event} is the time assigned to events in seconds. This constant is determined by looking at data files and their corresponding scaler files. The ratio of the scaler time to the event time for the same run is plotted in Fig. 8.2. The reason this isn't exact is the event time is only known when an event occurs. If no events are happening there can be a gap at the end of the run, which explains why sometimes the ratio is larger than the mean. Also, there were instances where events happened after the scaler clock stopped. It is unclear whether these events were included in the accumulated scalers and assigned the wrong event time or not. In any case, varying this constant did not change the raw asymmetry significantly.

Variable	Description
evt_type	the trigger type of event (1,2,3,4)
ev_time	the time of the event from the start of run
ntrack	number of tracks from VDC reconstruction
react_z	scattering location on target cell axis
tg_ph	horiz. scattering angle w. r. t. central angle of HRS
tg_th	vert. scattering angle w. r. t. central angle of HRS
tg_dp	relative difference in momentum w. r. t. central momentum of HRS
beta	the velocity of the particle over c
psh	pre-shower or the 1st layer of pion rejector value
sh	shower or 2nd layer of pion rejector value
cer	Čerenkov ADC sum

Table 8.1: *The variables used to find good electron events.*

8.1.4 Analyzing N-tuples

The values of N^+ and N^- in Eq. 4.5 are extracted for each run from the N-tuple output from ESPACE. This process consists of counting the number of good electrons of each helicity within the same spectrometer acceptance. The decision whether or not the event is an electron and that it lies within certain acceptance criteria is based on the values of the reconstructed variables associated with that event. The variables used to make that decision are listed in Table 8.1.

There are four types of cuts made on events: good trigger cuts, good electron cuts, acceptance cuts and event time cuts. Good trigger cuts are those made on trigger type and VDC tracking. Only events T_1 or T_3 (`evt_type==1 || evt_type==3`) and one good event track (`ntrack==1`) were considered good track events. Good electron cuts use the Čerenkov and lead glass detectors variables (`cer,psh,sh`) to separate electron events from pion events. In addition, `beta` is used to separate particles by velocity, which is an effective way of getting rid of cosmic rays that have Čerenkov and lead-glass detector signals, but a negative value for β. Acceptance cuts use the reconstructed scattering variables (`react_z,tg_ph,tg_th,tg_dp`) to keep electrons that are within the physical acceptance of the spectrometer and that

originate within the target. Since the spectrometer optics aren't well known through the whole acceptance, it is also important to keep only electrons that travel through an understood part of the spectrometer. Event time cuts come from the scaler analysis and are used to remove events during low current periods and when the scaler is not recording events.

All the asymmetry analyses, including physics production, false asymmetry and elastic asymmetry use these same techniques and software to create N-tuples and calculate the output values needed to calculate A_{raw}.

8.2 Establishing Sign Convention

The sign of the asymmetry calculated by this procedure needs to match the correct physical sign. To ensure this, a known longitudinal asymmetry and a known transverse asymmetry are measured. The sign of the longitudinal asymmetry is measured using polarized ^{3}He elastic scattering. The sign of the transverse asymmetry was measured using the polarized $\Delta(1232)$ resonance which has a large transverse asymmetry. The sign convention was established by data taken in the E99-117 experiment (which directly preceded E97-103) and is described in the thesis of Xiaochao Zheng [41]. The results of that analysis were used in E97-103 and are presented in Table 8.2. An important point in the asymmetry analysis is that sign of the longitudinal asymmetry is the same in both arms, while the sign of the transverse asymmetry is different in the two arms.

There were 12 target, beam and spectrometer combinations in E97-103 listed in Table 8.2. There were 4 combinations that measured the longitudinal asymmetry. These correspond to a target polarization direction of 0°. In principle, additional data could be taken with the target polarization at 180°, but the half-wave plates could not be aligned for the longitudinal and transverse lasers at the same time. Since the experiment ran much longer with the transverse lasers, it was decided

Beam 1/2 wave plate	target pol. direction	HRS	sign convention
OUT	0	left	positive
OUT	0	right	positive
IN	0	left	negative
IN	0	right	negative
OUT	90	left	positive
OUT	90	right	negative
IN	90	left	negative
IN	90	right	positive
OUT	270	left	negative
OUT	270	right	positive
IN	270	left	positive
IN	270	right	negative

Table 8.2: *Sign convention used for asymmetries during E97-103 for the various beam and target polarization combinations. No data was taken in the 180° target polarization direction in E97-103.*

not to use the 180° polarization direction. The other 8 configurations were used to measure the transverse asymmetry. Measuring the same quantity in multiple configurations is a powerful tool for eliminating false asymmetries.

8.3 Detector Cut Studies

8.3.1 Electron Identification Studies

Cuts on the Čerenkov and lead-glass detectors separate scattered electrons from other types of charged particles. The goal of the cuts is to maximize the number of scattered electron events, while minimizing the number of unwanted events. Usually, it is beneficial to err on the side of cutting out good electrons rather than let a significant number of unwanted events into the asymmetry analysis.

There are only two cuts done on the Čerenkov ADC sum values for each event as shown in Fig. 8.3. There is a Čerenkov cut minimum that does most of the work removing pions. This cut is usually on the left hand edge of the large electron peak. The small peak on the left of the Čerenkov peak are δ-electrons and need to be cut

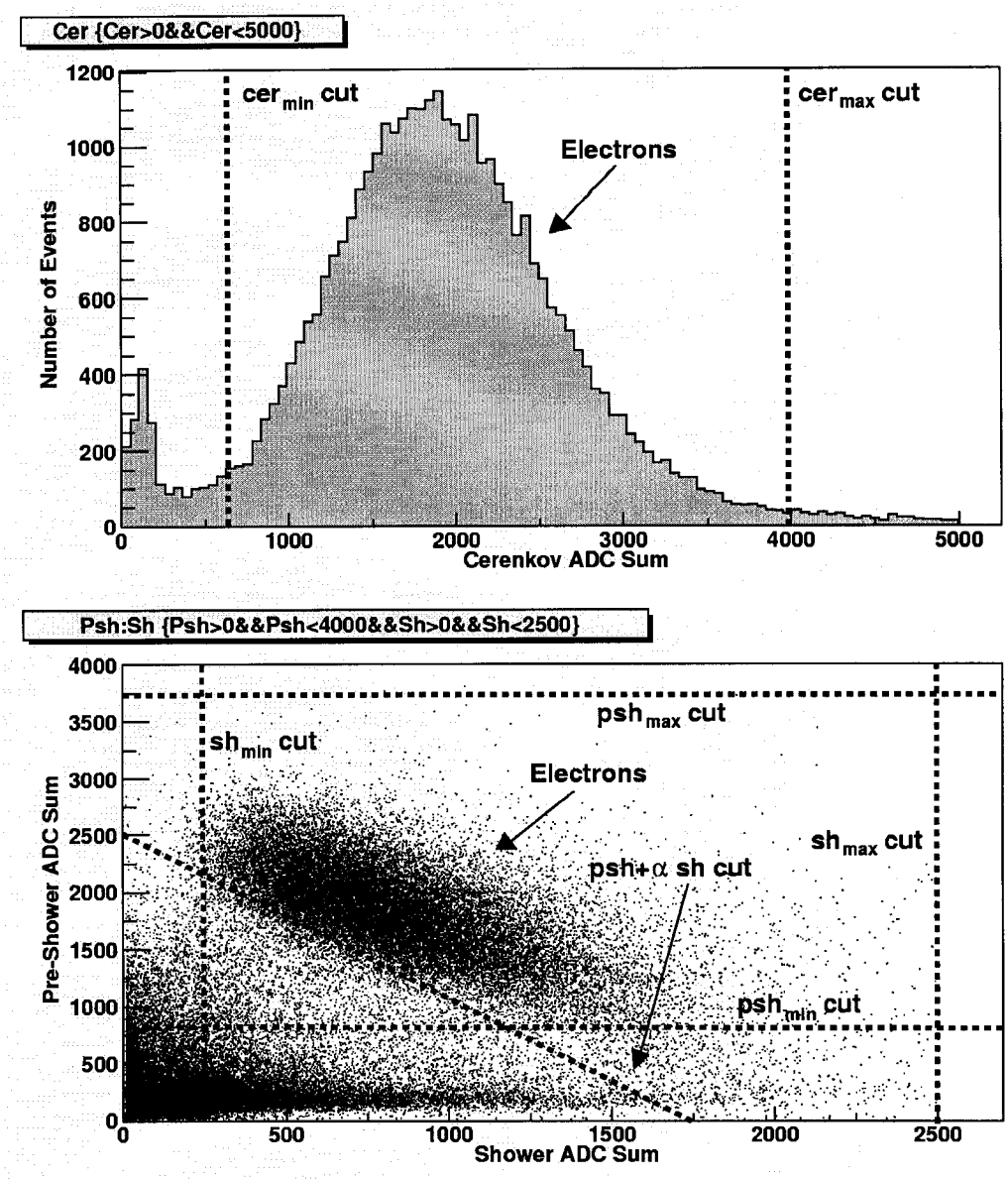

Figure 8.3: *A histogram of the Čerenkov ADC sum for a set of events (top) and a 2-D plot of pre-shower and shower ADC sums (bottom). Examples of cuts used in the asymmetry analysis are shown. The accepted region in the shower detector cuts is the five-sided area that contains the blob of electrons.*

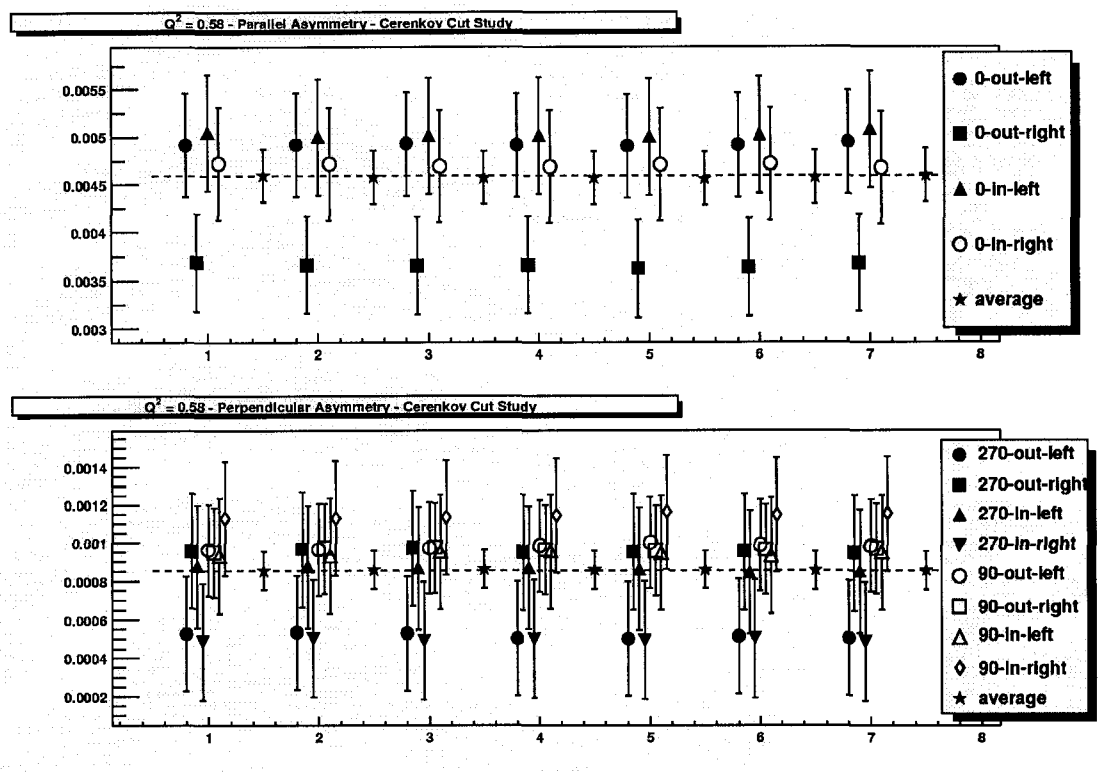

Figure 8.4: *A plot of the effect of different Čerenkov cuts on the physics asymmetry. The top plot is the effect of different cuts on the four longitudinal configurations and their average. The bottom plot is the effect on the eight transverse configurations and their average. The cuts become tighter from left to right.*

out. The second cut on the Čerenkov is a maximum value cut. Its purpose is to cut out some bad events in the top ADC channel. This cut can be left out with no effect on the asymmetry.

The goal of the pre-shower and shower cuts (or pion-rejector layer 1 and 2 cuts, referred from here on out as left arm pre-shower and shower cuts for convenience) is to cut out everything but the big blob of electrons in the middle of the lower plot in Fig. 8.3. Both the pre-shower and shower have minimum and maximum cuts to minimize unwanted events. There is an additional 2-D cut (referred to a **psh**+α**sh** cut on the plot) that is parallel to and set on the edge of the electron blob.

The effect of changing these cuts has been studied. The asymmetries for all configurations and kinematics were calculated and plotted. An example of one of

these studies is shown in Fig. 8.4. In that plot, the Čerenkov cut was changed from 500 to 1000 with no shower or pre-shower cuts at all and leaving all the acceptance cuts the same. In all the studies of the particle identification, it was found that as long as there was a cut on the Čerenkov detector above zero the asymmetry did not change significantly, even if there were no other cuts. This means that the Čerenkov detector was efficient enough by itself within the error bars of the raw asymmetry. However, the final analysis uses more conservative cuts on the Čerenkov and lead-glass detectors to err on the side of caution.

8.3.2 End Window Cut Studies

The end windows of the polarized ^{3}He glass cells are a source of a large quantity of scattered events. Not being events from ^{3}He, they need to be removed. Tight cuts on the electron scattering variable `react_z` will cut out most of the scattering from the windows. To do this each end window was fit with a Gaussian along `react_z`. The cuts were made 3 σ away from the mean of the Gaussian as shown in Fig. 8.5. Empty reference cell runs were taken to estimate the amount of background from the end windows, but because there were some residual gases in the reference cell it was difficult to estimate the background from the windows with 3 σ cuts. A conservative estimate is that $< 2\%$ of the events used in the asymmetry analysis come from the end windows.

8.3.3 Acceptance Cut Studies

Different cuts on the spectrometer acceptance variables were also studied to see the effect on the asymmetry. The cuts on the acceptance variables, as shown in Fig. 8.6, are all done in two dimension to maximize the size of the acceptance, while still cutting out unwanted events. The acceptance cut studies calculated the asymmetry starting with a loose cut and moving to a tight cut.

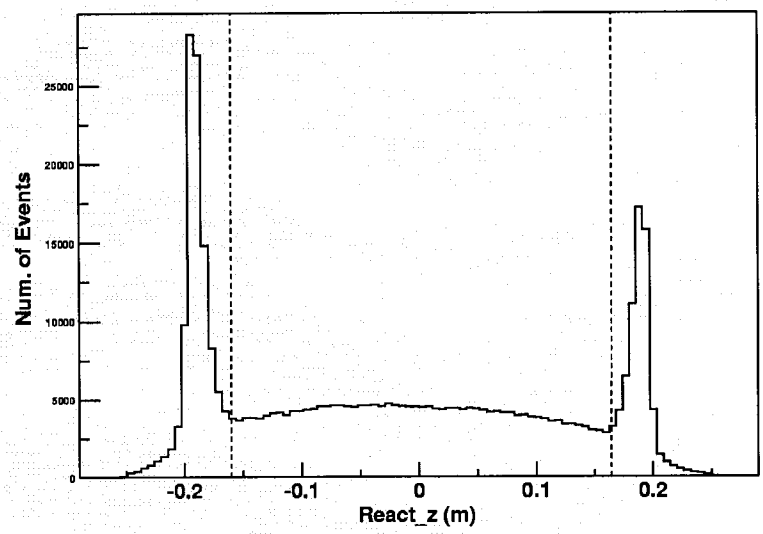

Figure 8.5: *A histogram of scattering position along the target cell axis showing the end window cut.*

The study plotted in Fig. 8.7, shows the electron asymmetry for all configurations and the average with 8 gradually tightening cuts on `tg_ph` and `react_z`. This study was repeated with a tight cut on `tg_th` and `tg_dp`. Then the same sort of study was done on `tg_th` and `tg_dp` with loose and tight cuts on `tg_ph` and `react_z`. All of these studies were repeated for the pion asymmetry and for all 5 kinematic settings.

From all of these studies no significant trends in the data were found. The average of the configurations never deviated from the average of the loosest cut by more than 1 σ for any of the cut studies. Often, a single configuration would deviate from the other configurations, but never more than 2 σ and never consistently through different kinematics. A configuration that deviated from average in the electron asymmetry would stay with the average in the pion asymmetry. Because of the consistency of the values for the asymmetry, the loosest cuts were chosen to calculate the asymmetry to minimize the statistical error of the experiment.

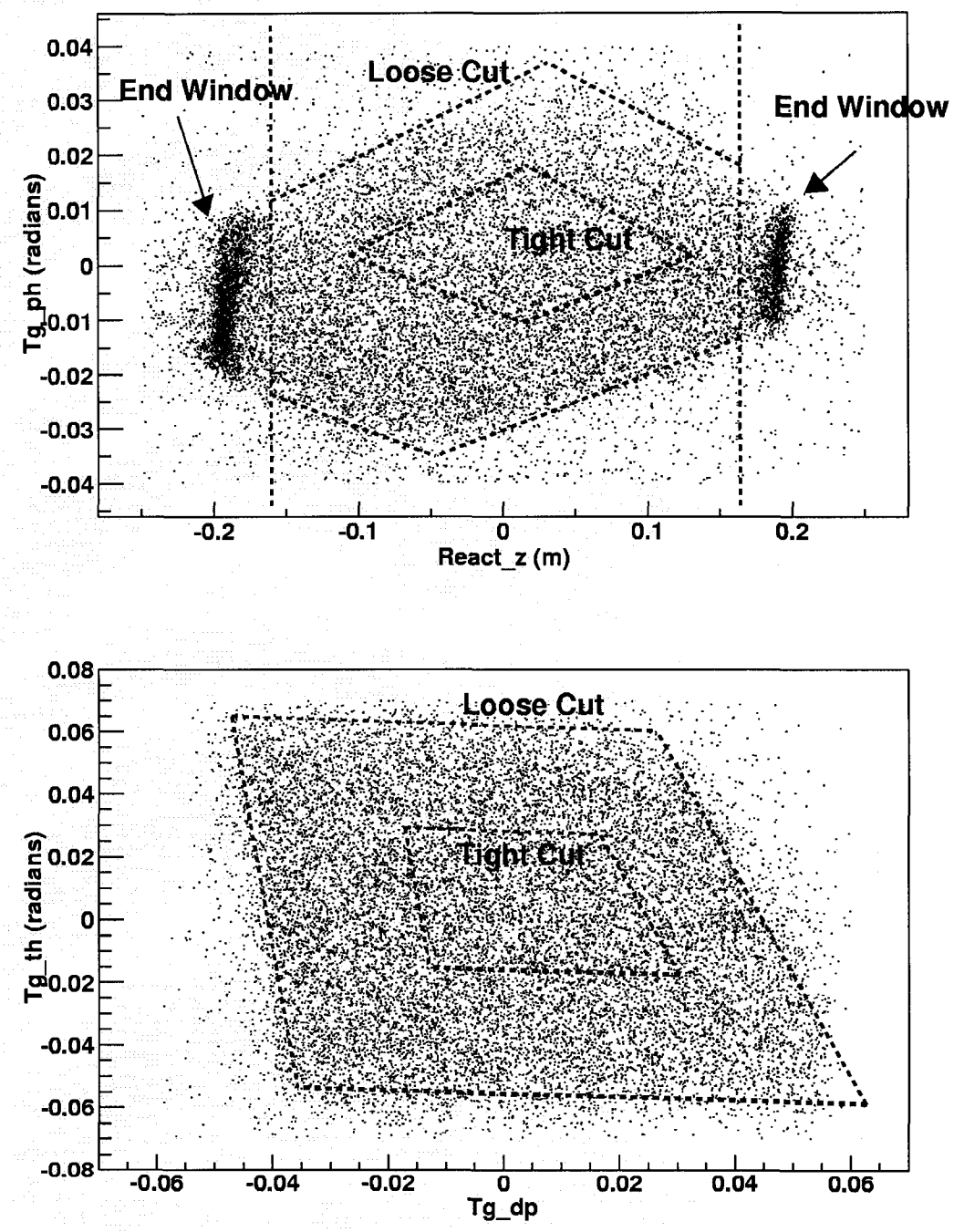

Figure 8.6: *The top plot is of the horizontal scattering angle ϕ vs. scattering point along the cell axis, react-z. The bottom plot is of the vertical scattering angle θ vs. the relative momentum difference of the event from the central momentum.*

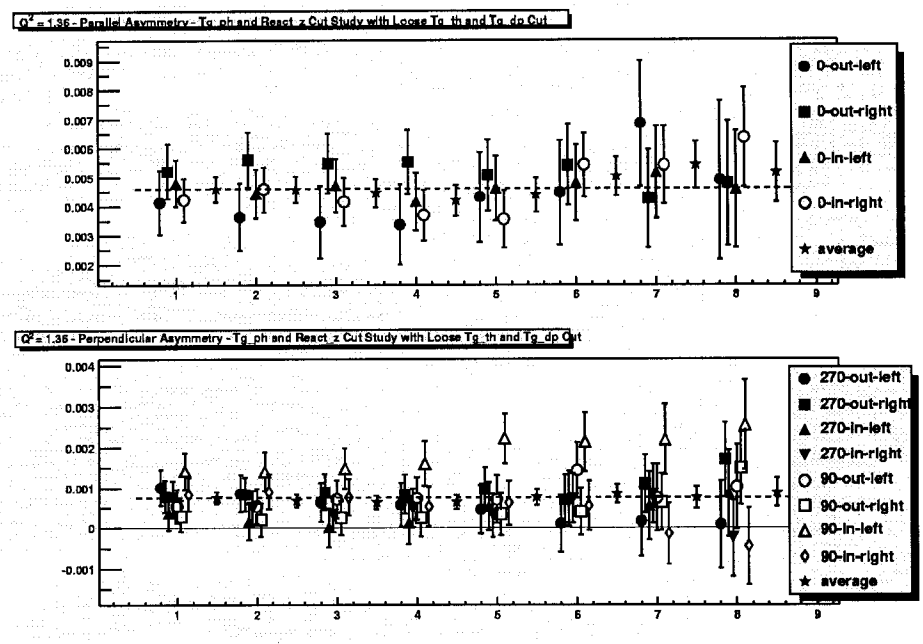

Figure 8.7: *A study of the effect of tightening cuts along the horizontal scattering axis and the target chamber axis. The dashed line is the value of the asymmetry with the loosest cuts.*

8.4 False Asymmetries

8.4.1 Removing Beam Ramping Periods

Because of the high statistics taken in the transverse polarization configuration, the experiment is potentially sensitive to false asymmetries. One false asymmetry of concern was the effect of ramping the beam on the charge asymmetry. Because of the thin end windows on the target cell, whenever the beam is first turned on, the current is ramped up slowly to avoid a thermal shock that could lead to a cell rupture. These beam ramping periods generally last around 30 seconds. During the experiment, it was noticed that the charge asymmetry was becoming much larger during these beam ramping periods [81]. If the charge asymmetry during these periods was large enough, the charge correction would not be enough to compensate for them.

To study this phenomena, the software described in section 8.1.3 was used to cut out periods in the data where the average current was below either 1 μA or

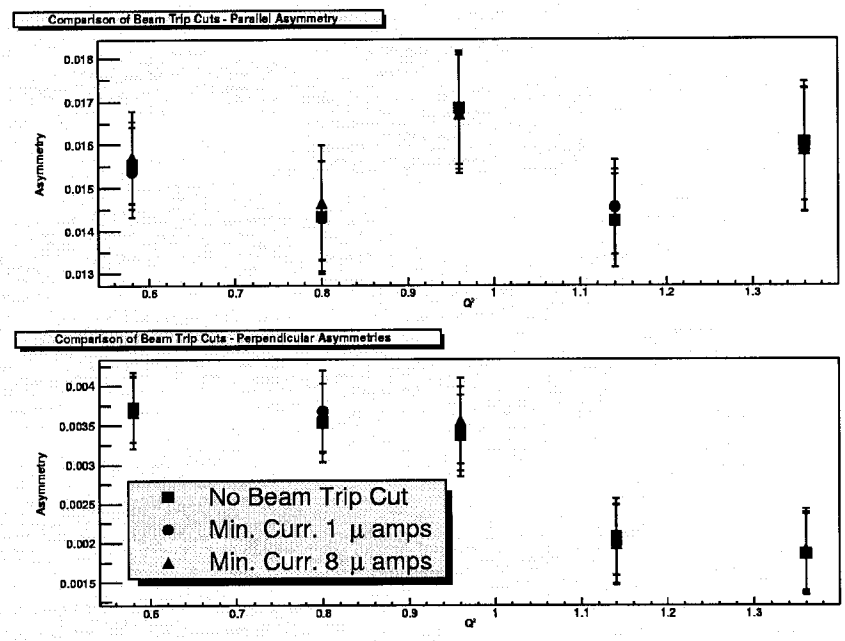

Figure 8.8: *A comparison of the physics asymmetries with different cuts on the minimum current.*

8 μA. This was compared to a calculation of the asymmetry where no cuts on the beam current were made. The results are shown in Fig. 8.8. Obviously, the effect of cutting the beam ramping either at the 1 μA or 8 μA level is not significant compared to the statistical errors of the experiment. In the final asymmetry analysis the beam current minimum was set to 1 μA to cut current levels that were below the range for the 3x gain amplifier of the BCMs.

8.4.2 The Effect of Holding Field Misalignment

Another source of false of asymmetry was mixing of the longitudinal and transverse asymmetry due to slight misalignment of the field. Because the longitudinal asymmetry was significantly larger than the transverse asymmetry, a misalignment might shift the transverse asymmetry. Measurement of the holding field was done as described in section 6.8.3. The direction surveys of the holding field mostly agreed, but disagreed by 0.5° in the 90° configuration. The two surveys of most interest is survey 3, which took place right before E97-103, and survey 4 which happened just

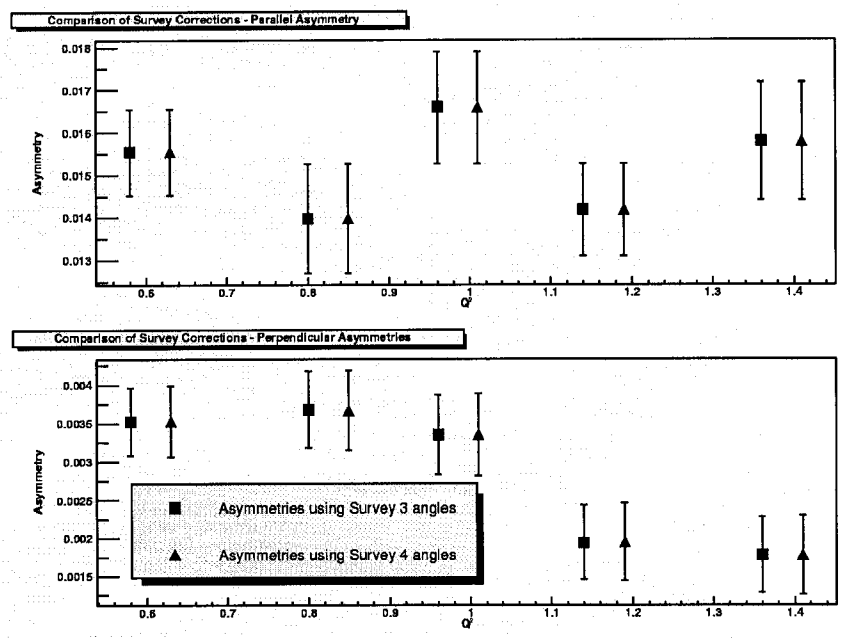

Figure 8.9: *A comparison of the physics asymmetries correcting the field alignment with the compass surveys. The Q^2 values of the fourth survey have been shifted slightly so they can be seen.*

after. Survey 3 was used to set the holding field angles in the experiment.

The effect of the discrepancy of the compass surveys on the physics asymmetries is shown in Fig. 8.9. The effect of correcting the asymmetries for the difference in compass surveys is negligible. This is because the longitudinal asymmetry doesn't change sign between the left and right spectrometer arm and the transverse asymmetry does. Therefore, when a longitudinal asymmetry appears when the target is tranversly polarized, it will cancel when the all the different configurations are added together. This is only the case, and it was the case in E97-103, if there is roughly an equal amount of data in both spectrometer arms for each configuration.

8.4.3 Carbon Quasi-Elastic Analysis

In an effort to measure false asymmetries, two days were spent running on the carbon foil target at E=1.197 GeV at quasi-elastic kinematics ($E' = 1.123$ GeV and $\theta = 18.6°$). Since the carbon foils are unpolarized and the parity violation

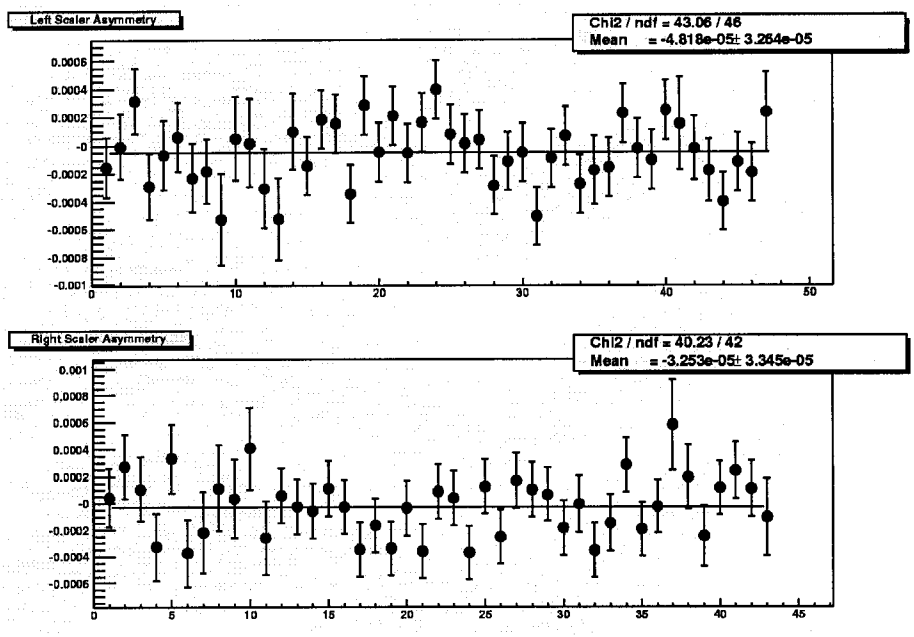

Figure 8.10: *The asymmetry in the left and right spectrometer arm during carbon quasi-elastic running using charge corrected scaler triggers. Each point represents a seperate run.*

asymmetry from electro-weak interactions is insignificant at this level of statistical error, the asymmetry measured from this data should be consistent with zero.

The carbon quasi-elastic asymmetry was measured in two ways. The first was to measure the charge-corrected asymmetry of the scaler T_1 and T_3 triggers. This has the advantage of higher statistics, but since the physics asymmetry is measured using detector events it is an incomplete measure of the false asymmetry. The results of this method are shown in Fig. 8.10. The second was to measure the asymmetry with detector events using minimal cuts. All that was required for an event to be accepted was that the event had a T_1 or T_3 trigger and a unique VDC track. The asymmetry is corrected for charge and dead-time in the usual way. The results from this method are shown in Fig. 8.11.

The false asymmetry data from the detector method was pre-scaled by a factor of 10 to keep from overburdening the Hall A DAQ. This creates complications in calculating the statistical error. The statistical error calculated using the number

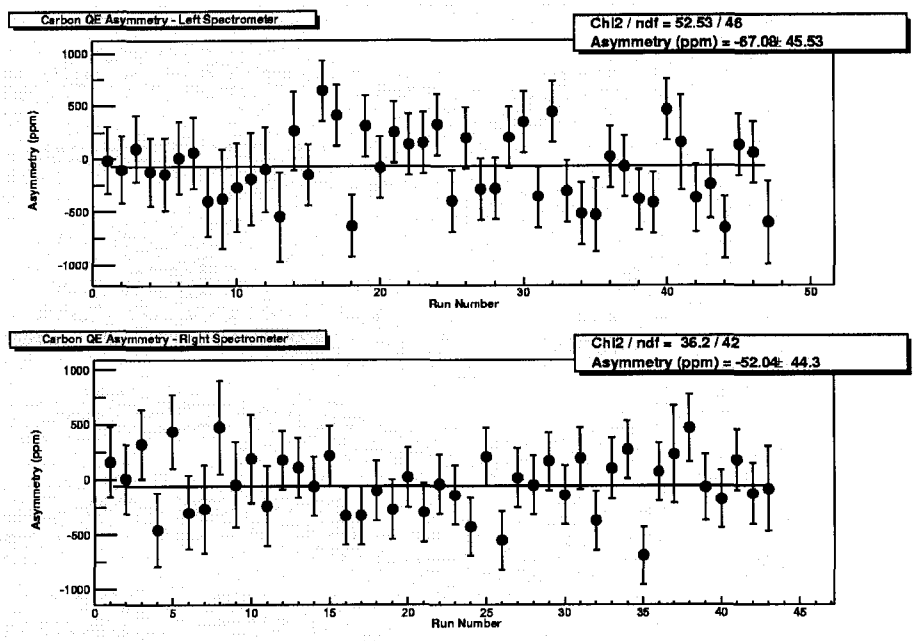

Figure 8.11: *The asymmetry in the left and right spectrometer arm during carbon quasi-elastic running using charge and dead-time corrected detector events. Error bars calculated as described in the text.*

of detector event results in a χ^2 much smaller than 1, meaning that the error bars are too large. On the other hand, multiplying the number of events by the pre-scale factor creates a χ^2 much larger than 1, meaning the error bars are too small. If there were no dead-time and no cuts on the data this would be the correct way to calculate the error bars. However, since there are both dead-time corrections and cuts on the data this method can't be used. An easy, but perhaps not completely accurate way of assigning error bars to this data set is to multiply the error bars by a correction factor until the χ^2 is on average 1 in both spectrometer arms. This has some validity since the error is statistical and ultimately whatever method used to calculate the error would have to have a $\chi^2 \approx 1$.

Both methods of measuring the false asymmetry are within 1.5 σ of zero. The false asymmetry from the scalers is smaller than the false asymmetry from the detector events data, providing evidence that the false asymmetry in the detector events data is a random deviation and not a true false asymmetry. However, there

is no way to tell if that is true and the detector events results are used for the value of the false asymmetry from carbon.

8.4.4 End Window False Asymmetries

The physics asymmetries are measured in such a way to cancel false asymmetries. This is seen in the holding field alignment where a false asymmetry on the order of the carbon false asymmetry canceled because of changing the sign of target and beam polarizations and the two symmetric spectrometer arms. Therefore, any false asymmetry that could enter the physics asymmetry would have to be correlated with these configuration changes.

Another method of measuring the false asymmetries is to measure the asymmetry from scattering off the glass end windows of the cell. This has the advantage of taking data in a manner similar to the physics asymmetry data which can be combined together in the same way. Any false asymmetry that survives will be correlated to the configuration changes. However, the difficulty is getting enough statistics from the end window scattering.

The asymmetry results of end window scattering are shown in Fig. 8.12. The statistical error is not as good as the carbon study and could be improved by widening the cuts on the end windows; however, this creates considerable uncertainty from an unknown amount of polarized ^{3}He contamination. The events accepted in this study include all events outside of the middle of the end window peak in `react_z`.

8.4.5 Calculating Error from False Asymmetry

Interpreting the error from the carbon and end window false asymmetry data is not straight forward. The most relevant result would be from the end window false asymmetry measurements, since this asymmetry measures the false asymmetry correlated with the configuration changes. However, the measurement presented

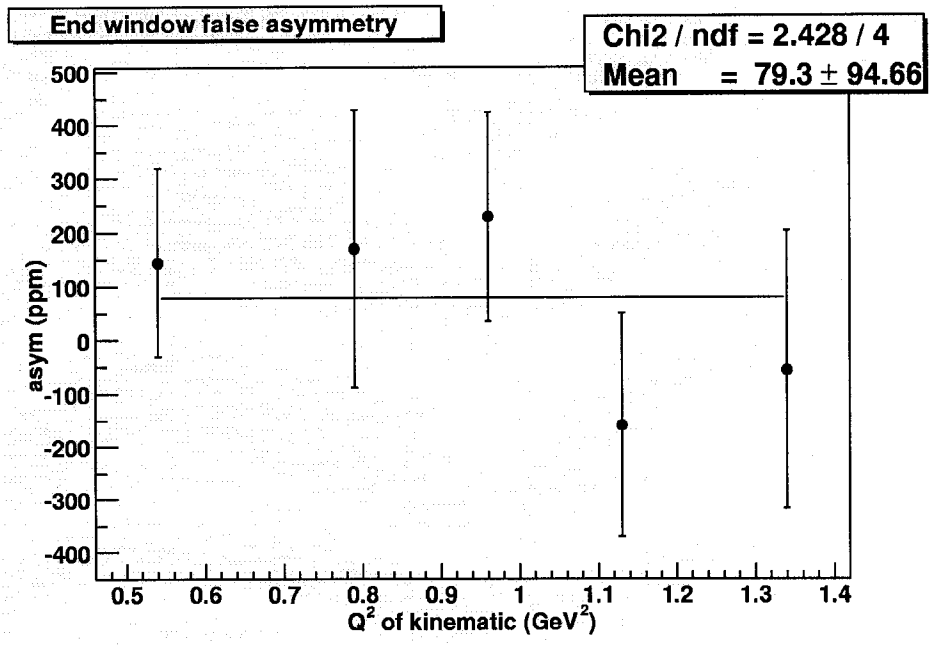

Figure 8.12: *The asymmetry calculated from accepting only events from the glass end windows.*

here is statistically limited and there would always be considerable uncertainty from contamination from polarized ^{3}He scattering. On the other hand, the results from scalers and detector events from the carbon quasi-elastic scattering are more statistically accurate, but any false asymmetry they would measure should cancel using the configuration changes.

It was decided to use 60 ppm as the false asymmetry error on the physics asymmetries, which is the average of the asymmetry in both spectrometer arms in the detector event analysis from carbon quasi-elastic scattering. This was chosen because this was a reasonable estimate of how well the false asymmetry was measured and it was consistent with the end window data analysis.

8.5 Nitrogen Dilution

8.5.1 Using the Reference Cell to Measure the Nitrogen Contribution

The polarized ^{3}He cells contain a small amount of nitrogen to improve the rubidium polarization in the pumping chamber. Events scattering from nitrogen

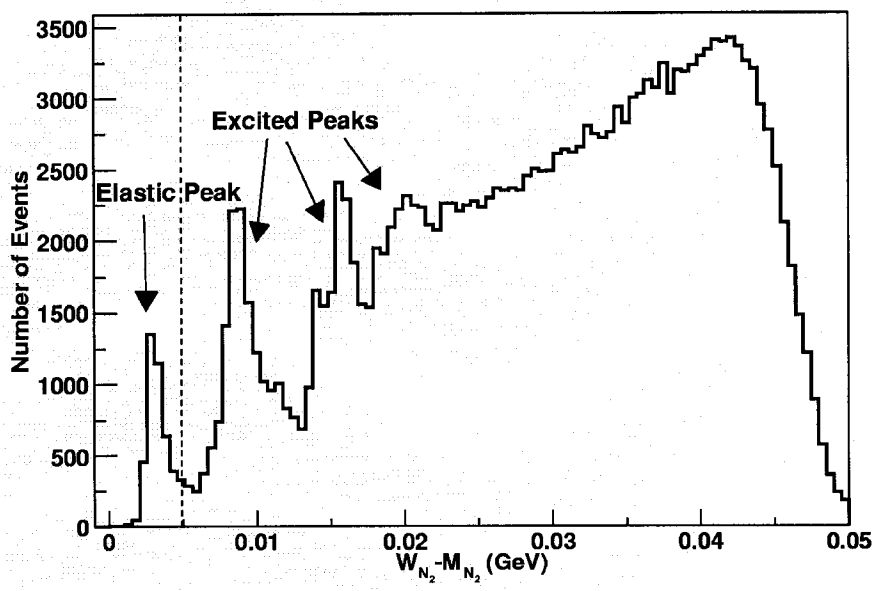

Figure 8.13: *A plot of $W_{N_2} - M_{N_2}$ for a nitrogen reference cell run.*

molecules can't be separated from those scattered from ^{3}He using detector information in the deep inelastic scattering regime. Since the nitrogen cross-section is larger than the ^{3}He cross-section, it contributes significantly to the unpolarized cross-section, thus diluting the asymmetry.

An attempt to measure the amount of nitrogen in the polarized ^{3}He cell was made using data taken on nitrogen in the reference cell. This was done at ^{3}He elastic kinematics so the elastic peak from nitrogen is in the acceptance. The nitrogen elastic peak can be clearly seen in the plot of $W_{N_2} - M_{N_2}$ in Fig. 8.13. This plot can be compared to the plot in Fig. 8.14 which is a set of data with the same cuts and kinematics, but on a polarized ^{3}He cell. The elastic peak of nitrogen is clearly separated from the ^{3}He elastic peak.

By comparing the yield from the elastic peak in the reference cell, which has a known number density, to the yield from the elastic peak in a polarized ^{3}He cell the number density in the polarized cell can be determined. The method used in this

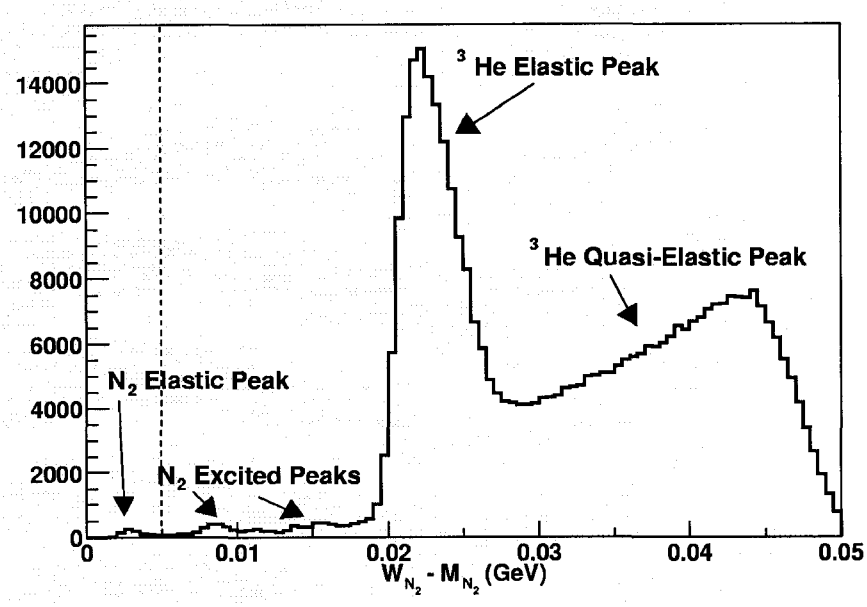

Figure 8.14: *A plot of* $W_{N_2} - M_{N_2}$ *from scattering from a polarized* ^3He *cell.*

analysis is:

$$n_{\text{pol. cell}} = \frac{Y_{\text{pol. cell}}}{Y_{\text{ref.cell}}} n_{ref.\ cell} \tag{8.5}$$

where the yield, Y, can be calculated:

$$Y = \frac{NT_{\text{tot}}}{T_{\text{acc}}Q} \tag{8.6}$$

where N is the number of events in the acceptance cuts, T_{tot} is the total triggers from scalers, T_{acc} is the number of triggers in the N-tuple and Q is the charge during the run. A cut of $W_{N_2} - M_{N_2} < 0.005$ was made to separate the nitrogen elastic peak from the rest of the electron scattering events. $W_{N_2} - M_{N_2}$ can be calculated with kinematic variables:

$$(W_{N_2} - M_{N_2})^2 = M_{N_2}^2 + 2M_{N_2}\nu - Q^2 \tag{8.7}$$

$$\nu = E - E'(1 + \delta p/p) \tag{8.8}$$

$$Q^2 = -\nu^2 + p_x^2 + p_y^2 + p_z^2 \tag{8.9}$$

$$p_x = -E'(1 + \delta p/p)\sin\theta \tag{8.10}$$

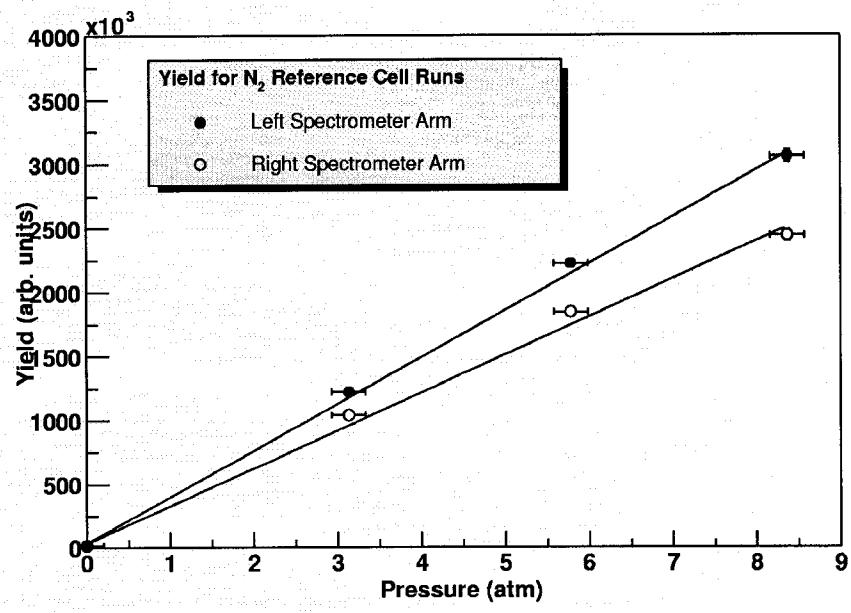

Figure 8.15: *The yield from increasing pressures of nitrogen in the reference cell for both the left and right spectrometer arms.*

$$p_y = -E'(1+\delta p/p)\cos\theta\sin(\phi_0+\phi) \tag{8.11}$$

$$p_z = E - E'(1+\delta p/p)\cos\theta\cos(\phi_0+\phi) \tag{8.12}$$

where M_{N_2} is the mass of nitrogen nucleus (13.047 GeV), E is the beam energy, E' is the central scattering energy, $\delta p/p$ is the relative difference in momentum from the central momentum of the spectrometer, θ is the vertical scattering angle, ϕ_0 is the central horizontal scattering angle of the spectrometer and ϕ is the horizontal scattering angle with respect to ϕ_0. It is important that ϕ_0 is positive for the left spectrometer and negative for the right spectrometer. The rest of the acceptance cuts were made tight since statistics were not a problem and the end window dilution needed to be kept to a minimum.

A plot of the yield for the nitrogen reference cell in the left and right arm is shown in Fig. 8.15. The pressures associated with each run have significant uncertainty since the reference cell leaked. The pressures for the reference cell were measured before and after the run and the leaking was assumed to be linear. The

Source	n_0 (Amagats)	Uncertainty (Amagats)
Left Arm Spectrometer	0.0828	0.083
Right Arm Spectrometer	0.111	0.088
Fill Density	0.0673	0.0034

Table 8.3: *Nitrogen densities extracted from elastic scattering data compared with nitrogen density measured during the cell fill.*

runs were short so the leakage wasn't large ($\approx 10\%$) during each run and the beam current was steady.

These plots can be used to calculate the pressure from nitrogen in the polarized ^{3}He cell. The fits to these curves are:

$$\begin{aligned} p_{\text{left}} &= 3.649 \times 10^5(\pm 7.9 \times 10^3) Y_{\text{left}} \text{ (atm/arb.units)} \\ &\quad +3.49 \times 10^5(\pm 3.5) \text{ atm} \end{aligned} \tag{8.13}$$

$$\begin{aligned} p_{\text{right}} &= 2.961 \times 10^5(\pm 6.6 \times 10^3) Y_{\text{right}} \text{ (atm/arb.units)} \\ &\quad +3.26 \times 10^4(\pm 2.9 \times 10^4) \text{ atm} \end{aligned} \tag{8.14}$$

where p is the nitrogen pressure from the yield on the left and right arm. Unfortunately, both fits show a significant background with a significant error in it. This would be okay if the nitrogen to be measured had a high pressure, but since it is a low pressure it creates a significant uncertainty in the measurement. The source of this background is unknown and warrants further investigation if this technique is going to be used in the future.

Using this fit and the yield extracted with the exact same cuts from the polarized ^{3}He runs, one can calculate the nitrogen number density. The results are shown in Table 8.3. To translate pressure into number density a reference cell temperature of 30 °C was used. The numbers extracted from this method agreed well with the number from the nitrogen density calculated from the time of the cell filling. This fill density is the same as presented in section 6.6.9, only for nitrogen. Because the fill density number is so much more accurate than the result from this technique, it

Kinematic (GeV^2)	Left f	Right f	Avg f	Uncertainty
Elastic	0.985	0.985	0.985	0.005
0.565	0.952	0.951	0.952	0.005
0.768	0.956	0.959	0.958	0.005
0.930	0.957	0.958	0.958	0.005
1.107	0.965	0.957	0.961	0.005
1.317	0.908	0.928	0.918	0.010

Table 8.4: *Dilution factors for the 5 kinematic points and the elastic scattering kinematic. Left and right refer to the left and right spectrometer arms.*

is used for the nitrogen dilution for the deep inelastic scattering data.

8.5.2 Dilution Factor from Fill Density

The dilution factor for all kinematics is calculated with

$$f = \frac{Y_{^3\mathrm{He}}}{Y_{^3\mathrm{He}} + Y_{\mathrm{N}_2}} = 1 - \frac{Y_{\mathrm{N}_2}^{\mathrm{ref.}}}{(Y_{^3\mathrm{He}} + Y_{\mathrm{N}_2})} \frac{n_{\mathrm{pol.}}}{n_{\mathrm{ref.}}} \tag{8.15}$$

where $Y_{\mathrm{N}_2}^{\mathrm{ref.}}$ is the yield from a nitrogen reference run, $Y_{^3\mathrm{He}} + Y_{\mathrm{N}_2}$ is the yield from a polarized ^{3}He cell with nitrogen in it, $n_{\mathrm{pol.}}$ is the nitrogen density in the polarized ^{3}He cell and $n_{\mathrm{ref.}}$ is the density of the nitrogen in the reference cell when the yield was extracted from it. The yields on the reference cell are extracted with the same cuts as from the polarized ^{3}He cell. The results of these calculation are presented in Table 8.4.

The dilution factor for the 1.317 GeV^2 kinematic is significantly lower because Virginia One has twice as much nitrogen (0.102 Amagats) in it than Shapiro (0.0552 Amagats).

8.6 Elastic Asymmetry Check

To check that everything in the asymmetry analysis is working correctly, a measurement of a known asymmetry is performed and compared to a simulation. During the commissioning period of the experiment, the polarized elastic asymmetry was measured at $E = 1.197$ GeV, $\phi_0 = 18.6°$ and $E' = 1.1950$ GeV.

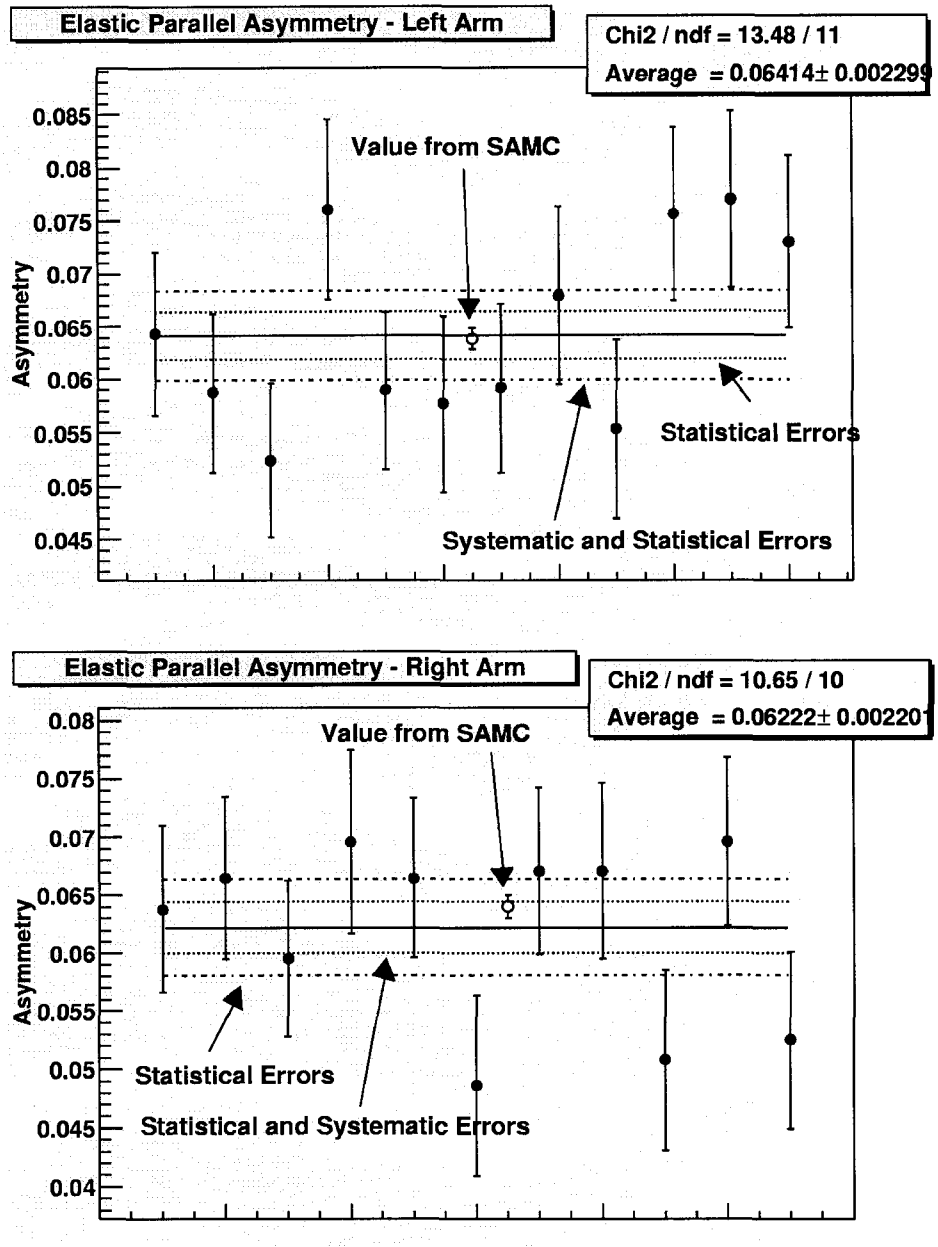

Figure 8.16: *The elastic measured in both spectrometers and compared to the simulated value from SAMC.*

The results of this measurement are shown in Fig. 8.16. The measured asymmetries were corrected for target polarization, dilution factor and beam polarization. The combined systematic and statistical error on the measurement was 6.7%.

The results of these measurements were compared to a value of SAMC (Single-Arm Monte Carlo), a simulation program written by Alexandre Deur specifically designed for simulating elastic scattering from the polarized ^{3}He target in Hall A [82]. It takes beam parameters, cell information and spectrometer settings, the world data of elastic form factors and simulates the experimental data including radiative corrections. More about this simulation can be found in [41], [74] and [82].

There is very good agreement between the simulation and the data taking during the commissioning period of E97-103. This increases the confidence in the DIS asymmetries measured in the experiment.

8.7 Final Corrected Asymmetries

The charge and dead-time corrected ^{3}He asymmetry measurements and the ^{3}He asymmetries corrected for target and beam polarization and dilution factor are presented in Table 8.5. The asymmetries were extracted using techniques presented in this chapter.

Q^2 (GeV^2)	$A_{\parallel}^{raw}$	Stat. Err.	$A_{\perp}^{raw}$	Stat. Err.
0.565	-0.00466	0.00032	0.00087	0.00011
0.768	0.00538	0.00044	-0.00105	0.00016
0.930	0.00438	0.00040	-0.00105	0.00015
1.107	-0.00478	0.00038	0.000582	0.00015
1.317	-0.00505	0.00046	0.000570	0.00016
Q^2 (GeV^2)	$A_{\parallel}$	Stat. Err.	$A_{\perp}$	Stat. Err.
0.565	-0.0156	0.0013	0.00371	0.00054
0.768	-0.0162	0.0015	0.00352	0.00058
0.930	-0.0148	0.0015	0.00363	0.00059
1.107	-0.0140	0.0013	0.00196	0.00055
1.317	-0.0151	0.0015	0.00182	0.00055

Table 8.5: *Tables of the ^{3}He physics asymmetries measured in E97-103. The top table has raw asymmetries which have only been corrected for dead-time and charge. The lower table asymmetries have been corrected for target polarization, beam polarization and dilution factor.*

CHAPTER 9

Radiative Corrections

9.1 Introduction to Radiative Corrections

In fixed-target inclusive electron scattering, the cross-section is measured by counting the rate of electrons that scatter from a target into a certain angle and momentum from an electron beam of known current and energy. The cross-sections computed from the spin-structure functions in Chapter 2 assume that the only interaction made by the scattered electron is a one-photon exchange with the target as represented by Fig. 9.1. Due to both experimental conditions and unavoidable consequences of QED, electrons can lose energy both before and after scattering from the target. This results in a measured cross-section different from the one-photon exchange cross-section (or Born cross-section, as it is commonly called). Fortunately, the various processes that produce the energy loss in the electrons are known and can be calculated. Adjustments made from these calculations to extract the Born cross-section are known as *radiative corrections.*

Radiative corrections are split into two types *internal* and *external.* Internal radiative corrections result from inherent complications in electron scattering such as

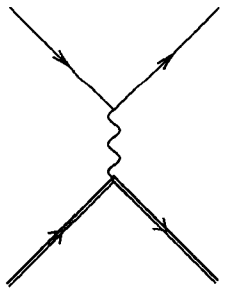

Figure 9.1: *Lowest-order electron scattering diagram.*

vacuum polarization and electron vertex corrections. External corrections are from electron interactions with material in the electron's path. A further contribution to the radiative corrections results from electrons that lose enough energy to undergo elastic and quasi-elastic scattering and end up in the acceptance of deep inelastic scattering. Because these types of scattering can be separated from the inelastic cross-section, their corrections are calculated independently.

Since E97-103 is a precision measurement of small asymmetries, accurate calculations of the radiative corrections is critical to reducing the final uncertainties. The world data, in particular the Jefferson Lab E94-010 experiment data set, was used to create the most accurate models possible to do the corrections. Nevertheless, because there are gaps and uncertainty in the world data, as much effort as creating the models must go into estimating the uncertainties resulting from them.

9.2 Methods of Calculating Radiative Corrections

9.2.1 Internal Radiative Corrections

The Born term is the leading order, and dominant term, in the QED perturbative expansion of the electron scattering cross-section. The next order involves interference terms between the Born scattering diagram and four higher-order diagrams [23]. The four diagrams are vertex corrections, two external leg corrections and the vacuum polarization. The vertex corrections and two external leg corrections contain infrared divergences that can be canceled by including bremsstrahlung diagrams. The calculations of these terms is complex, but well-known. A detailed discussion of these calculations can be found in [23].

The internal radiative corrections in this analysis were calculated using POLRAD 2.0 [83]. This program is based on radiative techniques developed in references [84] and [85]. It was chosen because it could handle both unpolarized radiative corrections and polarized radiative corrections.

However, for this analysis the models for the structure functions in POLRAD 2.0 needed to be updated with the latest data. For the inelastic calculations, this consisted of a straight-forward replacement of the structure functions in the code with improved fits to world data. However, for quasi-elastic scattering, the radiative procedure needed to be modified to incorporate quasi-elastic peaks of a finite width. This modified version of POLRAD 2.0 was written by Seonho Choi [20] for the E94-010 analysis and slight modifications were made by myself for this analysis. It was used only for the quasi-elastic and elastic tail calculations.

9.2.2 External Radiative Corrections

External radiative corrections result from electron interactions with matter, before and after scattering from the target. The majority of the external radiative correction is the energy loss from bremsstrahlung (electron straggling), but a small amount is also from energy loss due to ionization.

The method of calculating the external radiative corrections in this analysis was based on the work of Mo and Tsai [86] and developed further by Stein, *et al* [87]. This method uses the peaking approximation, which states that while many electrons lose energy to bremsstrahlung before or after scattering from the target, a negligible amount experience bremsstrahlung both before *and* after scattering from the target. This is true if the radiation length of material in the electron path is small.

The calculation of the external radiative corrections requires the internally radiated cross-section. For unpolarized scattering, an internal radiator can be used to calculate the internal cross-section as described by Mo and Tsai [86]. However, for a polarized cross-section, calculations from POLRAD are necessary.

The materials in the electron path for E97-103 are listed in Table 9.1 [88]. The average radiation length used for the incident electron path is 0.00781 cm. The

Before Scattering off Target			
Material	Rad. Length (g/cm^2)	Density (g/cm^3)	Thickness
Beryllium	65.19	1.848	16 mils (0.0406 cm)
Air	36.66	0.001205	5 cm
Aluminum	24.01	2.7	15 mils (0.0381 cm)
Cell End Window	19.5	2.76	0.0120 cm
^{3}He in cell	67.42	0.001374	20.0 cm
After Scattering off Target			
Material	Rad. Length (g/cm^2)	Density (g/cm^3)	Thickness
^{3}He in cell	67.42	0.001374	$0.8675/\sin\phi$ cm
cell wall	19.5	2.76	$0.145/\sin\phi$ cm
^{4}He	94.32	0.0001249	45.7 cm
Aluminum	24.01	2.7	15 mils (0.0381 cm)
Air	36.66	0.001205	65.1 cm
Kapton	40.56	1.42	14 mil (0.0356 cm)
Titanium	16.17	4.54	4 mil (0.0102 cm)

Table 9.1: *A list of materials and their radiation lengths and densities in the incident and scattering electron path, where ϕ is the central angle of the spectrometer.*

average radiation length used for the scattering electron path is 0.0750 cm for 18.6° and 0.0860 cm for 15.8°. The error on the incident path radiation length is $\approx 3\%$. The error on the scattering path radiation length is $\approx 10\%$. These errors are mostly due to uncertainties in the thickness of the materials in the electron path.

9.2.3 The Radiative Corrections Procedure

To use POLRAD to calculate radiative corrections, one gives the beam energy, x and $y = \nu/E$ as input, and POLRAD will calculate the internal radiative corrections to the unpolarized, longitudinally polarized and transversely polarized cross-sections. The external radiative corrections require a significant amount of cross-section information to be calculated; consequently, the internal cross-section needs to be calculated for many kinematics.

This calculation is based on models of the structure functions, which are based on the world data. If the Born cross-section plus the radiative correction does not agree with the experimental data, the model can be adjusted in areas where there is

Cross-section	$Q^2 = 0.54$	0.77	0.93	1.14	1.34 GeV^2
Internal Unpol.	1.052	0.4129	0.2258	0.1693	0.0966
Total Unpol	0.8547	0.3158	0.1791	0.1332	0.0767
Internal Long. Pol.	-0.0778	-0.0292	-0.0187	-0.01324	-0.0086
Total Long. Pol.	-0.0632	-0.0222	-0.0147	-0.0100	-0.0067
Internal Trans. Pol.	-0.0475	-0.0187	-0.0135	-0.0091	-0.0066
Total Trans. Pol.	-0.0397	-0.0148	-0.0109	-0.0071	-0.0054

Table 9.2: *Elastic tails for the five E97-103 kinematic points. All cross-sections are in nb/(GeV-Sr).*

uncertainty in the world data until the corrections agree with the experiment. This process usually requires several iterations to get the model and experimental data to agree.

9.3 Elastic and Quasi-Elastic Radiative Corrections

9.3.1 Elastic Radiative Corrections

The Born elastic cross-section is a delta function at $W^2 = M^2$, but because of radiative corrections can contribute at deep inelastic kinematics. However, in the case of E97-103 the contribution is small.

The ^{3}He elastic radiative corrections are calculated from the form factors in reference [16]. The internal radiation procedure was performed by Seonho Choi's modified edition of POLRAD 2.0. The external radiative corrections were calculated using the peaking approximation method presented in S. Stein,*et al* [87]. The results are presented in Table 9.2.

The uncertainty of the elastic tail calculations is estimated to be 10%. The major source of uncertainty is the knowledge of the radiation length. Other uncertainties include approximations made in the radiative procedure and knowledge of the ^{3}He form factors.

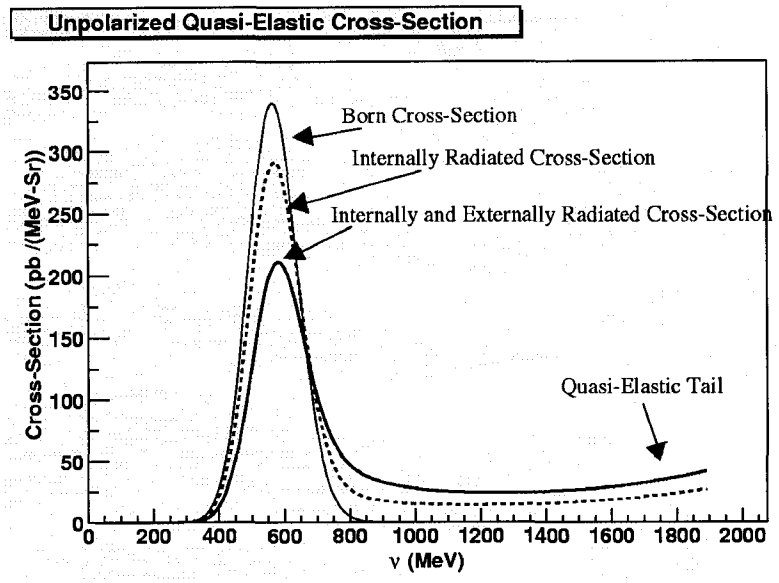

Figure 9.2: *A plot of the Born, internally radiated and externally radiative unpolarized quasi-elastic cross-section.*

9.3.2 Unpolarized Quasi-Elastic Cross-section

The quasi-elastic tail contributes substantially to the cross-section at E97-103 kinematics. To calculate the unpolarized part of the tail, a modified version of the QFS model developed by Lightbody and O'Connell [18, 89] was used. The cross-sections in the QFS model are derived from nucleons in carbon nuclei and additional modifications are necessary to model the ^{3}He nuclei. This has been done by Karl Slifer for the E94-010 analysis [90]. The modifications adjust the Q^2 dependence of the height of the quasi-elastic peak to fit the quasi-elastic data taken in E94-010. This version of the code is referred to as NQFS. Calculations of the unpolarized quasi-elastic internal and external radiative tail from NQFS are presented in Fig. 9.2.

The NQFS model for the unpolarized quasi-elastic cross-section was inserted into the modified version of POLRAD 2.0. This was done to increase confidence in the modified code, which has no cross-check for polarized radiative corrections. The calculations of the unpolarized tail from NQFS and the modified version of

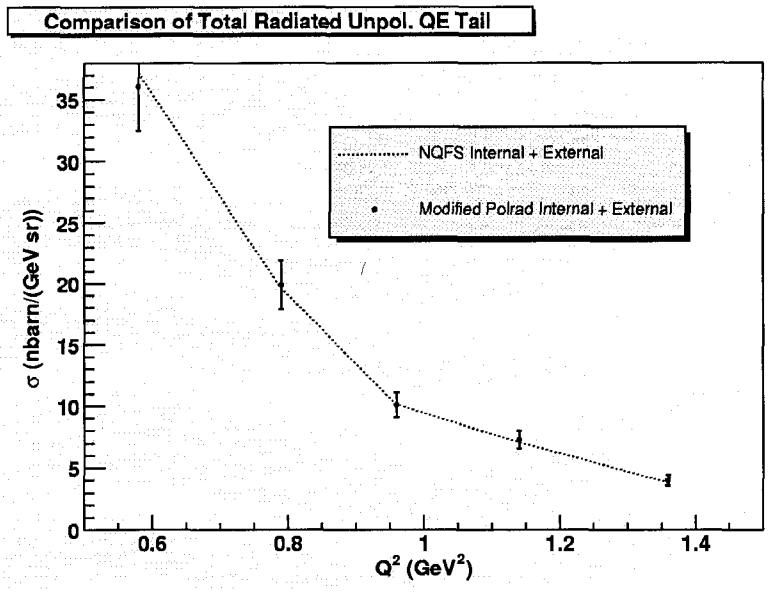

Figure 9.3: *Comparison of calculations based on E94-010 data and NQFS model calculations for the unpolarized QE tail.*

Cross-section	$Q^2 = 0.54$	0.77	0.93	1.14	1.34 GeV^2
Int. Unpol. QE	25.52	14.68	7.90	5.88	3.33
Tot. Unpol. QE	36.06	19.88	10.08	7.26	3.99

Table 9.3: *A list of the unpolarized tails from the quasi-elastic cross-section. Both the internal and total (internal + external) contributions are listed. All cross-sections are in units of nbarn/(GeV-Sr).*

POLRAD are shown in Fig. 9.3. The total corrections for both methods agree to the 3% level. This also builds confidence in that the procedure for calculating external radiative corrections, which is used for elastic, quasi-elastic and inelastic corrections, is correct.

The results from these calculations are listed in Table 9.3. The uncertainty in these calculations is 10% due to uncertainties in the external radiatve corrections, unpolarized quasi-elastic cross-section and radiative procedure.

9.3.3 Polarized Quasi-Elastic Radiative Corrections

The polarized quasi-elastic cross-sections were calculated based on a model of the E94-010 data for $g_1^{^3\mathrm{He}}$ and $g_2^{^3\mathrm{He}}$. This model is a fit of a Gaussian distribution

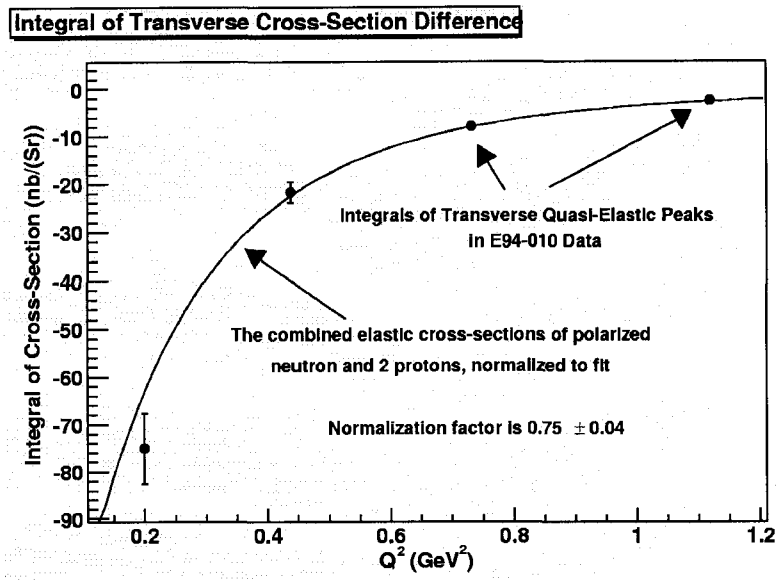

Figure 9.4: *Comparison of transverse polarized cross-section from E94-010 and model of the polarized quasi-elastic cross-section.*

to the quasi-elastic peak in both the longitudinal and tranverse cross-section differences, calculated from $g_1^{^3\mathrm{He}}$ and $g_2^{^3\mathrm{He}}$ for four values of Q^2. These integrals of the Gaussian in ν vs. Q^2 are fit using:

$$I(Q^2) = -A(P_n \Delta\sigma_n^{\mathrm{elas}}(Q^2) + 2P_p \Delta\sigma_p^{\mathrm{elas}}(Q^2)) \tag{9.1}$$

where A is a normalization factor, P_n is the polarization of the neutron in polarized ^{3}He, $\Delta\sigma_n^{\mathrm{elas}}$ is the polarized part of the elastic cross-section for the neutron, P_p is the proton polarization in ^{3}He and $\Delta\sigma_p^{\mathrm{elas}}$ is the polarized part of the elastic cross-section for the proton.

For the fit of the transverse cross-section $A = 0.745 \pm 0.037$ as shown in Fig. 9.4. This is suprising since it is expected to be near 1.0. There are a few effects that could decrease the quasi-elastic cross-section from the polarized elastic such as final state interactions and meson-exchange effects, but they are expected to be a less than a 10% effect. There is uncertainty in the fit to the E94-010 data at the 10-15% level, due to the error bars in the data and the fact that the quasi-elastic peak is not exactly Gaussian [91]. It is possible that these errors could be the

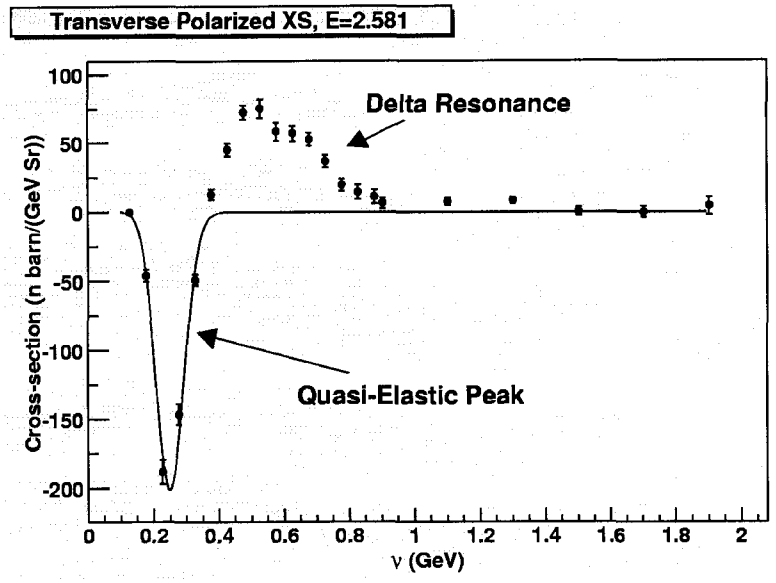

Figure 9.5: *Comparison of Transverse Polarized Cross-section from E94-010 and model of the polarized quasi-elastic cross-section.*

source of the discrepancy. A similar set of fits were done with the longitudinal cross-section differences, but since the longitudinal cross-section was significantly smaller it doesn't bring any insight into the problem. This analysis uses this normalization factor for both the longitudinal and transverse polarized quasi-elastic tail.

This Q^2 dependence of the width of quasi-elastic peak in the transversely polarized cross-section is:

$$w = (0.0185 \pm 0.0027 \text{ GeV}) + (0.0501 \pm 0.0054/\text{GeV})Q^2 \qquad (9.2)$$

where w is the width of the Gaussian fit to the transverse quasi-elastic peaks. A study of the quasi-elastic tail at E97-103 kinematics showed that large variations of the width had very small effects on the tail as long as the integral of the quasi-elastic peak was the same. Therefore the uncertainty in the width has little effect on the calculation of the quasi-elastic contribution. A comparison of the model using these fits to the E94-010 data is shown in Fig. 9.5.

Table 9.4 lists the contributions of the polarized quasi-elastic tail to the cross-section at E97-103 kinematics. The error in these tails is estimated to be 20% based

Cross-section	$Q^2 = 0.54$	0.77	0.93	1.14	1.34 GeV^2
Int. Trans. QE	-0.551	-0.309	-0.186	-0.128	-0.082
Tot. Trans. QE	-0.894	-0.482	-0.271	-0.182	-0.112
Int. Long. QE	0.186	0.102	0.071	0.049	0.036
Tot. Long. QE	0.247	0.131	0.084	0.056	0.040

Table 9.4: *Internal and total (internal+external) radiative tails from transverse and longitudingal polarized quasi-elastic scattering. All cross-sections in nb/(GeV-Sr).*

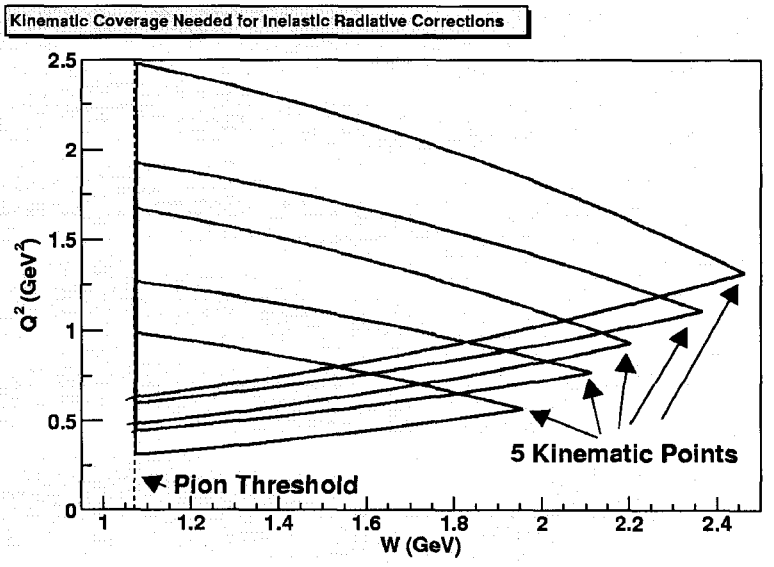

Figure 9.6: *The triangles represent the kinematic coverage needed for internal and external radiative corrections for the kinematic points of E97-103 at the right-hand corner of the triangle.*

on uncertainty in the model and uncertainty in external radiative corrections.

9.4 Inelastic Radiative Corrections

9.4.1 Models for Radiative Corrections

The accuracy of the inelastic radiative corrections depends on the quality of the models for the structure functions. The kinematic region the models need to cover is shown in Fig. 9.6. A section of the resonance region of this plot was measured experimentally by the Jefferson Lab E94-010 collaboration [62]. This, combined with the significant amount of world data in the DIS region, formed the basis of the models used to calculate radiative corrections. Table 9.5 list all the models used.

Struct. Func.	Kinematic region	Source
$F_2^{^3He}$	$Q^2 > 1.7$ GeV^2	NMC Fits for F_2^D and F_2^p [92] JLab E94-110 fits for F_2^p [93]
$F_2^{^3He}$	$Q^2 < 1.7$ GeV^2	E97-103 fit to of E94-010 unpol. data
R	All Q^2	JLab Hall C fit [93] SLAC R1998 fit [32]
$g_1^{^3He}$	$Q^2 > 1.7$ GeV^2	E99-117 fit g_1/F_1 [41] for proton and neutron
$g_1^{^3He}$	$Q^2 < 1.7$ GeV^2	E97-103 fit to E94-010 $g_1^{^3He}$
$g_2^{^3He}$	$Q^2 > 1.7$ GeV^2	g_2^{WW} from g_1 fit above
$g_2^{^3He}$	$Q^2 < 1.7$ GeV^2	E97-103 fit to E94-010 $g_2^{^3He}$

Table 9.5: *Source of models for structure functions used for the radiative corrections for E97-103.*

While the E94-010 data has been analyzed, no appropriate fit had been made of the data that could be used for the radiative corrections of E97-103. The data set consisted of unpolarized cross-sections, $g_1^{^3He}$ and $g_2^{^3He}$ for 6 beam energies and a spectrometer angle of 15.5° [62]. Therefore, considerable effort went into creating a usable interpolation of these data sets. In the case of the unpolarized data, $F_2^{^3He}$ was extracted from the unpolarized cross section data by using the world fit to R and then the fit was made to $F_2^{^3He}$.

The model of each of the three sets was constructed the same way. The data for the structure function for each beam energy was plotted vs. W. Looking at the plot in Fig. 9.7, these fits were made along the slanted lines connecting the dots. A fit was made of each plot with a series of second-order polynomial and Gaussian fits. No effort was made to assume any particular shape in the plots. The emphasis was on creating a smooth fit to the data with no bumps or kinks.

It would be possible to interpolate the data from these fits alone, but two problems occur. The first is that strong discontinuities can occur away from where the data set lies, particularly in regions at the edge of each data set in W. The second is that the E97-103 data need to be put into the model and it does not sit

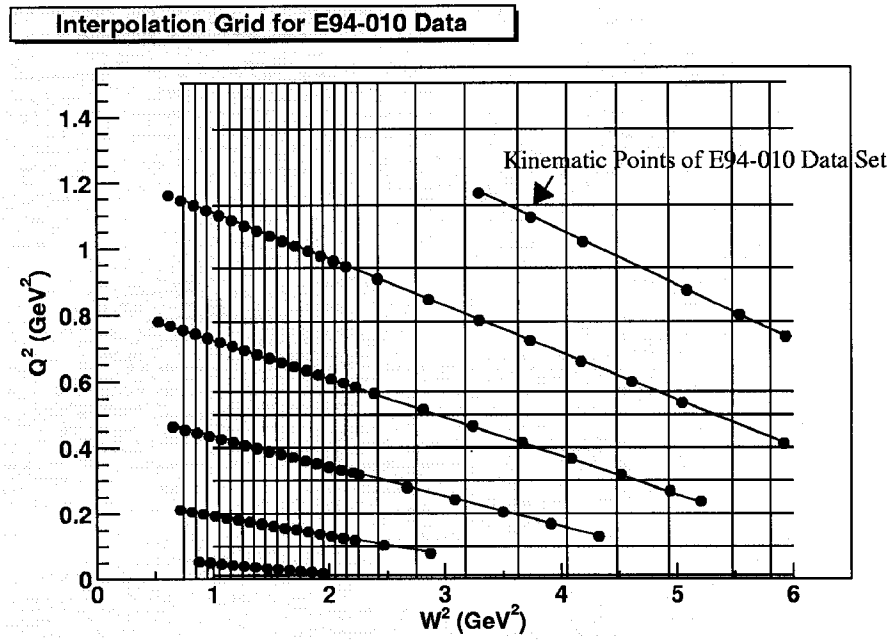

Figure 9.7: *The grid used for interpolating the E94-010 data set.*

on any one of these lines due to kinematic differences. Therefore a more robust technique is required.

The technique chosen was to use these fits to create data sets at constant W, represented by the vertical lines in Fig. 9.7. Each constant W data set had 5-7 points corresponding to 4-6 intersections of the E94-010 data plus a data point at 1.7 GeV^2 from the DIS fits to ensure a smooth transition between the regions. Fits were made of this data by using a string of 2nd order polynomials and exponential fits. Again an emphasis on smoothness of the fit was made. This was done for 26 values of W for the three structure function data sets.

Again, this is an adequate basis to do interpolation, but the variation between fits at different W's created many unphysical bumps in the structure functions. Therefore, another fit was done at constant values of Q^2, which correspond to the horizontal lines in Fig. 9.7. Each fit along constant Q^2 included 26 points, one from each W fit. Five of the constant Q^2 values were chosen to correspond to the five data points in E97-103. The fits along Q^2 were made of Gaussian and polynomial fits to

the points. Again an emphasis on smoothness and physical shapes was maintanined.

Once the set of fits at constant Q^2 were made, a code was written to interpolate between the fits at any x, and Q^2 below 1.7 GeV^2. The fits are merged with the higher Q^2 data by using a set of data at $Q^2 = 1.7$ GeV^2, from the higher Q^2 fits, in the interpolation. The interpolation is done by a routine based on the `polint` routine in *Numerical Recipes in C* [73]. The results of this interpolation can be compared back to the E94-010 data to see the sucess of the interpolation. The unpolarized data from E94-010 is plotted in Fig. 9.8 with the interpolation of the $F_2^{^3He}$ data and the world fit for R used to calculate the unpolarized cross-section. A comparison of the interpolations of $g_1^{^3\mathrm{He}}$ and the E94-010 data is shown in Fig. 9.9. A similar comparison for $g_2^{^3\mathrm{He}}$ is made in Fig. 9.10.

9.4.2 Summary of Inelastic Corrections

POLRAD 2.0 gives the radiative correction for the unpolarized, longitudinally polarized and tranversely polarized cross-sections. An example plot of the Born cross-sections and the internally radiated cross-sections for a constant beam energy and spectrometer angles corresponding to the first kinematic is shown in Fig. 9.11. These were calculated for all five kinematics and are presented in Table 9.6.

The uncertainty in the inelastic corrections is determined by varying the model in different ways and seeing what range of values the corrections produce in that cross-section. One has to do this in a way that the radiative corrections produce the correct experimental asymmetries from the model and can't vary significantly from the world data. From these studies it was found there was at most a 7% uncertainty in the final cross-section due to uncertainties in the radiative corrections.

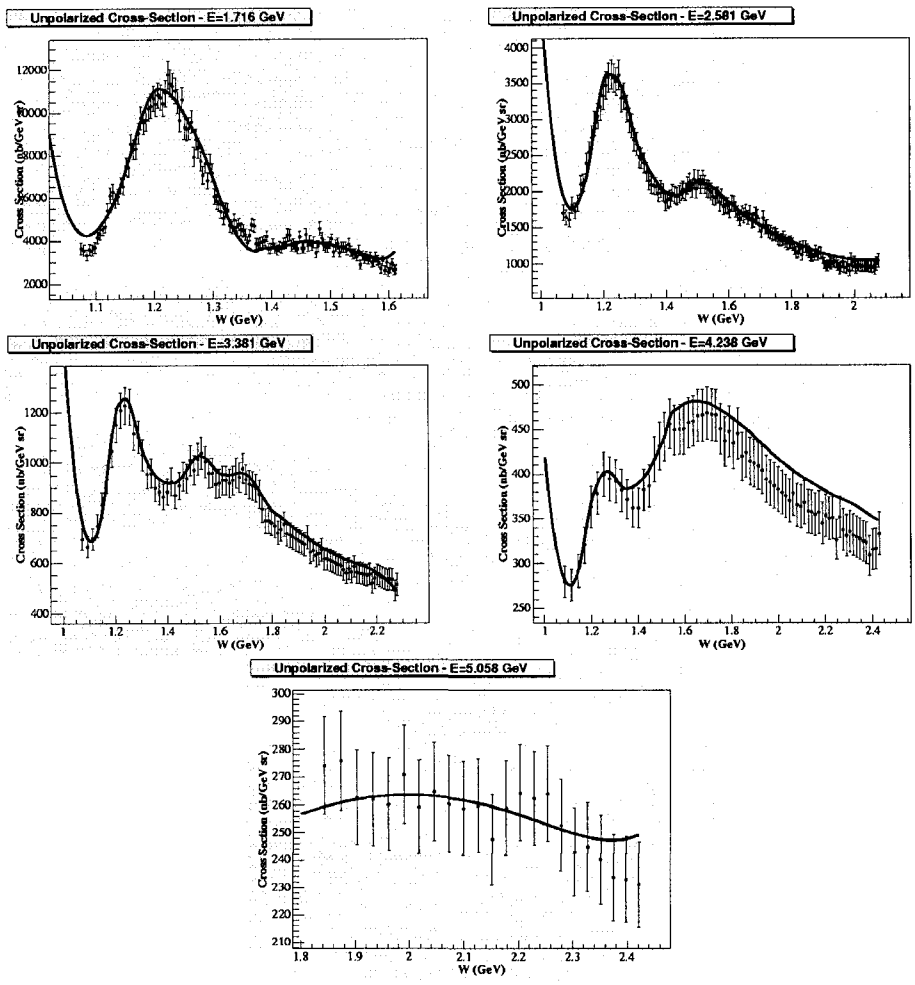

Figure 9.8: *Comparison plots between the E94-010 unpolarized cross-section and cross-section calculated from an interpolation of* $F_2^{^3\mathrm{He}}$.

Cross-section	$Q^2 = 0.54$	0.77	0.93	1.14	1.34 GeV^2
Unpol Born.	329	308	165.7	176.9	92.0
Unpol Int.	376	348	185.6	197.82	102.7
Unpol Tot.	400	361	192.1	202	104
Long. Pol. Born	-7.58	-5.83	-3.46	-3.11	-1.80
Long. Pol. Int	-8.06	-6.15	-3.68	-3.36	-1.95
Long. Pol. Tot.	-7.69	-5.68	-3.54	-3.25	-1.89
Trans. Pol. Born	1.47	1.54	0.929	0.467	0.244
Trans. Pol. Int.	2.11	1.86	1.05	0.650	0.270
Trans. Pol. Tot.	2.55	1.90	1.01	0.607	0.326

Table 9.6: *A table of the Born cross-sections from the models of the structure functions and the internal and total (internal+external) radiated cross-sections. All cross-sections in nbarn/(GeV-Sr).*

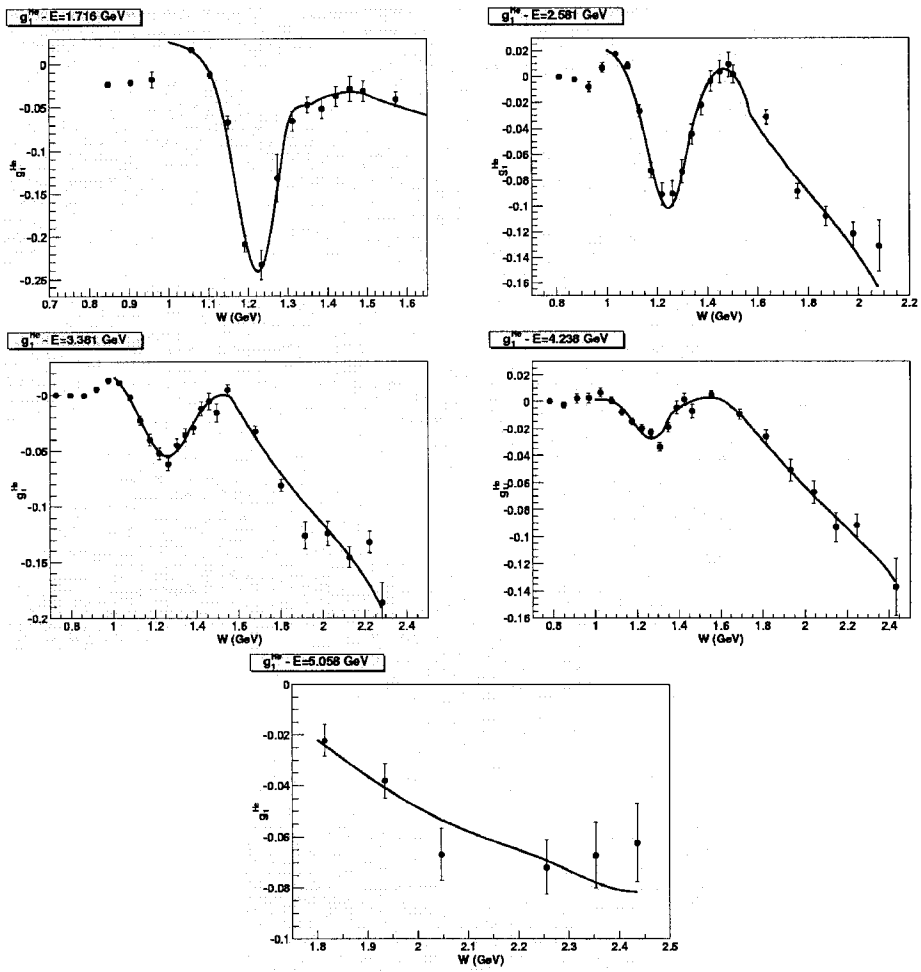

Figure 9.9: *Comparison plots between the E94-010 $g_1^{^3He}$ and an interpolatiation. The fits stop at the pion threshhold.*

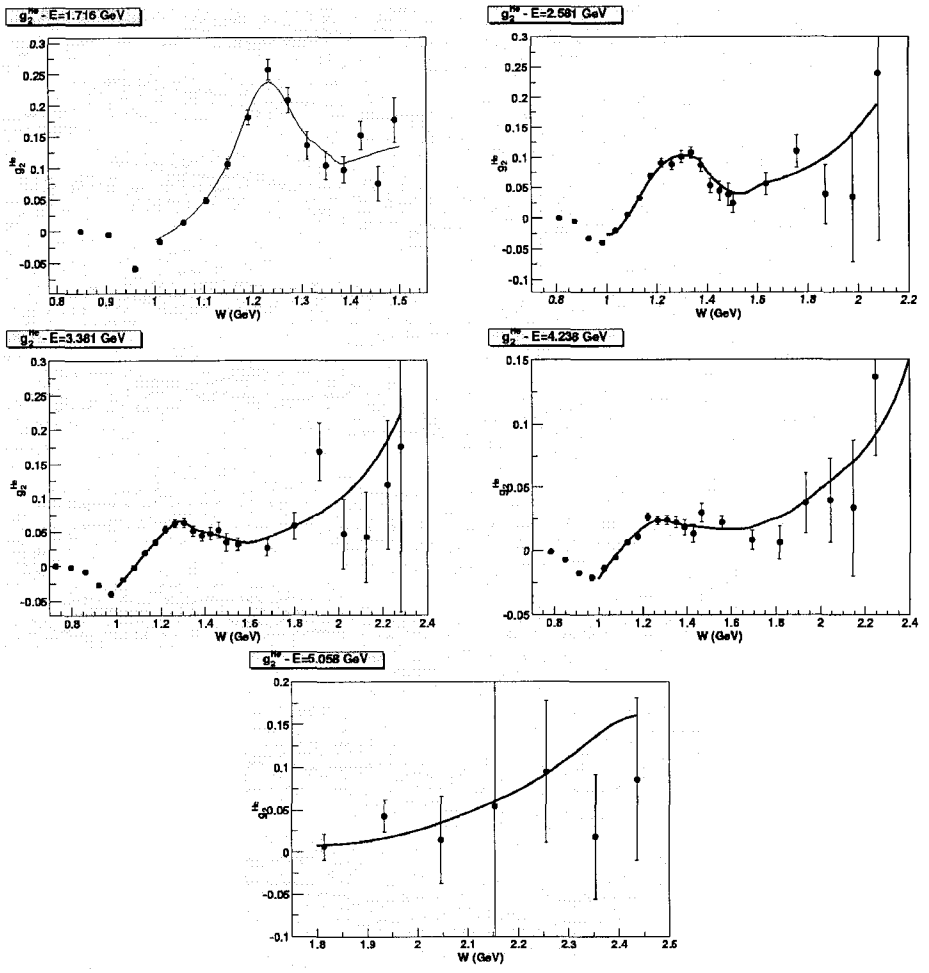

Figure 9.10: *Comparison plots between the E94-010 $g_2^{^3He}$ and an interpolatiation. The fits stop at the pion threshhold.*

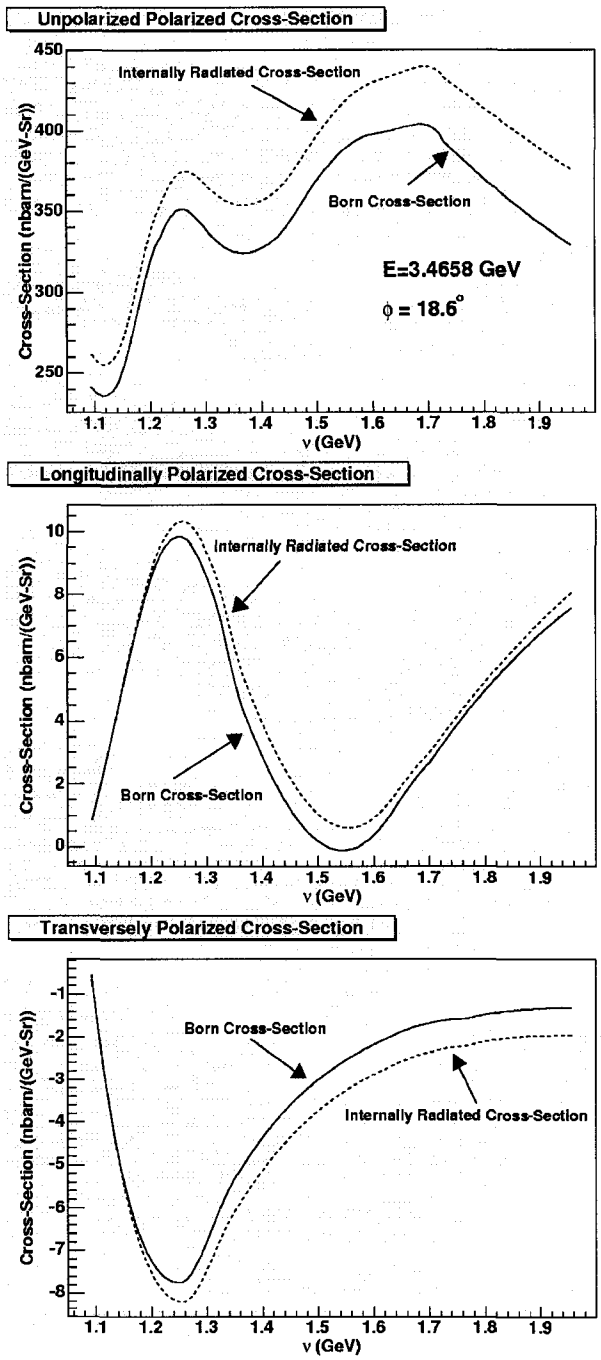

Figure 9.11: *Plots of the Born and internally radiated cross-section for the* $Q^2 = 0.57$ *GeV*^{2} *kinematic.*

CHAPTER 10
Unpolarized Cross-sections

10.1 The Need for Unpolarized Cross-section

The spin structure function $g_2^n(x, Q^2)$ is extracted from the change in the cross-section as a result of a change in target or beam polarization. As has been stated previously, this experiment extracts an asymmetry from the data and uses an unpolarized cross-section to get the desired polarized cross-section differences. This is method is easier than calculating the polarized cross-sections for each configuration individually since the asymmetry requires no knowledge of the acceptance and the unpolarized cross-section can be extracted with precision using only a small part of the acceptance, or from world data. In this chapter, the unpolarized cross-section is extracted from the data taken during E97-103 and compared to existing data.

10.2 The Experimental Unpolarized Cross-sections

10.2.1 Elastic Cross-section

The first step in extracting the unpolarized cross-sections is to use the experimental data taken at ^{3}He elastic scattering kinematics and compare them to the SAMC simulation, which was also used to calculated the elastic asymmetry in section 8.6. This will provide a reliable check of many parameters that go into calculation of the unpolarized cross-section. The SAMC simulation uses up-to-date values for the the ^{3}He elastic form-factors [16] combined with the best information about the spectrometer optics and has been cross-calibrated with other optics data for the E94-010 experiment [74, 82]. This simulation will be used to determine the acceptance of the spectrometers.

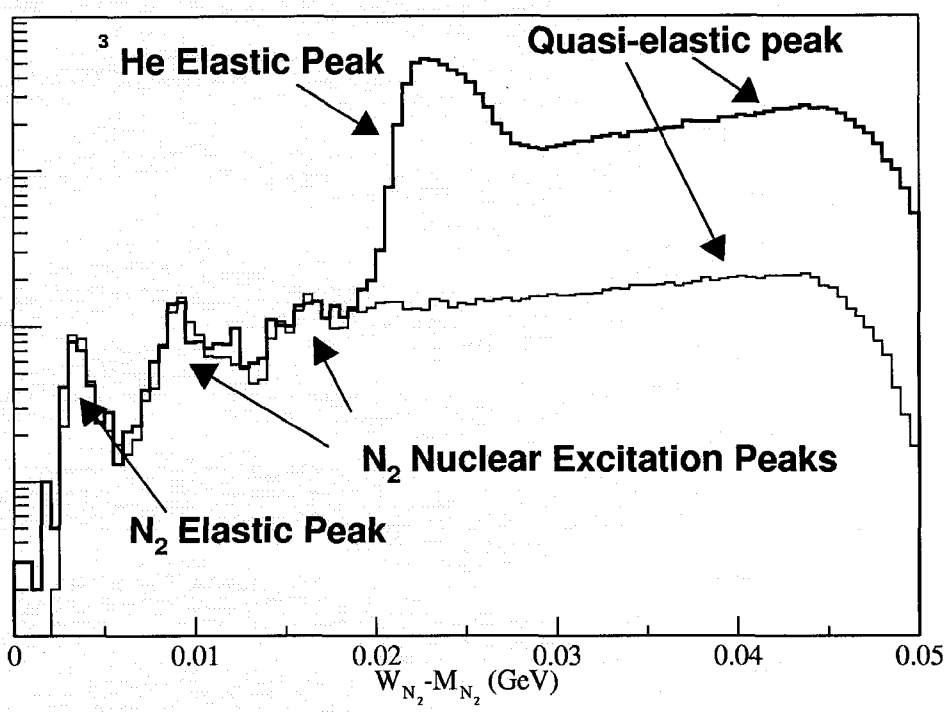

Figure 10.1: *A comparison of the missing mass spectrum of the ^{3}He target with a nitrogen run taken with the reference cell. The nitrogen data has been scaled so that the N_2 elastic peak is the same size in both histograms. This scaling factor is used to subtract nitrogen events from the ^{3}He elastic cross-section data.*

To compare the experimental data with the simulation, one must first subtract events from the small amount of nitrogen in the polarized target cell. The procedure for doing this is to decide on a set of cuts in $\phi_{\rm tgt}$, $\theta_{\rm tgt}$, $y_{\rm tgt}$ and for particle identification. Then $W_{\rm N_2} - M_{\rm N_2}$ is plotted for both the ^{3}He elastic data and a nitrogen reference cell run with these cuts, as shown in Fig. 10.1. The nitrogen data is weighted by a scaling factor so that the nitrogen elastic peaks are the same size in both data sets. Whenever a histogram of the ^{3}He elastic data is made, the correct number and correct distribution of nitrogen events can be subtracted from the histogram using the reference cell data times this scaling factor. Since the dilution factor in the nitrogen data is 2-3% this is a sufficiently accurate method of nitrogen background subtraction.

Once the nitrogen subtraction is done, histograms of the parameters in the experimental data can be compared to histograms from the simulation. To do a direct comparison one must weigh the events by their cross-section divided by the number of events in each histogram. For the simulation this is straight-forward since the cross-section is included for each event in the output N-tuple. For the experimental data one needs to weigh it by the average cross-section which can be calculated with

$$\sigma = \frac{N^{\rm data}}{(Q/e)\eta_{\rm dt}\eta_{\rm pid}\eta_{\rm track}\eta_{\rm trig.}} \frac{N^{\rm MC}_{\rm tot.}}{N^{\rm MC}_{\rm accp.}\rho_{\rm tgt}d_{\rm tgt,il}\Delta\phi_{\rm il}\Delta\theta_{\rm il}} \tag{10.1}$$

where $N^{\rm data}$ is the number of events in the experimental data with all cuts applied, (Q/e) is the charge delivered to target measured by the BCMs divided by the electron charge, $\eta_{\rm dt}$ is the correction for dead-time, $\eta_{\rm pid}$ is the correction for particle identification detector inefficiency, $\eta_{\rm track}$ is the correction for VDC tracking inefficiency, $\eta_{\rm trig.}$ is the correction factor for scintillator trigger inefficiency, $N^{\rm MC}_{\rm tot}$ is the number of events simulated in the SAMC simulation, $N^{\rm MC}_{accp.}$ is the number of events in the SAMC simulation that fall within the cuts on the experimental data, $\rho_{\rm tgt}$

is the number density of the target, $d_{\mathrm{tgt,il}}$ is the illuminated target length in the SAMC simulation, $\Delta\phi_{\mathrm{il}}$ is the illuminated ϕ acceptance of the spectrometer in the SAMC simulation and $\Delta\theta_{\mathrm{il}}$ is the illuminated θ acceptance of the spectrometer in the SAMC simulation. The "illuminated" parameters tell the simulation over what range to generate Monte Carlo events and therefore should be larger than the cuts made to the experimental data.

There are many subtle adjustments to be made to get the histograms of the different parameters in the experimental data and the simulation to match. The inputs that can be adjusted in the simulation are the spectrometer angle and central momentum, the radiation length of the material both before and after scattering, and incident beam energy. The shape of the elastic cross-section parameters are sensitive enough that changes within the experimental errors of these input variables make significant changes to the shape of the simulated data. Therefore, this exercise provides a lot of additional information about the experimental configuration that can be used later in the extraction of deep inelastic unpolarized cross-sections.

A tight cut around the central part of the spectrometer was found to provide the best matching and enough precision to compare to simulation. A comparison of the simulated data to the experimental data for the left and right spectrometer is shown in Fig. 10.2 and Fig. 10.3. The width of the histograms reflect the cuts made on the experimental and simulated data. These cuts will be used to calculate the unpolarized cross-sections for the deep inelastic data. To the eye, there is good agreement between the scattering parameters ϕ, θ, y and $\delta p/p$; however, there is a slight difference in the plot of $W_{^3\mathrm{He}} - M_{^3\mathrm{He}}$. Its likely a subtle difference in radiation lengths between the simulation and the experimental data, since the elastic peak in W is very sensitive to these values.

The average cross-section from the experimental data is compared to the average cross-section from the SAMC simulation in Table 10.1 and the systematic errors

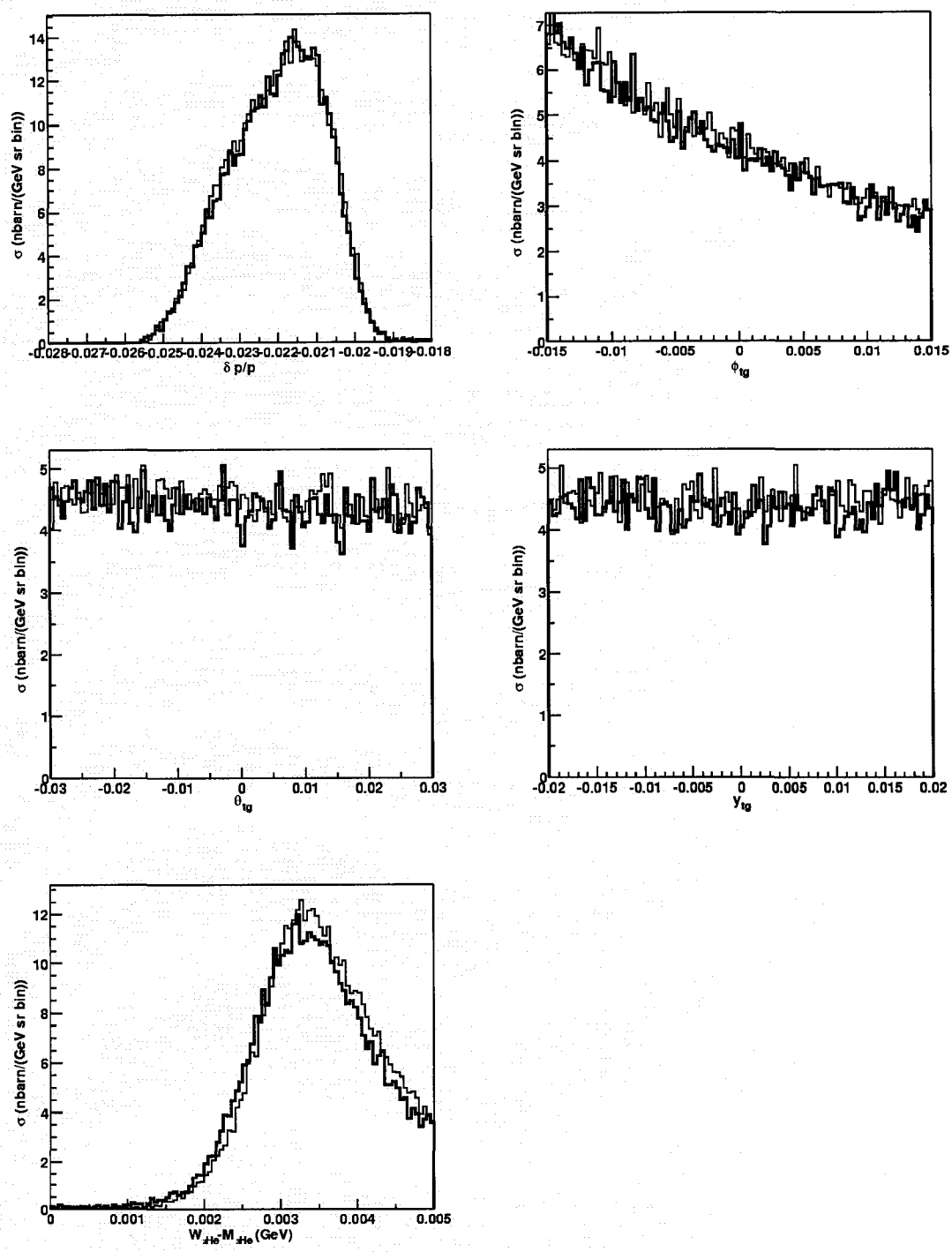

Figure 10.2: *A comparison of the scattering parameters of the nitrogen-subtracted experimental data (thick line) and the SAMC simulation (thin line) for the left HRS. The width of the histograms reflect the cuts made on the data for the average cross-section.*

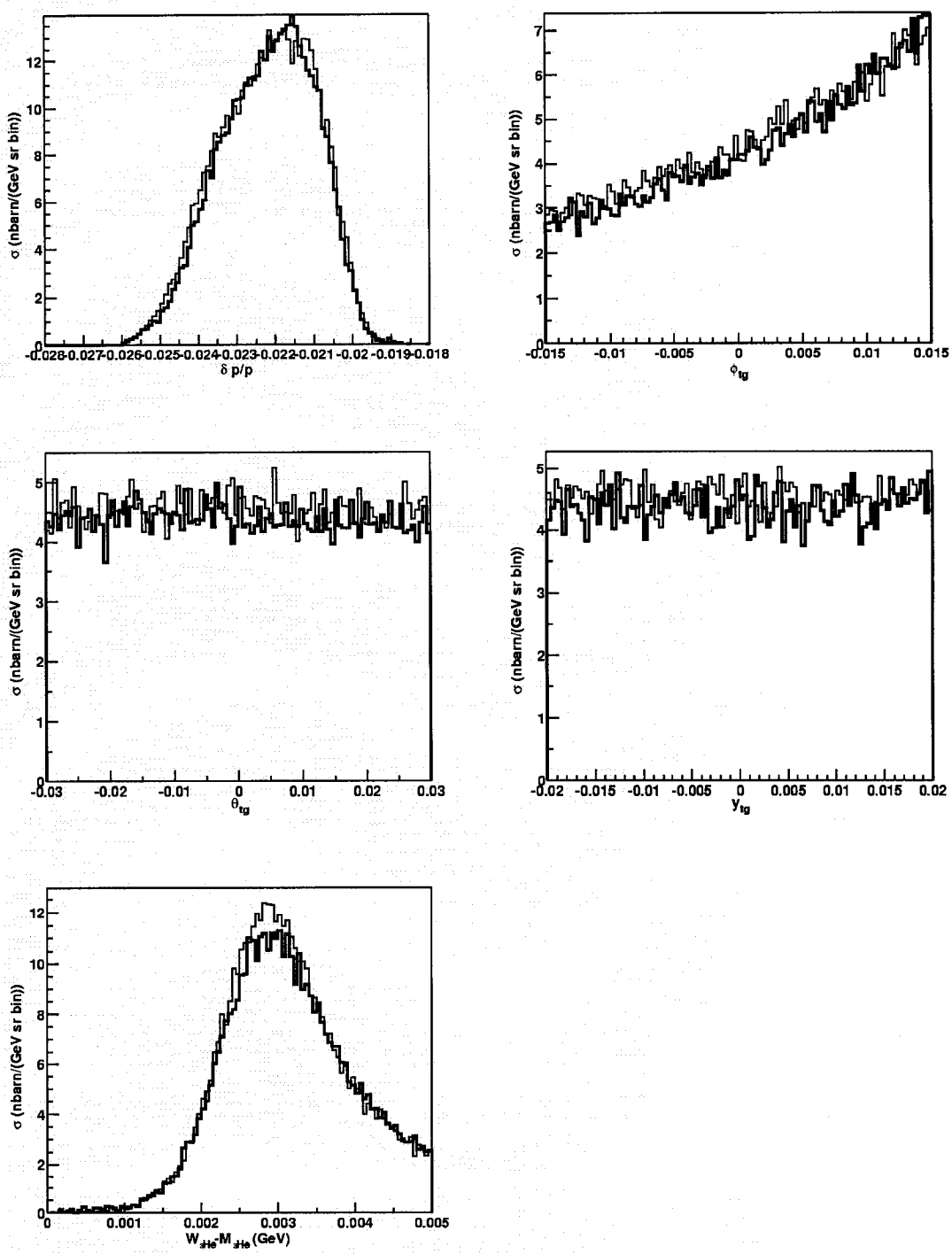

Figure 10.3: *A comparison of the scattering parameters of the nitrogen-subtracted experimental data (thick line) and the SAMC simulation (thin line) for the right HRS. The width of the histograms reflect the cuts made on the data for the average cross-section.*

	Left HRS (nbarn/sr)	Right HRS (nbarn/sr)
Simulation	456±22	459±22
Exp. Data	449±27	455±27

Table 10.1: *Values for the ^{3}He elastic cross-section for each spectrometer arm compared to values from the SAMC simulation. The systematic errors are shown. The statistical errors are negligible.*

Parameter	Systematic Error
Statistical Uncertainty	negl.
Beam Current	1.0%
Dead Time	negl.
PID Inefficiency	1.0%
Trigger Inefficiency	0.5%
Tracking Inefficiency	0.5%
$N_{\rm tot}^{\rm MC}/N_{\rm accp}^{\rm MC}$	5.0%
Target Density	3.0%
Total Systematic Error	6.0%

Table 10.2: *Contributions to the systematic error on average ^{3}He elastic cross-section from experimental data.*

for the experimental cross-section are broken down in Table 10.2. The agreement is good between experiment and simulation. The dominant error in the experimental cross-section comes from $N_{\rm tot}^{\rm MC}/N_{\rm accp}^{\rm MC}$ which represents the acceptance of the spectrometer as given by the optics description in SAMC. This ratio is sensitive to the kinematic inputs, radiation lengths and ^{3}He form factors to SAMC. The error is calculated by varying these values within their experimental values. The systematic error on the average cross-section from the simulation is due to uncertainty in these parameters as well.

10.2.2 Deep Inelastic Unpolarized Cross-sections

The average value for the DIS unpolarized cross-section is calculated in a similar way to the elastic cross-section. The cross-section is given by

$$\frac{d\sigma}{dE'd\Omega} = \frac{N^{\rm data}}{(Q/e)\eta_{\rm dt}\eta_{\rm pid}\eta_{\rm track}\eta_{\rm trig.}} \frac{N_{\rm tot}^{MC}}{N_{\rm accp.}^{\rm MC}\rho_{\rm tgt}d_{\rm tgt,il}\Delta p_{\rm il}\Delta\phi_{\rm il}\Delta\theta_{\rm il}} \tag{10.2}$$

Q^2 (GeV^2)	Left Arm (nbarn/(GeV sr))	Right Arm (nbarn/(GeV sr))	Average (nbarn/(GeV sr))
0.57	443±27	459±28	451±27
0.78	340±34	379±38	360±36
0.94	186±11	192±12	189±11
1.13	174±17	190±19	182±18
1.34	93±10	102±10	98±10

Table 10.3: *Experimental values for the unpolarized cross-section. The systematic errors are shown. The statistic error is negligible.*

where the only difference from the elastic cross-section is the momentum illumination, $\Delta p_{\rm il}$ is included. The simulation is used just to get the phase space acceptance of the spectrometer and requires no radiative corrections.

Since two of the kinematics ($Q^2 = 0.57$ GeV^2 and 0.94 GeV^2) were taken at the same spectrometer configuration as the elastic data, the kinematic parameters from the elastic analysis can be used for the deep-inelastic SAMC simulation. However, after these two kinematics the spectrometer angle was changed and there is no elastic data to check the spectrometer angle and central momentum. Therefore, those three kinematics points will have an increased uncertainty due to lack of knowledge of the acceptance.

The unpolarized cross-sections for the left and right spectrometers are listed in Table 10.3 along with their systematic error. The error for the kinematics $Q^2 = 0.57$ GeV^2 and $Q^2 = 0.94$ GeV^2 are set at 6.0% as they have the same set of errors that the elastic cross-section had. The left and right arm of the two spectrometers for these two kinematics agree well within the 5.0% error on the acceptance. The other three kinematics have large discrepancies between the left and right arms. It is likely these three points have acceptance problems, as this is the only distinct difference between the two points with the elastic scattering data and these three points, and the uncertainty on the accepatance has been increased to 10%

10.3 Unpolarized Cross-Section from World Data

The E94-010 experiment in Hall A has a set of unpolarized data on ^{3}He in the resonance region and a fit made to this data is described in Section 9.4.1. This fit can be used to calculate an unpolarized cross-section. To extract cross-section differences from the data one needs to add radiative corrections to the Born cross-section, which has also been done in Section 9.4.1.

The E94-010 data set is not ideal for calculating the unpolarized cross-section. This is because the coverage of the data was dense around the resonance region and significantly more sparse in the deep inelastic scattering region where the E97-103 data was taken. Because of the lack of constraint in the region where data is available, there is significant uncertainty in the interpolation. Also, the E94-010 data set does not go far beyond a $Q^2 > 1.0$ GeV^2. There are two Q^2 points in the E97-103 data set that are above this Q^2.

An alternative to using the E94-010 data set is to use the NMC and E94-110 fits for the proton and deuterium. These are already being used in the fit made for E94-010 data for data with a $Q^2 > 1.7$ GeV^2. However, the data for the NMC and E94-110 goes on below that. In particular, the Whitlow *et al* data from SLAC [94, 95, 96] has precision proton and deuterium data for F_2 and R down to a $Q^2 = 0.69$ GeV^2 at an $x \approx 0.2$. This covers all, but the lowest Q^2 point.

However, combining proton and deuterium data to get ^{3}He cross-sections introduces some uncertainty due to nuclear interactions. In the deep inelastic region, nuclear effects are expected to be small and therefore the proton and deuterium structure functions can be used. However, in the resonance region the difference between ^{3}He cross-sections and cross-sections calculated from proton and deuterium data is significant. In particular, the resonances get smeared out in ^{3}He because of the Fermi motion of the nucleons. Experiment E97-103 is in the deep inelastic

Born Cross-sections		
Q^2 (GeV^2)	E94-010 ^{3}He Interpolation (nbarn/(GeV sr))	NMC/JLab Proton and Deuterium Fits (nbarn/(GeV sr))
0.57	329±33	363±18
0.78	308±36	342±17
0.94	166±17	171±9
1.13	177±18	174±9
1.34	92±9	90±5
Cross-sections with Radiative Corrections		
Q^2 (GeV^2)	E94-010 ^{3}He Interpolation (nbarn/(GeV sr))	NMC/JLab Proton and Deuterium Fits (nbarn/(GeV sr))
0.57	436±34	470±18
0.78	381±32	420±17
0.94	202±17	213±10
1.13	208±18	210±10
1.34	108±11	111±7

Table 10.4: *A comparison of the unpolarized cross-sections for the E94-010 interpolation and the NMC/Jlab proton and deuterium fits. The top section lists just the Born cross-section and the corresponding systematic errors. The bottom section lists cross-section with radiative corrections along with the corresponding systematic error. Statistical error is negligible in both sections.*

scattering region, but a significant portion of the radiative corrections come from the resonance region especially in the Q^2 points below 1.0 GeV^2. Therefore, there are reasons that the unpolarized cross-section calculated from proton and deuterium data might disagree with unpolarized cross-sections measured on ^{3}He.

Looking at Table 10.4, one can see that there is some disagreement between the Born cross-sections for the lowest two Q^2 points in the E97-103 data set. The higher Q^2 cross-sections are in better agreement, but that is expected since the E94-010 interpolation merges into the NMC/JLab fits at $Q^2 > 1.0$ GeV^2. To get the cross-section needed to extract g_2^n, the results of these fits will have to be merged with the experimental data for the best estimate of the unpolarized cross-sections.

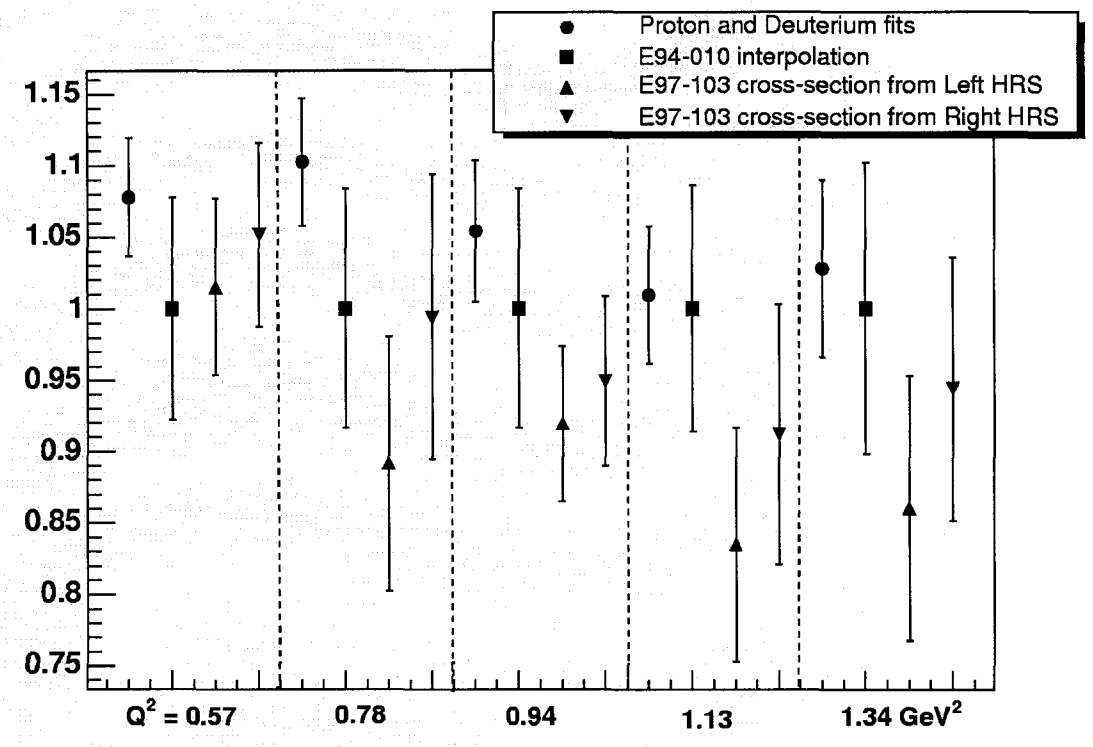

Figure 10.4: *A comparison of the different values for the unpolarized cross-section for all five kinematic points. The values and their error bars have been normalized to E94-010 interpolation value.*

Q^2 (GeV^2)	Cross-section (nbarn/(GeV sr))
0.57	458±27
0.78	398±32
0.94	199±12
1.13	201±16
1.34	105±8

Table 10.5: *Values used for the unpolarized cross-sections and their systematic errors.*

10.4 Combining World Data with E97-103 Data

The experimental values for the unpolarized cross-section are plotted along with the calculations from the world data in Fig. 10.4. The calculations from world data include radiative corrections calculated in Chapter 9. For all but the highest Q^2 kinematic, the data from the NMC/JLab fits have the highest cross-section. Also, the cross-section from the left arm spectrometer, especially in the data that was not checked by elastic scattering is systematically lower than the other values.

However, there is no real reason to dismiss any of these values. Since the data is in deep inelastic the proton and deuterium structure functions should work taking in account a certain amount of error for radiative corrections. In fact, the best agreement is at the lowest kinematic where one would expect the nuclear effects to be largest. However, there is no reason to exclude the experimental data especially with a large error for the acceptance. In particular, there is disagreement between the NMC/JLab fits and the experimental data in the $Q^2 = 0.94$ GeV^2 kinematic where the experimental acceptance has been checked with elastic scattering.

Because of this, the final value for the cross-section is a weighted average of the NMC/JLab fits, the E94-010 interpolation and the E97-103 experimental values for the left and right spectrometers. The error bar on the unpolarized cross-section is chosen to cover the spread of the data. In the case of the two kinematics where there is elastic data to check the acceptance, the error bar is left at the experimental value of 6.0%. In the other three cases, the error on the unpolarized cross-section is

set at 8.0%. A table of the final values are shown in Table 10.5.

CHAPTER 11

Results and Systematic Errors

11.1 Summary of Parameters and Their Systematic Errors

Table 11.1 lists all the parameters used to calculate the structure functions in E97-103 and the absolute values for their errors. The only value left out is the false asymmetry which is an additional 60 ppm error on the raw asymmetry. The source of these values and their errors are mentioned elsewhere in the thesis.

11.2 Extracting $g_1^{^3He}$ and $g_2^{^3He}$

To calculate $g_1^{^3He}$ and $g_2^{^3He}$ from the experimental data, the longitudinal and transverse cross-sections must be calculated using the unpolarized cross-section and radiative tails must be subtracted. The method for doing this in E97-103 is

$$\Delta\sigma_{||} = \sigma_{\text{Unpol.}} A_{||} - \Delta\sigma_{||}^{\text{Inelas.}} - \Delta\sigma_{||}^{\text{QE}} - \Delta\sigma_{||}^{\text{Elas.}} \tag{11.1}$$

$$\Delta\sigma_{\perp} = \sigma_{\text{Unpol.}} A_{\perp} - \Delta\sigma_{\perp}^{\text{Inelas.}} - \Delta\sigma_{\perp}^{\text{QE}} - \Delta\sigma_{\perp}^{\text{Elas.}} \tag{11.2}$$

where $\Delta\sigma_{||}$ and $\Delta\sigma_{\perp}$ refer to the polarized radiative tails for the longitudinal and transverse polarized target respectively. The two cross-section differences can be used to calculate $g_1^{^3He}$ and $g_2^{^3He}$ with

$$g_1^{^3He} = \frac{2EE'\sin\theta\Delta\sigma_{||} + Q^2\Delta\sigma_{\perp}}{\eta E'\sin\theta\left[Q^2 + 2E(E + E'\cos\theta)\right]} \tag{11.3}$$

$$g_2^{^3He} = \frac{-E'Q^2\sin\theta\Delta\sigma_{||} + (E + E'\cos\theta)Q^2\Delta\sigma_{\perp}}{2xM\eta E'\sin\theta\left[Q^2 + 2E(E + E'\cos\theta)\right]} \tag{11.4}$$

$$\eta = \frac{2\alpha^2 E'}{M\nu Q^2 E}. \tag{11.5}$$

The results for $g_1^{^3He}$ and $g_2^{^3He}$ are presented in Table 11.2.

Parameter	$Q^2 = 0.57$	0.78	0.94	1.13	1.34 (GeV^2)
$A_{\|\|}$ (Stat. Err.)	-0.00466 ±0.00032	-0.00438 ±0.00044	-0.00538 ±0.00040	-0.00478 ±0.00038	-0.00505 ±0.00046
$A_{\perp}$ (Stat. Err.)	0.00087 ±0.00011	0.00105 ±0.00015	0.00105 ±0.00016	0.00058 ±0.00015	0.00058 ±0.00016
P_{beam}	0.693 ±0.028	0.766 ±0.031	0.766 ±0.031	0.816 ±0.033	0.816 ±0.033
P_{tgt}	0.361 ±0.013	0.398 ±0.014	0.412 ±0.015	0.384 ±0.014	0.404 ±0.015
N_2 Dilution	0.952 ±0.005	0.958 ±0.005	0.957 ±0.005	0.961 ±0.005	0.918 ±0.010
E (GeV)	3.4658 ±0.003	4.5983 ±0.0014	4.5983 ±0.0014	5.7269 ±0.0011	5.7269 ±0.0011
E' (GeV)	1.6000 ± 0.00016	2.2900 ±0.0005	1.9900 ±0.0005	2.6300 ± 0.0005	2.2700 ±0.0005
θ (Degrees)	18.606 ±0.06	15.810 ±0.06	18.606 ±0.06	15.810 ±0.06	18.596 ±0.06
Unpol. XS ($\frac{\text{nbarn}}{\text{GeV sr}}$)	458 ±18	398 ±17	199 ±8.6	201 ±8.7	105 ±4.5
T. Pol. Inelas. Tail ($\frac{\text{nbarn}}{\text{GeV sr}}$)	1.08 ±0.19	0.37 ±0.09	0.11 ±0.04	0.10 ±0.05	0.12 ±0.03
T. Pol. QE Tail ($\frac{\text{nbarn}}{\text{GeV sr}}$)	-0.89 ±0.18	-0.48 ±0.10	-0.27 ±0.05	-0.18 ±0.04	-0.040 ±0.008
T. Pol. Elas. Tail ($\frac{\text{nbarn}}{\text{GeV sr}}$)	-0.040 ±0.004	-0.015 ±0.002	-0.011 ±-0.001	-0.0071 ±0.0007	-0.0054 ±-0.00054
L. Pol. Inelas. Tail ($\frac{\text{nbarn}}{\text{GeV sr}}$)	-0.11 ±0.18	0.15 ±0.08	0.08 ±0.08	-0.14 ±0.03	0.09 ±0.02
L. Pol. QE Tail ($\frac{\text{nbarn}}{\text{GeV sr}}$)	0.25 ±0.08	0.13 ±0.04	0.084 ±0.025	0.056 ±0.017	0.040 ±0.012
L. Pol. Elas. Tail ($\frac{\text{nbarn}}{\text{GeV sr}}$)	-0.063 ±0.01	-0.022 ±0.0033	-0.015 ±0.022	-0.0100 ±0.015	-0.0067 0.001
P_n	0.86 ±0.04	0.86 ±0.04	0.86 ±0.04	0.86 ±0.04	0.86 ±0.04
P_p	-0.028 ±0.009	-0.028 ±0.009	-0.028 ±0.009	-0.028 ±0.009	-0.028 ±0.009
g_1^p	0.140 ±0.026	0.175 ±0.026	0.195 ±0.026	0.210 ±0.026	0.220 ±0.026
g_2^p	0.035 ±0.015	0.011 ±0.015	-0.002 ±0.015	-0.012 ±0.015	-0.021 ±0.015

Table 11.1: *A list of the parameters used to calculate the results of E97-103 and their absolute errors.*

Q^2 (GeV^2)	x	$g_1^{^3He}$	Stat. Err.	Sys. Err.
0.57	0.16	-0.0754	0.0051	0.0065
0.78	0.18	-0.0684	0.0072	0.0071
0.94	0.19	-0.0643	0.0047	0.0055
1.13	0.19	-0.0612	0.0047	0.0059
1.34	0.20	-0.0560	0.0048	0.0056
Q^2 (GeV^2)	x	$g_2^{^3He}$	Stat. Err.	Sys. Err.
0.57	0.16	0.065	0.008	0.011
0.78	0.18	0.072	0.011	0.012
0.94	0.19	0.0706	0.0080	0.0078
1.13	0.19	0.0457	0.0082	0.0070
1.34	0.20	0.0422	0.0078	0.0069

Table 11.2: *Values for $g_1^{^3He}$ and $g_2^{^3He}$ for E97-103.*

11.3 Extracting Neutron Structure Functions from ^{3}He

The best method available for extracting the structure functions for the neutron from ^{3}He data comes from Bissey *et al* [17]. However, there are effects that appear in data points below $x \approx 0.2$ that aren't taken into account into these corrections. The most prominent one would be the anti-shadowing effect. It is thought since the E97-103 data lie in the deep inelastic scattering region and lie just on the edge of the $x = 0.2$ that anti-shadowing corrections would be small. There is presently no calculation available to quantify this, but it is an active area of research and hopefully will be sorted out by theorists in the near future.

The equations given by Bissey et al [17] are

$$g_1^n = \frac{1}{P_n + 0.056}\left[g_1^{^3He} + (0.014 - 2P_p)g_1^p\right] \quad (11.6)$$

$$g_2^n = \frac{1}{P_n + 0.056}\left[g_2^{^3He} + (0.014 - 2P_p)g_2^p\right] \quad (11.7)$$

where P_n and P_p are the effective neutron and proton polarization in ^{3}He. g_1^p is calculated from a fit in the E99-117 analysis [41]. g_2^p is calculated from $g_2^{p\ WW}$ as mentioned below.

The neutron and proton polarization in ^{3}He has been the subject of considerable

study that is summarized Bissey *et al* [17]. An estimate of the average value and uncertainty in the different calculations for P_n and P_p has been done by Xiaochao Zheng in her thesis [41] and the results are:

$$P_n = 0.86^{+0.036}_{-0.02},\ P_p = -0.028^{+0.0094}_{-0.004}. \tag{11.8}$$

11.4 Using Parton Distributions to Calculate g_2^{WW} and g_1^n

Higher twist effects cannot be identified in g_2^n unless there is an accurate calculation of g_2^{WW}. The method used for calculating g_2^{WW} in E97-103 was to use the parton distributions of Blümlein and Böttcher [97]. These parton distributions match the higher Q^2 data for g_1^n and can be evolved down to E97-103 kinematics using DGLAP evolution [97]. This calculation of $g_2^{n\ WW}$ and its uncertainty for E97-103 kinematics was done by Wolfgang Korsch [98].

These evolutions of the parton distributions are next-to-leading order in perturbative QCD. There is a large difference between the leading order (LO) calculation and the next-to-leading order (NLO) calculation for $g_2^{n\ WW}$. It is possible that there could be another shift in the value of $g_2^{n\ WW}$ if a next-to-next-to-leading order calculation is done [98].

In addition, these same distributions and procedures can be used to calculate an expected value for g_1^n. Since twist three and higher effects are suppressed by Q in g_1^n, any deviation of our measured g_1^n from the value evolved down from large Q^2 would represent very large higher twist effects.

11.5 Extracting g_1^n

Since the E97-103 experiment focused on measuring g_2^n, the measurement of g_1^n is a not significant improvement of the world data set. However, it can be compared to values of g_1^n calculated using the procedure in Blümlein and Böttcher [97] and give an additional measure of confidence that the experiment was performed correctly.

Q^2 (GeV^2)	x	g_1^n	Stat. Err.	Sys. Err.
0.57	0.16	-0.0716	0.0056	0.0084
0.78	0.18	-0.0613	0.0079	0.0091
0.94	0.19	-0.0552	0.0052	0.0078
1.13	0.19	-0.0508	0.0051	0.0082
1.34	0.20	-0.0443	0.0053	0.0078

Table 11.3: *Values for g_1^n from E97-103.*

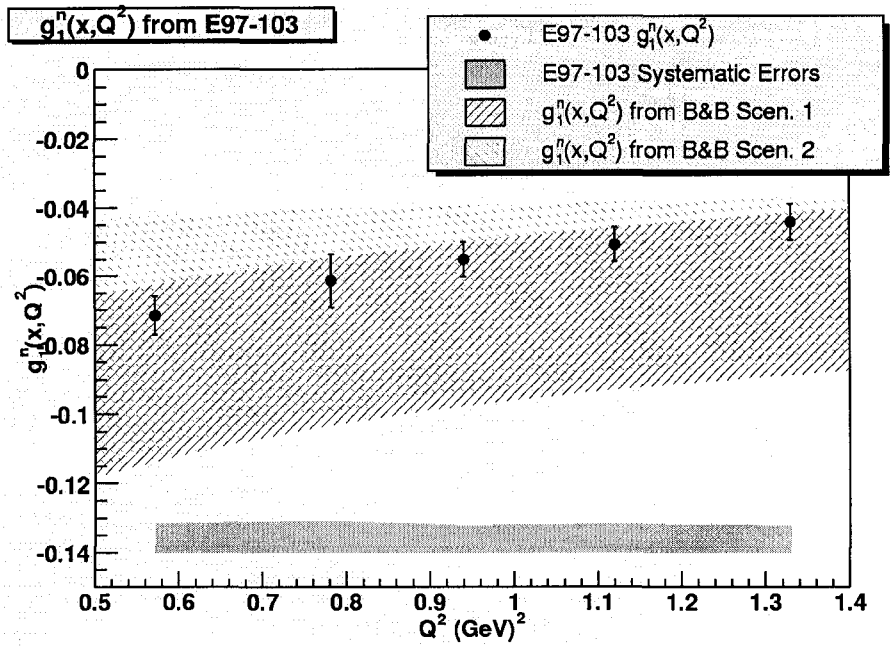

Figure 11.1: *The results for g_1^n and two calculations for g_1^n from the Blümlein-Böttcher parton distributions.*

Because Blümlein and Böttcher evolution uses g_1^n data at large Q^2 where higher twist effects should be small, any deviation from this g_1^n by our measured g_1^n is an indication of possible higher twist effects.

If higher twists were very large, then some deviation from expected values of g_1^n would be seen, but in all other cases the experimental data should agree with g_1^n.

The results for g_1^n are listed in Table 11.3 and plotted in Fig. 11.1. There is good agreement between the g_1^n presented here and the two scenarios from Blümlein and Böttcher. The largest systematic error associated with g_1^n is the systematic error on the unpolarized cross-section.

Q^2 (GeV^2)	x	g_2^n	Stat. Err.	Sys. Err.
0.57	0.16	0.0732	0.0083	0.0127
0.78	0.18	0.0791	0.0118	0.0132
0.94	0.19	0.0767	0.0088	0.0092
1.13	0.19	0.0488	0.0089	0.0078
1.34	0.20	0.0444	0.0086	0.0078

Table 11.4: *Values for g_2^n from E97-103.*

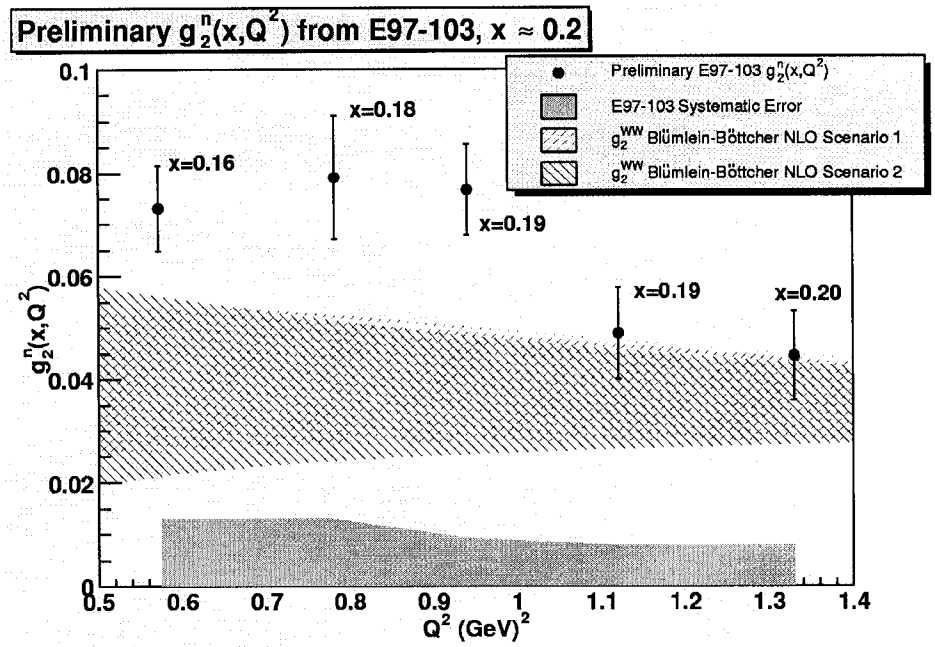

Figure 11.2: *The results for g_2^n and two calculations for $g_2^{n\ WW}$ from Blümlein and Böttcher.*

11.6 Results for g_2^n

The results of this analysis for g_2^n are presented in Fig. 11.2 and in Table 11.4. A comparison the data from the SLAC E155X and Jefferson Lab E99-117 experiments are shown in Fig. 11.3. The plot for g_2^n along Q^2 is accompanied by two calculations of g_2^{WW} by Blümlein and Böttcher. The comparison to the E155X data has two calculations of $g_2^{n\ WW}$, one at $Q^2 = 1.0$ GeV^2 and one at $Q^2 = 5.0$ GeV^2.

Looking at the plot of g_2^n vs. Q^2, significant deviation from $g_2^{n\ WW}$ is seen at the lower Q^2 points. An analysis of the deviation from g_2^{WW} is shown in Table 11.5. This table lists the number of standard deviations each experimental data point is

Q^2 (GeV^2)	Number of Standard Deviations from g_2^{WW}
0.57	2.3±1.2
0.78	2.5±0.8
0.94	3.1±1.1
1.13	1.0±0.9
1.34	0.8±0.8

Table 11.5: *The number of standard deviations from the central value for g_2^{WW} for each data point.*

from g_2^{WW}. A reasonable standard for asserting the presence of higher-twist effects is that the data points be two standard deviations from the nominal value for g_2^{WW}. Three of the points, $Q^2 = 0.57$ GeV^2, $Q^2 = 0.78$ GeV^2 and $Q^2 = 0.94$ GeV^2, have a $> 2\sigma$ deviation from the central value for g_2^{WW}. While this is not definitive, it is unlikely that this deviation is the result of systematic or statistical error in the experiment.

The deviations from g_2^{WW} in the $Q^2 = 0.78$ GeV^2 and $Q^2 = 0.94$ GeV^2 data are both positive and roughly double the size of the g_2^n. If the source of the deviation is higher twist effects, it means they are attractive and on the same order as the twist-two contribution to g_2^n. The lowest Q^2 point also shows a doubling of the nominal value of g_2^{WW}; however, the error bar on g_2^{WW} is larger at this kinematic and its difficult to make as clear a statement as the other two points.

Fig. 11.3 shows that E97-103 is a significantly more accurate measurement than the world data at any x. In fact, this is the first deep inelastic measurement of g_2^n that is clearly inconsistent with zero. This, in addition to any possible deviation from g_2^{WW}, is of considerable theoretical interest.

11.7 Summary of Systematic Errors on g_2^n

Table 11.6 shows the percentage error contribution to the structure function for each input parameter. The statistical error of the measurement is larger than any

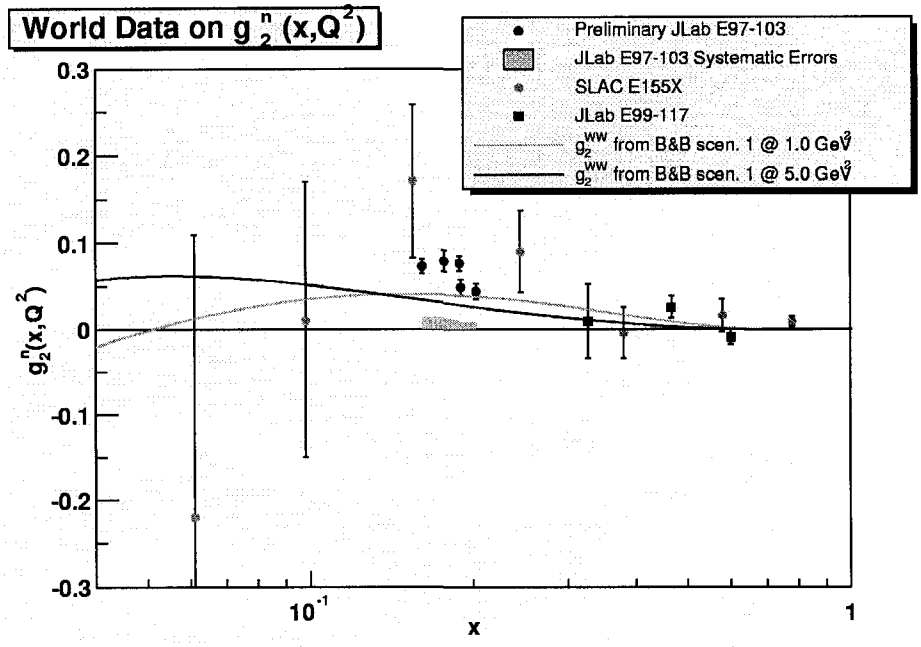

Figure 11.3: *The results for g_2^n vs. x plotted with E155X data.*

Parameter	$Q^2 = 0.57$	0.78	0.94	1.13	1.34 (GeV^2)
$A_{\|\|}$ Stat. Err.	2.1	2.5	1.9	2.8	3.6
$A_\perp$ Stat. Err.	11.3	14.9	11.4	18.2	19.4
False Asym.	6.2	6.0	4.2	7.2	7.2
P_{beam}	4.8	5.2	4.0	4.2	4.4
P_{trgt}	3.5	4.0	2.9	2.9	3.0
N_2 Factor	1.2	1.3	1.0	1.1	1.1
E	0.4	0.1	0.1	0.1	0.1
E'	0.02	0.03	0.02	0.02	0.02
θ	0.2	0.2	0.2	0.3	0.2
Unpol. XS	7.2	10.4	6.0	8.4	8.7
T. Pol. Inelas. RC	7.6	3.9	3.1	7.0	7.7
T. Pol. QE RC	9.2	6.5	5.3	6.1	7.6
T. Pol. Elas. RC	0.2	0.1	0.1	0.1	0.2
L. Pol. Inelas. RC	0.8	0.6	0.6	0.9	0.9
L. Pol. QE RC	0.5	0.3	0.3	0.3	0.3
L. Pol. Elas. RC	0.03	0.01	0.01	0.01	0.01
P_p	0.9	0.2	0.05	0.5	0.9
P_n	4.4	4.4	4.4	4.4	4.4
g_2^p	0.05	0.01	0.01	0.01	0.05
Tot. Stat. Err.	11.3	14.9	11.4	18.2	19.4
Tot. Sys. Err.	17.3	16.9	12.0	16.0	17.6

Table 11.6: *The percent error contribution to g_2^n.*

one source of systematic error. The largest source of error differs from kinematic to kinematic. The lowest Q^2 point has significant error from polarized radiative corrections from quasi-elastic scattering and from scattering above the pion-threshold. The other points have the unpolarized cross-section as the largest source of uncertainty, but it is not much larger than the uncertainty from radiative corrections and the false asymmetry.

Significant improvement of the systematic error bars is possible with the data already taken and the analysis available in this dissertation. It is hoped that the E97-103 collaboration will continue its work in extracting this important quantity.

One could improve the systematic error bars on g_2^n, if more polarized ^{3}He data in the quasi-elastic region and above pion-threshold and radiative corrections are re-calculated. Also improvement in the unpolarized cross-section could be made by a dedicated measurement on unpolarized ^{3}He. However, these improvements would not make a significantly clearer statement about g_2^n in relation to g_2^{WW} since the systematic errors are already on the order of the statical errors.

11.8 Conclusion

E97-103 has made a significant contribution to the world data of spin structure functions by making high-precision measurement of g_2^n at an $x \approx 0.2$. This data set is the first on g_2^n in the deep inelastic scattering region that shows significant deviation from zero. The statistical error bars on the data are an order of magnitude better than previous measurements of g_2^n in the kinematic region.

E97-103 has also found small deviations from $g_2^{n\ \mathrm{WW}}$ at two Q^2 points. The deviations are positive and are roughly the same size as g_2^{WW}. However, the deviations are not large enough to alleviate all possibility of consistency with g_2^{WW} and significant uncertainty is still present in the best calculation of g_2^{WW}.

It is unlikely a significantly more accurate measurement of g_2^n can be made in

this region with the technological resources available today. Consequently, the best way to improve the knowledge of higher-twists in g_2^n is to improve the accuracy of g_2^{WW}. This will take both theoretical and experimental effort. Considerable data will be taken in future years on polarized effective neutron targets that will have to be integrated into improved parton distributions. Also, a next-to-next-to-leading order calculation of g_2^{WW} is probably also necessary to reduce the uncertainty in the size of higher twist effects.

It is hoped that E97-103 will stimulate theoretical efforts to understand higher-twist contributions. It is also hoped that experimental efforts will follow in the path of measuring higher-twist contributions to the spin-structure functions so that a definitive picture of these important interactions can be made.

APPENDIX A

Magnetic Field Calibrations

Fig. A.1 and Fig. A.2 are plots of the holding field calibrations as described in section 6.8.1.

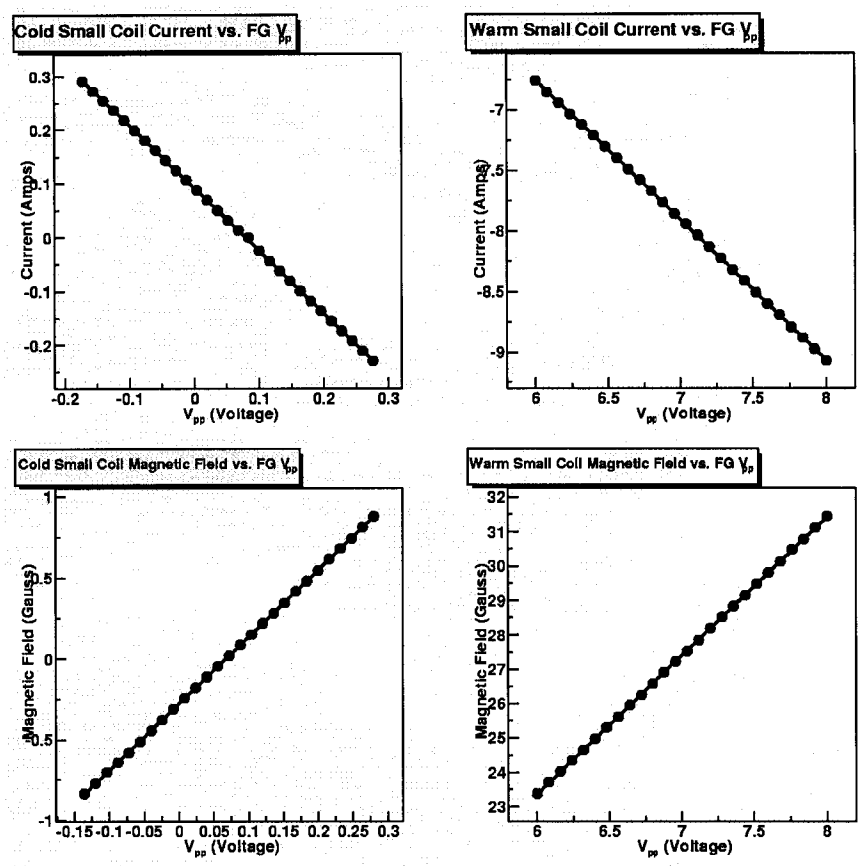

Figure A.1: *The calibrations of the small Helmholtz coils.*

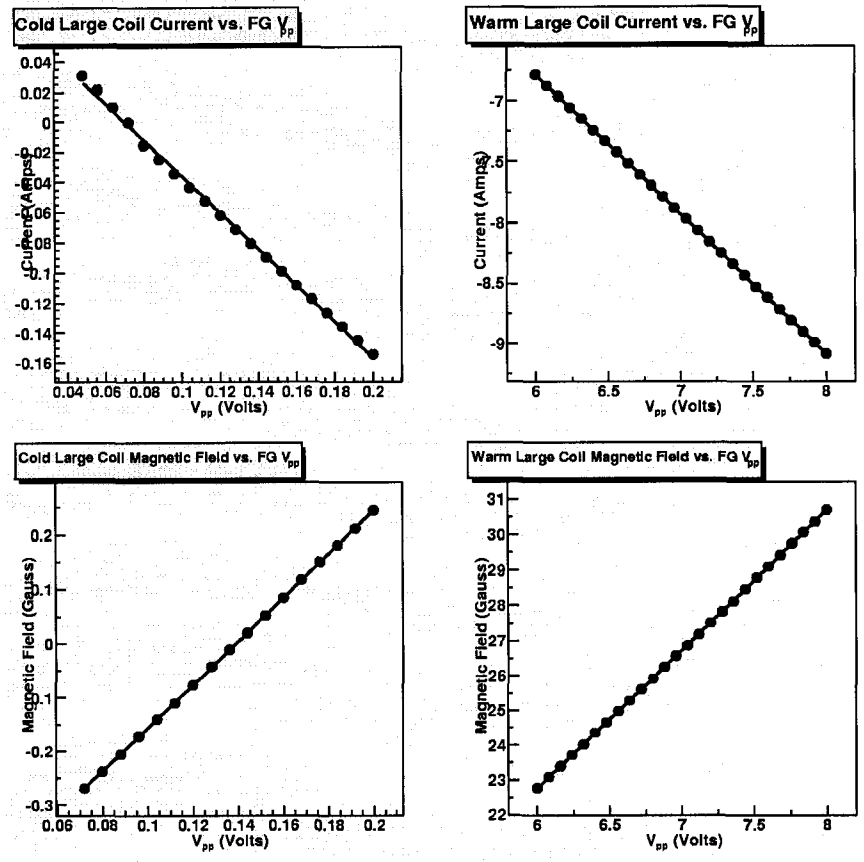

Figure A.2: *The calibrations of the large Helmholtz coils.*

APPENDIX B

Mapping of Holding Field Gradients

Fig. B.1 and Fig. B.2 are results of measuring the gradients of the holding field in the small and large coils detailed in section 6.8.2.

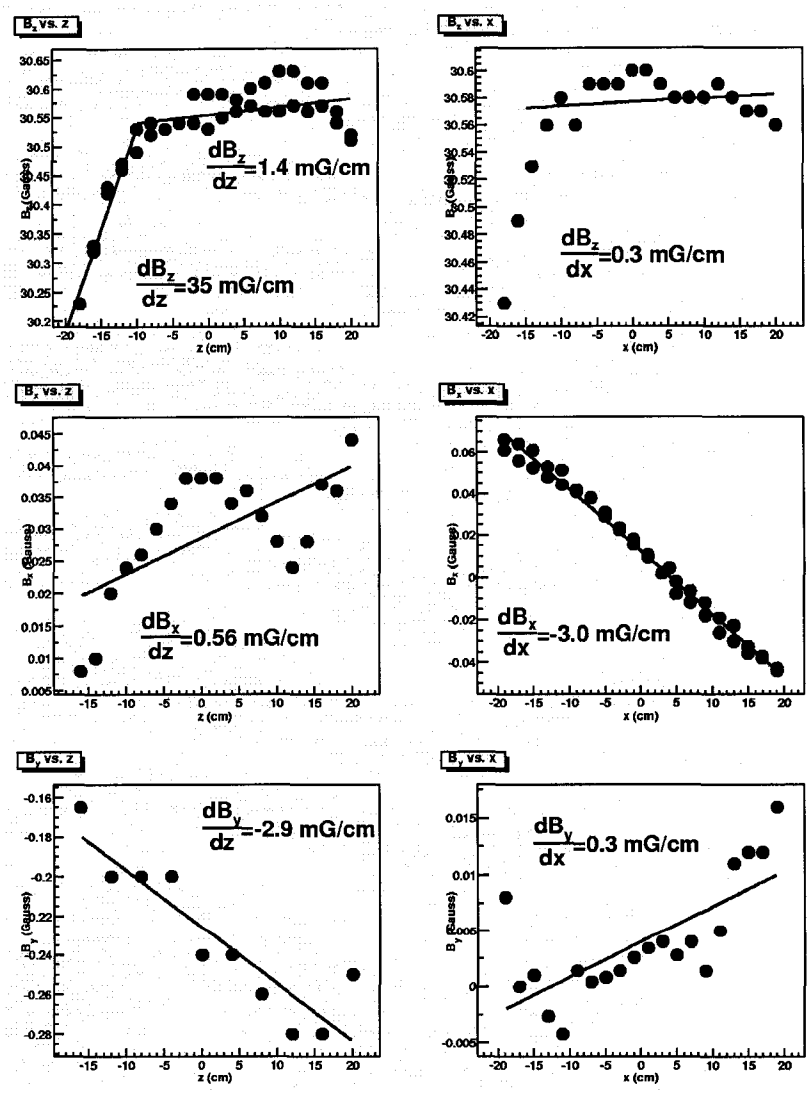

Figure B.1: *Holding field gradient measurements of the small Helmholtz coils.*

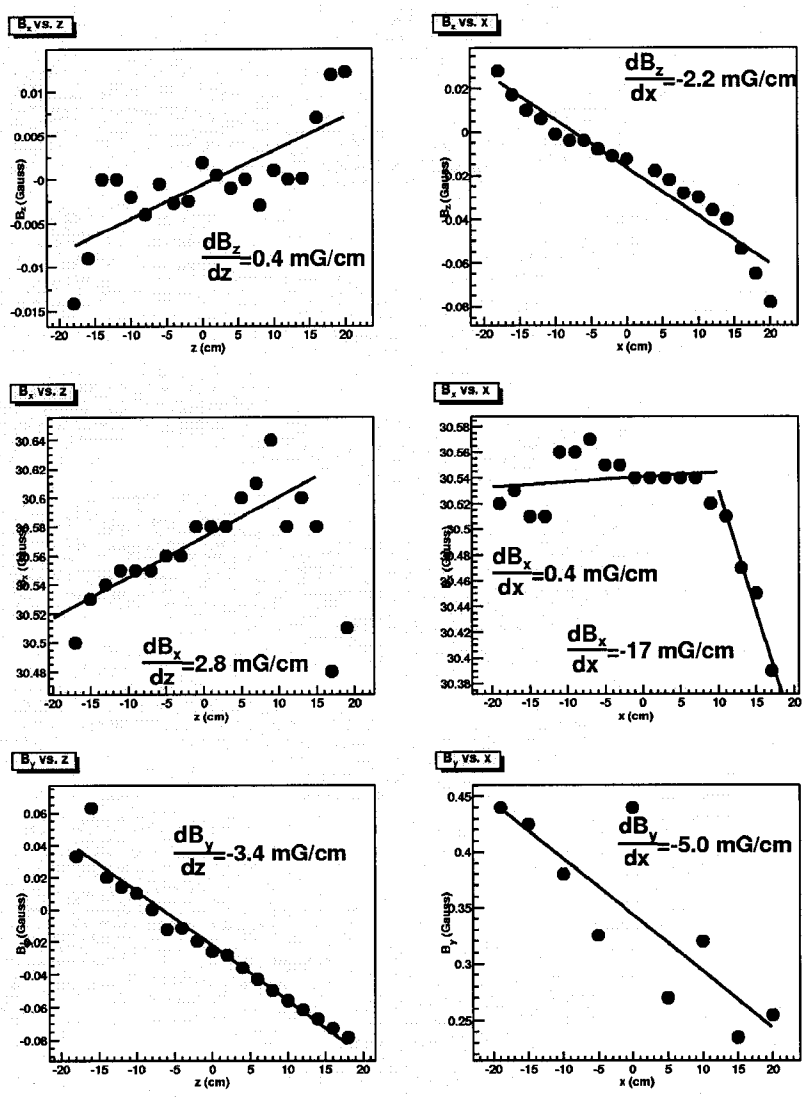

Figure B.2: *Holding field gradient measurements for the large Helmholtz coils.*

APPENDIX C

Results of Field Direction Surveys

There were four sets of surveys done of the polarized ^{3}He target holding field direction. All four were done with a compass and survey team as described in section 6.8.3. The surveyed angles are listed below accompanied by the calculations of the holding field direction based on the coil currents and the difference between the two. The currents in the gradient coils and some comments about the measurements are also listed.

24 May 2001			
Compass θ	Calibration θ	$\Delta\theta$	Comments
-0.230	-0.030	-0.200	flourescent light in scatt. chamber
-0.200	-0.030	-0.170	flourescent light removed
180.260	179.971	0.289	flip field direction
270.250	270.000	0.250	set field transverse
269.940	269.798	0.142	adjust field closer to 270°
88.930	88.918	0.012	flip field direction
89.770	89.775	-0.005	adjust field closer to 90°
89.830	89.775	0.055	set left arm Q1 to 3000 Amps

Table C.1: *Comparison of the results for the field direction of the compass survey with the holding field calibration.*

9 July 2001					
Compass θ	Calibration θ	$\Delta\theta$	L. Grad. I (Amps)	T. Grad. I (Amps)	Comments
0.040	-0.033	0.073	0.0	0.0	
180.430	179.962	0.468	0.0	7.0	
180.450	179.965	0.485	6.0	0.0	
180.440	179.965	0.475	6.0	0.0	
180.460	179.965	0.495	5.0	2.0	
180.430	179.965	0.465	0.0	0.0	adjusting current to 180°
180.270	179.982	0.288	0.0	0.0	
180.310	180.003	0.307	0.0	0.0	
180.310	180.023	0.286	0.0	0.0	
180.330	180.136	0.194	0.0	0.0	
179.580	177.908	1.672	0.0	0.0	
179.650	179.021	0.629	0.0	0.0	
180.030	179.578	0.452	0.0	0.0	
270.250	269.998	0.252	0.0	0.0	
270.260	269.998	0.262	5.0	2.0	
270.260	269.998	0.262	7.0	0.0	
270.250	269.998	0.252	0.0	7.0	
90.250	90.119	0.131	0.0	7.0	
90.260	90.120	0.140	6.0	0.0	
90.250	90.120	0.130	5.0	2.0	
90.260	90.121	0.139	0.0	0.0	
270.180	269.998	0.182	0.0	0.0	
270.570	269.998	0.572	0.0	0.0	after tapping compass
0.300	-0.029	0.329	0.0	0.0	
0.230	-0.029	0.259	0.0	0.0	after tapping compass

Table C.2: *Comparison of the results for the field direction of the compass survey with the holding field calibration.*

2 Aug 2001					
Compass θ	Calibration θ	$\Delta\theta$	L. Grad. I (Amps)	T. Grad. I (Amps)	Comments
-0.060	-0.026	-0.034	0.0	0.0	Spectrometer 45°
-0.040	-0.026	-0.014	5.0	5.0	
180.530	179.961	0.569	0.0	0.0	
180.290	179.962	0.328	0.0	0.0	
180.270	179.961	0.309	0.0	0.0	after tapping compass
90.590	90.125	0.465	0.0	0.0	
90.570	90.126	0.444	0.0	0.0	after tapping compass
90.570	90.127	0.443	5.0	5.0	
270.290	269.998	0.292	0.0	0.0	
270.280	269.998	0.282	5.0	5.0	
-0.450	-0.022	-0.428	0.0	0.0	Spectrometer 18.6°
-0.290	-0.023	-0.267	0.0	0.0	after tapping compass
-0.530	-0.264	-0.266	0.0	0.0	changed current
0.020	0.218	-0.198	0.0	0.0	changed current
-0.060	0.219	-0.279	5.0	5.0	tapped compass
180.170	179.958	0.212	0.0	0.0	
270.660	270.000	0.660	0.0	0.0	
270.510	270.000	0.510	0.0	0.0	
271.180	270.638	0.542	0.0	0.0	changed current
270.020	269.438	0.582	0.0	0.0	changed current
91.030	90.002	1.028	0.0	0.0	
89.920	88.930	0.990	0.0	0.0	changed current
89.910	88.929	0.981	5.0	5.0	
89.490	88.929	0.561	0.0	0.0	moved compass, Q1-R off
89.510	88.927	0.583	0.0	0.0	

Table C.3: *Comparison of the results for the field direction of the compass survey with the holding field calibration.*

18 Aug 2001					
Compass θ	Calibration θ	$\Delta\theta$	L. Grad. I (Amps)	T. Grad. I (Amps)	Comments
269.610	269.456	0.154	0.0	0.0	
269.590	269.458	0.132	2.0	5.0	
269.590	269.464	0.126	2.0	5.0	
89.080	89.131	-0.051	0.0	0.0	
89.110	89.131	-0.021	2.0	5.0	
89.080	89.131	-0.051	0.0	0.0	moved compass
89.080	89.129	-0.049	0.0	0.0	moved compass
89.090	89.128	-0.038	0.0	0.0	rotated compass
89.090	89.127	-0.037	0.0	0.0	changed fiducials
-0.480	-0.262	-0.218	0.0	0.0	
-0.490	-0.262	-0.228	2.0	5.0	
180.150	179.959	0.191	0.0	0.0	
180.160	179.959	0.201	2.0	5.0	

Table C.4: *Comparison of the results for the field direction of the compass survey with the holding field calibration.*

BIBLIOGRAPHY

[1] I. Estermann and O. Stern, Phys. Rev. **45**, 761 (1934).

[2] R. Frisch and O. Stern, Zeits. f. Physik **85**, 4 (1933).

[3] R. W. McAllister and R. Hofstadter, Phys. Rev. **102**, 851 (1956).

[4] R. P. Feynman, Phys. Rev. Lett. **23**, 1415 (1969).

[5] M. Gell-Mann, Phys. Lett. **8**, 214 (1964).

[6] G. Zweig, Cern Report **CERN-TH-412**, (1964).

[7] A. W. Thomas and W. Weise, *The Structure of the Nucleon* (Wiley-VCH, Berlin, Germany, 2001).

[8] S. Weinberg, Phys. Rev. Lett. **17**, 616 (1967).

[9] A. Salam, in *Elementary Particle Theory*, Nobel Symposium (Almquist and Forlag, Stockholm, Sweden, 1968), pp. 367–377.

[10] S. L. Glashow, J. Iliopoulos, and L. Maiani, Phys. Rev. **D2**, 1285 (1970).

[11] J. D. Bjorken and E. A. Paschos, Phys. Rev. **185**, 1975 (1969).

[12] Y. Kolomensky, Ph.D. thesis, University of Massachusets-Amherst, 1997.

[13] B. Filippone, in *14th Annual Hampton Users Graduate Studies* (World Scientific, Singapore, Singapore, 2001).

[14] O. Hansen, in *14th Annual Hampton Users Graduate Studies* (World Scientific, Singapore, Singapore, 2001).

[15] R.-W. Schulze and P. U. Sauer, Phys. Rev. C **48**, 38 (1993).

[16] A. Amroun *et al.*, Nucl. Phys. **A579**, 596 (1994).

[17] F. Bissey, V. Guzey, M. Strikman, and A. W. Thomas, Phys. Rev. **C65**, 064317 (2002).

[18] J. W. Lightbody and J. S. O'Connell, Computers in Physics **May/June**, 57 (1988).

[19] W. Leidemann *et al.*, Phys. Rev C **42**, 416 (1990).

[20] S. Choi, Private Communication, (Contact : Temple Unviersity, choi@jlab.org).

[21] M. Arneodo *et al.*, Nuclear Physics B **483**, 3 (1997).

[22] S. Wandzura and F. Wilczek, Phys. Lett. **B72**, 195 (1977).

[23] M. Peskin and D. Schroeder, *An Introduction to Quantum Field Theory* (Addison-Wesley, Reading, USA, 1995).

[24] A. V. Manohar, eprint hep-ph/9204208, 1992.

[25] B. W. Filippone and X.-D. Ji, Adv. Nucl. Phys. **26**, 1 (2001).

[26] R. L. Jaffe and X.-D. Ji, Phys. Rev. **D43**, 724 (1991).

[27] P. Mathews, V. Ravindran, and K. Sridhar, 1996, hep-ph/9607385.

[28] A. J. G. Hey and J. E. Mandula, Phys. Rev. **D5**, 2610 (1972).

[29] X. Song and J. S. McCarthy, Phys. Rev. **D49**, 3169 (1994).

[30] X. Song, Phys. Rev. **D54**, 1955 (1996).

[31] M. Stratmann, Z. Phys. **C60**, 763 (1993).

[32] K. Abe *et al.*, Phys. Rev. **D58**, 112003 (1998).

[33] A. Airapetian *et al.*, Phys. Lett. **B442**, 484 (1998).

[34] P. L. Anthony *et al.*, Phys. Lett. **B493**, 19 (2000).

[35] B. Adeva *et al.*, Phys. Rev. **D58**, 112001 (1998).

[36] J. Ashman *et al.*, Phys. Lett. **B202**, 603 (1988).

[37] K. Abe *et al.*, Phys. Rev. Lett. **75**, 25 (1995).

[38] P. L. Anthony *et al.*, Phys. Rev. **D54**, 6620 (1996).

[39] K. Ackerstaff *et al.*, Phys. Lett. **B404**, 383 (1997).

[40] K. Abe *et al.*, Phys. Rev. Lett. **79**, 26 (1997).

[41] X. Zheng, Ph.D. thesis, Massachusetts Institute of Technology, 2002.

[42] C. W. Leemann, D. R. Douglas, and G. A. Krafft, Ann. Rev. Nucl. Part. Sci. **51**, 413 (2001).

[43] R. Alley *et al.*, Nucl. Inst. Meth. **A365**, 1 (1995).

[44] J. Alcorn *et al.*, to be published in Nucl. Instrum. Meth. (Available at `http://hallaweb.jlab.org/`) (unpublished).

[45] J. P. Jorda *et al.*, Nucl. Instrum. Meth. **A412**, 1 (1998).

[46] J. Grames, Unique Electron Polarimeter Comparison and Spin-Based Energy Measurement, presented at IEEE Particle Accelerator Conference (PAC2001), Chicago, Illinois, 18-22 Jun 2001 (Available at `http://www.jlab.org/accel/inj_group/doc1.htm`).

[47] C. Jutier, Ph.D. thesis, Old Dominion University, 2001.

[48] J. Mitchell *et al.*, *Hall A Experimental Equipment Operations Manual*, The Hall A Collaboration, 2000, (Available at `http://hallaweb.jlab.org/document/OPMAN/`).

[49] K. Hagiwara *et al.*, Phys. Rev. **D66**, 010001 (2002).

[50] P. L. Anthony *et al.*, Phys. Lett. **B553**, 18 (2003).

[51] T. D. Averett *et al.*, Nucl. Instrum. Meth. **A427**, 440 (1999).

[52] K. Abe *et al.*, Phys. Lett. **B404**, 377 (1997).

[53] J. S. Jensen, Ph.D. thesis, California Institute of Technology, 2000.

[54] C. E. Jones *et al.*, Phys. Rev. **C47**, 110 (1993).

[55] J. Becker *et al.*, Eur. Phys. J. **A6**, 329 (1999).

[56] T. Chupp *et al.*, Phys. Rev. C **36**, 2244 (1987).

[57] M. V. Romalis, Ph.D. thesis, Princeton Unversity, 1997, uMI-97-27062.

[58] N. Newbury *et al.*, Phys. Rev. A **48**, 4411 (1993).

[59] K. Coulter *et al.*, Nucl. Inst. Meth. A **276**, 29 (1989).

[60] K. Bonin *et al.*, Phys. Rev. A **37**, 3270 (1988).

[61] I. Kominis, Ph.D. thesis, Princeton University, 2001.

[62] M. Amarian *et al.*, Phys. Rev. Lett. **89**, 242301 (2002).

[63] W. Xu *et al.*, Phys. Rev. Lett. **85**, 2900 (2000).

[64] W. H. Shoup, Private Communication, (Contact : University of Virginia, `whs7z@virginia.edu`).

[65] E. Hecht, *Optics*, 3rd ed. (Addison-Wesley, Reading, USA, 1998).

[66] A. Deur, E94-010 Technical Note 21, Jefferson Lab, (unpublished), (Available at `http://www.jlab.org/e94010`).

[67] S. Incerti, E94-010 Technical Note 9, Jefferson Lab, (unpublished), (Available at `http://www.jlab.org/e94010`).

[68] A. Abragam, *Principles of Nuclear Magnetism* (Oxford University Press, Oxford, UK, 1961).

[69] A. Thompson, Ph.D. thesis, Massachusets Institute of Technology, 1991.

[70] S. Incerti, E94-010 Technical Note 10, Jefferson Lab, (unpublished), (Available at `http://www.jlab.org/e94010`).

[71] S. Incerti, E94-010 Technical Note 21, Jefferson Lab, (unpublished), (Available at `http://www.jlab.org/e94010`).

[72] S. Incerti, E94-010 Technical Note 15, Jefferson Lab, (unpublished), (Available at `http://www.jlab.org/e94010`).

[73] W. Press *et al.*, *Numerical Recipes in C:The Art of Scientific Computing*, 2nd ed. (Cambridge, Cambridge, UK, 1992).

[74] A. Deur, Ph.D. thesis, Universite Blaise Pascal, 2000.

[75] N. Liyange, Ph.D. thesis, Massachusets Institute of Technology, 1999.

[76] K. Fissum, *Hall A VDC Manual V2.1*, Massachusets Institute of Technology, 1997, (Available at `http://www.jlab.org/~fissum/vdcs/documentation/docs.html`).

[77] A. Deur, E94-010 Technical Note 3, Jefferson Lab, (unpublished), (Available at `http://www.jlab.org/e94010`).

[78] *ESPACE Manual*, 2.9.0β ed., The Hall A Collaboration, (Available at `http://hallaweb.jlab.org/espace/index.html`).

[79] B. Reitz, Private Communication, (Contact : Jefferson Lab, `reitz@jlab.org`).

[80] R. Gilman, Private Communication, (Contact : Rutgers University, `gilman@jlab.org`).

[81] D. Armstrong, Private Communication, (Contact : The College of William and Mary, `armd@physics.wm.edu`).

[82] A. Deur, Hall A Tech Note JLab-TN-01-004, Jefferson Lab, (unpublished), (Available at `http://hallaweb.jlab.org/publications/Technotes/technote.html`).

[83] I. Akushevich *et al.*, Comput. Phys. Commun. **104**, 201 (1997).

[84] T. V. Kukhto and N. M. Shumeiko, Yad. Fiz. **36**, 707 (1982).

[85] I. V. Akushevich and N. M. Shumeiko, J. Phys. **G20**, 513 (1994).

[86] L. W. Mo and Y.-S. Tsai, Rev. Mod. Phys. **41**, 205 (1969).

[87] S. Stein *et al.*, Phys. Rev. **D12**, 1884 (1975).

[88] X. Zheng, Private Communication, (Contact : Argonne National Lab, xiaocho@jlab.org).

[89] J. S. O'Connell *et al.*, Phys. Rev. **C35**, 1063 (1987).

[90] K. Slifer, E94-010 Technical Note 44, Jefferson Lab, (unpublished), (Available at http://www.jlab.org/e94010).

[91] J. P. Chen, Private Communication, (Contact : Jefferson Lab, jpchen@jlab.org).

[92] M. Arneodo *et al.*, Phys. Lett. **B364**, 107 (1995).

[93] Y. Liang, Private Communication.

[94] L. W. Whitlow *et al.*, Phys. Lett. **B282**, 475 (1992).

[95] L. W. Whitlow *et al.*, Phys. Lett. **B250**, 193 (1990).

[96] L. W. Whitlow, Ph.D. thesis, Stanford University, 1990.

[97] J. Blumlein and H. Bottcher, Nucl. Phys. **B636**, 225 (2002).

[98] W. Korsch, Private Communication.

VITA

Kevin Michael Kramer

Kevin Michael Kramer was born in Rockledge, Florida, on 30 October 1972. Graduated from Langham Creek High School in Houston, Texas, in May 1991. Received a Bachelor of Science degree in physics from the University of Texas at Austin in Austin, Texas in May 1995. Entered the physics graduate program at the College of William and Mary in Virginia in 1997. Received a Master of Science degree in physics from the College of William and Mary in Virginia in May 1999. This dissertation was defended on August 1, 2003 at the College of William and Mary in Virginia.